Institute of Condensed Matter and Nanosciences
Molecular Chemistry, Materials and Catalysis division
Laboratory of Physical Chemistry
Prof. Tom Leyssens

# Influence of the solvent on the crystallization of multi-component compounds comprising chiral molecules

**Joséphine de Meester**

Louvain-la-Neuve 2024

# Jury members

Prof. T. Leyssens (Supervisor)

UCLouvain

Prof. E. Van Ruymbeke (Presidente)

UCLouvain

Prof. S. Hermans

UCLouvain

Prof. J. Wouters

UNamur

Prof. P. Subra-Paternault

Université de Bordeaux

Dr. C. Harscoat-Schiavo

Université de Bordeaux

# Remerciements

Je souhaite adresser mes remerciements les plus sincères à toutes les personnes qui ont joué un rôle essentiel dans la réalisation de cette thèse.

Tout d'abord, je tiens à exprimer ma profonde gratitude envers le Professeur Tom Leyssens, mon promoteur de thèse, pour son expertise, son soutien, sa disponibilité et les précieux conseils qu'il m'a donnés tout au long de ce parcours doctoral.

Je tiens également à remercier chaleureusement le Docteur Christelle Harscoat-Schiavo pour m'avoir accueilli dans son laboratoire lors de mon stage de recherche à l'université de Bordeaux. Son encadrement et ses conseils avisés, ainsi que ceux du Professeur Pascale Subra-Paternault, ont grandement enrichi mon expérience et ont contribué de manière significative à cette thèse. Je remercie également le Professeur Johan Wouters, avec qui j'ai eu le privilège de collaborer durant ces quatre dernières années.

Je tiens également à remercier les membres de mon jury de thèse, le Professeur Tom Leyssens, le Professeur Evelyne Van Ruymbeke, le Professeur Sophie Hermans, le Professeur Johan Wouters, le Professeur Pascale Subra-Paternault ainsi que le Docteur Christelle Harscoat-Schiavo pour leur expertise, leurs conseils ainsi que pour le temps qu'ils ont consacré à la lecture et la correction de cette thèse.

Un tout grand merci également au Docteur Koen Robeyns, au Docteur Oleksii Shemchuk et à Laurent Collard pour leur soutien précieux dans les analyses menées tout au long de ce projet, ainsi que pour leurs nombreux conseils et remarques qui auront été essentiels à ce travail. Je voudrais également exprimer ma reconnaissance envers François Billard et Jean-François Statsyns pour l'aide qu'ils ont apportée lors des manipulations ainsi pour que les nombreuses discussions que nous avons eues ensemble.

Lors de cette thèse, j'ai eu la possibilité d'encadrer des étudiants qui réalisaient un stage ou leur mémoire de fin de master. Ainsi, je souhaite également exprimer ma gratitude envers Kadiatou Barry, Maximilien Garry et Simon Baillieux, pour leur contribution précieuse à ce travail de recherche.

À mes chers collègues devenus amis, Camila, Chloé, Guillaume, Ting, Yihua, Job, Daniel, Carole, Natalia et Crystal, ainsi que tout le b1, je vous adresse mes plus sincères remerciements pour votre soutien, votre camaraderie et les beaux moments partagés.

Un tout grand merci également à l'ensemble des personnes que j'ai pu côtoyer lors de mon séjour à Bordeaux, et tout particulièrement à Patrick Layrisse, avec qui j'ai eu le plaisir de travailler en équipe lors de cet échange.

Un grand merci au Docteur Michael Guillot, qui a été mon encadrant de mémoire et qui a su éveiller en moi la passion pour la recherche.

Enfin, je tiens à remercier du fond du cœur ma famille et mes amis pour leur soutien inconditionnel, leur encouragement et leur compréhension tout au long de ce parcours académique.

À tous ceux qui ont contribué de près ou de loin à cette thèse, je vous suis infiniment reconnaissante.

# List of Publications

Guillot, M.; de Meester, J.; Ter Horst, J. H.; Riant, O.; Leyssens, T. Fungicide precursor racemization kinetics for deracemization in complex systems. *European Journal of Organic Chemistry*, **2021**, *2021* (3), 473-482.

Guillot, M.; de Meester, J.; Collard, L.; Riant, O.; Leyssens, T. Co-crystallization-induced spontaneous deracemization: an optimization study. *Organic Process Research & Development*, **2021**, *25* (4), 884-891.

Sabarwal, A.; van Rooyen, J. C.; Caburet, J.; Avgenikos, M.; Dheeraj, A.; Ali, M.; Mishra, D.; de Meester, J.; Stander, S.; van Otterlo, W. A. L.; Kaschula, C. H.; Singh, R. P. A novel 4′-brominated derivative of fisetin induces cell cycle arrest and apoptosis and inhibits EGFR/ERK1/2/STAT3 pathways in non-small-cell lung cancer without any adverse effects in mice. *The FASEB Journal*, **2022**, *36* (12), e22654.

de Meester, J.; Shemshuk, O.; Collard, L; Wouters, J.; Baillieux, S.; Robeyns, K.; Leyssens, T. Using the nature of the achiral solvent to orient chiral resolution. *CrystEngComm*, **2024**, *26* (15), 2056-2059.

de Meester, J.; Layrisse, P.; Marchivie, M;. Collard, L.; Wery, G.; Brandel, C.; Cartigny, Y.; Subra-Paternault, P.; Leyssens, T.; Harscoat-Schiavo, C. Towards a new approach in chiral resolution: pressurized-$CO_2$ assisted preferential cocrystallization. *The Journal of Supercritical Fluids*, **2024**, 212, 106339.

de Meester, J.; Shemshuk, O.; Collard, L; Wouters, J.; Robeyns, K.; Leyssens, T. Combining two chiral compounds: the importance of the solvent for resolution. To be submitted

# List of Abbreviations

| | |
|---|---|
| ACN | Acetonitrile |
| benz | Benzene |
| BINOL | 1,1'-bi-2-naphtol |
| CCDC | Cambridge crystallographic data centre |
| CDR | Chiral derivation reagent |
| CD | Circular dichroism |
| $CO_2$ | Carbon diaoxide |
| CPC3 | Continuous preferential crystallization using three flasks |
| CSP | Cchiral stationary phase |
| DACH | *trans*-cyclohexane-1,2-diamine |
| DADPE | *N,N'*-dimethyl-1,2-diphenylethane-1,2-diamine |
| DCM | Dichloromethane |
| DSC | Differential Scanning Calorimetry |
| *ee* | Enantiomeric excess |
| EtOAc | Ethyl acetate |
| EtOH | Ethanol |
| FDA | Food and drug administration |
| GAS | Gaseous antisolvent |
| $H_2O$ | Water |
| HPLC | High-performance liquid chromatography |
| IPA | Isopropanol |
| k | Rate constant |
| MA | Mandelic acid |
| MeOH | Methanol |
| nefi | Nefiracetam |
| NMR | Nuclear Magnetic Resonance |
| SC-$CO_2$ | Supercritical carbon dioxide |
| SC-XRD | Single Crystal X-ray diffraction |
| SFC | Supercritical fluid chromatography |
| TGA | Thermogravimetric Analysis |
| tolu | Toluene |
| TS | Transition state |
| UV | Ultraviolet |
| VT-XRPD | Variable Temperature Powder X-ray Diffraction |
| XRPD | X-ray powder diffraction |

# Abstract

Crystallization-based resolution methods are of utmost importance in industrial applications. Yet the understanding of the solvent influence in such processes remains poorly developed in the literature. Therefore, this work investigates the pivotal role of solvent in crystallization phenomena, focusing specifically on chiral molecules and on the development of resolution methodologies.

The present study investigates three distinct systems.

First, we meticulously explored the interplay between two racemic compounds, 1,1'-bi-2-naphtol (BINOL) and *trans*-cyclohexane-1,2-diamine, across various solvent environments. We highlighted how the nature of the solvent can have an important impact on the type of multicomponent solid obtained. Complete characterization of the obtained phases demonstrated that when developing a chiral resolution process, the solvent must be chosen carefully. This chapter emphasizes both the potential complexity introduced by the solvent and the profound impact of the solvent choice on the efficiency of a chiral resolution process.

Second, diastereomeric resolution of BINOL using (*R*,*R*)-*N*,*N*′-dimethyl-1,2-diphenylethane-1,2-diamine as a resolving agent was developed in two achiral solvents, toluene and benzene. We discovered how the solvent choice dictates the obtained thermodynamic form, enabling to recover by crystallization either (*S*)- or (*R*)-BINOL, when using respectively toluene or benzene. Isoplethal ternary diagrams were constructed in order to optimize resolution conditions and facilitate scalability.

Finally, we developed the preferential crystallization of the Mandelic acid-Nefiracetam cocrystal-conglomerate system, using pressurized $CO_2$ as an antisolvent. First, we demonstrated the proof-of-concept of preferential crystallization through pressurized $CO_2$ and studied various parameters influencing resolution. Secondly, system optimization enabled simultaneous resolution of both enantiomers.

These investigations underline the underestimated role of solvent, highlighting its potential as a passive medium or as an active tool, shaping resolution processes and allowing to tailor the desired crystalline forms to target a specific enantiomer.

# Table of Contents

# Chapter 1. General introduction

# General introduction

In the vast landscape of scientific research, two areas are shaping the future of pharmacology, materials design and molecular synthesis: crystal engineering and chirality. These two fields, although distinct, are converging harmoniously to offer innovative perspectives in areas ranging from pharmacology to asymmetric catalysis.

Crystal engineering aims to design and control the solid state in order to obtain specific properties.[1] In parallel, chirality, a fundamental property of molecules that exist in two non-superimposable enantiomeric forms, has captivated the interest of researchers for decades for its profound implications in chemistry and biology.[2]

In this introduction, we will explore how these two fields meet and influence each other. We will begin by a rapid introduction of crystal engineering. Subsequently, we will take an in-depth look at chirality, its definition, why it is important from a biological point of view, how to obtain enantiopure compounds, and how crystal engineering can be exploited in achieving this goal.

# 1. Crystal engineering

Crystal engineering is the construction of crystalline materials from molecules or ions using noncovalent interactions.[1] It finds applications across diverse fields, including electrics,[3] dyes,[4] catalysis,[5] $CO_2$ trapping,[6] $H_2$ storage,[7] and pharmaceutical development.[8–11] However, before reaching its status of a distinct branch of chemistry in continuous and rapid evolution, several important milestones were taken.

The term "crystal engineering" was first introduced by Pepinsky at the meeting of the American Physical Society in Mexico City in 1955 as a concept for engineering crystals with advantageous properties.[12,13] Few years later, in 1989, Desiraju characterized crystal engineering as *"*the understanding of intermolecular interactions in the context of crystal packing and the utilization of such understanding in the design of new solids with desired physical and chemical properties*"*.[13,14] Concurrently, Charles Pedersen, Donald Cram and Jean-Marie Lehn were awarded the Nobel Prize in Chemistry in 1987 for their work on supramolecular chemistry.[15] Subsequent developments, such as the introduction of concepts like supramolecular synthons in 1995[13] and hetero-synthons, highlighted the logic behind crystal structures, providing a better understanding of supramolecular assemblies.[11]

Crystal engineering allows to navigate between different solid-state forms (Figure 1.1). When considering solids, they may exist in either amorphous or crystalline state, with the latter characterized by an ordered arrangement of molecules, ions or atoms. Indeed, a crystal is a three-dimensional arrangement wherein a pattern, termed as asymmetric unit, is repeated through different symmetry operations yielding to a unit cell. The regular repetition of this unit cell through translation gives rise to the crystal structure. On the contrary, a solid is designated as amorphous when its order at the solid state is confined to local domains.[16]

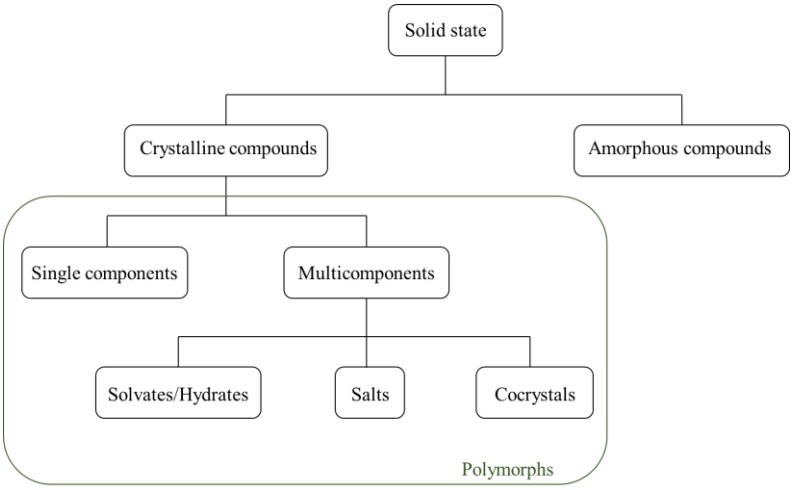


Figure 1.1. Solid state classification.

Polymorphs and multicomponent crystals, such as cocrystals, salts, and solvates, are actively studied in crystal engineering because of their ability to systematically modify the physicochemical properties (as pharmacokinetics or mechanical properties) of molecules.[16–18]

## 1.1 Polymorphs

Polymorphism refers to the phenomenon where compounds exist in multiple crystalline forms, despite having the same chemical composition. These different forms, known as polymorphs, exhibit a different structure and hence show different properties such as melting point, chemical stability, solubility or even color.[19–22] Polymorphism exists for mono- and multicomponent crystals.[17] A classical example is carbon, which can crystallize as either diamond or graphite, depending on crystallization conditions.[20]

Polymorphs differ in free energy, with one form being thermodynamically most stable under specific conditions of temperature and pressure. If various polymorphs can be readily accessed, they typically exhibit free energy differences of less than 10 kJ/mol.[19,22] Forms that fall outside this range are usually inaccessible from an experimental point of view, thus narrowing the infinite theoretical possibilities to a finite yet extensive array of realistic options. This aligns with McCrone's statement that the number of known forms for a compound correlates with the research effort invested in studying that compound.[19] A striking example is the case of solid water, highly studied. In 2020, the total number of polymorphs discovered was 18, thanks to intensive studies, some of them conducted theoretically or under extreme pressure and temperature conditions (Figure 1.2).[23–25]

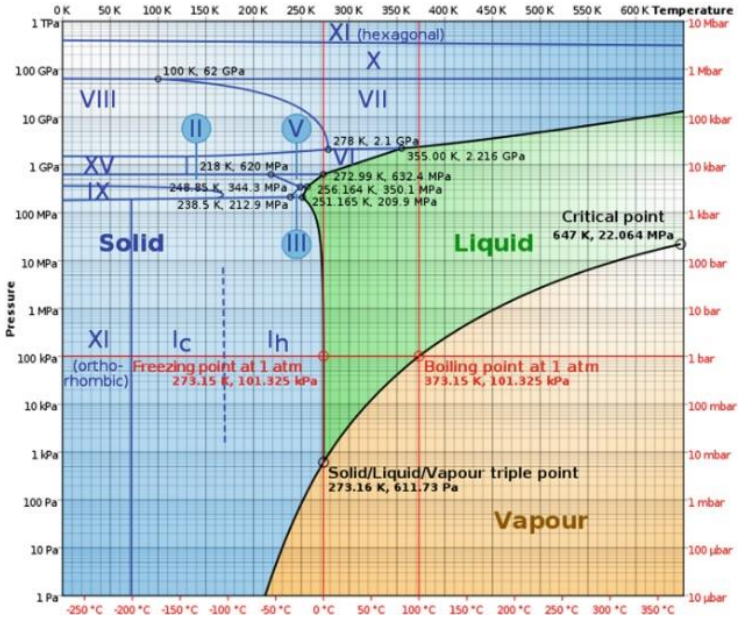


Figure 1.2. Pressure-temperature phase diagram of water.[25]

The appearance of one polymorph over another depends on nucleation kinetics and polymorph stability. The thermodynamically favored form is not always the one that crystallizes first. Starting with a supersaturated solution, a polymorphic system often evolves first to the easiest attainable state, even if metastable, before reaching equilibrium with the most stable form. The equilibrium is established when the overall stable form is reached. This can lead to the sudden appearance or disappearance of one crystalline form. Therefore, a complete understanding of the kinetics and mechanism of phase transformation is of utmost importance in pharmacology, as it can lead to serious consequences, as those encountered with the drug Ritonavir (Figure 1.3).[16,17]

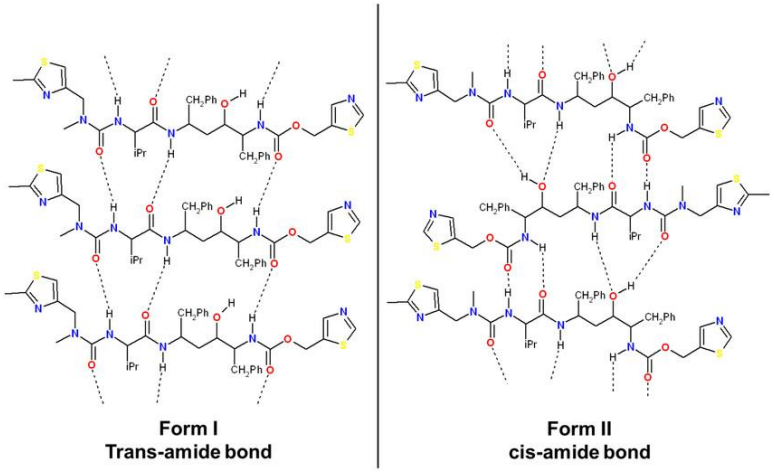


Figure 1.3. Hydrogen bonds present in the crystal structures of Ritonavir forms I and II.[26]

Ritonavir was approved in 1996 as a protease inhibitor for the treatment of AIDS. During the development of the drug, only one crystal form (I) was identified.
The compound was formulated in capsules in an ethanol/water solution. However, in 1998, crystals of an undesirable polymorph (II) were discovered in these capsules. This newly discovered form II had a reduced solubility compared to form I, therefore diminishing its bioavailability. This led to the withdrawal of Ritonavir from the pharmaceutical market until 1999, when the drug was reintroduced after an improved formulation.[21] When comparing the crystal structures of forms I and II (Figure 1.3), we can see differences in the relative arrangement of the molecules, consequently affecting the hydrogen bond pattern.[26] Eventually, other polymorphic forms, as well as different solvates, were discovered, all less stable than form II.[27,28]
This incident led to systematic polymorph screening prior to drug market entry.[19,22]

## 1.2 Solvates/Hydrates

Polymorph screening and crystallization techniques are usually conducted in solution. During these processes, the compound may crystallize with solvent molecules incorporated into the crystal lattice, resulting in the formation of a solvate. If water is the solvent involved, the resulting crystalline phase is then called a hydrate.[29,30]

The stability of solvates depends on the temperature and the thermodynamic activity of the solvent in the surrounding liquid. In the absence of a liquid phase, the stability of solvates relies on temperature and partial pressure of the solvent in the vapor phase. Therefore, solvates can be avoided by working at elevated temperatures and/or decreasing the solvent activity around the molecule of interest.[31]

Commonly utilized techniques for characterizing and studying solvates include thermogravimetric analysis (TGA) and differential scanning calorimetry (DSC). TGA quantifies the solvent loss upon heating, facilitating the determination of stoichiometry. DSC provides insights into desolvation enthalpy and may reveal the existence of recrystallization phenomena.[29,32]

## 1.3 Organic salts

Salts are neutral multicomponent crystalline solids that are composed by two or more charged species: cation(s) and anion(s).[33,34]

Organic salts result from the partial or complete replacement of the acid hydrogens by a metal.[35] Due to charged-assisted hydrogen bonds and ionic interactions, they exhibit a favorable enthalpy of hydration, rendering them water-soluble. [9] Thus, salt formation stands as the primary approach to address issues of poor solubility and dissolution rate of a drug, thereby improving the bioavailability of an active pharmaceutical ingredient. It is estimated that around 50% of drugs are marketed as salts.[8,36]

## 1.4 Cocrystals

The definition of a cocrystal is widely recognized as a crystalline multicomponent material composed of at least two neutral components, called coformers, that are solid under normal conditions and are bonded to each other through non-covalent intermolecular interactions, such as hydrogen bonds, halogen bonds, π stacking, and van der Waals interactions.[9,13,37,38] For a molecule of interest, if the selection of its coformer is based on trial and error, it is guided by the identification of supramolecular synthons (repetitive interaction patterns that facilitate cocrystallization) between both molecules.[8,13,39,40] The term heterosynthon is used when molecular recognition arises from different moieties, while homosynthon refer to similar moieties (Figure 1.4).[39]

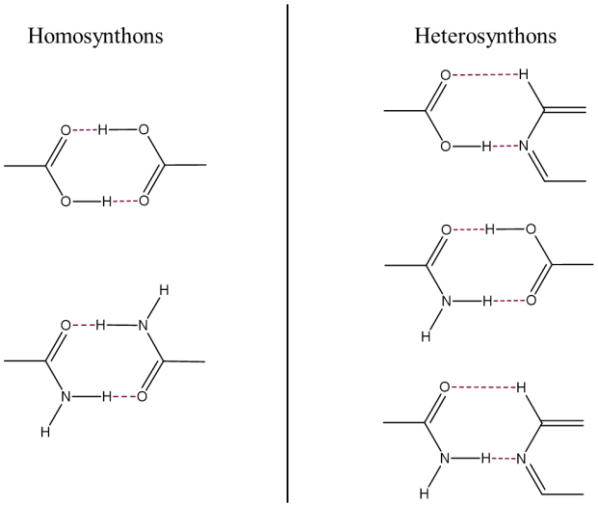


Figure 1.4. The most common synthons encountered in crystal engineering.

Common methods for cocrystal synthesis include solid-state cocrystallization (which encompasses different approaches such as neat and liquid-assisted grinding, and contact formation) and conventional solvent-mediated techniques (as slow evaporation, cooling, antisolvent addition, supercritical fluid methods, and slurry crystallizations). These latter techniques are widely used in industry as they are easily scalable.[8,39,41]

When the cocrystal is placed in a solvent, two types of systems are identified: congruent systems, where the cocrystal is formed under a stoichiometric ratio of the component in that solvent, and incongruent systems, where stoichiometric ratio of the molecules leads to the precipitation of either one of the pure components or a mixture of pure components and cocrystals.[37] In Figure 1.5a, both compounds A and B have similar solubilities in the solvent, leading to the formation of an A-B cocrystal when the compounds are added to the solvent in a (1:1) ratio. However, when compounds A and B have different solubilities (Figure 1.5b), the experiment in a molar ratio (1:1) results in the obtention of one of the parent compounds.

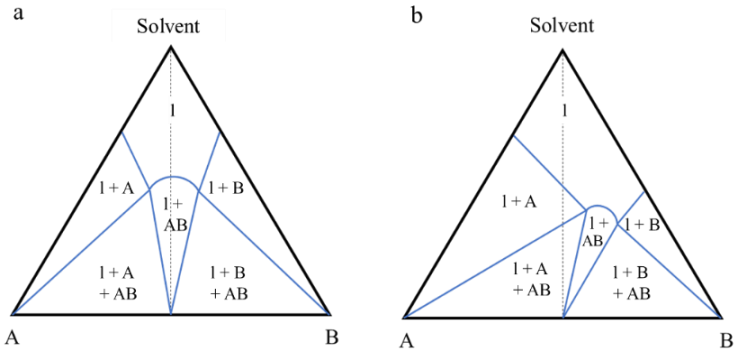


Figure 1.5. Ternary isothermal phase diagrams of an AB cocrystal system for the two possible systems: a) congruent, b) incongruent.

Distinguishing between cocrystals and salts can be difficult. Generally, the ΔpKa rule is used to predict the formation of cocrystals or salts. As a general guideline, a ΔpKa (pKa of the conjugate acid or base – pKa of the acid) greater than 3 leads to the formation of a salt and a ΔpKa less than 0 leads to the formation of a cocrystal. However, when ΔpKa is between 0 and 3 a cocrystal-salt continuum appears (Figure 1.6).[13,39]

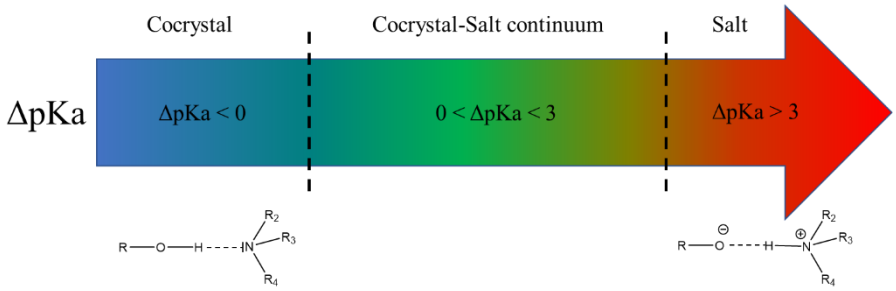


Figure 1.6. ΔpKa rule used to predict the formation of cocrystals (ΔpKa < 0) or salts (ΔpKa > 0), and the cocrystal-salt continuum (0 < ΔpKa < 3). Adapted from[42]

# 2. **Chirality**

## 2.1 Definition

Chirality is omnipresent in nature, at different scales, from the celestial region where the presence of circularly polarized light is certified,[43] to macroscopic entities (*e.g.* *Paenibacillus vortex* colonies expand radially[44,45] (Figure 1.7a) and our two hands (Figure 1.7b)) –, to molecules. The word "chiral" comes from the Greek χειρ (keir), "hand". An object exhibits chirality when it lacks mirror plane symmetry, meaning it cannot be superimposed onto its mirror image.[46,47]

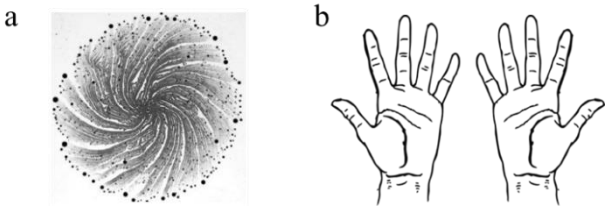


Figure 1.7. Illustration of two macroscopic chiral entities, a) radial expansion of *Paenibacillus vortex* colony[45], b) hands.

When applied to molecules, chirality results in the existence of two enantiomers, which are non-superimposable mirror images of the same substance (the right- and the left-handed compounds).[46–48]

The most encountered chiral molecules are defined by a stereogenic center (carbon, phosphorus, nitrogen, silicon, boron or sulphur linked to all different substituents), but three other types of chirality exist, planar, axial and helical (Figure 1.8).

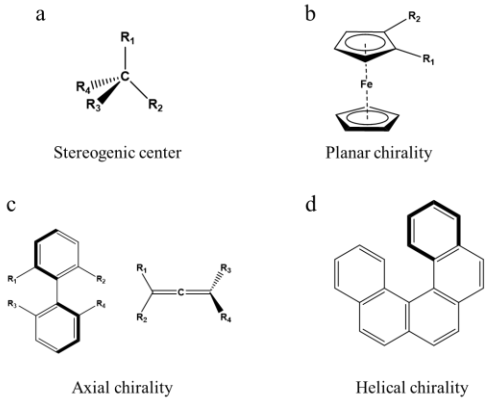


Figure 1.8. The four possible types of chirality a) stereogenic center, b) planar chirality represented with a ferrocene-type molecule, c) axial chirality represented by biaryls and alleles, d) helical chirality.

The Cahn-Ingold-Prelog (CIP) rules are used to systematically name enantiomers. They specify the spatial arrangement of substituent groups around a stereogenic center by including a descriptor in the systematic name of the molecule, which depends on the priority of the groups. This allows to accurately describe the stereochemistry of organic compounds. The CIP rules are as follows (Figure 1.9): [2,47]

- Priority Assignment: Priority is assigned to each substituent attached to the stereogenic function, according to the atomic number of the atoms directly bonded to it. The higher the atomic number, the higher the priority. If there is a tie, the next linked atom is used, until a difference is found.
- Orienting the Molecule: The molecule is oriented so that the lowest priority group is pointing away from the viewer.
- Clockwise or Counterclockwise: Determine whether the sequence of priority groups (highest to lowest) around the chiral function is clockwise (*R*) (for rectus or right) or counterclockwise (*S*) (for sinister or left).

A sample with an equimolar composition of two enantiomers is called a racemic mixture or racemate. It is therefore described as (*R*,*S*) or (*rac*).[2]

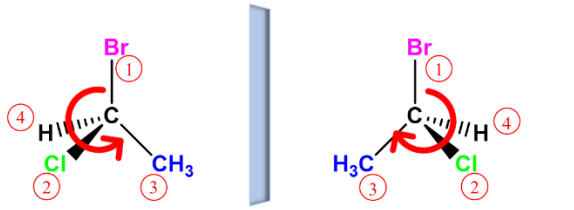


(*S*)-1-bromo-1-chloroethane (*R*)-1-bromo-1-chloroethane

Figure 1.9. CIP rules applied for describing 1-bromo-1-chloroethane.

The enantiomeric excess (*ee*) is used to express the excess of one enantiomer over the second in a mixture. It is expressed as:

$$ee\ (\%) = \frac{\left|((R) - \text{enantiomer}) - ((S) - \text{enantiomer})\right|}{\left|((R) - \text{enantiomer}) + ((S) - \text{enantiomer})\right|} \text{x } 100$$

An enantiopure compound corresponds to an *ee* of 100%, whereas a racemic mixture corresponds to an *ee* of 0%.[49]

While enantiomers are mirror images and possess identical Gibbs free energy, compounds with multiple stereogenic units may be non-superimposable without being mirror images, they are then termed as diastereomers (Figure 1.10). Unlike enantiomers, diastereomers possess different Gibbs free energy values, resulting in different physicochemical properties in an achiral environment.[2,47,49]

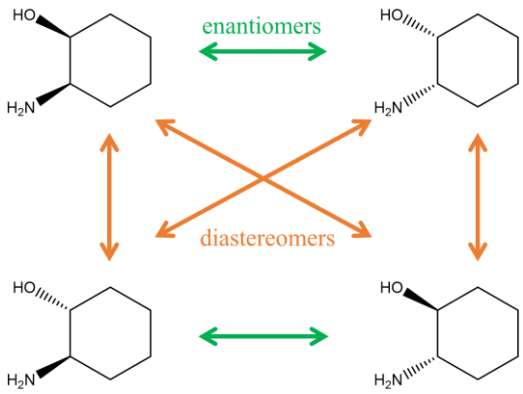


Figure 1.10. Schematic diagram showing the diastereomeric and enantiomeric relationships in 2-Aminocyclohexanol, a chiral molecule comprising two stereogenic centers.

From a physicochemical perspective, a pair of enantiomers exhibits identical properties in an achiral environment. Therefore, parameters such as melting point, boiling point, and solubility are equivalent for both enantiomers.[2,50] However, one notable difference observable at a macroscopic level is their ability to rotate plane-polarized light in opposite directions. Enantiomers exhibit either clockwise (dextrorotatory) or counterclockwise (levorotatory) rotation of plane-polarized light. Hence, they can be designated (+) or *d;* or (-) or *l* respectively.[2,51,52] Nevertheless, since the specific rotation experienced by polarized light ((+) or (-)) is not linked to the absolute configuration ((*R*) or (*S*)) of a molecule, enantiomers are denoted as (*R*)-(+) or (*R*)-(-) and (*S*)-(-) or (*S*)-(+).

We can also mention the uppercase notations L and D that are also utilized to define enantiomeric forms.[53] This nomenclature, established in the early 20th century, relies on glyceraldehyde as a reference for assignment of many chiral biomolecules (such as carbohydrates and amino acids). Typically, these substances are depicted using the Fisher projection, where an asymmetric carbon is represented as the point where two perpendicular lines intersect. In this convention, the carbon chain is consistently shown with the carbonyl function positioned at the top of the backbone, with horizontal branches indicating bonds projecting towards the viewer, and vertical lines representing bonds extending away from the viewer. Depending on whether the lowest -OH or -$NH_2$ group is positioned on the left or right side of the Fisher projection, glyceraldehyde or amino acids are termed L- or D-, respectively (Figure 1.11). [53]

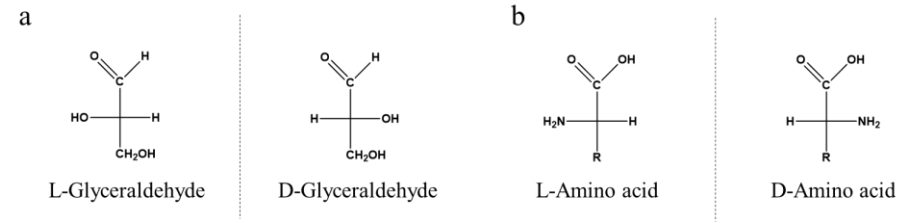


Figure 1.11. Fisher projection of a) Glyceraldehyde, b) a typical amino acid.

Usually, all natural carbohydrates exist as D-enantiomers whereas amino acids are L-forms in biological systems.[54]

## 2.2 Importance of chirality in the pharmaceutical field

If two enantiomers have identical physicochemical properties in achiral environments, when they are introduced in a chiral environment, they have different properties. The human body exemplifies such an environment, with proteins, enzymes, nucleosides, DNA, alkaloids, and certain hormones exhibiting enantiopurity.[54,55]

Despite ongoing researches, the precise origins of biological homochirality remain elusive.[56,57] Nevertheless, its effect is obvious with different physiological responses to two enantiomers of a chiral molecule.[54,55] To explain the biological stereoselectivity observed in enzymes and drug receptors when they interact with chiral compounds, the Easson-Stedman three-point attachment model is the frequently used (Figure 1.12). According to this theory, the substituents of the active enantiomer, denoted A, B and C, bind to the three complementary regions a, b and c of the drug receptor, forming the complexes Aa, Bb and Cc. The opposite enantiomer, on the other hand, can only bind to a maximum of two sites, so cannot activate the receptor.[2,52]

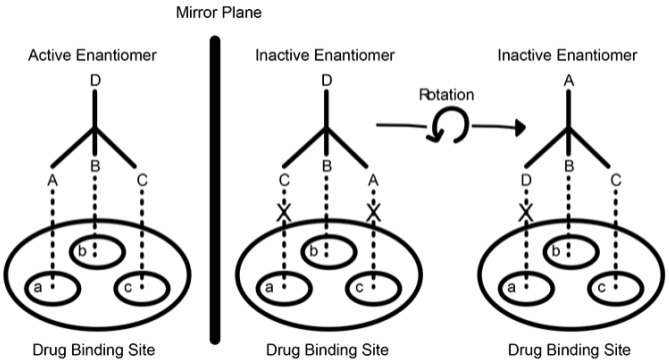


Figure 1.12. The Easson-Stedman model. Adapted from[2]

The enantiomer responsible for the desired biological activity is termed the "eutomer," while the inactive or less active enantiomer is referred to as the "distomer".

The different biological properties of enantiomers are particularly evident in the realm of odor perception, where enantiomers can evoke distinct olfactory sensations. For instance, (*R*)-carvone is characterized by a strong spearmint smell, while its (*S*)-enantiomer exhibits a cumin smell (Figure 1.13).[58]

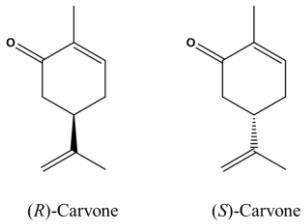


Figure 1.13. (*R*)- and (*S*)-enantiomers of carvone.

In pharmacology, the selective recognition of enantiomers by receptors can significantly impact the efficacy and safety of drugs. Certain receptors may only interact with a specific enantiomer, rendering it pharmacologically active, while its counterpart remains inert or, in some cases, may induce adverse effects. Only a few numbers of molecules have equally bioactive enantiomers (such as fluoxetine, which is an antidepressant).[2] The tragic case of the drug Thalidomide (Figure 1.14) serves as a notorious example of a chiral molecule with two enantiomers exhibiting different biological activities. Thalidomide was initially marketed as a racemic drug used as a treatment for morning sickness in pregnant women. It was widely prescribed in many countries from the 1950s into the early 1960s. However, while (*R*)-Thalidomide was indeed active against morning sickness, the (*S*)-enantiomer was later found to interfere with fetal development, resulting in teratogenic effects on the fetus.[46]

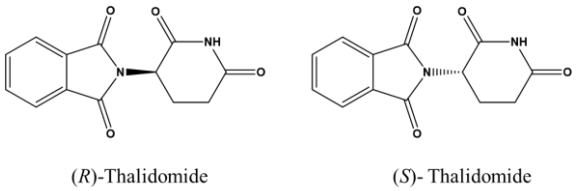


Figure 1.14. (*R*)- and (*S*)-enantiomers of thalidomide.

Despite this, Thalidomide is still used today to treat various medical conditions (such as erythema nodosum leprosum, Behcet's syndrome and has been assayed for organ transplantation, some autoimmune diseases such as chronic lupus erythematosus, rheumatoid arthritis, and some forms of cancer).[2] However, its use is highly regulated,

being strictly contraindicated in pregnant women and requiring close monitoring and pregnancy prevention measures during treatment.[2]

In response to the Thalidomide scandal, the FDA implemented regulations in 1992 concerning stereoisomeric drugs. These regulations covered various aspects, including the requirement that experimental procedures must be capable to identify the stereoisomers present in a chiral medicine and attribute biological effects to each of them.[59] Consequently, there has been a heightened focus on the development of enantiopure medicines to enhance drug efficacy and reduce adverse effects on the human body.[46,48] This shift has led to a market exceeding $200 billion USD in annual sales of enantiopure drugs in 2005, with a growth rate of 15% since 2010.[55] The transition towards single-enantiomer drugs aim to improve therapeutic effectiveness while minimizing harmful side effects. Moreover, this move towards enantiomerically pure substances extends beyond medicinal chemistry to other industries such as agrochemicals, food, and materials.[49,51]

## 2.3 Towards enantiopure compounds

Enantiopure approaches can be divided into three different techniques being chiral pool synthesis, asymmetric synthesis, and resolution of a racemic mixture (Figure 1.15).[48,49,51,52]

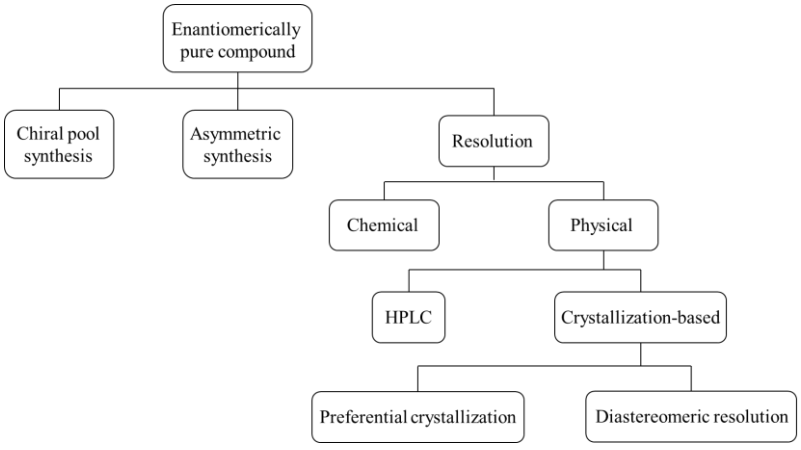


Figure 1.15. Common approaches for obtaining enantiomerically pure compounds.

Chiral pool synthesis utilizes naturally occurring chiral starting materials as precursors for the synthesis of more complex compounds. Components found in the chiral pool include, among others, carbohydrates, amino acids, terpenes, and alkaloids. The enantiopure starting materials undergo a series of reactions employing

achiral reagents that maintain the chirality of the precursor. It results in the desired molecule in an enantiomerically pure form. However, this method is limited by the availability of starting material, therefore, alternative approaches are needed for achieving enantiopure chemicals.[48,51,60]

Enantioselective synthesis is used to convert an achiral molecule into a chiral compound through the utilization of chiral catalysts, enzymes, solvents, or auxiliaries. Implementing this method on a large scale is challenging due to the expense of enantiopure materials and the inherent complexities of the process itself.[48,51,60]

An alternative to the chiral pool and asymmetric synthesis involves starting from racemic molecules and isolating the desired enantiomer.[48,51,61] On an industrial scale, chiral resolutions, and particularly crystallization-based methods, serve as the primary pathways to obtain enantiopure compounds. Indeed, these methods are relatively cost-effective and offer high selectivity.[50,61,62]

## 2.4 Emphasis on resolution techniques

The following part will examine the current status of the most commonly encountered resolution techniques. These can be categorized into two main groups: chemical and physical resolution methods, with physical resolution being itself divided into different categories (Figure 1.15).

### *2.4.1 Chemical resolution*

Chemical resolution is a kinetic approach used to separate enantiomers based on their reaction rates, hence it is also termed kinetic resolution. The method consists in reacting a racemic mixture with a chiral catalyst or reagent, causing one enantiomer to react faster than the other. Consequently, a mixture of enantioenriched starting material and product is obtained.[63,64] It is crucial to halt the reaction before reaching 100% completion to prevent equal production of both products.[51]

The difference in reaction rate between the two enantiomers stems from the difference in energy of their transition states (Figure 1.16). A greater difference in reaction rate enhances the efficacy of the resolution process.

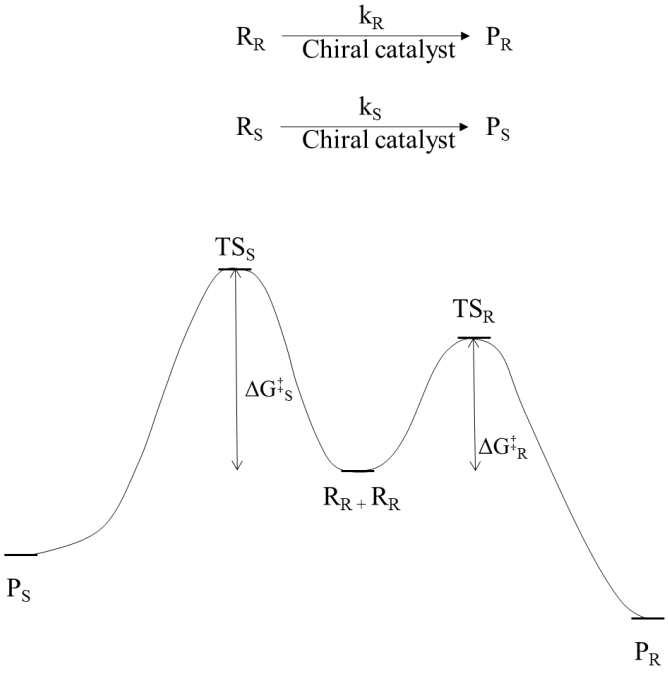


Figure 1.16. General scheme of kinetic resolution and energy diagram behind its principle. The mixture of enantiomers ($R_R$ and $R_S$) are reacted with a chiral catalyst to yield the products $P_R$ and $P_S$. As the transition state of the (*R*)-enantiomer ($TS_R$) is lower in energy than $TS_S$, the rate constant $k_R$ is higher than $k_S$.

Recently, Kawabata *et al.* developed a strategy for the enantioselective preparation of chiral rotaxanes using kinetic resolution. The researchers have developed asymmetric acylation of the hydroxy group of racemic rotaxanes in the presence of a chiral catalyst, yielding enantioenriched acylated rotaxane. On the other hand, the unacylated reagent is recovered with a high enantiopurity (*ee* > 99.9%) (Figure 1.17). They have demonstrated the key role of the NHNs group in the asymmetric reaction, leading to molecular recognition between the rotaxane compound and the enantiopure catalyst.[65]

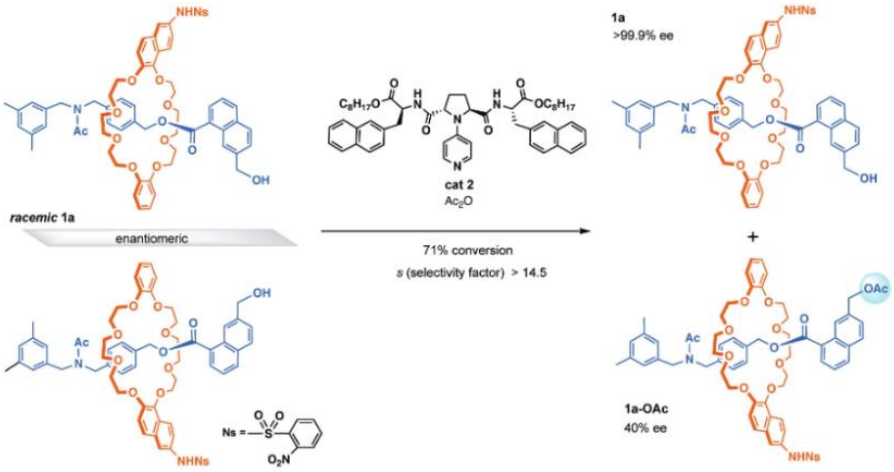


Figure 1.17. Highly efficient acylative kinetic resolution of racemic rotaxane.[65]

In parallel, the promise of enzymatic transformation in kinetic resolution presents notable advantages, including enhanced biocompatibility, heightened selectivity, and milder reaction conditions compared to the use of costly and hazardous chemical compounds. Consequently, numerous research efforts have been dedicated to enzyme screening and structural modifications.[66,67] Among others, Hailes *et al.* conducted research on the kinetic resolution of several *α*-Methyl-substituted aldehydes using Norcoclaurine synthase. This resulted in the formation of Tetrahydroisoquinolines with one or two defined stereocenters (depending on the product formed), in a single step and with high conversion rates (Figure 1.18). They subsequently demonstrated the possible scale-up of the resolution.[67]

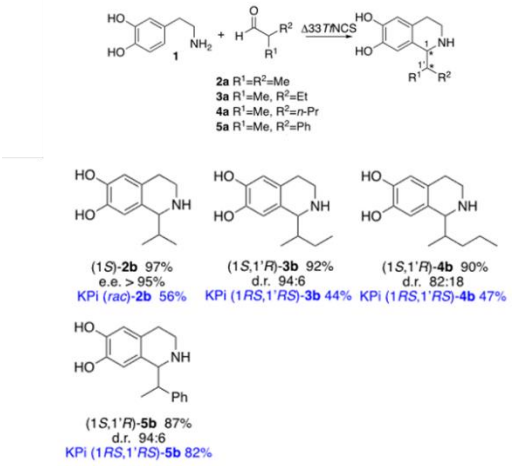


Figure 1.18. Kinetic resolution of α-Methyl-substituted aldehydes by the wild type *Thalictrum flavum* Norcoclaurine synthase (Δ33*Tf*NCS).[67]

However, the utilization of kinetic resolution methods is limited due to the need of identifying suitable reaction partners and by the high costs associated with enantiopure reagents, catalysts or enzymes.[46,64]

### 2.4.2 Physical resolution

#### Chiral chromatography

Different types of chiral chromatography techniques exist, among them chiral high-performance liquid chromatography (*c*HPLC) is the most encountered.[47,51,68,69] *c*HPLC techniques are themselves divided into two categories: indirect and direct methods.[47,51,54,69,70]

The indirect method is the oldest approach. It requires the molecule of interest to react with an enantiopure chiral derivation reagent (CDR) to yield to two diastereomeric products, which are subsequently separated by an achiral HPLC method.[69] Even though different applications of this technique were developed, nowadays, it is rarely used due to several reasons. One of the primary challenges lies in the requirement for the chiral compound to analyze to possess a functional group that can undergo derivatization, limiting the method's applicability to specific chemical structures. Moreover, the CDR used must be enantiomerically pure, a condition rarely met in practice. Consequently, additional sample preparation steps are often necessary to overcome this and to avoid the formation of misleading diastereomeric peaks during analysis, complicating quantification and data interpretation. Furthermore, unwanted side reactions during derivatization can introduce strong background noise or non-attributable peaks, complexifying the analysis process. Moreover, incomplete conversion due to kinetic factors can alter diastereomeric ratios, leading to discrepancies in analytical results. Finally, developing specific CDRs tailored to different types of compounds adds another layer of complexity, requiring significant time and resources.[47,51,54,69]

On the opposite, direct separation techniques rely on using a chiral selector in the mobile phase or, more common, a chiral stationary phase (CSP). Since the selector or the stationary phase are chiral, they encounter stereospecific interactions with the molecule of interest. This allows diastereomeric complexes formation, allowing different retention times for both enantiomers to analyze. [47,71]

On the one hand, when using chiral selectors, these compounds need to be enantiopure, not interfere with the detection method (for example, if UV-detection is employed, they should not absorb UV light), and a high quantity of this compound is necessary for an effective separation.[47,54] Despite these constraints, Cui *et al.* highlighted a link between the presence of D-amino acid in rat plasma and

Alzheimer's disease. For this, they used (*S*)-*N*-(4-nitrophenoxycarbonyl) phenylalanine methoxyethyl ester (Figure 1.19) as a chiral selector in the mobile phase, and developed a method applied on 18 different amino acids.[72]

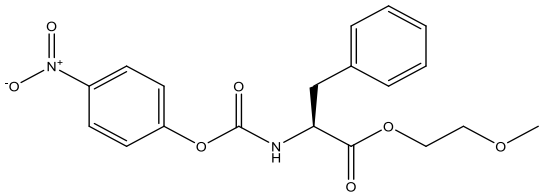

Figure 1.19. Molecule of (*S*)-*N*-(4-nitrophenoxycarbonyl) phenylalanine methoxyethyl ester used as a chiral selector in chiral HPLC resolution.

On the other hand, processes using CSPs are usually the most convenient and straightforward. The support of the stationary phase is usually composed of silica-based gel, on which chiral molecules are grafted. The interactions with the molecule of interest allow the obtention of two different diastereomeric complexes, with one interaction stronger compared to the other one. The enantiomer bonded more strongly has therefore the highest retention time.[71]

CSPs can be classified following the interactions between the column and the solute to analyse:[71]

- Type I differentiates enantiomers by the formation of complexes through attractive interactions like hydrogen bonds, π-π interactions and dipole stacking. The selectors are directly bonded on the surface of the silica and are commonly called brush-type.
- Type II differentiates enantiomers by a combination of attractive interactions and inclusion complexes. It is differentiated from Type I columns due to the position of the chiral selectors that are inside cavities or folds of polysaccharide structures that compose the base of the column.
- Type III differentiates enantiomers by formation of inclusion complexes.
- Type IV differentiates enantiomers by the formation of diastereomeric-metal complexes.
- Type V differentiates enantiomers by a combination of hydrophobic and polar interactions. In this case, the CSP is composed of proteins.

The majority of commercially available and commonly used CSPs fall into several categories: polysaccharide-based (Type II), brush-type (Type I), macrocyclic-antibiotic-based (Type III), and cyclodextrin-based (Type III) (Figure 1.20).[68,71]

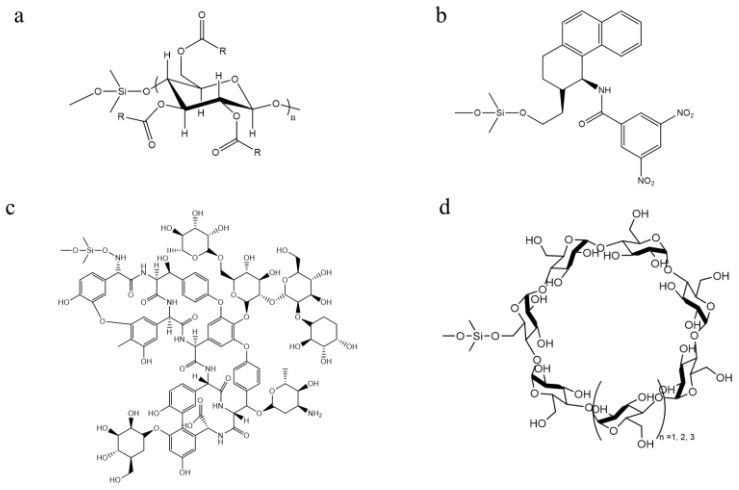


Figure 1.20. Examples of the most common categories of CSP grafted on silica-based gel, a) polysaccharide-based, b) brush-type, c) macrocyclic-antibiotic-based, d) cyclodextrin-based.

For the development of a resolution method, in addition to finding the appropriate CSP for resolving the target molecule, the composition of the mobile-phase also needs to be determined. Common solvents used as mobile-phase include n-hexane, heptane, acetonitrile, isopropanol, ethanol, methanol and water, depending on whether the chromatography mode is normal or reverse. Different combinations and ratios of these solvents are employed to prepare the mobile phase.[71]

In medical analyses, the detection of trace amounts of enantiomers, typically D-amino acids, in human physiological fluids requires high selective and sensitive analytical methods. To enhance the quality of chromatographic analysis, 2D- and 3D-HPLC techniques have been developed, employing two or three sequential columns.[73–75] Hamase *et al*. utilized a 3D-HPLC system composed of three different separation modes (the first is a reversed-phase column, the second is an anion exchange column, and the third is an enantiomeric separation column) to quantify L-/D-Serine, Threonine, and Allo-threonine in human plasma (Figure 1.21). Following each analytical step, the targeted amino acids were collected and introduced in the subsequent analysis. The achiral analyses were used to separate the targeted amino acids from interfering substances, before the quantification with the chiral column. This sophisticated system enabled the identification of D-amino acids, with concentrations ranging from 0.02% to 1.5% of the corresponding L-amino acids.[75]

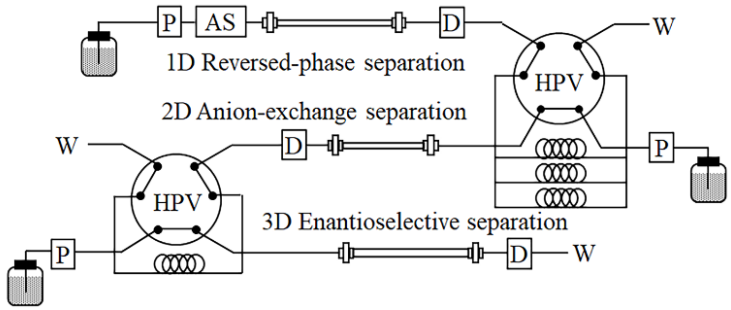


Figure 1.21. 3D-HPLC montage with AS: Auto sampler, D: Detector, HPV: High pressure valve, P: Pump, W: Waste. [75]

*c*HPLC stands as a powerful separation method in analytical laboratories, owing to its sensitivity, reproducibility, and versatility, explained by the broad spectrum of options afforded by adjusting both mobile and stationary phases.[51,69] However, the practical application of chromatographic separations is often limited due to challenges such as large solvent volumes, extended separation times, relatively high costs associated with chiral chromatography supports, and the utilization of hazardous and flammable solvents.[46,64]

Recognizing these limitations, chiral supercritical fluid chromatography (*c*SFC) has emerged as an alternative tool, due to its advantages in both preparative and analytical scales. Notably, the viscosity of a supercritical fluid is analogous that of a gas. This reduces process resistance, allowing operation at higher flow rates and enhancing productivity.[46] Furthermore, preparative systems tailored for bulk-scale SFC purification enable the purification of large quantities of drug substances.[70]

## Resolution based on crystallization

As previously mentioned, crystallization-based resolution methods are highly favored in industry thanks to their cost-effectiveness and scalability.[46,61] Before going into detail about the different resolution techniques, the packing arrangements of chiral molecules during crystallization will be introduced, as it serves as the basis for designing the appropriate chiral separation method.

### ○ *Racemic compounds vs. conglomerates vs. solid solutions*

The application of crystallization for the separation of enantiomers requires a comprehensive knowledge of the fundamental solid–liquid equilibria.[76] The construction of binary diagrams (melt phase systems) and ternary solubility diagrams informs about these equilibria. Moreover, it shows that racemic mixtures can

crystallize as three different types of solids that are racemic compounds, conglomerates, and pseudoracemates (Figure 1.22).[49,51]

Racemic compounds are composed by a stoichiometric mixture of enantiomers well arranged in the same crystal packing. The vast majority of chiral molecules (90-95%) crystallize as racemic compounds.[77]

Conglomerates are composed of two enantiomers crystallizing as distinct enantiopure solid phases. This leads to the obtention of a mechanical mixture of crystals formed by homochiral molecules. Only 5-10% of chiral compounds lead to the obtention of conglomerates.[49,51]

Pseudoracemates, also called solid solutions, occur when the crystal lattice contains both enantiomers, similar to racemic compounds. However, unlike racemic compounds, in pseudoracemates, the enantiomers are mixed randomly within the crystal lattice. These types of crystals are only found in 1% of chiral molecules. [49,51]

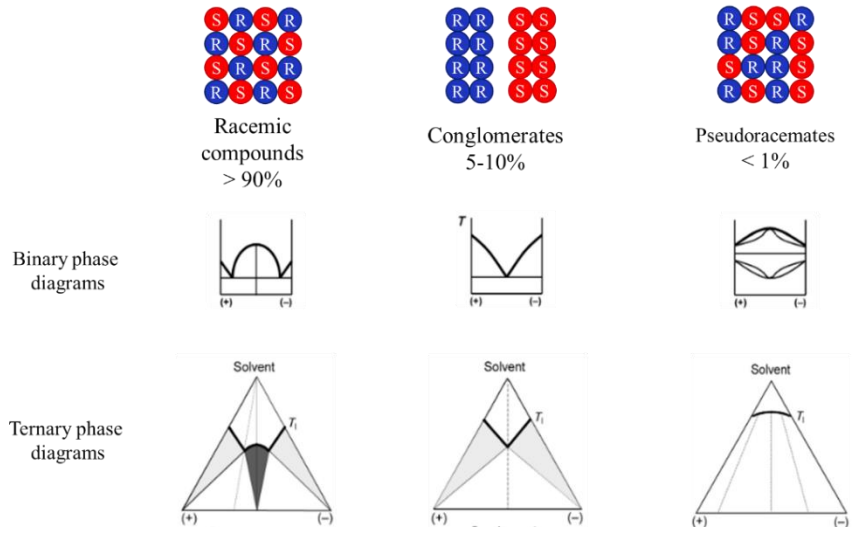


Figure 1.22. Possible crystallization behaviors of racemates and their binary and ternary phase diagrams. Reworked image from [51]

Since enantiomers share identical physical properties such as melting points, enthalpies of fusion, and solubilities, both binary and ternary phase diagrams are symmetrical with respect to the racemic composition.

The choice of an appropriate crystallization-based resolution method depends on the type of crystallized racemate obtained. For instance, if Pasteur manually separated both enantiomers of Sodium ammonium tartrate in 1848, based on his observation of the existence of two types of dissymmetric crystals, it is explained by the fact that the

compound crystallizes as a conglomerate, leading to macroscopic differences of both types of crystals (Figure 1.23).[46,78]

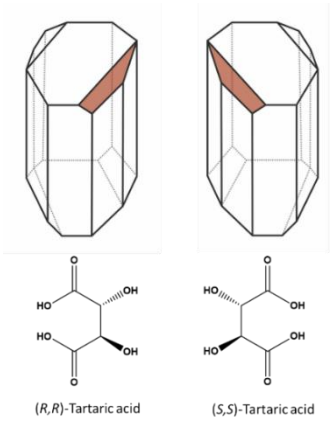


Figure 1.23. Dissymmetric hemihedral crystals of Sodium ammonium tartrate and chemical structures of Tartaric acid.

However, chiral resolution based on macroscopic observation of crystals is not possible on an industrial scale. Therefore, an approach allowing direct separation of enantiomers has recently been used on Asparagine monohydrate (Asn•$H_2O$).[46,49,79] Wan *et al*. developed a resolution process based on the magnetic response of one of the enantiomers by selectively integrating magnetic nanoparticles into one of the two forms and not into the other. They crystallized the two enantiomers by seeding each of them in solution (but with only one integrating the magnetic particles) then separated the two kind of crystals using a permanent magnet (Figure 1.24).[79]

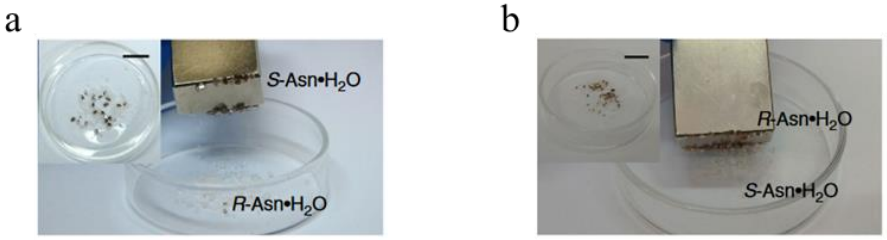


Figure 1.24. Resolution of (*rac*)-Asn•$H_2O$ crystals by using magnetic nanoparticles as additive, a) the (*S*)-enantiomer integrates the nanoparticles, b) the (*R*)-enantiomer integrates the nanoparticles.[79]

This exotic resolution does not represent a commonly used method. Today, resolution processes are mostly divided into preferential crystallization (applicable only to conglomerates) and diastereomeric resolution (applicable on all types of chiral molecules).

- ***Preferential crystallization***

Preferential crystallization is a kinetic process allowing direct and stereoselective crystallization of one enantiomer from a racemic solution. This resolution method is only applicable when enantiomers crystallize as distinct enantiopure phases and, thus, it is only effective for conglomerates-forming crystals. This forms a major limitation to the methodology, as a mere 5 to 10% of chiral molecules are conglomerate-forming systems.[51,77]

The process involves introducing an enantiopure seed crystal into a supersaturated mother liquor containing both enantiomers. The seeded enantiomer crystallizes preferentially due to the lower energy barrier for its secondary nucleation and crystal growth compared to the spontaneous primary nucleation of the non-seeded enantiomer. This energetic difference provides a kinetic advantage that allows the formation of enantiopure crystals while keeping the opposite enantiomer in solution. The process must be halted at the right time to prevent nucleation of the opposite enantiomer, leading to an intrinsic kinetic window that limits the maximum amount of enantiopure crystalline material that can be recovered from a single crystallization event from a racemic solution.[51,77] Therefore, multiple crystallization cycles, allowing the consecutive crystallization of one and then the other enantiomer, are necessary to achieve sufficiently high yield of enantiopure compounds.[51,77]

To address this limitation, simultaneous crystallization or continuous preferential crystallization was developed. This approach allows enantiomers to crystallize simultaneously but locally separated from a solution that remains close to the racemic composition. This method, applicable on larger scales, involves careful management of crystallization conditions to crystallize both enantiomers during a single experiment.[51,77] Different variations of this approach exist, among them, continuous preferential crystallization using three flasks (CPC3) is the most employed (Figure 1.25). This technique employs a three-container setup comprising two crystallizers connected in parallel to a dissolver. The racemic compound is continuously introduced into the dissolver tank, where it dissolves at a temperature $T_1$. The solution flows bidirectionally from the tank to the two crystallizers and vice versa. Both crystallizers are maintained at a temperature $T_2$ (where $T_2<T1$), allowing simultaneous crystallization of both enantiomers seeded in each tank.[77]

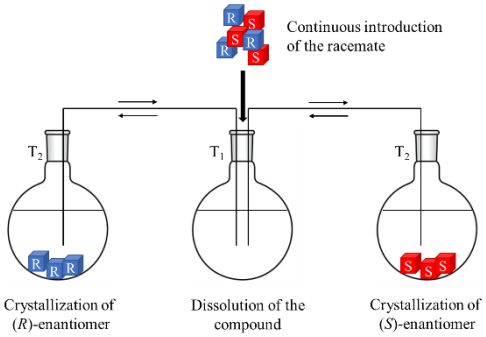


Figure 1.25. Continuous preferential crystallization using three flasks process leading to the simultaneous resolution of both (*S*)- and (*R*)-enantiomers of the molecule of interest.

More recently, efforts have been made to circumvent the limitation of the exclusive use of conglomerates. To expand the applicability of this technique, ongoing research efforts aim to convert racemic compounds into conglomerates. Various crystal engineering strategies[80,81] have been employed in this context including metastable polymorphs[82,83], salt[84,85], solvate[86,87] and cocrystal[62,88–90] formation.

Seidel-Morgenstern *et al.* studied 2-Chloromandelic acid, an intermediate compound for the synthesis of (*S*)-Clopidogrel, which is an antiplatelet agent utilized in the treatment of coronary artery and vascular diseases (Figure 1.26). Their research revealed that the molecule was a racemic compound-forming substance, which also exhibits a metastable conglomerate from both melts and solutions (in solvents such as water, methanol, and ethyl acetate). Through their physicochemical analyses of the compound, they suggested the possible application of a preferential crystallization process applied on 2-Chloromandelic acid.[82]

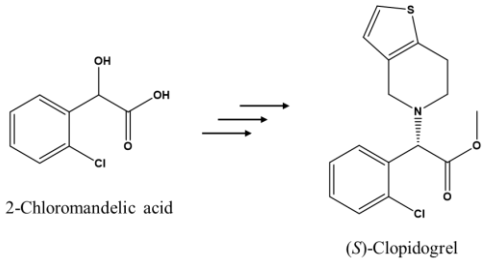


Figure 1.26. Chemical structure of 2-Chloromandelic acid, an intermediate compound for the synthesis of (*S*)-Clopidogrel.

In 2020, Coquerel *et al.* and Leyssens *et al.* independently pioneered preferential crystallization of racemic compounds through cocrystal formation. They both outlined conglomerate formation of their target molecule when cocrystallizing it with an

achiral molecule. Coquerel *et al.* successfully resolved the monohydrate cocrystal Proxyphylline-Salicylic acid-water (Figure 1.27a), while Leyssens *et al.* achieved resolution of Mandelic acid through its cocrystallization with Nefiracetam (Figure 1.27b).[87,88]

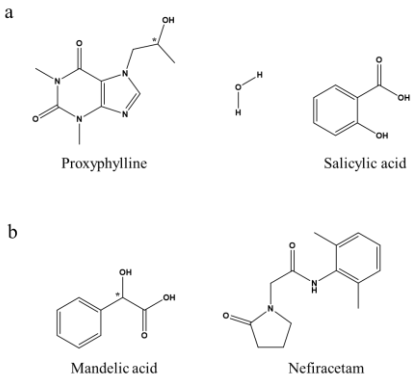


Figure 1.27. Systems used by Coquerel *et al.*[87] and Leyssens *et al.*[88] to demonstrate preferential crystallization of racemic compounds through cocrystal formation.

Subsequently, Leyssens *et al.* expanded upon their work by establishing a conglomerate cocrystal system composed of two racemic compounds, Mandelic acid and Etiracetam. They furthermore used this finding to develop, for the first time, the simultaneous resolution of both compounds through preferential crystallization, working with toluene (Figure 1.28).[89]

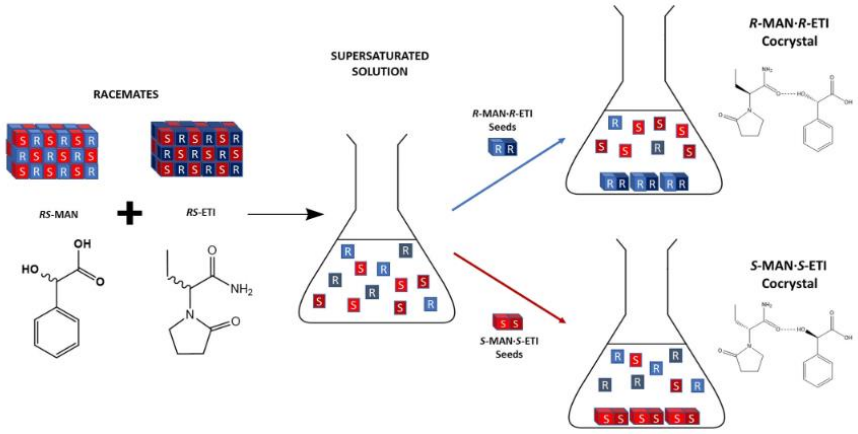


Figure 1.28. Simultaneous resolution of two racemic compounds (Mandelic acid and Etiracetam) though their conglomerate-cocrystal formation.[89]

Alternative methodologies can also be used to reveal metastable cocrystal conglomerates. For example, Subra-Paternault *et al* studied the cocrystallization of

racemic Naproxen with achiral Nicotinamide in acetone using supercritical $CO_2$ as an antisolvent. Whereas both Naproxen and its cocrystal with Nicotinamide crystallize as racemic compounds, the study demonstrates the existence of a metastable cocrystal conglomerate when $CO_2$ is added at a high rate (20 g/min), while this conglomerate behavior is not observed when $CO_2$ is added at lower rate (2 and 11 g/min) (Figure 1.29).[83]

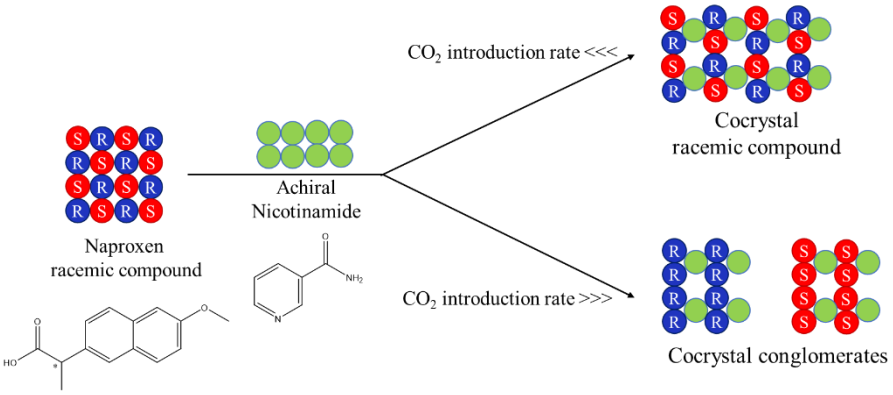


Figure 1.29. Naproxen forms with Nicotinamide a (2:1) cocrystal. Depending on $CO_2$ introduction rate, the cocrystal can crystallize as racemic compound or conglomerate.

### ○ *Diastereomeric resolution*

The most classical and widespread chiral resolution technique is diastereomeric crystallization. In the initial version of the method, a racemic mixture was reacted with an enantiopure resolving agent to form a diastereomeric salt pair. By their differences in physicochemical properties (*e.g.* solubility), the diastereomerically related salts are separated, most of the time by selective crystallization. Finally, the salt is decomposed by treatment with either an acid or a base, to recover the pure enantiomer. This method can be applicable to any compound with an acidic or a basic functional group.[2,46,76,77]

Recently, Demeter *et al.* developed a diastereomeric salt resolution applied on a system composed of racemic monohydrated Pregabalin, L-Tartaric acid, and water (Figure 1.30). (*S*)-Pregabalin-L-Tartaric acid monohydrate is more stable than (*R*)-Pregabalin-L-Tartaric acid monohydrate, hence it is the most stable diastereomer, so the less soluble. It is recovered by cooling the saturated solution from 30°C to 20°C.[76]

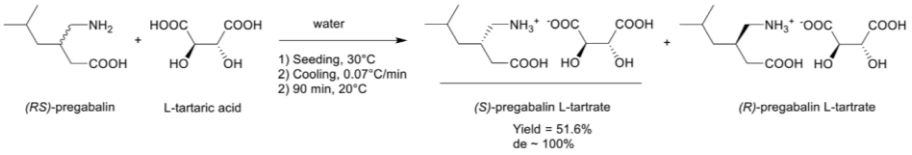


Figure 1.30. Diastereomeric salt resolution applied on a system composed of racemic monohydrated Pregabalin, L-Tartaric acid, and water.[76]

Antisolvent crystallization can also be used to recover the most stable diastereisomer. With this approach, Székely *et al.* studied the possible resolution of Ibuprofen by diastereomeric salt formation with (*R*)-1-Phenylethylamine as the resolution agent (Figure 1.31) in ethanol, methanol and a mixture ethanol:methanol (1:1, v:v) in a gaseous antisolvent (GAS) process, with supercritical $CO_2$. Their study revealed that the washing duration directly impacted the diastereomeric excess (*de*) and yield of the recovered powder, with a higher washing duration implying an improved *de* and a lower yield. Additionally, they explored the influence of pressure in a range of 9 MPa to 20 MPa, at a fixed temperature and solution concentration. They showed that pressure does not have significant effect on the *de* but it impacts the yield. Specifically, increasing the pressure lowers the salt yield. [91]

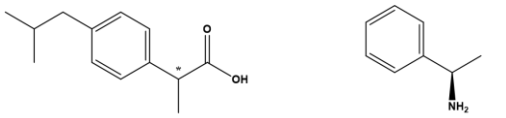


Figure 1.31. Chemical structures of Ibuprofen and (*R*)-1-Phenylethylamine.

Resolution through diastereomeric salts is easy to scale up, it requires simple equipment while offering high productivity and enantioselectivity. These advantages account for the significant adoption of the method in industrial processes.[46,61,77] For example, Duloxetine (antidepressant), Frovatriptan (used to treat migraines), and Cinacalcet (used to treat secondary hyperparathyroidism) are three substances industrially resolved by diastereomeric salt resolution.[92]

The major limitation of this approach arises from the nature of the interaction between the chiral agent and the target enantiomer. Classical diastereomeric resolution involves the formation of diastereomeric salts, necessitating the racemic compound to have acidic or basic functionality to ensure the creation of a salt.[77] To encompass this shortcoming, diastereomeric resolution has also been enabled by cocrystallization, using an enantiopure coformer as the resolving agent.

Höpfl *et al.* studied resolution of Praziquantel (Figure 1.32), a medicine used to treat gastrointestinal parasites, via diastereomeric cocrystal formation with L-Malic acid as

an enantiopure coformer in both acetone and ethyl acetate. The (*R*)-Praziquantel-L-Malic acid cocrystal being the most stable form, it crystallizes first. After its recovery, it undergoes a treatment with water to separate both components of the crystalline phase, allowing to recover (*R*)-Praziquantel hemihydrate by filtration.[93]

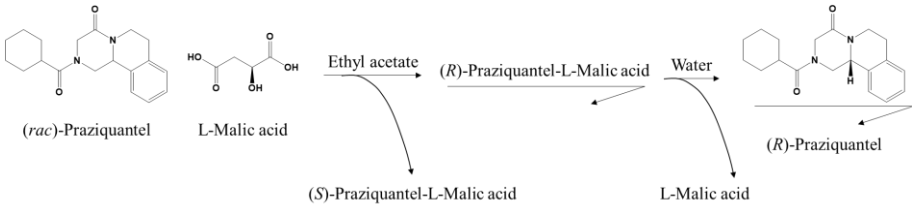


Figure 1.32. Diastereomeric resolution of (*rac*)-Praziquantel in the presence of L-Malic acid in ethyl acetate, followed by treatment of the (*R*)-Praziquantel-L-Malic acid cocrystal with water to recover (*R*)-Praziquantel.

Going a step further, Shemchuk *et al.* showed how either enantiomers of a racemate can be crystallized using the same resolution agent (so of the same handedness). By discovering the existence of two thermodynamically stable but stoichiometrically different cocrystals: (*R*)-Mandelic acid-L-Proline and (*S*)-Mandelic acid-2L-Proline, they were able to resolve Mandelic acid in ethanol and recover each of its enantiomers by adjusting the amount of L-Proline as the resolving agent. They constructed the ternary diagram of the system (Figure 1.33), in order to target each of the possible cocrystals.[94]

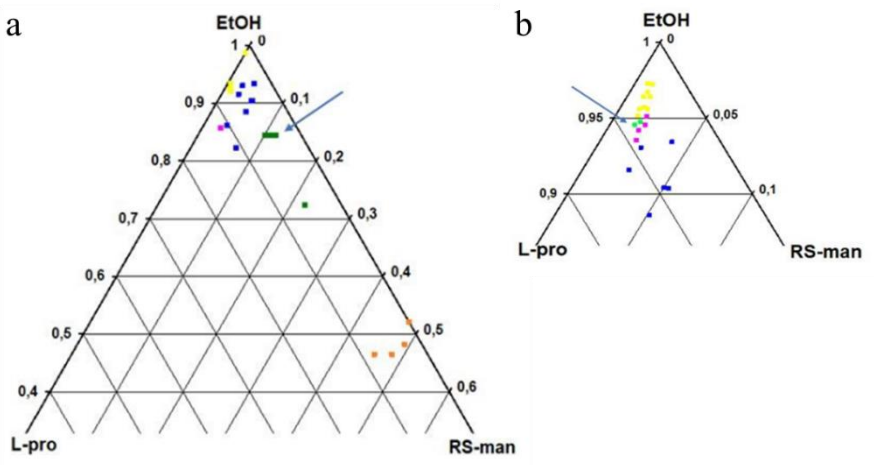


Figure 1.33. Ternary diagram of the L-Proline, (*rac*)-Mandelic acid, ethanol system showing the existence of two areas allowing the recovery of (*R*)-Mandelic acid-L-Proline (a. dark green) and and (*S*)-Mandelic acid-2L-Proline (b. light green). [94]

Alternatively, it is possible to achieve chiral resolution through the formation of enantiospecific cocrystals, therefore involving only one new crystalline phase. This is generally accompanied by a less complicated phase diagram (as there are less different solid phases in presence) and a greater difference in solubility between the cocrystal and the unbound enantiomer (unlike the difference in solubility between two diastereomers).[61]

Leyssens *et al.* studied the enantiospecific cocrystallization resolution of (*rac*)-Etiracetam with (*S*)-Mandelic acid (Figure 1.34 a). They observed only the formation of the (*S*)-Etiracetam-(*S*)-Mandelic acid cocrystal, having never obtained the (*R*)-Etiracetam-(*S*)-Mandelic acid form, probably due to the hydrogen bond arrangement in the cocrystal structure.[95] They further described each facet of the quaternary phase diagram of the system in acetonitrile, as well as its racemic cross-section, using chiral and achiral HPLC, as well as XRPD measurements of the solid forms, in order to identify the optimum resolution parameters.[96] Recently, ter Host *et al.* deepened this research further, by re-evaluating the data with UV-CD spectroscopy. They proposed a more precise representation of the quaternary diagram (Figure 1.34 b, c).[50]

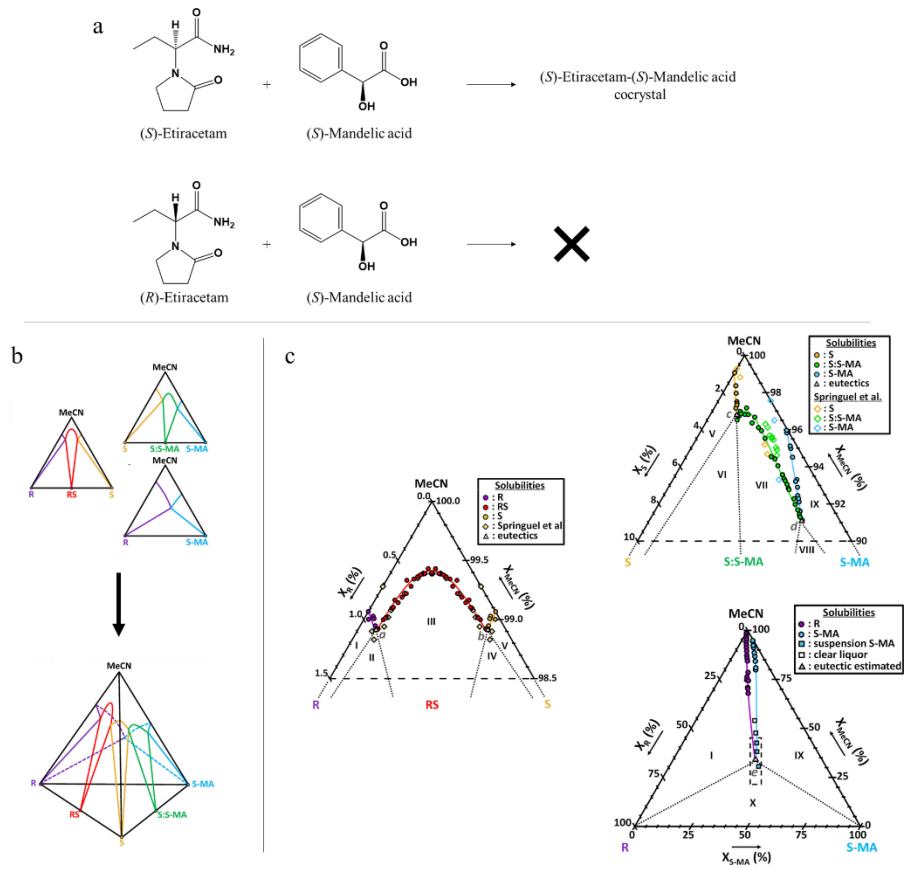


Figure 1.34. a) Enantiospecific cocrystallization resolution of (*rac*)-Etiracetam with (*S*)-Mandelic acid, b) Schematic quaternary phase diagram of the corresponding four components system, in which R and S represent (*R*)- and (*S*)-Etiracetam, S-MA represents (*S*)-Mandelic acid and MeCN represents acetonitrile[50], c) Quantitative ternary phase diagrams proposed by ter Horst *at al.* and compared to these described by Leyssens *et al.*[50]

# Chapter 2. Aim of the thesis

# Aim of the thesis

This research was conducted within the laboratory of Professor Tom Leyssens in Louvain-la-Neuve, focusing on crystal engineering and its practical applications in chiral resolution processes. Additionally, a part of this work took place in the laboratory of Doctor Christelle Harscoat-Schiavo in Bordeaux, as part of a collaborative scientific exchange. Dr. Harscoat-Schiavo's expertise in utilizing supercritical $CO_2$, particularly in crystallization processes, greatly contributed to our research.

As already reported in Chapter 1, crystallization-based resolution methods are highly favored in industry. However, studies about the role of the solvent in such processes rarely exist in the literature. Therefore, the central theme of this thesis revolved around investigating the role of the solvent in the crystallization of chiral molecules and in the development of chiral resolution methods. To achieve this objective, the experimental aspect of this work is divided into three parts, each dedicated to the study of a specific system.
Three cocrystal systems, already known in the literature, were chosen: 1,1'-bi-2-naphtol-*trans*-cyclohexane-1,2-diamine (BINOL-DACH) (Chapter 3), 1,1'-bi-2-naphtol-*N,N'*-dimethyl-1,2-diphenylethane-1,2-diamine (BINOL-DADPE) (Chapter 4) and Nefiracetam-Mandelic acid (nefi-MA) (Chapter 5). For each of these systems, we will vary the solvents in which the molecules crystallize, in order to study whether a change of solvent induces modifications in the solid form obtained, and if so, how this influences resolution.

In Chapters 3 and 4, we will focus on the BINOL-DACH and BINOL-DADPE systems. DACH and DADPE are two diamine molecules that interact via hydrogen bonds with the hydroxyl groups of BINOL. We will place these systems in different solvents ((a)polar and (a)protic) to study whether a change of solvent induces modifications of the solid form obtained. If so, will we see a link between the solvent and the obtained crystalline form? And will we obtain similar results for both systems? In addition, we will investigate whether we observe any influence of the solvent on the resolution of Binol and/or the diamines DACH and DADPE.

In Chapter 5, we will focus on integrating pressurized fluid technology into traditional crystallization methods to induce chiral resolution. Specifically, we will explore the use of pressurized $CO_2$ as an anti-solvent in a preferential crystallization process.

First, we will attempt to obtain the nefi-MA cocrystal under supercritical conditions and in different solvents in order to identify the optimal solvent for the resolution process. Subsequently, we will attempt to develop the preferential crystallization of the system, assisted by pressurized fluid. Since this process requires seeding, which has never been implemented in a supercritical reactor, we will first have to establish an experimental set-up before moving on to the development of our proof of concept.

Overall, this thesis underscores the intricate role of solvents in crystallization processes, offering insights into the manipulation of solvents for achieving specific crystalline forms, targeting the desired enantiomeric form, and using it as a tool in crystallization processes.

# Chapter 3. Combining two chiral compounds: the importance of the solvent for resolution

In this chapter, we undertook an in-depth study of the interactions between two chiral molecules: 1,1'-bi-2-naphtol (BINOL) and *trans*-cyclohexane-1,2-diamine (DACH).

While exploring various solvents for developing a resolution process of the compounds, we revealed a multitude of solid phases. This chapter analyzes the different crystalline forms obtained in the selected solvents, underscoring the critical importance of the solvent choice for the development of a chiral resolution process.

This work is currently being drafted for publication. It is therefore still work in progress and not a finalized paper as such.

*SC-XRD characterizations were conducted by Koen Robeyns and Oleksii Shemchuk.*

# Combining two chiral compounds: the importance of the solvent for resolution

## 1. Introduction

Chirality plays a pivotal role, influencing a spectrum of chemical and biological processes across various fields, including pharmaceuticals, material science, catalysis, and agronomy.[49,51] The separation of enantiomers, non-superimposable mirror images, stands as a fundamental aspect in these fields and can be achieved through various methods.[46,49,61,68] Processes based on crystallization are among the most widespread, due to their advantages in terms of economical consumption and ease of manufacturing.[49,51,68,97] In the field of crystallization, the use of cocrystals offers different pathways to chiral resolution, including techniques such as enantiospecific[95,98] or diastereomeric[93,99] cocrystal resolution, the establishment of chiral matrices with selective inclusion cavities targeting only one enantiomer,[49,68,93] and the formation of conglomerates from racemic compounds that can ultimately lead to resolution via preferential crystallization.[62,88,89]

When looking for a potential resolution system, researchers often focus solely on the parent compounds, introducing solvent considerations at a later stage. However, in a recent contribution, we underscored the critical role of solvent selection in the resolution processes, demonstrating how a mere switch of the solvent's nature drastically altered the direction of resolution.[100]

In this study, we further highlight the importance of the achiral solvent in the context of resolution, focusing on BINOL, and combining it with *trans*-cyclohexane-1,2-diamine (DACH). Two cocrystals – (*R*)-BINOL-(*R,R*)-DACH (*R-RR*)[101] and (*S*)-BINOL-(*R,R*)-DACH (*S-RR*)[101] – of this system are already reported in literature along with a (*R*)-BINOL-(*R,R*)-DACH-toluene (*R-RR*-tolu) cocrystal-solvate.[102] We investigate here the resolution potential of this system in various solvents, exploring the solid form landscape of all possible BINOL-DACH chiral combinations through crystallization experiments in different solvent environments. Through this approach, we highlight the importance of solvatism on the outcome of the interaction between two chiral compounds, and on the underlying resolution potential of the system.

# 2. Materials and Methods

## 2.1 Materials

(*S*)-1,1'-bi-2-naphtol (Merck), (*R*)-1,1'-bi-2-naphtol (Fluorochem), (*rac*)-1,1'-bi-2-naphtol (Acros Organics), (*1S,2S*)-*trans*-cyclohexane-1,2-diamine (Apollo Scientific), (*1R,2R*)-*trans*-cyclohexane-1,2-diamine (Apollo Scientific), (*rac*)-*trans*-cyclohexane-1,2-diamine (Thermo scientific), toluene (VWR chemicals), benzene (TCI), methanol (VWR chemicals), acetonitrile (VWR chemicals), ethanol (VWR chemicals), and ethyl acetate (VWR chemicals) were purchased from commercial sources and used without further purification.

## 2.2 Slurry experiments

Slurry experiments were performed preparing equimolar suspensions (1 mmol) of BINOL with DACH at 20°C in toluene, benzene, methanol, acetonitrile, ethanol, and ethyl acetate (V=1-1.5 mL). The suspensions were stirred in a Cooling thermomixer HLC at 500 rpm. After 1 day of stirring, the vials were seeded with all possible solid forms, and then left to equilibrate for 7 days. The suspensions were filtered, the powders washed, dried and analyzed using XRPD.

## 2.3 Single Crystal Formation

### *2.3.1 By cooling*

Single crystals of (*rac*)-BINOL-(*rac*)-DACH-EtOAc (*rac*-*rac*-EtOAc) and (*rac*)-BINOL-(*rac*)-DACH-MeOH (*rac*-*rac*-MeOH) were obtained by cooling crystallization from the solvent, starting from an undersaturated equimolar solution of BINOL and DACH at RT. The vials were placed at 9°C. Once crystals formed, a suitable crystal was retrieved and analyzed by SC-XRD.

### *2.3.2 By slow evaporation*

Single crystals of (*R*)-BINOL-(*R,R*)-DACH-benzene (*R*-*RR*-benz), (*rac*)-BINOL-(*rac*)-DACH (*rac*-*rac*), and (*rac*)-BINOL-(*R,R*)-DACH-EtOH (*rac*-*RR*-EtOH) were obtained by slow evaporative crystallization from the different solvents, starting from an undersaturated equimolar solution of BINOL and DACH. The solution was left to evaporate slowly at RT. Once crystals formed, a suitable crystal was retrieved and analyzed by SC-XRD.

## 2.4 Thermal analyses

### *2.4.1 Thermogravimetric analyses (TGA)*

TGA analyses were conducted using a Mettler Toledo TGA/DSC $3^+$ instrument, varying the temperature from 25 to 600°C, with a heating rate of 10°C/min, under nitrogen with a flow rate of 50mL/min. Solid samples (5-10 mg) were placed in alumina pans.

### *2.4.2 Differential scanning calorimetry analyses (DSC)*

DSC analyses were conducted using a TA Instrument DSC2500. The temperature range employed for the analyses was from 25°C to *desired temperature* (determined through TGA), at a heating rate of 5°C/min under nitrogen with a flow rate of 50 mL/min. Solid samples (5-10 mg) were placed in aluminum pans with perforated lid.

## 2.5 X-ray powder diffraction (XRPD)

XRPD data were collected using either a Siemens D5000 diffractometer or a Bruker D8 Discover diffractometer. Both are equipped with a Cu X-ray source operating at 40 kV and 40 mA. A secondary monochromator was used to select the Kα radiation of Cu (k = 1.5418 Å). A scanning range of $2\theta$ values was applied from 5° to 35° or 5° to 25°.

## 2.6 Single crystal X-ray diffraction (SC-XRD)

SC-XRD data were collected on a MAR345 image plate detector using Mo Kα radiation (λ = 0.71073 Å), generated by an Incoatec IμS microfocus source. The collected data was integrated and reduced using CrysAlis$^{PRO}$ [103] and the implemented absorption correction was applied. Structure solution was achieved using the dual-space algorithm in SHELXT[104] and the structure was further refined against $F^2$ by SHELXL.[105] Non-hydrogen atoms were refined anisotropically; CH atoms were added in calculated positions; OH and NH atoms were either located from a Fourier map or added in calculated positions and refined riding on their respective carbon, nitrogen or oxygen atoms. Symmetry analysis and validation were carried out using PLATON.[106] Figures were generated using the molecular visualization software Mercury v4.3.4.[107]

### 2.7 Chiral High-Performance Liquid Chromatography (*c*HPLC)

The separation of (*R*)- and (*S*)-BINOL was performed by Chiral HPLC using a Waters Arc HPLC coupled with a 2998 PDA detector. Both enantiomers of BINOL were separated on a Daicel Chiralpak IA column 250 x 4.6 mm 5 µm with a mix of 90 vol.% isohexane, 10 vol.% isopropanol as mobile phase. The separation was performed at 25°C with a flow rate of 1 mL/min.

### 2.8 Nuclear magnetic resonance (NMR)

$^1$H NMR spectra were measured either on a 300 MHz or on a 400 MHz spectrometer (Bruker). Chemical shifts are reported in parts per million (ppm) and were referenced regarding the chemical shift of the peak of the deuterated solvent used ($(CD_3)_2SO$ at 2.50 ppm). Spectral multiplicities are described as follows: singlet (s), doublet (d), triplet (t), quartet (q), and multiplet (m).

$^1$H NMR of BINOL (300 MHz, DMSO) δ 9.21 (s, 2H), 7.92 – 7.78 (m, 4H), 7.31 (d, *J* = 8.9 Hz, 2H), 7.26 – 7.11 (m, *J* = 20.0, 8.1, 6.8, 1.3 Hz, 4H), 6.93 (d, *J* = 8.1 Hz, 2H).

$^1$H NMR of DACH (300 MHz, DMSO) δ 2.09 – 1.96 (m, 2H), 1.75 – 1.65 (m, 2H), 1.61 – 1.53 (m, 2H), 1.21 – 1.10 (m, 2H), 1.02 – 0.89 (m, 2H).

## 3. Results and discussion

In order to explore the possible outcomes when combining BINOL and DACH (Figure 3.1), varying their stereochemical combination, five combinations need to be considered (Table 3.1) as all other can be obtained by mirror symmetry. As the *R*-*RR* and *S*-*RR* cocrystals, and the *R*-*RR*-toluene cocrystal-solvate have already been described in the literature[102] and a complex *R*-*RR*-benzene suspected to be formed[101], we decided to focus on investigating the impact of solvatism on the outcome of these combinations concentrating on six different solvents (Table 3.2). Besides toluene and benzene (chosen to compare our results with those reported in the literature), five other solvents were selected with different polarity and proticity. Therefore, the chosen solvents can be divided into three groups: non-polar and aprotic solvents toluene and benzene; polar and aprotic solvents ethyl acetate (EtOAc) and acetonitrile (ACN); and polar and protic solvents methanol (MeOH) and ethanol (EtOH).

All solvent-based experiments were performed using a (1:1) stoichiometry as this is also the stoichiometry of the already reported cocrystals.

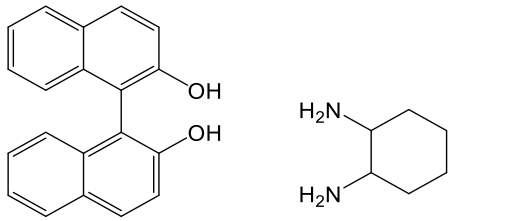


1,1'-bi-2-naphthol *trans*-cyclohexane-1,2-diamine

Figure 3.1. Molecular structures of BINOL and DACH.

Table 3.1. The five studied combinations between BINOL and DACH.

| **Stereochemical combination** | | | **Mirror image symmetry** | | |
|---|---|---|---|---|---|
| (*R*)-BINOL | + | (*R,R*)-DACH | (*S*)-BINOL | + | (*S,S*)-DACH |
| (*S*)-BINOL | + | (*R,R*)-DACH | (*R*)-BINOL | + | (*S,S*)-DACH |
| (*rac*)-BINOL | + | (*R,R*)-DACH | (*rac*)-BINOL | + | (*S,S*)-DACH |
| (*R*)-BINOL | + | (*rac*)-DACH | (*S*)-BINOL | + | (*rac*)-DACH |
| (*rac*)-BINOL | + | (*rac*)-DACH | | | |

A screening process was carried out using three different approaches: slurry-based, cooling-based, and slow-evaporation based. Eleven different crystalline phases were isolated. For almost all systems, a single solid phase was obtained irrespective of the method used, with the exception of (*rac*)-BINOL and (*rac*)-DACH in EtOAc, for which the slow evaporation and slurry methodologies led to two different crystalline phases. Out of the eleven phases, eight are herein reported for the first time, five of which are structurally characterized: *R-RR*-benz, *rac-rac*, *rac-rac*-EtOAc, *rac-rac*-MeOH, and 4*rac*-4*RR*-3EtOH-1$H_2O$ (Table 3.2). Crystallographic details of these five phases are reported in Table SI-3.1.

Table 3.2. Slurry and SC-XRD results of the screening of the five combinations between BINOL and DACH obtained in six different solvents. In blue are colored the multicomponent crystal phases already discovered in the literature[102].

| Combination | Toluene | Benzene | EtOAc | ACN | MeOH | EtOH |
|---|---|---|---|---|---|---|
| (*R*)-BINOL + (*R,R*)-DACH | *R-RR*-tolu (1:1:1) | *R-RR*-benz (1:1:1) | *R-RR* (1:1) | *R-RR* (1:1) | *R-RR* (1:1) | *R-RR* (1:1) |
| (*S*)-BINOL + (*R,R*)-DACH | *S-RR* (1:1) | *S-RR* (1:1) | *S-RR* (1:1) | *S-RR* (1:1) | *S-RR* (1:1) | *S-RR* (1:1) |
| (*rac*)-BINOL + (*R,R*)-DACH | *R-RR*-tolu (1:1:1) | *R-RR*-benz (1:1:1) | 2*rac*-2*RR*-EtOAc (2:2:1) (not structurally characterized) | *R-RR* (1:1) | *rac-RR*-MeOH (1:1:1) | 4*rac*-4*RR*-3EtOH-$H_2O$ (4:4:3:1) |
| (*R*)-BINOL + (*rac*)-DACH | *R-RR*-tolu (1:1:1) | *R-RR*-benz (1:1:1) | <*R-RR, R-SS*> (1:1) | *R-RR* (1:1) | *R-RR* (1:1) | *R-RR* (1:1) |
| (*rac*)-BINOL + (*rac*)-DACH | *R-RR*-tolu + *S-SS*-tolu (1:1:1) | *R-RR*-benz + *S-SS*-benz (1:1:1) | Slow evap yields *rac-rac*-EtOAc (1:1:1) Slurry yields *rac-rac* (not structurally characterized) | *rac-rac* (1:1) | *rac-rac*-MeOH (1:1:1) | *rac-rac*-EtOH (1:1:1) (not structurally characterized) |

### Combination 1: (*R*)-BINOL and (*R,R*)-DACH

The already reported *R-RR* cocrystal (CDCC ref code: DIFFOO[102]) is obtained when combining (*R*)-BINOL and (*R,R*)-DACH by slurry experiments in EtOAc, ACN, MeOH, and EtOH (Figure SI-3.1). The solid is characterized by two formula units in the asymmetric unit (Z'=2). Overall, both pairs have the same conformation, apart from the orientation of the OH and $NH_2$ hydrogens, resulting in different hydrogen bonding interactions (Figure 3.2b, Table SI-3.2), with 1D hydrogen bond chains orthogonal to each other (Figure 3.2a).

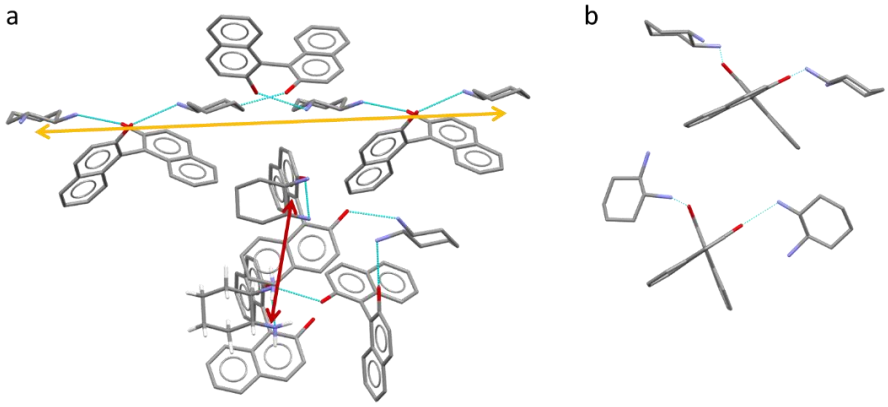


Figure 3.2. Extended view of the hydrogen bond patterns of *R-RR* structure, highlighting the orientation of the interactions. a) Orthogonal BINOL-DACH chains, with arrows indicating their orientation, b) BINOL-DACH chains disposed in space to compare their hydrogen bond directions.

Upon heating, the *R-RR* cocrystal shows a single endothermic melting event at 157°C (Figure SI-3.24). TGA analysis (Figure SI-3.13) shows degradation to occur upon melting.

The *R-RR* structure is readily obtained both from aprotic polar (EtOAc and ACN) or protic polar solvents (MeOH and EtOH) (Figure SI-3.1). However, from toluene and benzene, isostructural *R-RR*-solvent (1:1:1) cocrystal-solvates are obtained, driven by CH-π interactions (Figures 3.3 and SI-3.1). Although benzene (with its six symmetry elements) has higher symmetry than toluene (which has only one symmetry element), this isostructurality is explained by the disorder of toluene in the crystal structure.

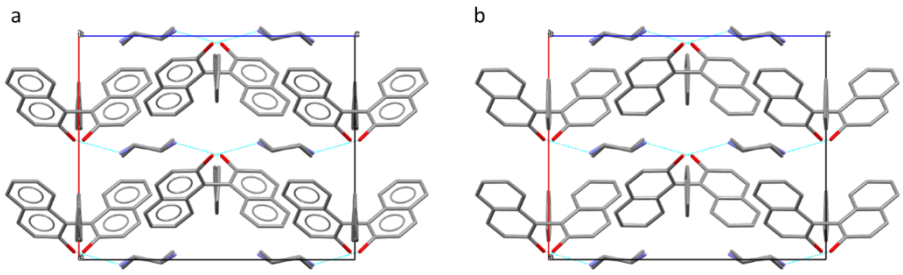


Figure 3.3. Crystal packing of the cocrystal solvates, view along *b*-axis, a) *R-RR*-tolu, b) *R-RR*-benz.

Compared to the non-solvated forms, the main hydrogen bonding motifs between alternating BINOL and DACH molecules are preserved (Figure 3.4, Tables SI-3.3 and SI-3.5), but additional CH-π interactions between the aromatic solvent molecules and the naphthalene units of BINOL are formed (Tables SI-3.4 and SI-3.6 and Figures SI-3.9 and SI-3.10) and all hydrogen bond chains oriented parallel to one another.

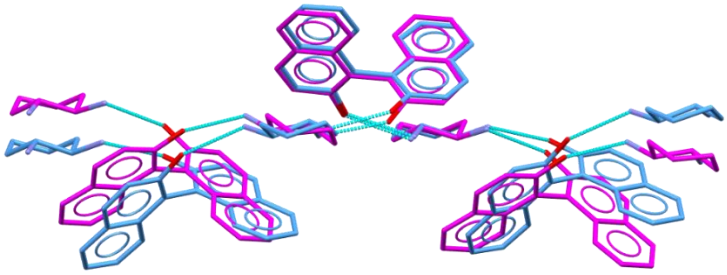

Figure 3.4. Superposition of *R-RR* (pink) and *R-RR*-tolu (blue) chains.

Thermal analyses confirm the loss of 1 equivalent of solvent upon heating, resulting in large endothermic desolvation signals in the DSC analyses (Figures SI-3.25 and SI-3.26) starting around 90°C, and a clear solvent step-weight loss in the TGA analysis (Figures SI-3.14 and SI-3.15). After desolvation, both structures lead to the obtention of the stable *R-RR* cocrystal phase (Figure SI-3.2)

### Combination 2: (*S*)-BINOL and (*R,R*)-DACH

When combining (*S*)-BINOL and (*R,R*)-DACH, slurry experiments in all tested solvents allowed to obtain the already reported *S-RR* cocrystal (CDCC ref code: SUVNEC[102]) (Figure SI-3.3).

The *S-RR* phase contains two formula units per asymmetric unit, with (*S*)-BINOL and (*R,R*)-DACH engaged in similar hydrogen bonding interactions as observed for the *R-RR* cocrystals (Figure 3.5, Table SI-3.7).

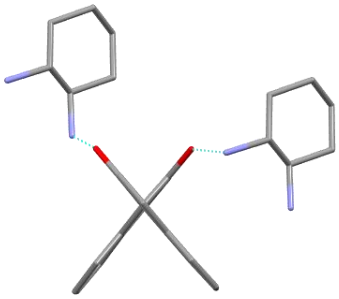

Figure 3.5. Extended view of the hydrogen bond patterns for both BINOL molecules of the *S*-*RR* structure, highlighting the orientation of the interactions.

Thermal analysis shows a single endothermic melting event at 137°C (Figure SI-3.27), followed by degradation. The 20°C lower melting point of the *S*-*RR* diastereomer compared to the *R*-*RR* one, indicates this diastereomer to be the less stable one.

Interestingly, *S*-*RR*-toluene or -benzene solvates are not found. In a previous study, we have reported a similar solvent effect, allowing only one specific chiral combination to be solvated.[100]

### Combination 3: (*rac*)-BINOL and (*R,R*)-DACH

When racemic BINOL is combined with enantiopure (*R,R*)-DACH, effective resolution occurs in acetonitrile, as well as in toluene and benzene (Figures SI-3.46 to SI-3.48). In the former solvent, the *R*-*RR* cocrystal is obtained – this result confirms the *R*-*RR* diastereomer to be more stable (less soluble) compared to the *S*-*RR*. For the latter two solvents the *R*-*RR*-solvent cocrystal-solvate comes out (Figure SI-3.4), keeping in mind the *S*-*RR*-solvates likely not exist. Acetonitrile, toluene, and benzene can therefore effectively be used to develop a resolution process of BINOL using (*R,R*)-DACH as the resolution agent.

At this stage, we can already highlight the importance of the solvent on the resolution process, as resolution is no longer possible when using EtOAc, MeOH or EtOH. For all of these, a multicomponent solvate phase is formed, which combines (*rac*)-BINOL and (*R,R*)-DACH (Figure SI-3.4). Resolution potential is hereby shown to be strongly solvent dependent.

The use of EtOAc resulted in the formation of a crystalline material, which we were unsuccessful in characterizing structurally. To obtain information on the composition of the obtained phase, the powder was analyzed by NMR, TGA, DSC, and *c*HPLC. $^{1}$H NMR analysis shows the obtention of a phase composed by 1 equivalent of BINOL, 1 equivalent of DACH and 0.5 equivalent of EtOAc (Figure SI-3.49). Upon

heating (Figures SI-3.19, SI-3.30), this compound shows a clear desolvation signal to occur at around 70-80°C, confirming the presence of solvent in the structure. *c*HPLC analysis shows the obtention of a racemic mixture of BINOL (Figure SI-3-44), allowing us to confirm the formation of the multicomponent 2*rac*-2*RR*-EtOAc (2:2:1) phase.

The solid phase obtained in methanol shows an XRPD pattern superposable to the simulated *rac*-*rac*-MeOH (1:1:1) pattern (Figure SI-3-4), which will be discussed in the section "Combination 5: (*rac*)-BINOL and (*rac*)-DACH". We therefore suspected the *rac*-*rac*-MeOH phase to form a solid solution with respect to DACH. Upon heating (Figures SI-3.17, SI-3.28), the *rac*-*RR*-MeOH compound remains stable up to 60-65°C.

The ethanol solvate, shows a unit cell composed of four negatively charged molecules of BINOL (2 *R* and 2 *S*), and four positively charged molecules of (*R,R)*-DACH, three EtOH molecules, and one water molecule (Figure 3.6). Within the structure, disorder between EtOH and water molecules occurs (Figure SI-3.11, Table SI-3.8). Upon heating (Figures SI-3.18, SI-3.29), the 4*rac*-4*RR*-3EtOH-$H_2O$ (4:4:3:1) compound remains stable up to 70°C, at which point a large endothermic event occurs, corresponding to a desolvation/melting event.

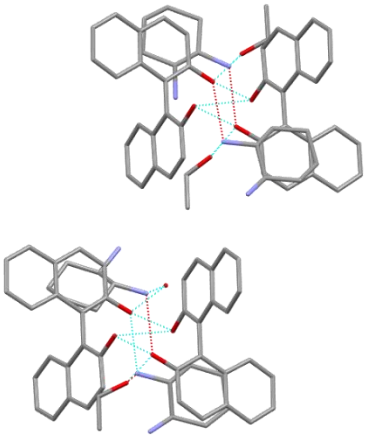

Figure 3.6. Asymmetric unit of 4*rac*-4*RR*-3EtOH-$H_2O$, view along *a*-axis. EtOH and $H_2O$ molecules are disordered. Here, only one possibility is shown for clarity.

Desolvation of the powder recovered from slurrying (*rac*)-BINOL and (*R,R*)-DACH in EtOAc, MeOH and EtOH led to the obtention of three different diffraction patterns, which most likely correspond all to different polymorphs of the *rac*-*RR* combination (Figure SI-3.5). This combination is not obtained from non-solvate forming solvents.

### Combination 4: (*R*)-BINOL and (*rac*)-DACH

When components (*R*)-BINOL and (*rac*)-DACH are slurried in EtOAc, ACN, MeOH, or EtOH, they yield in the powders whose PXRD patters are superposable on that of the *R-RR* cocrystal, while the two cocrystal-solvates *R-RR*-tolu and *R-RR*-benz are obtained, respectively, in toluene and benzene (Figure SI-3.6). Each phase was analyzed by DSC (Figures SI-3.37 to SI-3.42). These analyses showed that a solid solution was obtained when EtOAc was used as solvent. The other five phases are characterized as racemic compounds. This demonstrates the possibility of chiral resolution of (*rac*)-DACH with (*R*)-BINOL as the resolving agent in the five solvents toluene, benzene, ACN, MeOH and EtOH.

Moreover, this, once more, highlights the increased stability of the *R-RR* diastereomer with respect to the *R-SS* (equivalent to the *S-RR*) cocrystal phase.

### Combination 5: (*rac*)-BINOL and (*rac*)-DACH

The role of the solvent is even more crucial when combining both racemates.

Using toluene and benzene yields XRPD patterns superimposable with those of the simulated pattern of the cocrystal-solvate *R-RR*-solvent (Figures 3.7a and 3.8a), seemingly indicative of a conglomerate formation.

Indeed, in the literature, the *R-RR*-toluene cocrystal-solvate was referenced as a conglomerate.[102] To gather further evidence confirming this hypothesis and disprove the occurrence of a solid solution, *c*HPLC of hand-picked crystals obtained by a slow-evaporative experiment of (*rac*)-BINOL and (*rac*)-DACH in toluene was carried out. The analysis showed both enantiomers (*R*)- and (*S*)-BINOL coexisting in the same crystal (Figure 3.7b). Therefore, we have identified these crystals not as true conglomerates but as being twinned, containing domains of both *R-RR* and *S-SS*. As their unit cells have the same dimensions, a mixture between them is possible.

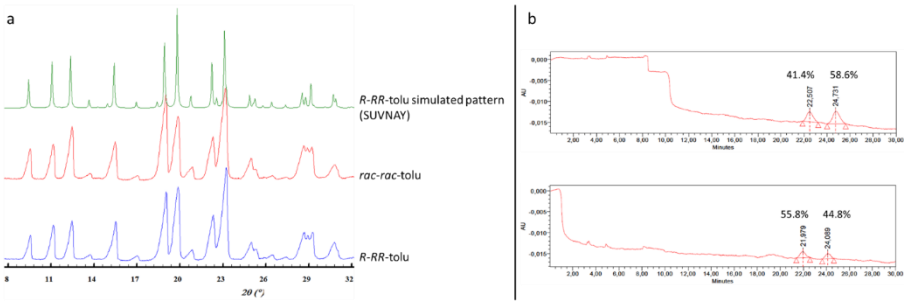


Figure 3.7. a) Comparison of the XRPD patterns between the slurry in toluene of (*R*)-BINOL and (*R,R*)-DACH (blue) with (*rac*)-BINOL and (*rac*)-DACH (red) and the simulated pattern of *R-RR*-tolu cocrystal-solvate. b) *c*HPLC chromatograms of randomly chosen single crystals yielding to mixtures of both enantiomers of BINOL.

When turning to benzene, a real conglomerate was expected to be obtained from two racemic compounds, permitting their simultaneous resolution by preferential crystallization, a currently highly studied process.[62,89] However, a similar behavior as with toluene was observed, with both XRPD patterns of enantiopure and racemic cocrystal superimposable (Figure 3.8a), but with *c*HPLC of a single crystal showing both enantiomers (Figure 3.8b), again suggesting the occurrence of twining.

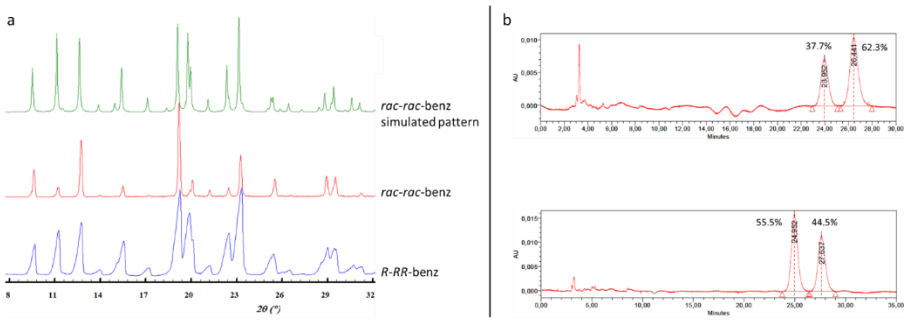


Figure 3.8. a) Comparison of the XRPD patterns between the slurry in benzene of (*R*)-BINOL and (*R,R*)-DACH (blue) with (*rac*)-BINOL and (*rac*)-DACH (red) and the simulated pattern of *rac-rac*-benz cocrystal-solvate. b) *c*HPLC chromatograms of randomly chosen single crystals yielding to mixtures of both enantiomers of BINOL.

Using any other solvent, both racemic compounds combine in a single solid form (Figure SI-3.7). Therefore, none of the other investigated solvents allowed the formation of conglomerates, rendering chiral resolution of BINOL or DACH by preferential crystallization impossible.

ACN led to the obtention of a *rac-rac* (1:1) cocrystal (Figure 3.9, Table SI-3.11) with a (1:1) stoichiometric ratio. Thermal analysis (Figures SI-3.21 and SI-3.34) shows this cocrystal to be stable up to 113-146°C, at which it melts. Melting is accompanied by immediate degradation.

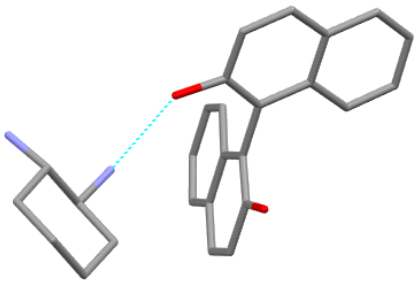

Figure 3.9. Asymmetric unit of the *rac-rac* cocrystal, view along *c*-axis.

In EtOAc, two different structures are recovered. Indeed, the XRPD patterns of the slurry outcome and that simulated of the single crystal obtained by slow evaporation differ (Figure SI-3.7).
SC-XRD analysis of the phase obtained by slow evaporation shows the obtention of a 2*rac*-2*rac*-EtOAc (2:2:1) cocrystal-solvate (Figure 3.10). EtOAc molecules are found disordered on an inversion, indicating the solvent molecules merely occupy cavities in the packing, rather than being strongly engaged in stabilizing the structure. This is also explained by the absence of hydrogen bonds with the EtOAc solvent molecule (Table SI-3.10).

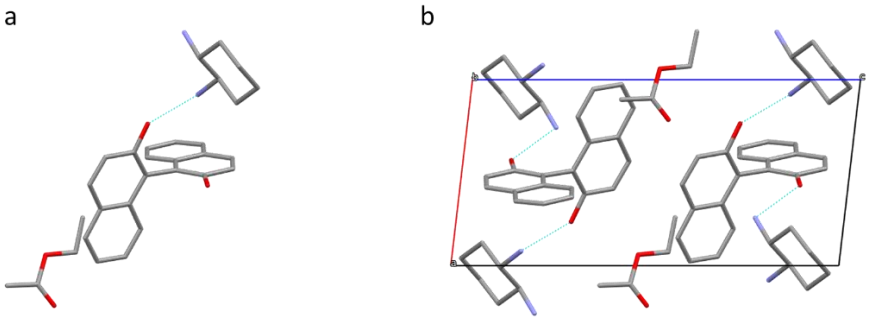


Figure 3.10. Structure of the *rac*-*rac*-EtOAc cocrystal-salt-solvate obtained by slow evaporation, with the major compounds represented. a) Asymmetric unit, view along *b*-axis, b) Crystal packing, view along *b*-axis.
EtOAc molecules are disordered. Only one molecule is shown for clarity.

To obtain information on the composition of the phase obtained by the slurry experiment in EtOAc, the powder was analyzed by NMR, TGA, DSC and *c*HPLC. $^{1}$H NMR analysis shows the obtention of a phase composed by 1 equivalent of BINOL and 1 equivalent of DACH without any EtOAc molecule (Figure SI-3.50). TGA analysis of the powder recovered from the slurry experiment in EtOAc exhibited a two-stage mass loss (Figure SI-3.20). The first mass loss occurs at 111°C and the material is completely degraded at 315°C. DSC analysis of the powder recovered from the EtOAc suspension experiment displayed a single melting peak, with onset of 145°C (Figure SI-3.33). Finally, *c*HPLC analysis confirmed BINOL to be racemic (Figure SI-3.43).

Both racemic compounds are also combined when using methanol as a solvent. SC-XRD analysis resulting from a slow evaporative experiment of (*rac*)-BINOL and (*rac*)-DACH in MeOH leads to the formation of the *rac*-*rac*-MeOH (1:1:1) cocrystal-salt-solvate, with a negatively charged BINOL molecule and positively charged DACH molecule (Figure 3.11, Table SI-3.9).
The simulated XRPD pattern matches that of the powder recovered from the (*rac*)-BINOL-(*R*,*R*)-DACH slurry experiment in MeOH (Figure SI-3.4). However, the

structure formed is not a conglomerate as the material crystallizes in the centrosymmetric space group *P*-1. Therefore, due to a point of inversion, both enantiomers of BINOL and DACH are present in the same crystal lattice (Figure 3.11b). The component crystallized as a solid solution with respect to DACH. Indeed, while BINOL molecules are well ordered, DACH molecule exhibit *S*-*R* disorder with a ratio of 51-49 (Figure SI-3.12), explaining the good correspondence of XRPD patterns between *rac*-*rac*-MeOH and *rac*-*RR*-MeOH. TGA analysis shows desolvation/melting of MeOH (Figure SI-3.22) upon heating with an onset at 71°C, followed by a recrystallization step at 97°C. The resulting compound undergoes a small endothermic event at 100°C and finally, melts at 143°C.

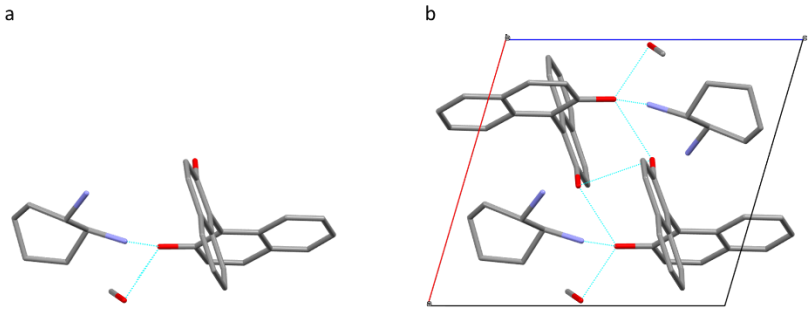


Figure 3.11. Structure of the *rac*-*rac*-MeOH cocrystal-salt-solvate, with the major compounds represented. a) Asymmetric unit, view along *b*-axis, b) Crystal packing, view along *b*-axis.
DACH molecules show *R*-*S* disorder. Only the most occupied molecule (51%) is shown for clarity.

In parallel, the slurry outcome of the mixture (*rac*)-BINOL and (*rac*)-DACH in EtOH could not be structurally characterized. $^{1}$H NMR analysis was used to determine the composition of the obtained phase. The analysis shows that the phase was composed by 1 equivalent of BINOL, 1 equivalent of DACH, and 1 equivalent of EtOH (Figure SI-3.51). This result is corroborated by the TGA analysis of the material recovered after the slurry experiments in EtOH (Figures SI-3.23). Indeed, the compound shows three distinct mass losses. The first one occurs at 60°C and is a desolvation step, corresponding in the loss of one molecule of EtOH. DSC analysis (Figure SI-3.36), confirms this desolvation with an onset at 71°C, followed by melting at 144C°. *c*HPLC analysis confirmed BINOL to be racemic in the powder.

After their desolvation, powders recovered from slurrying *(rac)*-BINOL and *(rac)*-DACH in toluene, benzene, MeOH and EtOH exhibited identical XRPD patterns, which can also be superposed to the one obtained from the slurry of (*rac*)-BINOL and (*rac*)-DACH in EtOAc (Figure SI-3.8). This observation confirms that a *rac*-*rac* (1:1)

crystal phase is obtained in EtOAc, different from the *rac*-*rac* cocrystal obtained in ACN, and that a *rac*-*rac*-EtOH (1:1:1) crystalline form is obtained in EtOH.
DSC of the powders recovered from toluene, benzene, MeOH and EtOH (Figures SI-3.31, SI-3.32, SI-3.35, and SI-3.36) allow to gather further evidence on the formation of a similar *rac*-*rac* phase after desolvation. Indeed, all thermograms show a melting peak occurring around 145°C.

## 4. Conclusion

The main goal of this study was the rational and systematic analysis of the interactions between DACH and BINOL molecules, with six different types of solvent. The solvents (toluene, benzene, ethyl acetate, acetonitrile, methanol, and ethanol) were selected based on their polarity and proticity to investigate the potential of solvatism of the BINOL-DACH systems. This led to the obtention of 11 multicomponent phases, out of which three were already known: *R*-*RR*, *S*-*RR*, and *R*-*RR*-tolu. Of the eight newly discovered phases, five are structurally resolved in this work: *R*-*RR*-benz, *rac*-*rac*, *rac*-*rac*-EtOAc, *rac*-*rac*-MeOH, and 4*rac*-4*RR*-3EtOH-1$H_2O$.

We observed that the two non-polar and aprotic solvents, toluene and benzene, which are both aromatic, yielded similar results, due to their CH-π interactions with BINOL. The crystallization outcome is therefore influenced by their aromatic nature.
The solvents ethyl acetate and acetonitrile give entirely different results. Although both are polar and aprotic, their structural differences significantly affect the outcome of the crystallization.
Finally, methanol and ethanol yielded very similar results. These two polar and protic solvents are both small alcohols, which likely contributes to their similar behavior. Therefore, a more hindered alcohol, such as *tert*-butanol, or a larger one, such as isobutanol, might not allow the incorporation of the solvent in the crystal lattice when combining (*rac*)-BINOL and (*R*,*R*)-DACH or (*rac*)-BINOL and (*rac*)-DACH.

Through this study, we observed that the *R*-*RR*-tolu compound, previously reported as a conglomerate, does not allow preferential resolution, due to twinning in the crystals formed. Moreover, none of the other solvents studied allowed conglomerates to form, making it impossible to resolve BINOL or DACH by preferential crystallization. However, BINOL and DACH can be resolved by diastereomeric crystallization. Specifically, BINOL can be resolved in toluene, benzene, and acetonitrile, while DACH can be resolved in toluene, benzene, acetonitrile, methanol, and ethanol. By this study, we have shown that diastereomeric resolution may not be achievable in all solvents, of the six solvents tested here, only three of them – toluene, benzene, and acetonitrile – allow resolving BINOL and DACH, demonstrating the importance of solvent selection in resolution processes.

# Chapter 4. Using the nature of the solvent to orient chiral resolution

This chapter again focuses on the chiral resolution of BINOL.

The idea of this research originated from contradictory findings in the literature. On the one hand, (*R*)-BINOL was successfully resolved through crystallization with (*R*,*R*)-*N*,*N*′-dimethyl-1,2-diphenylethane-1,2-diamine ((*R*,*R*)-DADPE), suggesting the existence of a cocrystal phase (*R*)-BINOL-(*R*,*R*)-DADPE.[101] On the other hand, the crystalline structure of the diastereomeric counterpart (*S*)-BINOL-(*R*,*R*)-DADPE, which appeared to be the most accessible of the two diastereomers, was elucidated.[102]

Confronted with this disparity, our objective was to determine which of these two phases was indeed the most stable, and thus the most likely to be obtained through crystallization. To this end, we explored various solvents enabling the resolution of BINOL with (*R*,*R*)-DADPE. We stumbled upon a though-provoking observation: both (*R*)- and (*S*)-enantiomers of BINOL can be resolved through cocrystallization with the same resolving agent, (*R*,*R*)-DADPE, by adjusting the solvent used.

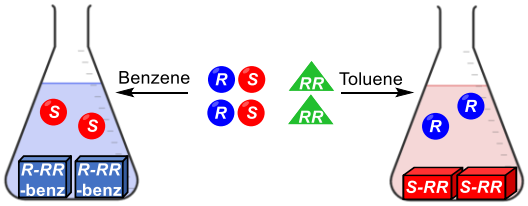


This chapter is based on the communication published by Joséphine de Meester, Oleksii Shemchuk, Laurent Collard, Johan Wouters, Simon Baillieux, Koen Robeyns, Tom Leyssens, *CrystEngComm*, **2024**, *26*, 2056-2059.

*SC-XRD characterizations were conducted by Koen Robeyns and Oleksii Shemchuk.*

# Using the nature of the solvent to orient chiral resolution

## 1. Abstract

We demonstrate the unprecedented phenomenon of solvent-oriented resolution of 1,1'-bi-2-naphtol (BINOL). Using a resolution agent of a fixed handedness (*R*,*R*)-*N*,*N*′-dimethyl-1,2-diphenylethane-1,2-diamine (DADPE), we are able to resolve either the (*S*)- or (*R*)-enantiomer of BINOL by a mere change of the achiral solvent.

## 2. Communication

Over 50% of marketed drug compounds contain a stereogenic unit. Whereas one enantiomer (the eutomer) shows a desired pharmacological effect, the other (the distomer) potentially has no, a similar, or in worst cases an adverse effect. For these latter, the drug can only be marketed as an enantiopure compound.[2,48,49,70,76] The most prominent approach to enantiopure drugs still involves the formation of a racemic mixture by non-asymmetric synthesis. The eutomer can then be resolved using a chiral resolution agent.[46,49,51,70]

BINOL (1,1'-bi-2-naphtol) is such a highly versatile agent being used both in resolution,[101,108] as well as asymmetric reactions.[101,102,109,110] Accessing enantiopure BINOL has substantial economic and scientific interest.[111–113] In 1993, Hirata et al. resolved BINOL by cocrystallization with enantiopure N,N′-dimethyl-1,2-diphenylethane-1,2-diamine (DADPE) in benzene.[101] They suspected the existence of a (*R*)-BINOL-(*R*,*R*)-DADPE cocrystal phase ((*R*)-(*R*,*R*)) (Scheme 1). In parallel, Gawronski et al. resolved the crystalline structure of the diastereomeric counter-pair (*S*)-BINOL-(*R*,*R*)-DADPE ((*S*)-(*R*,*R*)), which was seemingly the most accessible of the two diastereomers (Scheme 4.1).[102]

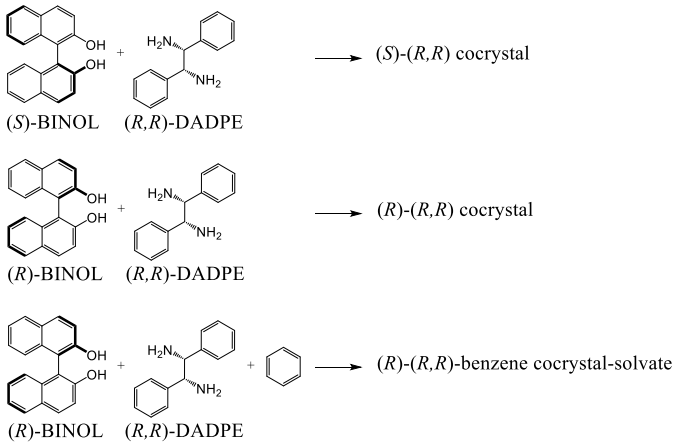


Scheme 4.1. (*R*)-BINOL and (*S*)-BINOL cocrystallize with (*R*,*R*)-DADPE, leading to a (1:1) diastereomeric cocrystal pair. (*R*)-BINOL also forms an enantiospecific cocrystal-solvate with (*R*,*R*)-DADPE and benzene.

This apparent contradiction, incited us to explore this system in detail. Astonishingly, we found that either of the enantiomers of (*rac*)-BINOL can be resolved using (*R*,*R*)-DADPE by merely changing the nature of the solvent (Figure 4.1). This surprising feature originates from the fact that the (*S*)-(*R*,*R*) cocrystal is more stable compared to the (*R*)-(*R*,*R*) diastereomer, leading to resolution of (*S*)-BINOL in all tested solvents, but benzene. Using this latter, a stable (*R*)-(*R*,*R*)-benzene cocrystal-solvate forms (Scheme 4.1). As this solvate is even more stable than the (*S*)-(*R*,*R*) cocrystal, (*R*)-BINOL can be resolved when using benzene as a solvent (Figure 4.1). To the best of our knowledge, we are the first to highlight how the nature of an achiral solvent can be used to direct the outcome of a chiral resolution process.

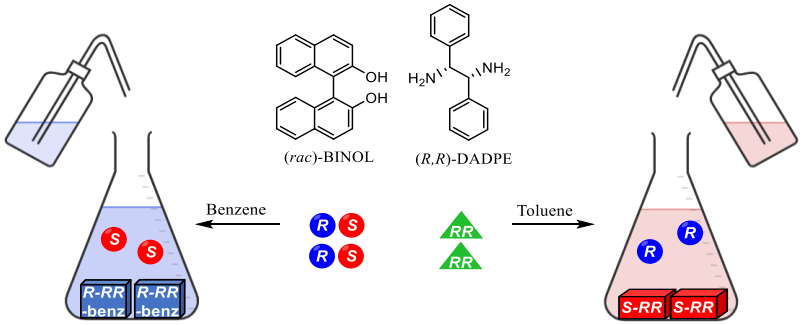


Figure 4.1. A mere choice of solvent allows targeting either one of the two enantiomers of BINOL using (*R*,*R*)-DADPE as resolution agent.

Our initial investigation of this system, started by performing congruency tests both for the (*S*)-(*R*,*R*) and (*R*)-(*R*,*R*) systems in various solvents (Table 4.1). As in Chapter

3, three groups of solvents were chosen: non-polar and aprotic solvents toluene and benzene; polar and aprotic solvents ethyl acetate (EtOAc) and dichloromethane (DCM); and polar and protic solvents methanol (MeOH), ethanol (EtOH) and isopropanol (IPA). Benzene was initially selected to compare our results with those reported in the literature. Toluene, being less hazardous, was subsequently chosen to assess its potential as a substitute for benzene. The differing outcomes observed with toluene and benzene when combining (*R*)-BINOL and (*R,R*)-DADPE (Figures 4.3 and 4.4) prompted us to expand the range of solvents examined in this study.

Table 4.1. Experimental data for solvent screening for BINOL:DADPE systems.

| Reagent | | Solvent | BINOL :DADPE (mole ratio) | m (mg) | | V solvent (mL) | P-XRD result |
|---|---|---|---|---|---|---|---|
| | | | | BINOL | DADPE | | |
| (*S*)-BINOL | (*R.R*)-DADPE | MeOH | 1 :1 | 285.89 | 211.42 | 2 | (*S*)-(*R.R*) cocrystal **DICVUH** |
| (*S*)-BINOL | (*R.R*)-DADPE | EtOH | 1 :1 | 186.02 | 211.12 | 2 | (*S*)-(*R.R*) cocrystal **DICVUH** |
| (*S*)-BINOL | (*R.R*)-DADPE | EtOAc | 1:1 | 143.3 | 106.3 | 0.5 | (*S*)-(*R.R*) cocrystal **DICVUH** |
| (*S*)-BINOL | (*R.R*)-DADPE | DCM | 1 :1 | 143.1 | 106.3 | 0.3 | (*S*)-(*R.R*) cocrystal **DICVUH** |
| (*S*)-BINOL | (*R.R*)-DADPE | toluene | 1 :1 | 285.53 | 212.02 | 2 | (*S*)-(*R.R*) cocrystal **DICVUH** |
| (*S*)-BINOL | (*R.R*)-DADPE | IPA | 1 :1 | 143.2 | 106.7 | 0.5 | (*S*)-(*R.R*) cocrystal **DICVUH** |
| (*S*)-BINOL | (*R.R*)-DADPE | benzene | 1 :1 | 143.6 | 106.4 | 2 | (*S*)-(*R.R*) cocrystal **DICVUH** |
| (*R*)-BINOL | (*R.R*)-DADPE | MeOH | 1 :1 | 286.91 | 212.44 | 0.5 | (*R*)-(*R.R*) cocrystal CCDC: **2295235** |
| (*R*)-BINOL | (*R.R*)-DADPE | EtOH | 1 :1 | 286.29 | 211.9 | 2 | (*R*)-(*R.R*) cocrystal CCDC: **2295235** |
| (*R*)-BINOL | (*R.R*)-DADPE | EtOAc | 1 :1 | 143.5 | 105.6 | 0.3 | (*R*)-(*R.R*) cocrystal CCDC: **2295235** |
| (*R*)-BINOL | (*R.R*)-DADPE | DCM | 1 :1 | 143.6 | 106.9 | 0.2 | (*R*)-(*R.R*) cocrystal CCDC: **2295235** |
| (*R*)-BINOL | (*R.R*)-DADPE | toluene | 1 :1 | 186.07 | 211.97 | 2 | (*R*)-(*R.R*) cocrystal CCDC: **2295235** |
| (*R*)-BINOL | (*R.R*)-DADPE | IPA | 1 :1 | 143.2 | 105.1 | 0.5 | (*R*)-(*R.R*) cocrystal CCDC: **2295235** |
| (*R*)-BINOL | (*R.R*)-DADPE | benzene | 1:1 | 143.5 | 105.9 | 2 | (*R*)-(*R.R*)-benzene cocrystal-solvate CCDC: **2295236** |

At 20°C, the (*S*)-BINOL-(*R*,*R*)-DADPE cocrystal behaves congruently in all tested solvents, with the cocrystal phase being identical to that reported previously (CCDC ref code: DICVUH[102]) (Figure 4.2).

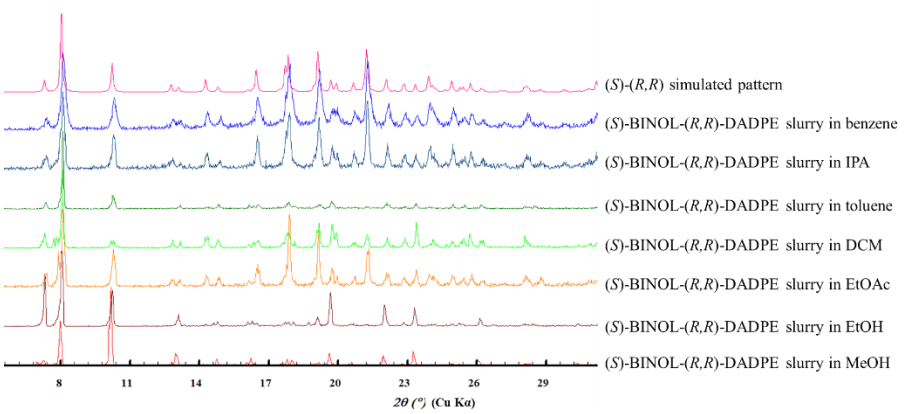


Figure 4.2. Comparison of the X-ray diffraction patterns (using Cu Kα) between 1:1 slurry outcomes of (*S*)-BINOL and (*R*,*R*)-DADPE in MeOH (red), EtOH (brown), EtOAc (orange), DCM (light green), toluene (dark green), IPA ( dark blue) and benzene (light blue) and the simulated pattern of the reported (*S*)-(*R*,*R*)-cocrystal **DICVUH**[102] (fuchsia).

Surprisingly, the combination of (*R*)-BINOL and (*R*,*R*)-DADPE resulted in two distinct phases (Figures 4.3 and 4.4).

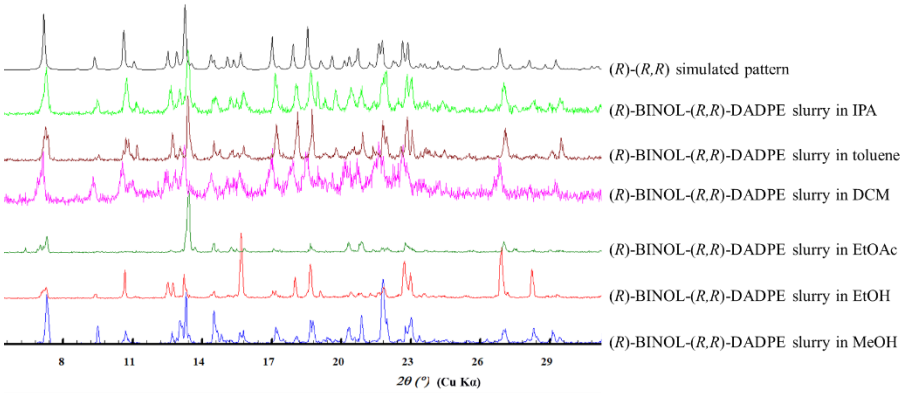


Figure 4.3. Comparison of the X-ray diffraction patterns (using Cu Kα) between the 1:1 slurry outcome of (*R*)-BINOL and (*R*,*R*)-DADPE in MeOH ( blue), EtOH (red), EtOAc (dark green), DCM (rose), toluene (brown) and IPA (in light green) and the simulated pattern of the (*R*)-(*R*,*R*)-cocrystal (black, current work – CCDC: **2295235**).

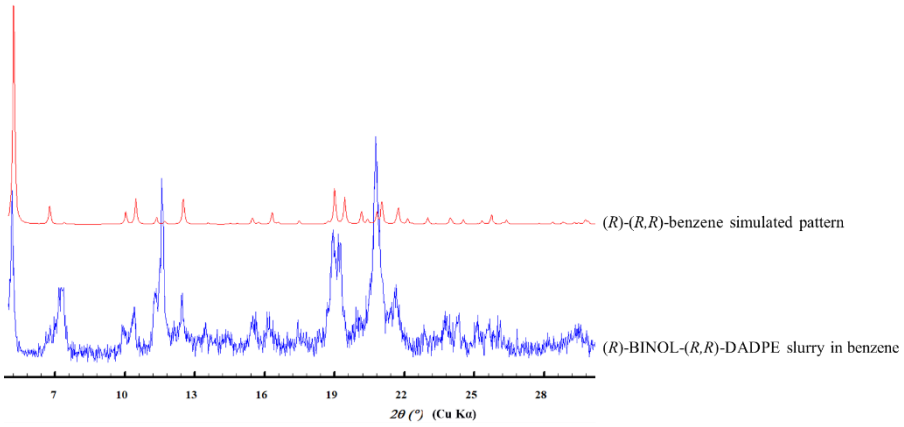


Figure 4.4. Comparison of the X-ray diffraction patterns (using Cu Kα) between the 1:1 slurry outcome of (*R*)-BINOL and (*R*,*R*)-DADPE in benzene (blue) and the simulated pattern of the (*R*)-(*R*,*R*)-benzene cocrystal-solvate (in red, current work – CCDC: **2295236**).[a]

Identical patterns were obtained in MeOH, EtOH, EtOAc, DCM, toluene, and IPA, matching the simulated pattern of the (*R*)-(*R*,*R*) cocrystal, which structure we determined (Table SI-4.1, Figures 4.3 and SI-4.1).[2] In benzene, however, a different solid form was obtained. Single crystal analysis shows this form to be a co-crystal-solvate (Table SI-4.1, Figures 4.2, 4.4, and SI-4.2)[b] characterized by a porous structure, with two distinct benzene sites. The first site, shows benzene located in a pocket surrounded by aromatic rings in close proximity to a crystallographic 2-fold axis (Figure 4.5, in blue) while the second site shows benzene covering the surface of a channel along the 4-fold axis (Figure 4.5, in green). The crystal diffracted poorly, allowing only partial localization of the benzene solvent molecules.

[a] There are some intensity differences for low-angle peaks between simulated and experimental patterns. This can be explained by varying degree of pore filling.

[b] Deposition Numbers 2295235 (a), and 2295236 (b) contain the Supplementary Crystallographic Data for this paper. These data are provided free of charge by the Joint Cambridge Crystallographic Data Centre and Fachinformationszentrum Karlsruhe Access Structures Service.

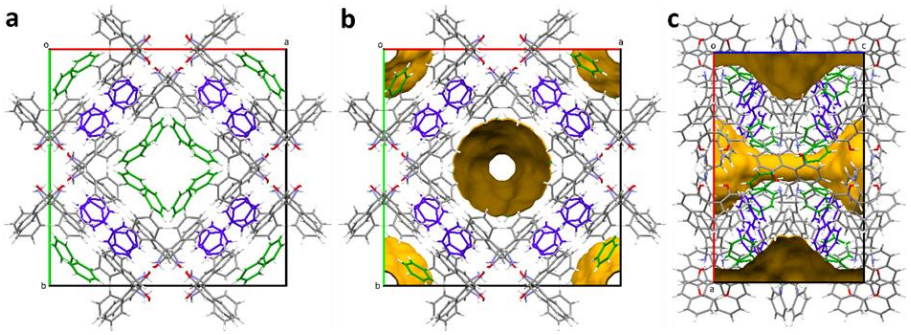


Figure 4.5. Packing of the (*R*)-(*R*,*R*)-benzene cocrystal-solvate viewed along the c-axis (a and b) and along the b-axis (c). Benzene molecules occupying different sites are represented in blue (surrounded by aromatic rings) and in green (surface of the channel). Voids are shown in (b) and (c), they are represented using Mercury, with a probe radius of 1.2Å, an approx. grid spacing of 0.3Å and calculated using the contact surface.

Thermal analysis confirms the presence of distinct solvate sites.[c] Gravimetric analysis (Figure 4.6) shows a first gradual mass loss occurring up to 50°C likely corresponding to benzene loosely retained inside the channels. This loss is no longer present after having stored the sample for multiple days under ambient conditions (Figure SI-4.10). At 50°C a more abrupt loss is observed, corresponding to remaining benzene covering the inside of the voids (green in Figure 4.5). Both combined losses correspond to an 8.7% weight loss representing 0.6 equivalents of benzene.

[c] Slight variations in onset temperature can occur due to different experimental setups between TGA, DSC, and VT-XRPD.

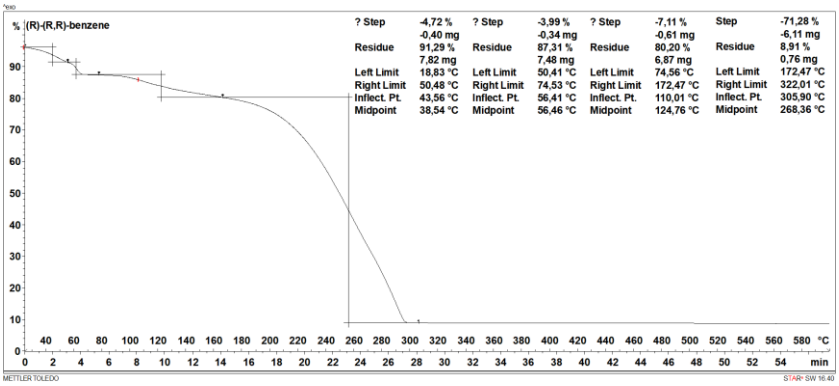


Figure 4.6. TGA of the (*R*)-(*R*,*R*)-benzene cocrystal-solvate, analyzed directly after filtration and obtained slurrying a 1:1 ratio in benzene. The thermogram is expressed as the weight loss (%) with respect to temperature. The thermogram shows multiple mass changes. The two first ones start at 19°C and consist in desolvation and evaporation of benzene inside the solvent channel (loss of 0.61 equivalent of benzene), the second mass change starts at 75°C and also represents desolvation (loss of 0.49 equivalent of benzene), the third mass change starts at 171°C and consists in the degradation of the compound.

A DSC-endotherm at 50°C (Figure SI-4.13) aligns with this first desolvation process, with VT-XRPD (Figures 4.7, and SI-4.15 to SI-4.17) showing minor peak modifications at 55°C characteristic of a slight change in the crystal structure. The loss of the benzene molecules located at the second site (blue in Figure 4.5), is observed at 75°C, characterized by a weight loss of 7.11%, corresponding to 0.5 equivalents of benzene. DSC shows the characteristic desolvation endotherm, with a VT-XRPD showing a transition to the non-solvated (*R*)-(*R*,*R*) cocrystal phase.

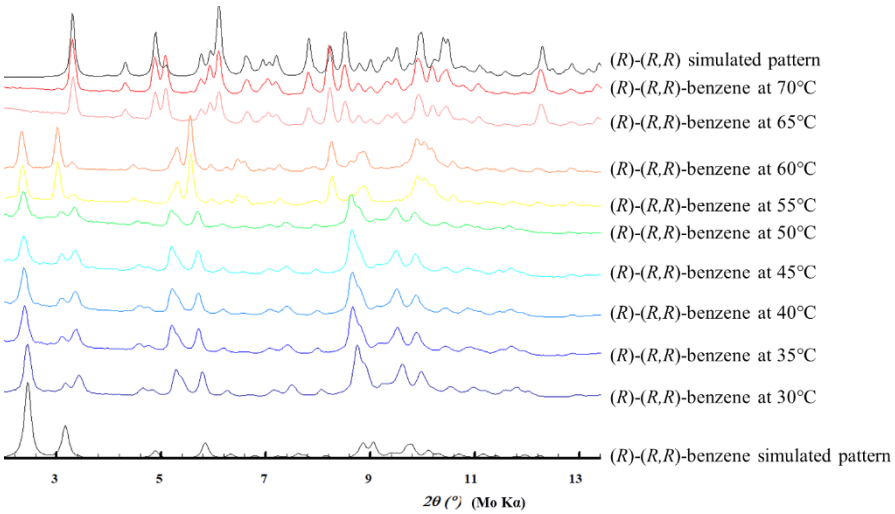


Figure 4.7. Variable temperature PXRD patterns (using Mo Kα) for the (*R*)-(*R*,*R*)-benzene cocrystal-solvate, obtained slurrying a 1:1 mixture in benzene and compared to the simulated patterns of the compounds (*R*)-(*R*,*R*)-benzene and (*R*)-(*R*,*R*) (black).

The similar structural motifs of the non-solvated and solvated phases (Figure SI-4.3) are indicative of a true solid-solid transition during desolvation, with the non-solvated phase no longer presenting a pore-like structure and a resulting higher density (Table SI-4.1). The non-solvated cocrystal melts at 130°C (Figure SI-4.12 and SI-4.13).

To identify the potential diastereomeric (*S*)-(*R*,*R*)-benzene cocrystal-solvate a multitude of experiments were performed. Several months of work did not lead to the successful identification of such a form, allowing us to conclude the solvated system behaves enantiospecifically,[95] with the (*S*)-(*R*,*R*)-benzene never crystallizing. To our knowledge, this is the first occurrence of a solvent inducing cocrystal enantiospecificity, with the non-solvated system behaving diastereomerically.

The relative stability between the non-solvated diastereomeric (*R*)-(*R*,*R*) and (*S*)-(*R*,*R*) cocrystals was determined based on their solubility in various solvents, excluding benzene. The (*S*)-(*R*,*R*) diastereomer is the less soluble of both (Table 1), and hence thermodynamically more stable in the range of 10°C to 60°C (Figures SI-4.18 to SI-4.21).[50,114] This implies that (*R*,*R*)-DADPE can be used to resolve (*S*)-BINOL from a racemate using any tested solvent but benzene.

Switching to benzene, the (*R*)-(*R*,*R*)-benzene cocrystal-solvate shows lower solubility compared to the (*S*)-(*R*,*R*) cocrystal (Table 4.2 and Figure SI-4.22). This (*R*)-(*R*,*R*)-benzene cocrystal solvate is therefore thermodynamically favored in a benzene

suspension.[d] Interestingly, this implies (*R*,*R*)-DADPE can once more be used, but this time to resolve (*R*)-BINOL from a racemate.

While, in general, the handedness of the resolution agent needs to be changed to target the counter-enantiomer of a molecule to resolve,[114] here we show an original approach where the nature of the non-chiral solvent orients the resolution process. Using the same resolution agent, (*R*,*R*)-DADPE, (*S*)-BINOL can be recovered using benzene, whereas (*R*)-BINOL can be recovered using any other tested solvent.

Table 4.2. Solubility of the solid forms in various solvents, at 20°C. The values were taken from the solubility curves (Figures SI-4.18 to SI-4.22).

| | MeOH | EtOH | IPA | Toluene | Benzene |
|---|---|---|---|---|---|
| $C_{(R)\text{-}(R,R)}$ (mg/mL) | 204 | 78[a] | 34 | 48[a] | - |
| $C_{(S)\text{-}(R,R)}$ (mg/mL) | 199 | 66[a] | 14[a] | 6[a] | 40 |
| $C_{(R)\text{-}(R,R)\text{-benzene}}$ (mg/mL) | - | - | - | - | 18[b] |

[a] The solubility values were determined by extrapolation of the solubility curves.

[b] The solubility of the cocrystal-solvate is expressed in mg of (*R*)-(*R*,*R*)-benzene solvate vs. overall amount of benzene present.

We showcase this potential focusing on processes based on toluene and benzene. Both were chosen as they are structurally similar and furthermore toluene shows a significant solubility difference between the two diastereomeric cocrystals.

To establish the resolution processes isoplethal ternary phase-diagrams of both the (*rac*)-BINOL-(*R*,*R*)-DADPE-toluene and (*rac*)-BINOL-(*R*,*R*)-DADPE-benzene systems were constructed. These are cross-sections of the full quaternary diagram[50,76,94,96], for which the apexes are composed of (*R*)-BINOL ; (*S*)-BINOL ; (*R*,*R*)-DADPE and the solvent. For both isoplethal diagrams the overall composition in BINOL (solid and solution phases combined) is always racemic. The diagrams serve to determine conditions under which resolution occurs. To construct these cross-sections a set of vials with varying composition of (*rac*)-BINOL, (*R*,*R*)-DADPE, and the solvent (Tables SI-4.8 and SI-4.9), were prepared, seeded with all possible forms,

[d] The stability of a solvate depends on the temperature. Figure SI-22 shows the benzene solvate to be stable up to 40°C at least.

and left to equilibrate. Upon filtration, the solid phases were analyzed. Figure 4.8 displays both diagrams showing the thermodynamically stable phases in suspension.

Both diagrams show similar features. Looking at the lower parts of the diagrams (lower amount of solvent), from left to right, a first zone corresponds to suspensions where (*rac*)-BINOL is the only stable phase in suspension, as would be expected for overall compositions containing a large excess of (*rac*)-BINOL (Figure 4.8, yellow squares). As more (*R*,*R*)-DADPE is added, a zone is found, characterized by a suspension of (*rac*)-BINOL combined with the most stable cocrystal (Figure 4.8a: (*rac*)-BINOL + (*S*)-(*R*,*R*) in red triangles; Figure 4.8b: (*rac*)-BINOL + (*R*)-(*R*,*R*)-benzene in red dots). Increasing the amount of (*R*,*R*)-DADPE even further, the second, less stable cocrystal also appears, leading to a zone containing three solid forms in suspension (Figure 4.8a: (*rac*)-BINOL + (*S*)-(*R*,*R*) + (*R*)-(*R*,*R*) in pink triangles; Figure 4.8b: (*rac*)-BINOL + (*R*)-(*R*,*R*)-benzene + (*S*)-(*R*,*R*) in orange dots). Still higher amounts of (*R*,*R*)-DADPE lead to a suspension of the two cocrystal phases, with this zone being larger using benzene as a solvent (Figure 4.8a: (*S*)-(*R*,*R*) + (*R*)-(*R*,*R*) as a purple triangle; Figure 4.8b: (*R*)-(*R*,*R*)-benzene + (*S*)-(*R*,*R*) in violet dots). Further addition of (*R*,*R*)-DADPE, then leads to the zone of interest for resolution, with only the targeted cocrystal being the stable phase in suspension (Figure 4.8a: (*S*)-(*R*,*R*) in blue diamonds; Figure 4.8b: (*R*)-(*R*,*R*)-benzene in pink diamonds). When the amount of (*R*,*R*)-DADPE added becomes too important, a zone is encountered where the cocrystal of interest crystallizes simultaneously with (*R*,*R*)-DADPE (Figure 4.8a: (*S*)-(*R*,*R*) + (*R*,*R*)-DADPE in dark blue triangles; Figure 4.8b: (*R*)-(*R*,*R*)-benzene + (*R*,*R*)-DADPE in dark blue dots). Finally, excessive amounts of (*R*,*R*)-DADPE lead to a suspension of this compound only (Figure 4.8: rightmost regions of the diagrams, green squares).

For higher amounts of solvent, a similar behavior occurs going from left to right throughout the diagrams, with the difference that suspensions containing three solid forms no longer occur.

As mentioned, these diagrams allow setting conditions for the effective resolution of both enantiomers of BINOL using (*R*,*R*)-DADPE as a resolution agent, using respectively toluene or benzene.

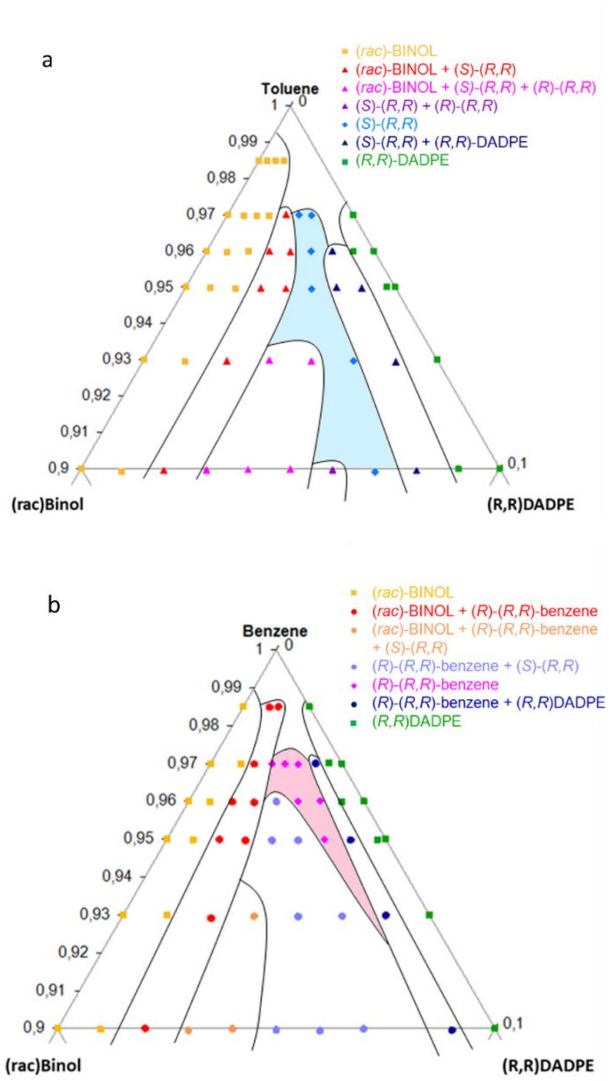


Figure 4.8. Isoplethal ternary phase diagram of the system (*rac*)-BINOL-(*R*,*R*)-DADPE-solvent, at 20°C, in toluene (a) and benzene (b). Delimiting lines are only guides for the eye.

Based on these diagrams, resolution was successfully conducted on a 2-gram scale using both toluene or benzene as solvent. This led to the recovery of (*S*)- and (*R*)-BINOL with respectively an *ee*>97% (Figures SI-4.24 and SI-4.25) and *ee*>99%

(Figures SI-4.26 and SI-4.27).[e] The amount of DADPE and the volume of solvent (toluene or benzene) required to resolve BINOL were calculated to correspond to the colored areas of the ternary diagrams (Figure 4.8 (a) blue or (b) pink), allowing only the desired pure multicomponent solid (*S*-*RR* cocrystal or *R*-*RR*-benzene cocrystal-solvate) to be collected. To highlight the symmetry of the system, resolution of BINOL was performed using (*S*,*S*)-DADPE in benzene, leading as expected to the recovery of the (*S*)-(*S*,*S*)-benzene cocrystal-solvate (Figure SI-4.23).

This contribution showcases the use of an achiral solvent to orient the outcome of a resolution process. We are the first to show how both (*R*)- and (*S*)-BINOL can be resolved from a racemic mixture using (*R*,*R*)-DADPE as a resolving agent. To achieve this astonishing feature, we merely adapt the nature of the solvent, using toluene to target the (*S*)-, and benzene to target the (*R*)-enantiomer. This peculiarity finds its origin in the existence of both a diastereomeric cocrystal system, as well as an enantiospecific benzene solvate system. Guided by the thermodynamics of the system, we successfully developed an upscaled resolution–leading to the recovery of (*S*)-BINOL with an *ee*>97% using toluene and (*R*)-BINOL with an *ee*>99% using benzene. We believe such systems will be further explored as the number of cocrystal solvates increases.[33,115–119]

## 3. Acknowledgements

The authors would like to thank the FNRS (PDR T.0262.20) for funding.

[e] The resolution processes presented here are conducted at 20°C, and could be further optimized working at different temperatures.

# Chapter 5. Towards a new approach in chiral resolution: pressurized-$CO_2$ assisted preferential cocrystallization

This chapter was conducted as part of a scientific research stay in the laboratory of Dr. Christelle Harscoat-Schiavo.

The project aimed to develop a preferential crystallization process through the addition of pressurized $CO_2$. To achieve this, we focused on the Nefiracetam-Mandelic acid cocrystal-conglomerate system. In this chapter, pressurized $CO_2$ is considered as an anti-solvent, allowing the crystallization of the cocrystal.

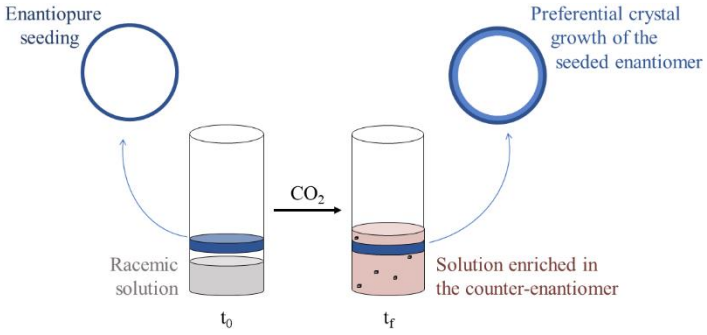


This chapter is based on the article written by Joséphine de Meester, Patrick Layrisse, Mathieu Marchivie, Laurent Collard, Guillaume Wery, Clément Brandel, Yohann Cartigny, Pascale Subra-Paternault, Tom Leyssens, Christelle Harscoat-Schiavo, submitted to *The Journal of Supercritical Fluids*.

# Towards a new approach in chiral resolution: pressurized-$CO_2$ assisted preferential cocrystallization

## 1. Abstract

We here report the first occurrence of a preferential cocrystallization process assisted by compressed carbon dioxide. Our study focuses on the Nefiracetam-Mandelic acid conglomerate forming system. The cocrystal conglomerate was successfully crystallized using compressed $CO_2$ as antisolvent, and acetone, ethyl acetate, or isobutanol as solvents for starting solutions in the so-called GAS process. We then focus on acetone to successfully perform preferential cocrystallization supported by compressed $CO_2$. A critical step in the design of the process is the adaptation of the set-up to allow the introduction of enantiopure seeding inside the reactor. Based on the use of seeded rings, we test several seeding configurations to enhance enantioseparation through the simultaneous crystallization of both enantiomers in two different areas of the reactor.

## 2. Introduction

Chirality, the property of molecules to exist in distinguishable mirror-image forms, plays a pivotal role across various industries, including agrochemical, food, pharmaceutical, materials, ….[2,49,51,120] The demand for enantiopure compounds arises from the distinct physicochemical properties exhibited by enantiomers in asymmetric environments, such as the human body.[2,49,51] Consequently, extensive research efforts are focused on developing methods for the production of enantiopure molecules. These processes can be roughly divided into two categories: asymmetric synthesis and chiral resolution. In asymmetric synthesis, the aim is to selectively synthesize the desired enantiomer,[49,51] whereas for resolution methodologies, racemic mixtures are produced, and enantiomers are subsequently separated using a physical separation technique.[51,88] Various methods of chiral resolution have been developed over the recent decades, one of which is preferential crystallization.[51,77,88]

Preferential crystallization is a kinetic process that relies on a difference in crystallization rate of enantiomers through the use of homochiral seeds. The technique requires the compound to crystallize as a conglomerate – a physical mixture of enantiopure crystals.[77] This forms a major limitation to the methodology, as a mere 5 to 10% of chiral molecules crystallize as a conglomerate.[51,77,88] To broaden the scope

of this technique, ongoing research endeavors aim to convert racemic compounds – containing equal amounts of both enantiomers in the crystal unit cell – into conglomerates. Various crystal engineering strategies[80] have been applied in this context over the recent years including salt,[84,85] solvate,[86] and cocrystal[62,87–90] formation. As an example, Buol et al,[88] illustrated the cocrystal approach, transforming the racemic compound mandelic acid (MA) into a conglomerate through a (1:1) cocrystallization with nefiracetam (nefi) (Figure 5.1). They furthermore used this finding to develop a resolution through preferential cocrystallization, working with acetonitrile.

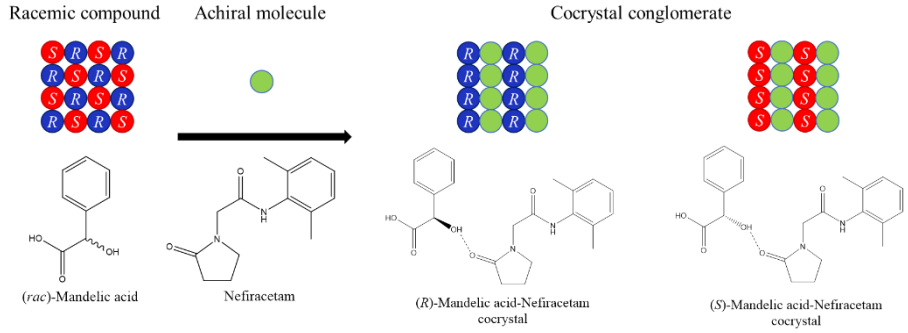


Figure 5.1. Conversion of the racemic compound mandelic acid into a conglomerate through cocrystallization with nefiracetam.

In this work, we want to take this system one step further. We pioneer in showing how pressurized carbon dioxide can be successfully used in the context of preferential crystallization.

The recent increase in pressurized carbon dioxide, and particularly supercritical carbon dioxide (SC-$CO_2$), research reflects the growing interest in this fluid. Indeed, SC-$CO_2$ is considered as non-toxic, non-flammable, chemically inert, and is recyclable through pressure reduction.[120–124]

The versatility of SC-$CO_2$ spans various processes. Its relatively low critical temperature (31°C) allows the extraction of thermally unstable compounds. Moreover, it serves as a solvent for various reactions,[122,125] or even as an antisolvent for particle micronization[126,127] and cocrystallization.[128–131] Furthermore, SC-$CO_2$ finds applications in polymer synthesis, and textile dyeing.[127]

This study contributes to the continuous expanding field of compressed $CO_2$ research, by exploring its potential in chiral resolution. While SC-$CO_2$ processes have already been successfully studied in the context of diastereomeric salt resolution,[121,132–135] here we broaden the scope by showcasing the feasibility to develop preferential cocrystallization assisted by pressurized $CO_2$. We do so, focusing on the chiral

resolution of the nefi-MA cocrystal, using $CO_2$ as an antisolvent. We began by exploring the ability of SC-$CO_2$ to induce conglomerate cocrystal formation, to then develop a preferential crystallization process assisted by $CO_2$. With our study, we lay the next brick for the consolidation of $CO_2$ processes as alternative tools for chiral resolution.

# 3. Materials and methods

## 3.1 Materials

Nefiracetam (LSherb), (*rac*)-mandelic acid (TCI Chemicals), (*R*)-mandelic acid (TCI Chemicals), (*S*)-mandelic acid (TCI Chemicals), acetone (HPLC grade, Atlantic labo), ethyl acetate (EtOAc, analytical grade, Atlantic labo), isobutanol (analytical grade, Atlantic labo), isohexane (analytical grade, Atlantic labo), absolute ethanol (Atlantic labo) , 2-propanol (Atlantic labo), trifluoroacetic acid (Atlantic labo), phosphoric acid (Atlantic Labo), acetonitrile (HPLC grade, Atlantic labo) and carbon dioxide ($CO_2$, 99.5%, Messer) were purchased from commercial sources and used as such.

For convenience, nefiracetam will be abbreviated as nefi, and mandelic acid as MA throughout the rest of the document.

## 3.2 Enantiopure seed preparation

Enantiopure seeds were obtained on larger scale (approximately 20 g) from ethyl acetate. Equimolar amounts of nefiracetam (15.00 g) and (*R*)-MA or alternatively (*S*)-MA (9.27 g) were introduced in a reactor vessel filled with ethyl acetate (100 mL). The suspension was stirred at 300 rpm for 48 h at RT. Subsequently, the suspension was filtered and the resulting powder was washed with ethyl acetate and dried. This material served as the seeding material for preferential crystallization experiments.

## 3.3 X-ray powder diffraction (XRPD)

Two instruments were used for the XRPD data collection.

Part of the samples were measured using a Siemens D5000 diffractometer equipped with a Cu X-ray source operating at 40 kV and 40 mA. The instrument uses a secondary monochromator to select the Kα radiation of Cu ($\lambda$ = 1.5418 Å). A scanning range of 2θ values spanned from 5° to 35°.

Alternatively, XRPD data were collected using a PANalytical X'pert PRO MPD diffractometrer equipped with a secondary monochromator and X′Celerator multi-strip detector with copper radiation ($\lambda$ = 1.5418 Å). A scanning range of 2θ values spanned from 4° to 38°.

The samples were gently ground to limit preferred orientations. The powders were then placed uniformly on sample holders made of aluminium alloy and flattened with a razor blade.

## 3.4 Chiral High-Performance Liquid Chromatography (*c*HPLC)

Chiral HPLC was used to determine the relative amount of both enantiomers of mandelic acid. Samples were prepared by dissolving the sample in a solution composed of 80 vol.% isohexane, 20 vol.% EtOH. Two instruments were used for chiral high-performance liquid chromatography (*c*HPLC).

Part of the analyses were carried out using a Waters Alliance 2695 coupled with a Waters 996 Photodiode Array Detector (PDA) (λ = 220nm). The column used was a Daicel Chiralpak IC, 4.6 × 250 mm, 5 μm, the sample injection volume was 10 μL. A mobile phase consisting of 95 vol.% isohexane, 5 vol.% 2-propanol, 0.1 vol.% trifluoroacetic acid was used. The separation was achieved in 30 min, at RT with a flow rate of 1 mL/min. After three sample runs, the column was washed with isohexane/ethanol (80/20, v/v) at a rate of 1 mL/min for 30 min.

Alternatively, enantiomeric quantification was performed using an Agilent Infinity 1260 system (Agilent Technologies) equipped with a degasser, a quaternary pump, an automatic injector, a diode array detector (DAD) and Chemstation software for data acquisition. The column and method used were identical to the procedure described above.

Each data point is the average of two distinct samples of 20 mg powder in 20 mL solution.

Enantiomeric excess was calculated for each sample. It is used to express the excess of one enantiomer over the second in a mixture. The formula used is as follows:

$$ee\ (\%) = \frac{\big((R) - \text{enantiomer}\big) - \big((S) - \text{enantiomer}\big)}{\big((R) - \text{enantiomer}\big) + \big((S) - \text{enantiomer}\big)} \text{x}\ 100$$

A compound with an enantiomeric excess of 0% is racemic, while when the enantiomeric excess is 100%, the compound is enantiopure.

## 3.5 Reverse High-Performance Liquid Chromatography (*r*HPLC)

Reverse HPLC is used to quantify exact amounts of nefiracetam vs mandelic acid. The compounds were dissolved in a solution composed by 50 vol.% acetonitrile, 50 vol.% Milli-Q water. Calibration curves for reverse high-performance liquid

chromatography (*r*HPLC) were built correlating the area under the curve (AUC) with the concentration used following a linear equation. Calibration lines (at λ = 210 nm) are reported in Figures SI-1 and SI-2.

For dosing nefi:MA molar ratios, samples were prepared by dissolving the sample in a solution composed by 50 vol.% acetonitrile, 50 vol.% Milli-Q water. The instrument used was an Agilent Infinity 1260 system (Agilent Technologies) equipped with a degasser, a quaternary pump, an automatic injector, a diode array detector (DAD) (λ = 210nm) and Chemstation software for data acquisition. The column used was a Kinetex C18 F5 (Phenomenex), 100x4.6 cm, 2.6 µm, the sample injection volume was 5 µL. The separation, performed at 40 °C with a flow rate of 1 mL/min, was achieved in 14 min. The mobile phase consisted of a gradient of solution A – water + 0.1 vol.% phosphoric acid ($H_3PO_4$) and solution B – acetonitrile + 0.1 vol.% $H_3PO_4$ in the following sequence: 0 to 0.5 min at 30% B, followed by increasing B from 30% to 90% in 5 min, a step of 1 min at 90% B and reequilibration at 30% B during the remaining 7.5 min.

Each data point is the average of two distinct samples of 10 mg powder in 20 mL solution.

## 3.6 Cocrystallization using $CO_2$ as an antisolvent

The experimental set-up used is a custom-built Gaseous Anti Solvent (GAS) equipment (Scheme 5.1). The process starts by loading the pre-heated reactor with a volume of solution and subsequently introducing $CO_2$. Nefi and MA were dissolved in 30 mL of acetone, EtOAc or isobutanol at various concentrations and molar ratios. The solution was placed in an ultrasonic bath for approximately 3 minutes to ensure complete dissolution of all starting materials, then it was pre-heated on a hot plate. The 0.49 L reactor is equipped with three sapphire windows, and a stainless-steel filter topped with a 0.2 µm pore size membrane at its bottom. A mechanical stirrer ending with a hollow Rushton turbine plunged into the solution and allowed direct dispersion of the $CO_2$ into the solution. The stirring rate was set to 300 rpm. A glass cylinder covering the inner surface of the reactor was used for easy recovery of the crystals obtained. The reactor temperature (40 °C) was regulated by a heating tape and monitored by a sensor centrally positioned about 2 cm above the Rushton turbine. Compressed $CO_2$ was first cooled in a cryostat at 0 °C and its introduction was carried out using an SFE (Model HPP400-B, SFE Process) pump at a rate of 11 g/min. During this step, as $CO_2$ was added gradually, the pressure inside the vessel increased and the solvent-$CO_2$ mixture shifted from a liquid-vapor system to a monophasic fluid. At the same time, the solubility of components decreased, leading to a precipitation event that could be observed through the sapphire windows. Once the desired pressure of 10.0 MPa was reached, the formed $CO_2$-solvent mixture was drawn from the bottom

of the reactor while fresh $CO_2$ was added to the system at 35 g/min to maintain the pressure and to dry the obtained powder. The pressure in the reactor was controlled at 10.0 ± 0.5 MPa by an exit metering valve. At the end of the process, the system was depressurized through the exit line, and particles were collected, weighed and analyzed.

The resulting powder was collected in different fractions: on the stirrer shaft, inside the reactor, and inside the outlet collector.

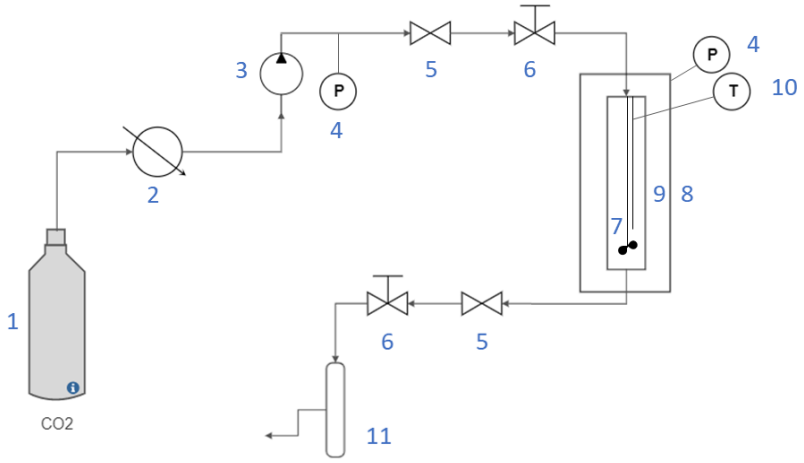


Scheme 5.1. GAS set-up, with 1. $CO_2$ tank; 2. cooler; 3. $CO_2$ pump; 4. pressure gauge; 5. valve; 6. metering valve; 7. mechanical stirrer; 8. reactor; 9. glass cylinder; 10. thermocouple; 11. outlet collector.

## 3.7 Preferential cocrystallization using a $CO_2$ antisolvent process

The method and instrumentation used are identical to the one described in Section 3.6 (Cocrystallization using $CO_2$ as an antisolvent), with exception of the moment the solution was withdrawn from the vessel. The process was halted when the experimenter observed the solution to become turbid, which occurred at different pressures for each experiment (between 6.6 and 7.2 MPa). As preferential crystallization requires seeding, an enantiopure seeding set-up was used to guide the outcome of the process. Seeding material was added on the inner face of the glass cylinder, above the solution level, at a height of 4.5-5.5 cm. To do this, enantiopure seed was slurried in acetone, the slurry was subsequently applied on the surface of the cylinder and acetone was allowed to evaporate, leaving a solid enantiopure crust on the cylinder. Initial experiments used a one-piece cylinder. Subsequently, a transition was made to a cylinder composed of three parts (respectively of 4.5 cm – 1 cm – 16.5

cm) to facilitate the seeding process, and the collection of crystals after the experiment.

Upon completion of the process, the resulting powder was collected in the various parts of the reactor: on the stirrer shaft, on the seeded cylinder (powder crystallizing on the enantiopure seeds), inside the reactor (remaining powder inside the reactor), and inside the outlet collector. Prior to powder collection on the seeded cylinder, meticulous sampling was performed on both the outer surface and deeper inside the layer, closer to the seed, utilizing a thin spatula. To do this, we first collected a small amount of surface powder, and then dug for collecting powder at greater depth.

# 4. Results and discussions

## 4.1 Enabling the conglomerate cocrystallization process

First, our investigation focused on the feasibility of forming the nefi-MA cocrystal using a $CO_2$ antisolvent process. Initial attempts aimed at selecting a solvent. To achieve this, (1:1) stoichiometric ratios of nefi and enantiopure or racemic MA were dissolved in ethyl acetate (EtOAc), acetone, or isobutanol (Table 5.1). $CO_2$ was introduced until achievement of a final pressure of 10 MPa. In all experiments, the mixture became turbid before reaching this pressure. This shows that crystallization had occurred prior to reaching 10 MPa and that $CO_2$ effectively acts as an antisolvent in this process. All experiments led to the formation of the cocrystal (Figure 5.2). Moreover, experiments involving enantiopure mandelic acid (Runs 1-3), led to the crystallization of pure cocrystal material, as confirmed by XRPD (Figure 5.2) and *r*HPLC (Table 5.1). With racemic mandelic acid, however, experiments resulted in cocrystal formation combined with concomitant crystallization of the nefi parent compound for all of the three solvents used (Runs 4-6, Figure 5.2), indicating the need to adapt the nefi:(*rac*)-MA ratio in these solvents. When using EtOAc or acetone, *r*HPLC data aligns with XRPD results, confirming the slight excess of nefi in the obtained powders, while with isobutanol, the excess of nefi is only observable with XRPD analysis. The low *ee*'s obtained when starting from racemic mandelic acid fall within experimental error, and indicate that chiral resolution did not occur spontaneously. This is expected as both enantiomeric cocrystals show identical crystallization kinetics in the absence of a chiral external factor. As in classical preferential crystallization processes, enantiopure seeding is a necessity to promote selective growth of a given enantiomer.[77]

Table 5.1**.** Cocrystallization experiments of nefi and MA by GAS in EtOAc, acetone, and isobutanol.

| Run | Initial compounds | Solvent | C(nefi + MA) (g/L) | Crystallization yield* (%) | Product | Nefi:MA molar ratio of the recovered powder** | *ee* reactor*** |
|---|---|---|---|---|---|---|---|
| **1** | nefi + (*S*)-MA (1:1) | EtOAc | 48.4 | 63.3 | nefi-(*S*)-MA cocrystal | (1:1) | - |
| **2** | nefi + (*S*)-MA (1:1) | Acetone | 66.4 | 64.6 | nefi-(*S*)-MA cocrystal | (1:1) | - |
| **3** | nefi + (*S*)-MA (1:1) | Isobutanol | 66.4 | 28.5 | nefi-(*S*)-MA cocrystal | (1:1) | - |
| **4** | nefi + (*rac*)-MA (1:1) | EtOAc | 48.4 | 64.0 | nefi-(*rac*)-MA cocrystal + nefi | (1.1:1) | -2 |
| **5** | nefi + (*rac*)-MA (1:1) | Acetone | 66.4 | 48.8 | nefi-(*rac*)-MA cocrystal + nefi | (1.1:1) | 0 |
| **6** | nefi + (*rac*)-MA (1:1) | Isobutanol | 66.4 | 22.1 | nefi-(*rac*)-MA cocrystal**** | (1:1)**** | 0 |

*The crystallization yield was determined as the amount recovered on the stirrer shaft, and inside the reactor at the end of the experiment compared to the total amount of material used. Remaining powder was found in the outlet collector.

**Nefi:MA molar ratios of the obtained products were determined by *r*HPLC.

****ee* were determined by *c*HPLC.

****Traces of nefi are observed by XRPD.

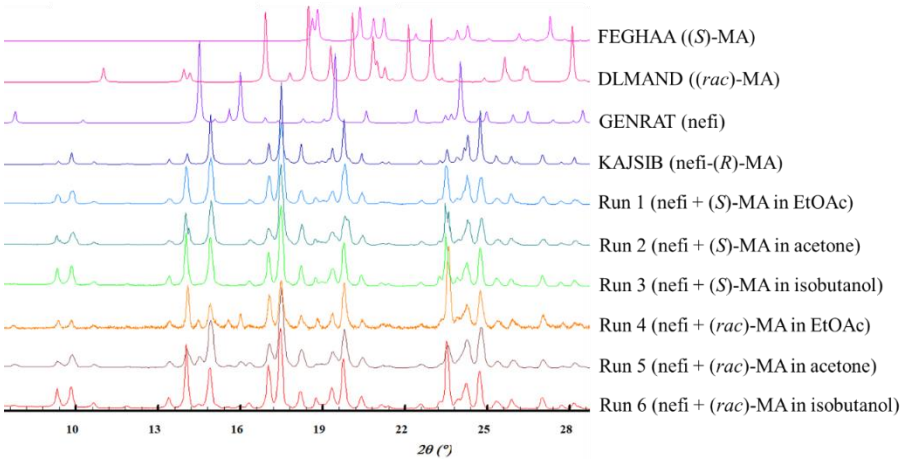


Figure 5.2. Comparison of the XRPD patterns of nefi-(*rac*)-MA (1:1) cocrystallization through GAS in isobutanol (red), acetone (brown), EtOAc (orange), nefi-(*S*)-MA (1:1) cocrystallization through GAS in isobutanol (light green), acetone (dark green), and EtOAc (light blue), and the simulated patterns of the reported nefi-(*R*)-MA-cocrystal (CCDC refcode KAJSIB) [88] (dark blue) and parent compounds nefi (CCDC refcode GENRAT) [136] (violet), (*rac*)-MA (CCDC refcode DLMAND) [137] (magenta), and (*S*)-MA (CCDC refcode FEGHAA) [138] (pink).

Overall, these results show that any of the three solvents above can be successfully used to crystallize both enantiopure, and the conglomerate cocrystal using SC-$CO_2$ technology. We then moved to the next step, being the development of a preferential crystallization process.

## 4.2 Preferential crystallization

### *4.2.1 Process design*

Even though all three solvents seemed appropriate, acetone was selected for the remainder of the study, based on our expertise with this solvent in the frame of crystallization using $CO_2$ as an antisolvent [128,129,139,140]. As starting from (*rac*)-MA, some amount of nefiracetam crystallizes together with the cocrystal conglomerate, experiments were performed adjusting the nefi:(*rac*)-MA molar ratio (Table 5.2, Runs 7-11). As confirmed by XRPD and *r*HPLC analysis, decreasing the ratio to (0.7:1) resulted in the production of pure cocrystal material. This optimized ratio was used in all subsequent resolution experiments.

As mentioned above (Runs 4-6), and as expected, processes performed without enantiopure seeding always resulted in the crystallization of both enantiomers. To incorporate seeding in a $CO_2$ antisolvent process, we designed a set-up wherein a

cylinder is coated with seed material at a given height (Figure 5.3a). To prevent these seeds from dissolving in contact with the solution initially introduced, this seed material is set above the solution level (Figure 5.3b, $t_0$). Upon $CO_2$ introduction, as $CO_2$ is miscible with the used solvent, the solution expands while the solubility of the compounds in the newly expanded $CO_2$-solvent solution decreases. The solution should become supersaturated prior to reaching the seed material. Upon reaching this latter (Figure 5.3b, $t_f$), preferential growth can theoretically be initiated on the seeded cylinder (Figure 5.3c). The seeding height, therefore, needs to be carefully controlled, depending both on the nature of the solvent as well as the overall concentration. If the seed material is reached too rapidly, the overall solution might still be undersaturated and the seeds would dissolve. If the seed coating is positioned too high, spontaneous concomitant crystallization of both enantiomers from a highly supersaturated solution occurs prior to reaching the seed material. In our set-up, a 1 cm seeded coating ring was always placed at a height of 4.5-5.5 cm.

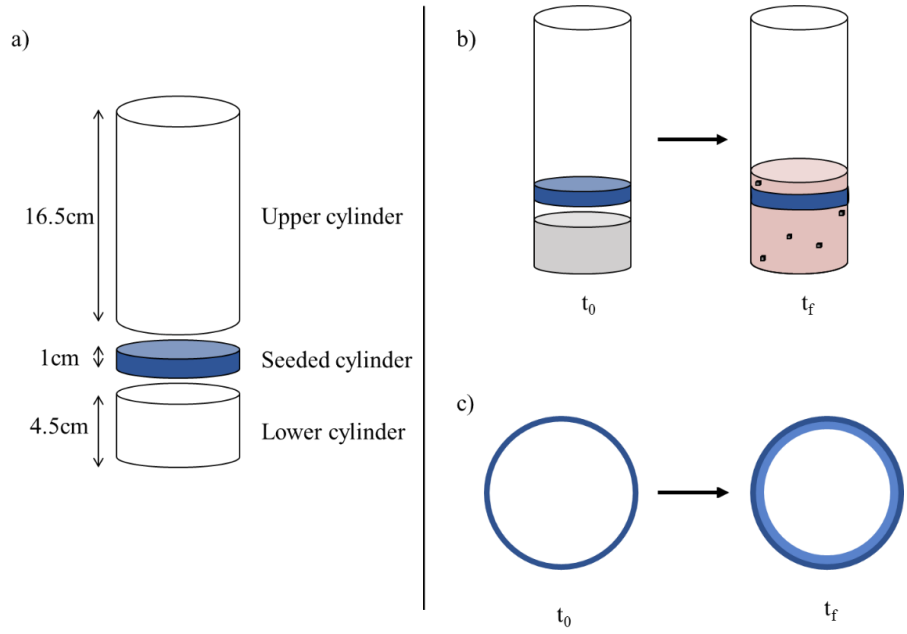


Figure 5.3. Preferential crystallization principle. a) Set-up of the cylinder, with the seed material at a height of 4.5-5.5 cm, b) Evolution of the experiment over time, with the racemic initial solution in grey and the final solution, enriched in counter-enantiomer, in pink, c) Schematic theoretical crystal growth on the seeded cylinder at the end of the process, with the seed material in dark blue and the outcome of the crystallization in light blue.

The set-up presented here also requires the establishment of an endpoint. As for all preferential crystallization processes, if supersaturation keeps being increased, the

counter-enantiomer will inevitably also crystallize out. In our case, if upon initial crystallization, $CO_2$ keeps on being injected, the supersaturation of the counter-enantiomer continues to increase until its spontaneous crystallization. It was, therefore, decided to stop the process as soon as turbidity was observed in the reactor through the sapphire windows, for a pressure between 6.6 and 7.2 bar (Table 5.2). At this stage, if preferential crystallization occurred, an enantiomeric excess in favor of the seed enantiomer should be observable in the recovered powder.[a] Three experiments were stopped while the solution was still limpid, at pressures ranging between 6 and 6.5 bar (Table 5.2). These indeed showed almost no crystallization occurred within the reactor, and that no additional mass was recovered atop the seeds (Table 5.2, Runs 12-14), confirming that the onset of turbidity can be taken as the point at which cocrystallization takes place.

As already highlighted by experiments 4-6, resolution does not occur in absence of seeding. This was confirmed, conducting two experiments using non-seeded cylinders (Table 5.2, Runs 15-16). A first trial was performed using a (1:1) nefi:(*rac*)-MA molar ratio, while for a second experiment, this ratio was adjusted to (0.7:1). Both experiments were stopped when turbidity was observed. As expected, extra nefi was observed in Run 15 by XRPD analysis, while Run 16, with the (0.7:1) adjusted ratio, led to pure cocrystal (Figure SI-5.3, Table 5.2). In both cases, racemic mixture material was obtained in all parts of the reactor (stirrer, cylinder, reactor) and outlet collector. These experiments, therefore, once more confirm spontaneous preferential growth of neither nefi-(*R*)-MA nor nefi-(*S*)-MA occurs in any point of the experimental set-up in the absence of seeds. As for solution-based preferential crystallization processes, seeding is also a prerequisite in a pressurized-$CO_2$ set-up if preferential crystallization is to be induced.

Table 5.2. GAS-assisted preferential crystallization experiments.

[a] Seeding height, and concentrations used are appropriate for acetone. These parameters need to be adapted when using isobutanol or EtOAc.

| | Run | Nefi : (rac)-MA initial ratio | Initial solution cc. (g/L) Nefi | Initial solution cc. (g/L) MA | Seeded enantiomer | $m_{seed}$ (mg) | Pressure at flush (MPa) | Crystallization $yield_{tot}$ (%) | Crystallization $yield_{cyl}$ (%) | Nefi:MA molar ratio of the recovered powder * | *ee* cyl** (%) | *ee* stirrer** (%) | *ee* reac** (%) | *ee* coll** (%) |
|---|---|---|---|---|---|---|---|---|---|---|---|---|---|---|
| **Adaptation of nefi:MA ratio + Introduction of enantiopure seeding** | **7** | (1:1) | 41.06 | 25,31 | *R* | 548 | 6.7 | 33.0 | 16.7 | (1.1:1) | 34 | -13 | -9 | --- |
| | **8** | (0.8:1) | 32.80 | 25,37 | *R* | 296 | 6.8 | 40.1 | 15.3 | (1:1)*** | 12 | -9 | -4 | -1 |
| | **9** | (0.8:1) | 32.70 | 25,32 | *R* | 314 | 6.9 | 39.6 | 18.2 | (1.1:1) | 15 | -20 | -10 | 1 |
| | **10** | (0.7:1) | 28.76 | 25,43 | *R* | 279 | 6.9 | 35.3 | 16.1 | (1:1) | 27 | -32 | -22 | 1 |
| | **11** | (0.7:1) | 28.68 | 25,36 | *R* | 263 | 6.6 | 49.0 | 12.2 | (1:1) | 40 | -20 | -21 | 4 |
| **Process stopped before turbidity** | **12** | (0.8:1) | 32.62 | 25.39 | *R* | 264 | 6.0 | 1.9 | 0 | --- | --- | --- | --- | --- |
| | **13** | (0.8:1) | 32.75 | 25.35 | *R* | 293 | 6.2 | 1.9 | 0 | --- | --- | --- | --- | --- |
| | **14** | (0.8:1) | 32.76 | 25.36 | *R* | 309 | 6.5 | 5.9 | 0 | --- | --- | --- | --- | --- |
| **No seeding** | **15** | (1:1) | 40.97 | 25.36 | --- | --- | 7.1 | 56.2 | 25.3 | --- | 1 | 0 | 0 | --- |
| | **16** | (0.7:1) | 28.91 | 25.61 | --- | --- | 6.8 | 46.3 | 12.5 | (1:1) | 2 | -2 | 1 | 1 |
| **Decreasing seeds amount** | **17** | (0.7:1) | 28.87 | 25.45 | *S* | 104 | 6.9 | 46.8 | 19.0 | (1:1) | -24 | 26 | 15 | -6 |
| | **18** | (0.7:1) | 28.78 | 25.40 | *R* | 3 | 6.9 | 52.2 | 7.6 | --- | 31 | -3 | -5 | 0 |
| **Decreasing concentration** | **19** | (0.7:1) | 22.68 | 20.03 | *R* | 3 | 7.2 | 52.5 | 7.9 | --- | 44 | -20 | 6 | 3 |
| | **20** | (0.7:1) | 22.68 | 20.01 | *S* | 4 | 6.9 | 46.2 | 13.0 | --- | -49 | 25 | 13 | 0 |
| **Simultaneous seeding of both enantiomers** | **21** | (0.7:1) | 28.93 | 25.61 | *S* | 7 | 6.9 | 39.2 | 9.9 | (1:1)*** | -37 | 1 | 2 | 0 |
| | | | | | *R* | 4 | | | 7.3 | (1:1) | 33 | | | |
| | **22** | (0.7:1) | 28.90 | 25.58 | *S* | 2 | 6.9 | 27.0 | 3.9 | --- | -23 | -5 | -1 | 2 |
| | | | | | *R* | 2 | | | 5.7 | --- | 24 | | | |
| | **23** | (0.7:1) | 28.78 | 25.38 | *S* | 3 | 6.7 | 41.2 | 4.2 | --- | -65 | 1 | 5 | 0 |
| | | | | | *R* | 1 | | | 4.7 | --- | 34 | | | |
| | **24** | (0.7:1) | 28.78 | 25.44 | *S* | 1 | 6.9 | 36.6 | 6.3 | --- | -20 | -4 | -2 | 1 |
| | | | | | *R* | 2 | | | 4.8 | --- | 44 | | | |
| | **25** | (0.7:1) | 28.75 | 25.47 | *R* | 3 | 6.8 | 48.3 | 6.0 | --- | 8 | -1 | 2 | 0 |
| | | | | | *S* | 3 | | | 2.8 | --- | -18 | | | |
| | **26** | (0.7:1) | 28.73 | 25.41 | *R* | 4 | 6.9 | 50.2 | 12.4 | --- | 21 | 2 | 1 | 0 |
| | | | | | *S* | 5 | | | 9.0 | --- | -38 | | | |

*Nefi:MA molar ratios of the obtained products were determined by *r*HPLC.

***ee* were determined by *c*HPLC, a positive result represents an enrichment in nefi-(*R*)-MA, and a negative result represents an enrichment in nefi-(*S*)-MA. The *ee* of the cylinder corresponds to that of the supplementary material that crystallized on top of the seed material. To calculate this *ee*, the seed-mass was subtracted from the total mass recovered, and *r*HPLC and *c*HPLC were used to estimate the *ee* of the supplementary material.

***Traces of nefi are observed by XRPD and a low excess of nefi is observed by *r*HPLC.

### *4.2.2 Inducing preferential crystallization*

#### Introduction of enantiopure seeding

A first set of experiments comprising various molar ratios of nefi:MA (Table 5.2, Runs 7-11) was performed, with the cylinder seeded with nefi-(*R*)-MA. It was confirmed that all experiments resulted in an increase of the mass deposited on the seed material.

The global crystallization yield (crystallization $yield_{tot}$) was calculated for all experiments by summing the mass of crystals recovered on the seeded cylinder, the stirrer shaft, and inside the reactor (this amount was corrected for the amount of seed material initially used) compared to the initial amount of the compounds introduced in the solvent. The remaining mass was always recovered in the outlet reactor as crystalline powder.[b] For Runs 7-11, between a quarter and up to half of the total crystallized powder was found on the seeded cylinder.

XRPD (Figure SI-5.3) and *r*HPLC measurements confirmed the presence of pure cocrystal formation on the seeded cylinder when using a nefi:MA initial ratio of (0.7:1), while containing some supplementary nefiracetam for the higher stoichiometric ratios. Interestingly, the crystal mass deposited on the seed materials during crystallization was systematically found to have an enantiomeric excess in favor of nefi-(*R*)-MA. This result highlights the first successful occurrence of

[b] For example, for Run 7, the mass recovered on the seeded cylinder (0.881 g), the stirrer shaft (0.081 g), and inside the reactor (0.244 g) was corrected for the amount of seed (0.548 g), resulting in a crystallization mass of 0.658 g, while the initial mass of compounds in acetone was 1.991 g. This leads to a crystallization yield of 33.0%. In comparison, the crystallization yield on the seeded cylinder (crystallization $yield_{cyl}$) corresponds to the mass recovered on the seeded cylinder (corrected for the initial seed amount), compared with the maximum amount recoverable. For Run 7, this corresponds to 0.333 g (0.881 g corrected for the seed, which was 0.548 g) compared with 1.991 g, resulting in a 16.7% crystallization yield on the cylinder.

enantioenrichment induced through $CO_2$-assisted preferential crystallization. The fact that the material is not enantiopure (with *ee*'s ranging from 12 to 40%), is indicative of the counter-enantiomer also crystallizing at a given moment, as is typically the case in preferential crystallization processes.[c]

Further evidence of preferential crystallization is shown by analyzing the powders recovered in the remaining parts of the set-up. For Runs 7-11, both reactor and stirrer recovered materials are enriched in the opposite enantiomer nefi-(*S*)-MA. This aligns with preferential crystallization principles. As more of the nefi-(*R*)-MA crystallized on the seeded cylinder, the remaining solution is enriched in nefi-(*S*)-MA, resulting in more of this enantiomer crystallizing in the reactor and on the stirrer. At the end of the process, the compound remaining in solution (and recovered in the outlet collector) is a racemic mixture. This behavior is observed across all seeded experiments. Therefore, mass balances can be calculated for all experiments.[d]

Additionally, we were able to orient resolution towards one or the other enantiomer. Runs 17 and 20 indeed show that the use of (*S*)-seeds leads to preferential growth, and hence enantioenrichment, of the seed-ring in nefi-(*S*)-MA while the material recovered on reactor and stirrer becomes enriched in nefi-(*R*)-MA.

To gain more insight into the crystallization occurring on the seeded ring, the *ee* of the material that crystallized on the cylinder was examined along its depth (Figure 5.4). To do this, careful sampling was performed on both the outer surface and deeper inside the layer (so closer to the seed). Table 5.3 illustrates the gradual and preferential crystal growth phenomena. As the seeded layer is enantiopure – typically nefi-(*R*)-MA in our examples – it is first covered by a growth layer enriched in this enantiomer. As a result, the solution becomes enriched in the counter-enantiomer – nefi-(*S*)-MA – , which crystallizes, more strongly, in the outer layers. Table 5.3 shows that the outer

[c] In their original contribution, Buol et al.[88] limited the crystallization yield of each cycle to 5% to avoid the counter-enantiomer of appearing. To achieve such low yields was impossible using the current set-up, explaining the spontaneous crystallization of the counter-enantiomer at a given stage of our process.

[d] For Run 11, for example, powders collected on the stirrer and in the reactor have a mass of respectively 0.229 g and 0.367 g, with respective *ee* values of -20% (*R*-*S* ratio of 0.40-0.60) and -21% (*R*-*S* ratio of 0.395-0.605). Taken together, these materials result in 0.237 g of nefi-(*R*)-MA and 0.359 g of nefi-(*S*)-MA. The quantity of powder collected on the cylinder is 0.198 g with an *ee* of 40% (*R*-*S* ratio of 0.70-0.30). It corresponds to 0.139 g of nefi-(*R*)-MA and 0.059 g of nefi-(*S*)-MA. The remaining powder is found in the outlet collector and corresponds to a mass of 0.827 g with an *ee* of 4% (*R*-*S* ratio of 0.52-0.48), which corresponds to 0.430 g of nefi-(*R*)-MA and 0.397 g of nefi-(*S*)-MA. In total, the recovered amounts of (*R*)- and (*S*)-cocrystal correspond respectively to 0.805 g and 0.816 g. The material balance is therefore respected, with an error attributed to the recovery of the powder in each part of the set-up.

surface, indeed, always exhibits an increased amount of counter-enantiomer compared to the inner layers. In some scenarios (Table 5.3, Run 10 A and B, Run 11 A and C), the outer layer is even favored with respect to the counter-enantiomer. It should however be noted that the overall *ee* of the cylinder material remains enriched in nefi-(*R*)-MA used as seed. For the samples taken across the crystallized material (designated as A, B, C and D), only a few milligrams of powder were taken each time. Considering the inhomogeneity of the newly crystallized layer and given that sampling along the depth of the seed-cylinder is tedious and not evident, Table 5.3 shows overall behavior rather than exact *ee*'s.

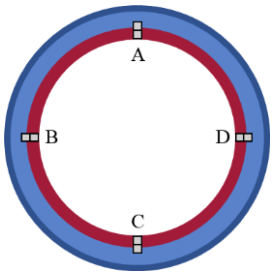


Figure 5.4. Crystal growth occurs in layers on the seeded cylinder. As one moves away from the initial seed layer to the outer surface, the enrichment in nefi-(*R*)-MA becomes less pronounced. In dark blue, enantiopure seeding, *e.g.* nefi-(*R*)-MA; in light blue crystalline material still enriched in nefi-(*R*)-MA; in dark red, crystalline material enriched in counter-enantiomer, nefi-(*S*)-MA. The different samples taken are represented as grey squares.

Table 5.3. *c*HPLC results of the samples taken across the crystallized material on the cylinder for Runs 10 and 11. Samples are recovered on outer layer, as well as closer to the surface of the cylinder (inner).

| Run | *ee* cyl (%) | *ee* A | | *ee* B | | *ee* C | | *ee* D | |
|---|---|---|---|---|---|---|---|---|---|
| | | Outer | Inner | Outer | Inner | Outer | Inner | Outer | Inner |
| **10** | 27 | -24 | -11 | -25 | -17 | 12 | 16 | 13 | 30 |
| **11** | 40 | -1 | 16 | 16 | 31 | -1 | 13 | 12 | 9 |

**ee* were determined by *c*HPLC, a positive result represents an enrichment in nefi-(*R*)-MA, and a negative result represents an enrichment in nefi-(*S*)-MA.

These observations suggest a rapid and preferential growth of nefi-(*R*)-MA on the seed material at the onset of the process. The surrounding solution consequently enriches in nefi-(*S*)-MA. As $CO_2$ addition continues, supersaturation rapidly increases, leading to nucleation of nefi-(*S*)-MA and simultaneous rapid crystal growth

of both enantiomers on the outer ring. As nefi-(*S*)-MA shows higher concentration in solution, faster crystallization of this enantiomer is then expected in the outer layers.

### Decreasing initial solution concentration

In an attempt to reduce nucleation and crystal growth kinetics of the counter-enantiomer, Runs 19 and 20 were carried out decreasing the initial solution concentration. The initial reduced concentration should lead to a less supersaturated solution reaching the seed-material. Both runs indeed show a lower yield recovered on the cylinder (7.9 and 13.0% respectively), with increased *ee*'s (44 and 49% respectively). However, spontaneous crystallization of the counter-enantiomer still occurs, as no enantiopure material is obtained.

### Decreasing seeding amount

Concurrently, attempts were made to reduce the quantity of enantiopure material used as seeds. Reducing the amount of seeds (first slightly reducing it with Run 17, then drastically reducing seeding amount with Run 18 vs Runs 10-11) does not seem to have any substantial impact on the crystallization kinetics, since comparable *ee* and yield were obtained. This aspect is advantageous for the economic evaluation of the process.

From Runs 7-20, it is clear that reproducibility is the main limitation of the GAS-induced preferential crystallization set-up. Ideally in preferential crystallization processes, nucleation of the counter-enantiomer is avoided and/or rapid crystal growth of this latter reduced. In a classical-solution based batch process, multiple factors such as temperature, seed amount, stirring, and reactor set-up have an impact on the final result [77]. However, in our GAS set-up, additional factors, such as pressure evolution and $CO_2$ addition rate also impact this process, requiring careful control. Moreover, since $CO_2$ is continuously added and mixed with the solvent, the herein process is a non-equilibrium method in terms of fluid phases. Additionally, mixing is not an instantaneous phenomenon, and the compounds also have their own induction time (the time taken for the first nuclei to appear in response to the decrease in solubility [141]).

Importantly, however, our work highlights the robustness of the nefi-MA cocrystal-conglomerate system. Indeed, all experiments allowed the formation of the cocrystal, as confirmed by XRPD (Figure SI-5.3). Moreover, the feasibility of performing preferential crystallization through GAS is clearly highlighted. Based on our findings, future endeavors should orient towards an appropriate engineering of GAS-technology so that it is best-compatible with preferential crystallization. We initiated such development, investigating alternative set-ups of the cylinder.

### 4.2.3 Steps towards an ideal preferential crystallization GAS set-up

Our focus was placed on adapting the seeding configuration, aiming at achieving simultaneous crystallization of both enantiomers but in distinct areas of the reactor. By promoting their concurrent crystallization, we aimed at reducing the risk of spontaneous nucleation of the counter-enantiomer. We explored two alternatives to the seeding set-up used initially.

In a first alternative (Table 5.2, Runs 21-24), the seeded cylinder was covered on one side with nefi-(*R*)-MA seed material, and with nefi-(*S*)-MA on the other side (Figure 5.5). Using this set-up, we were able in all runs to control the preferential crystallization process by orienting it to a specific side of the seed-ring. In all cases, the supplementary material crystallizing on top of the seed is the nefi-MA cocrystal (Figure SI-5.4). Moreover, it is effectively enriched in the same enantiomer as the seed, with overall higher total *ee*'s compared to experiments where only a single enantiomer seed was used. Interestingly, with the solution being simultaneously depleted in both enantiomers, the material recovered elsewhere in the reactor (stirrer, reactor, and outlet collector) remains a racemic mixture, contrasting with set-ups using only one type of seed material.

Further evidence of a more controlled preferential crystallization process is given by sampling across the crystalline layer deposited on the seeded cylinder (Figure 5.5, Table 5.4). In contrast to the single-enantiomer-seeded experiments discussed above (Table 5.3), here, the outer layer no longer exhibits an enrichment in the counter-enantiomer. Both outer and inner layers are now showing an excess in favor of the seed-enantiomer used. Moreover, there is very little difference in *ee*'s of the inner and outer layers (Table 5.4).

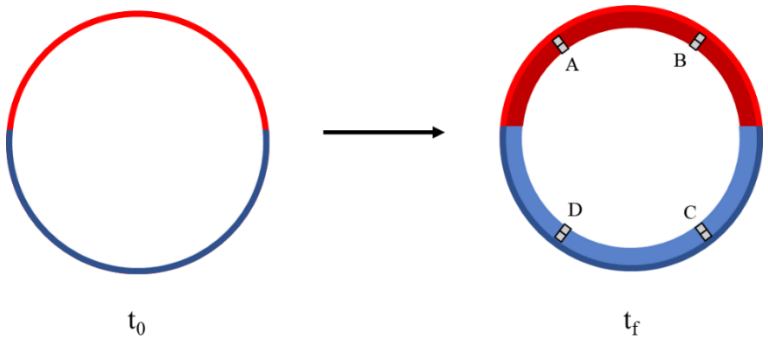


Figure 5.5. Cylinder seeded on one side with nefi-(*R*)-MA (dark blue) and the other with the nefi-(*S*)-MA (light red). Over time, a layer half enriched in nefi-(*R*)-MA (light blue) and half in nefi-(*S*)-MA (dark red), grows. The different samples taken are represented as grey squares.

Table 5.4. *c*HPLC results of the samples taken across the crystal material on the cylinder for Runs 21 and 23. Samples are recovered on the outer layer, and an inner layer closer to the seed material.

| Run | *ee* cyl (%) | (*S*)-seeded half cylinder | | | | (*R*)-seeded half cylinder | | | |
|---|---|---|---|---|---|---|---|---|---|
| | | *ee* A | | *ee* B | | *ee* C | | *ee* D | |
| | | Outer | Inner | Outer | Inner | Outer | Inner | Outer | Inner |
| 21 | -37 | -29 | -40 | -25 | -25 | --- | --- | --- | --- |
| | 33 | --- | --- | --- | --- | 49 | 37 | 56 | 58 |
| 23 | -65 | -48 | -66 | -47 | -57 | --- | --- | --- | --- |
| | 34 | --- | --- | --- | --- | 15 | 29 | 61 | 64 |

**ee* were determined by *c*HPLC, a positive result represents an enrichment in nefi-(*R*)-MA, and a negative result represents an enrichment in nefi-(*S*)-MA.

In a second alternative, seeding was performed by superposing two seeded cylinders (Table 5.2, Runs 25 and 26). In this configuration, the bottom cylinder was coated with nefi-(*R*)-MA, while the upper one was coated with nefi-(*S*)-MA (Figure 5.6).

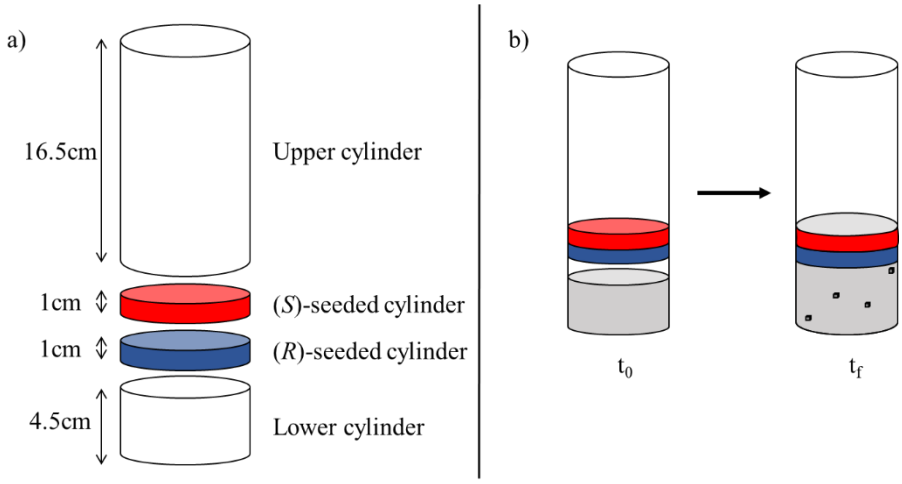


Figure 5.6. Preferential crystallization principle when superposing two seeded cylinders. a) Set-up of the cylinder with two different seed materials at a height of 4.5-5.5cm and 5.5-6.5cm, b) Evolution of the experiment over time.

Both pieces of the seed-cylinder show supplementary crystallized material, to be the nefi-MA cocrystal (Figure SI-5.5), enantioenriched according to the nature of seed material used, while powder recovered elsewhere in the reactor and on the stirrer is a racemic mixture. This indicates the success of this set-up in a controlled depletion of

both enantiomers. The bottom-seeded cylinder – nefi-(*R*)-MA – shows less enrichment compared to the upper-seeded cylinder – nefi-(*S*)-MA – (*e.g.* Run 26 shows an *ee* of +21% for the lower cylinder, whereas an *ee* of -38% is obtained for the upper cylinder). This finding is coherent with a supersaturated solution reaching the first cylinder, where nefi-(*R*)-MA crystallizes more rapidly due to the *(R)*-seeding, albeit some of the nefi-(*S*)-MA also crystallizing concomitantly. The solution reaching the upper cylinder then shows a stronger depletion in nefi-(*R*)-MA. The upper (*S*)-seeded cylinder, enhances the crystal growth of nefi-(*S*)-MA. Nucleation and growth kinetics of nefi-(*R*)-MA are less important, due to the lower supersaturation in (*R*)-cocrystal at this stage.

Looking at both configurations, it seems that parallel seeding, depleting the solution simultaneously of both enantiomers, is the preferred option. An optimization of this process can therefore be studied by playing on various parameters (concentration of the species, temperature at which the process takes place, height of seeding, $CO_2$ introduction rate, stirring rate…).

## 5. Conclusion

We here present the first occurrence of a GAS assisted preferential cocrystallization process.

Focusing on the nefiracetam-(*rac*)-mandelic acid system, we show that not only conglomerate formation can be induced in a GAS context, but that seeding can be used to orient the preferential crystallization of a given enantiomer in a specific area of the reactor. This is, to the best of our knowledge, the first occurrence of seed introduction in a supercritical reactor, in order to induce preferential crystal growth.

Our results highlight that the absence of seed-material leads to concomitant crystallization of both enantiomers, whereas the use of enantiopure seeding, leads to material enriched in the same enantiomer. As GAS is an antisolvent process, rapid creation of supersaturation, however, always led to spontaneous nucleation of the counter-enantiomer as the process advanced (in the outer layers deposited). First steps, in achieving a higher degree of control over supersaturation, and the preferential crystallization process, highlighted the potential of using a parallel seeding set-up, with half of the seed-cylinder seeded with one enantiomer and the other half with the counter-enantiomer. This set-up indeed allowed increased control over the process, with simultaneous depletion of both enantiomers, higher overall enrichment on both sides of the reactor, and less spontaneous nucleation of the counter-enantiomer in the outer deposited layers.

At this stage, we also emphasize the complexity of the process. Preferential crystallization is a kinetic process, requiring careful control over crystallization

process parameters (concentration, temperature, seeding, …), which combined with the parameters of a GAS process ($CO_2$ addition rate, pressure control, mixing between $CO_2$ and the solvent, …) set future challenges for an optimal process design. We are convinced that careful control of all these parameters, with an adapted reactor allowing for slower crystallization kinetics, will ultimately lead to a set-up allowing full resolution through $CO_2$ assisted preferential crystallization.

## 6. Acknowledgements

This work was supported by the Fonds de la Recherche Scientifique – FNRS – *Financement Mobilité* under Grant n°40020442. The authors would also like to thank the FNRS (PDR T.0262.20) for funding. The financial support of french ANR Project CYPRES - ANR-18-CE07-0047 is greatly acknowledged.

# Chapter 6. Conclusion and perspectives

# Conclusion and perspectives

## 1. Conclusion

The aim of this thesis was to examine the role, too often neglected, of the solvent in resolution processes. While the first two chapters focused on diastereomeric resolution of 1,1'-bi-2-naphthol (BINOL) with two different resolving agents (*trans*-cyclohexane-1,2-diamine (DACH) and *N*,*N*′-dimethyl-1,2-diphenylethane-1,2-diamine (DADPE)), the third chapter concentrates on preferential crystallization assisted by pressurized $CO_2$ applied on the Mandelic acid-Nefiracetam cocrystal-conglomerate system. Our investigations highlighted the impact of the solvent:

1. To obtain specific crystal forms (Chapter 3),
2. In targeting the desired enantiomeric form (Chapter 4),
3. As a tool in preferential crystallization processes (Chapter 5).

What stands out in Chapter 3 is the formation of multiple different phases depending on the solvent chosen.
Firstly, this raises the question whether such diversity of solvates is a general phenomenon across all systems or not. Our subsequent research indicates that this phenomenon is not universal. Indeed, in Chapter 4, despite the use of a wide range of solvents, only one solvate was identified, whereas in Chapter 5, none of the three solvents chosen led to the formation of a solvate.
Subsequently, we can point out that this variability of solid forms obtained can be perceived as negative, complexifying the system due to the solvent choice leading to the formation of multiple phases. However, it also has a positive aspect, offering the possibility of identifying the optimum solvent to obtain the desired solid form, ultimately enabling resolution. This underlines the necessity of careful solvent selection to ensure optimal yield and enantiopurity of the desired enantiomer.

The importance of solvent selection was further underscored in the resolution of BINOL by DADPE, in Chapter 2, where the solvent served as an active agent, inducing the direction of the resolution towards the desired outcome, rather than being only the medium.

In the same vein, we continued to use the solvent as a tool in the third chapter. Here, pressurized $CO_2$ was used not as the resolution medium but as an antisolvent to crystallize the desired form. Herein, we have developed a new technique for resolution by preferential crystallization using $CO_2$ as an antisolvent.

These investigations underline the dual nature of solvent: it could act as a passive medium or an active tool shaping the resolution process. Through this research, we have used crystal engineering to develop chiral resolution techniques, opening the door to future discoveries.

As general considerations, in Chapters 3 and 4, we used benzene, a known carcinogenic solvent. While we are fully aware of its toxicity, its use was scientifically justified for our study as it allowed us to compare our results with existing literature. Nonetheless, it is important to acknowledge that benzene is unlikely to be adopted in pharmaceutical applications due to its hazardous nature, making part of our research not applicable in industry.
Conversely, we employed pressurized $CO_2$ in Chapter 5, which introduced certain limitations. For instance, the difficulty of controlling $CO_2$ leaks implies that we could only work with solvents that were not excessively toxic (making the use of toluene, benzene or DCM infeasible). The use of $CO_2$ as an antisolvent is also limited by the requirement that it must be miscible with the solvent. Additionally, predicting the efficacy of $CO_2$ as an antisolvent can be challenging. If the molecule of interest is too soluble in the solvent, $CO_2$ will not enable it to crystallize; conversely, if it is not soluble enough, the crystallization yield will be very low. However, thanks to its non-toxicity, non-flammability and its chemically inertness, pressurized $CO_2$ is considered a viable option in pharmaceutical applications.
It is imperative to recognize the potential dangers associated with the compounds and solvents we employ. Appropriate safety measures and protocols must be rigorously adhered to in order to mitigate these risks.

## 2. Perspectives

The discovery of numerous crystal phases between BINOL and DACH in Chapter 3 significantly enhances our understanding of intermolecular interactions. Despite substantial advancements in crystal engineering, the critical step in designing cocrystals still relies heavily on trial-and-error methods for selecting appropriate coformers.[40,41] Thus, gaining a deeper insight into these interactions remains essential for the rational design of cocrystals. Our research lies therefore in this vein.

Another crucial next step is predicting solvate formation. To achieve this, it is essential to consider the interactions between the molecule(s) of interest and the solvent. The Cambridge Crystallographic Data Centre (CCDC) can be a valuable resource in this context, either through the analysis of similar solvate-forming compounds or through the identification of already existing solvates of the molecule of interest within the CCDC database. Additionally, evaluating the stability of the non-solvated compound is crucial for predicting solvate formation.

In Chapter 3, we studied the impact of different solvents on the BINOL-DACH system. The non-polar, aprotic solvents chosen (toluene and benzene) are both aromatic and yielded similar results due to their CH-π interactions with BINOL. Future experiments could explore the use of non-aromatic, non-polar, aprotic solvents (*e.g.* cyclohexane or n-hexane) to observe how the BINOL-DACH system behaves in these environments. Additionally, the use of an aromatic, polar, protic solvent (*e.g.* phenol) can be interesting to explore which weak interaction will be preferentially formed: CH-π, H bonds or both of them? Furthermore, solvents such as xylene isomers and trimethylbenzene isomers could be tested to determine if they produce similar phases to those comprising benzene or toluene. Finally, a study in ethylbenzene and propylbenzene could help identify the point at which the length of the substituted chain hinders the formation of a stable solvate.

Finally, we could investigate the impact of chiral solvents (both racemic and enantiopure) on the BINOL-DACH system. Solvents such as 5-ethyl-5-propylundecane (slightly polar, aprotic), limonene (polar, aprotic), 2-methyl-1-butanol (polar, protic), and 2,2,2-trifluoro-1-phenylethanol (aromatic, polar, protic) could be tested to compare the results with those obtained using the solvents of this current work. Furthermore, if the BINOL-DACH system behaves congruently in these chiral solvents, we could observe the potential formation of diastereomeric or enantiospecific solvates. This would enable us to study the resolution of BINOL and/or DACH compounds from a different perspective: driven by the solvent and not by the coformer.

Chapter 4 investigates the diastereomeric resolution of BINOL by (*R,R*)-DADPE, leading to the crystallization of solid forms comprising either (*S*)- or (*R*)-BINOL, depending on the chosen solvent. Although the search for solvates is a current subject in crystal engineering, we remain cautious and do not expect to discover a large number of similar solvent-guided resolution systems. As the recent publication of Shemchuk *et al.* demonstrating how either the enantiomers of Mandelic acid can be crystallized by adjusting the amount of L-Proline as the resolution agent (due to the existence of two thermodynamically stable cocrystals (*R*)-Mandelic acid-L-Proline and (*S*)-Mandelic acid-2L-Proline),[94] this research, while representing a “one-shot” demonstration, highlights the untapped potential of crystal engineering. It underscores the need for further explorations to fully exploit its potential.

Finally, we explored preferential crystallization through pressurized $CO_2$ of the Mandelic acid-Nefiracetam system in Chapter 5. We have concluded this chapter by outlining various parameters for the optimization of the presented process (temperature conditions, stirring speed, $CO_2$ addition rate, species concentration, and the seeding zone length).

Looking ahead, we envision the development of a continuous crystallization process, to increase its industrial appeal. While an initial Mixed-suspension, Mixed-Product-Removal (MSMPR)-type process may be feasible, involving the recycling of the compounds recovered in the outlet collector for a subsequent resolution process, our ultimate goal is to establish a continuous tubular crystallizer process. This system would allow the continuous introduction of a racemate solution, allowing continuous crystallization of enantioenriched powder and withdrawal of the remaining solution.

The development, for the first time, of a seeding set-up in a supercritical reactor opens the door to further purification work. This would involve creating a one-pot process comprising the synthesis of a chiral compound in the reactor, followed by its purification and resolution through $CO_2$ addition. This approach would involve the same set-up configuration as the herein developed preferential crystallization with parallel seeding of each enantiomers on both halves of the cylinder. The reagents and reaction solvent would be introduced (with the seeding height above the solution level), and the synthesis would take place without the addition of $CO_2$ (under atmospheric pressure). Upon synthesis completion, $CO_2$ addition would allow the expansion of the solution and the decrease of the product solubility, until the solution reach the seeded area, leading to the crystallization of each enantiomer on their respective seeded coat. Therefore, this method would allow at the same time their purification and resolution. The reagents in excess would be eliminated in the outlet collector. The limitations of this process, would be that the compound of interest crystallizes as a conglomerate and is not soluble in $CO_2$. In this context, two different processes can be investigated, the synthesis, purification and chiral purification of Aspartic acid (Scheme 6.1) and 2-((2-methylbenzylidene)amino)-2-phenylacetamide (Scheme 6.2).

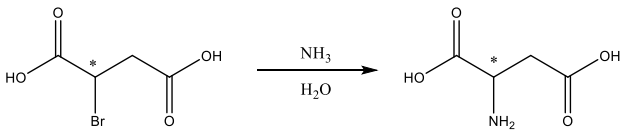


Scheme 6.1. Reaction scheme for the synthesis of Aspartic acid.

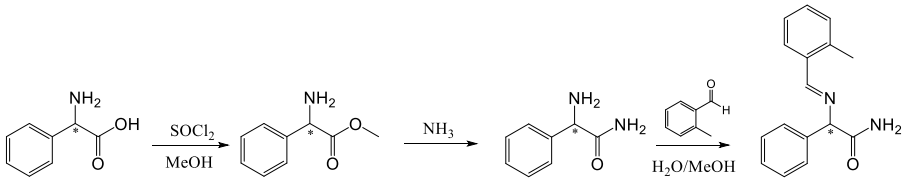


Scheme 6.2. Reaction scheme for the synthesis of 2-((2-methylbenzylidene)amino)-2-phenylacetamide.

Such a versatile process, capable of synthesis, purification, and chiral resolution, is very promising for industry, saving space (fewer different reactors), manpower (if fewer reactors, fewer different teams to manage them) and time, making it economically attractive. Moreover, its applicability extends beyond chiral resolution to the purification of various molecules, indicating its potential impact across diverse branches of chemistry.

Finally, the use of pressurized $CO_2$ as an anti-solvent could also be applied to study the BINOL-DACH system, which leads to numerous solvates. Initially, we could examine the (*rac*)-BINOL-(*rac*)-DACH combinations using ethyl acetate and acetonitrile as the solvents.
For ethyl acetate, depending on the crystallization technique (slow evaporation or slurry), we obtained two different phases: *rac*-*rac*-EtOAc and *rac*-*rac*. By employing $CO_2$ as the anti-solvent, we could determine which phase is preferentially obtained – one of the two identified in this study or another solid form. Additionally, the combination of (*rac*)-BINOL and (*rac*)-DACH in acetonitrile resulted in the crystallization of a *rac*-*rac* polymorph, different from that obtained in EtOAc. We could then investigate whether this polymorph could be obtained using pressurized $CO_2$ as an anti-solvent in acetonitrile and compare the results with those obtained in ethyl acetate.

# Bibliography


(1) Grepioni, F.; Casali, L.; Fiore, C.; Mazzei, L.; Sun, R.; Shemchuk, O.; Braga, D. Steps towards a Nature Inspired Inorganic Crystal Engineering. *Dalton Trans.* **2022**, *51* (19), 7390–7400. https://doi.org/10.1039/D2DT00834C.

(2) Nguyen, L. A.; He, H.; Pham-Huy, C. Chiral Drugs: An Overview. *Int. J. Biomed. Sci.* **2006**, *2* (2), 85–100.

(3) Nwambaekwe, K. C.; John-Denk, V. S.; Douman, S. F.; Mathumba, P.; Yussuf, S. T.; Uhuo, O. V.; Ekwere, P. I.; Iwuoha, E. I. Crystal Engineering and Thin-Film Deposition Strategies towards Improving the Performance of Kesterite Photovoltaic Cell. *J Mater Res Technol* **2021**, *12*, 1252–1287. https://doi.org/10.1016/j.jmrt.2021.03.047.

(4) Dhir, A.; Rajkumar, M.; Desiraju, G. R. Cocrystal Hydrate of Bandrowski's Base and Clotrimazole: A Prospective Ingredient for Hair Dye Formulations. *CrystEngComm* **2021**, *23* (32), 5421–5424. https://doi.org/10.1039/D1CE00751C.

(5) Brammer, L. Developments in Inorganic Crystal Engineering. *Chem. Soc. Rev.* **2004**, *33* (8), 476. https://doi.org/10.1039/b313412c.

(6) Ding, M.; Flaig, R. W.; Jiang, H.-L.; Yaghi, O. M. Carbon Capture and Conversion Using Metal–Organic Frameworks and MOF-Based Materials. *Chem. Soc. Rev.* **2019**, *48* (10), 2783–2828. https://doi.org/10.1039/C8CS00829A.

(7) Oh, H.; Tumanov, N.; Ban, V.; Li, X.; Richter, B.; Hudson, M. R.; Brown, C. M.; Iles, G. N.; Wallacher, D.; Jorgensen, S. W.; Daemen, L.; Balderas-Xicohténcatl, R.; Cheng, Y.; Ramirez-Cuesta, A. J.; Heere, M.; Posada-Pérez, S.; Hautier, G.; Hirscher, M.; Jensen, T. R.; Filinchuk, Y. Small-Pore Hydridic Frameworks Store Densely Packed Hydrogen. *Nat. Chem.* **2024**. https://doi.org/10.1038/s41557-024-01443-x.

(8) Wong, S. N.; Chen, Y. C. S.; Xuan, B.; Sun, C. C.; Chow, S. F. Cocrystal Engineering of Pharmaceutical Solids: Therapeutic Potential and Challenges. *CrystEngComm* **2021**, *23* (40), 7005–7038. https://doi.org/10.1039/D1CE00825K.

(9) Couillaud, B. M.; Espeau, P.; Mignet, N.; Corvis, Y. State of the Art of Pharmaceutical Solid Forms: From Crystal Property Issues to Nanocrystals

Formulation. *ChemMedChem* **2019**, *14* (1), 8–23. https://doi.org/10.1002/cmdc.201800612.

(10) Yousef, M. A. E.; Vangala, V. R. Pharmaceutical Cocrystals: Molecules, Crystals, Formulations, Medicines. *Cryst. Growth Des.* **2019**, *19* (12), 7420–7438. https://doi.org/10.1021/acs.cgd.8b01898.

(11) Nangia, A. K.; Desiraju, G. R. Crystal Engineering: An Outlook for the Future. *Angew Chem Int Ed* **2019**, *58* (13), 4100–4107. https://doi.org/10.1002/anie.201811313.

(12) Pepinsky, R. Crystal Engineering: A New Concept in Crystallography. *American physical society*. Mexico city, Mexico 1955.

(13) Bolla, G.; Sarma, B.; Nangia, A. K. Crystal Engineering of Pharmaceutical Cocrystals in the Discovery and Development of Improved Drugs. *Chem. Rev.* **2022**, *122* (13), 11514–11603. https://doi.org/10.1021/acs.chemrev.1c00987.

(14) Desiraju, G. ; Parshall, G. W., Crystal Engineering: The Design of Organic Solids, Materials Science Monographs. Elsevier, 1989, 54, 312-326.

(15) Desiraju, G. R. Chemistry beyond the Molecule. *Nature* **2001**, *412* (6845), 397–400. https://doi.org/10.1038/35086640.

(16) Vippagunta, S.; Brittain, H.; Grant, D. Crystalline Solids. *Advanced Drug Delivery Reviews* **2001**, *48* (1), 3–26. https://doi.org/10.1016/S0169-409X(01)00097-7.

(17) Braga, D.; Casali, L.; Grepioni, F. The Relevance of Crystal Forms in the Pharmaceutical Field: Sword of Damocles or Innovation Tools? *IJMS* **2022**, *23* (16), 9013. https://doi.org/10.3390/ijms23169013.

(18) Czapik, A.; Jelecki, M.; Kwit, M. Chiral Cocrystal Solid Solutions, Molecular Complexes, and Salts of N-Triphenylacetyl-l-Tyrosine and Diamines. *IJMS* **2019**, *20* (20), 5004. https://doi.org/10.3390/ijms20205004.

(19) Lévesque, A.; Maris, T.; Wuest, J. D. ROY Reclaims Its Crown: New Ways To Increase Polymorphic Diversity. *J. Am. Chem. Soc.* **2020**, *142* (27), 11873–11883. https://doi.org/10.1021/jacs.0c04434.

(20) Yu, L. Polymorphism in Molecular Solids: An Extraordinary System of Red, Orange, and Yellow Crystals. *Acc. Chem. Res.* **2010**, *43* (9), 1257–1266. https://doi.org/10.1021/ar100040r.

(21) Bauer, J.; Spanton, S.; Henry, R.; Quick, J.; Dziki, W.; Porter, W.; Morris, J. Ritonavir: An Extraordinary Example of Conformational Polymorphism. *Pharmaceutical Research* **2001**, *18* (6), 859–866.

(22) Nyman, J.; Day, G. M. Static and Lattice Vibrational Energy Differences between Polymorphs. *CrystEngComm* **2015**, *17* (28), 5154–5165. https://doi.org/10.1039/C5CE00045A.

(23) Samanta, P. K.; Burnham, C. J.; English, N. J. Stability-Ranking of Crystalline Ice Polymorphs Using Density-Functional Theory. *Crystals* **2020**, *10* (1), 40. https://doi.org/10.3390/cryst10010040.

(24) Roman, T.; Groß, A. Polymorphism of Water in Two Dimensions. *J. Phys. Chem. C* **2016**, *120* (25), 13649–13655. https://doi.org/10.1021/acs.jpcc.6b05435.

(25) Haji-Akbari, A. Ice and Its Formation. In *Antifreeze Proteins Volume 1: Environment, Systematics and Evolution*; Springer International Publishing, 2020; pp 13–52.

(26) Thakuria, R.; Thakur, T. S. Crystal Polymorphism in Pharmaceutical Science. In *Comprehensive Supramolecular Chemistry II*; Elsevier, 2017; pp 283–309. https://doi.org/10.1016/B978-0-12-409547-2.12570-3.

(27) Yao, X.; Henry, R. F.; Zhang, G. G. Z. Ritonavir Form III: A New Polymorph After 24 Years. *J. Pharm. Sci.* **2023**, *112* (1), 237–242. https://doi.org/10.1016/j.xphs.2022.09.026.

(28) Morissette, S. L.; Soukasene, S.; Levinson, D.; Cima, M. J.; Almarsson, Ö. Elucidation of Crystal Form Diversity of the HIV Protease Inhibitor Ritonavir by High-Throughput Crystallization. *Proc. Natl. Acad. Sci. U.S.A.* **2003**, *100* (5), 2180–2184. https://doi.org/10.1073/pnas.0437744100.

(29) Bērziņs, A.; Trimdale, A.; Kons, A.; Zvaniņa, D. On the Formation and Desolvation Mechanism of Organic Molecule Solvates: A Structural Study of Methyl Cholate Solvates. *Cryst. Growth Des.* **2017**, *17* (11), 5712−5724. https://doi.org/10.1021/acs.cgd.7b00657.

(30) Boothroyd, S.; Kerridge, A.; Broo, A.; Buttar, D.; Anwar, J. Why Do Some Molecules Form Hydrates or Solvates? *Cryst. Growth Des.* **2018**, *18* (3), 1903–1908. https://doi.org/10.1021/acs.cgd.8b00160.

(31) Veith, H.; Luebbert, C.; Sadowski, G. Correctly Measuring and Predicting Solubilities of Solvates, Hydrates, and Polymorphs. *Cryst. Growth Des.* **2020**, *20* (2), 723–735. https://doi.org/10.1021/acs.cgd.9b01145.

(32) Zvoníček, V.; Skořepova, E.; Dušek, M.; Babor, M.; Žvátora, P.; Šoós, M. First Crystal Structures of Pharmaceutical Ibrutinib: Systematic Solvate Screening and Characterization. *Cryst. Growth Des.* **2017**, *17* (6), 3116−3127. https://doi.org/10.1021/acs.cgd.7b00047.

(33) Grothe, E.; Meekes, H.; Vlieg, E.; ter Horst, J. H.; de Gelder, R. Solvates, Salts, and Cocrystals: A Proposal for a Feasible Classification System. *Cryst. Growth Des.* **2016**, *16* (6), 3237–3243. https://doi.org/10.1021/acs.cgd.6b00200.

(34) *The IUPAC Compendium of Chemical Terminology: The Gold Book*, 4th ed.; Gold, V., Ed.; International Union of Pure and Applied Chemistry (IUPAC): Research Triangle Park, NC, 2019. https://doi.org/10.1351/goldbook.

(35) Aitipamula, S.; Banerjee, R.; Bansal, A. K.; Biradha, K.; Cheney, M. L.; Choudhury, A. R.; Desiraju, G. R.; Dikundwar, A. G.; Dubey, R.; Duggirala, N.; Ghogale, P. P.; Ghosh, S.; Goswami, P. K.; Goud, N. R.; Jetti, R. R. K. R.; Karpinski, P.; Kaushik, P.; Kumar, D.; Kumar, V.; Moulton, B.; Mukherjee, A.; Mukherjee, G.; Myerson, A. S.; Puri, V.; Ramanan, A.; Rajamannar, T.; Reddy, C. M.; Rodriguez-Hornedo, N.; Rogers, R. D.; Row, T. N. G.; Sanphui, P.; Shan, N.; Shete, G.; Singh, A.; Sun, C. C.; Swift, J. A.; Thaimattam, R.; Thakur, T. S.; Kumar Thaper, R.; Thomas, S. P.; Tothadi, S.; Vangala, V. R.; Variankaval, N.; Vishweshwar, P.; Weyna, D. R.; Zaworotko, M. J. Polymorphs, Salts, and Cocrystals: What's in a Name? *Cryst. Growth Des.* **2012**, *12* (5), 2147–2152. https://doi.org/10.1021/cg3002948.

(36) Gupta, D.; Bhatia, D.; Dave, V.; Sutariya, V.; Varghese Gupta, S. Salts of Therapeutic Agents: Chemical, Physicochemical, and Biological Considerations. *Molecules* **2018**, *23* (7), 1719. https://doi.org/10.3390/molecules23071719.

(37) Qiao, N.; Li, M.; Schlindwein, W.; Malek, N.; Davies, A.; Trappitt, G. Pharmaceutical Cocrystals: An Overview. *Int. J. Pharm.* **2011**, *419* (1–2), 1–11. https://doi.org/10.1016/j.ijpharm.2011.07.037.

(38) Saikia, B.; Pathak, D.; Sarma, B. Variable Stoichiometry Cocrystals: Occurrence and Significance. *CrystEngComm* **2021**, *23* (26), 4583–4606. https://doi.org/10.1039/D1CE00451D.

(39) Singh, M.; Barua, H.; Jyothi, V. G. S. S.; Dhondale, M. R.; Nambiar, A. G.; Agrawal, A. K.; Kumar, P.; Shastri, N. R.; Kumar, D. Cocrystals by Design: A Rational Coformer Selection Approach for Tackling the API Problems. *Pharmaceutics* **2023**, *15* (4), 1161. https://doi.org/10.3390/pharmaceutics15041161.

(40) Guo, M.; Sun, X.; Chen, J.; Cai, T. Pharmaceutical Cocrystals: A Review of Preparations, Physicochemical Properties and Applications. *Acta Pharmaceutica Sinica B* **2021**, *11* (8), 2537–2564. https://doi.org/10.1016/j.apsb.2021.03.030.

(41) Kumar Bandaru, R.; Rout, S. R.; Kenguva, G.; Gorain, B.; Alhakamy, N. A.; Kesharwani, P.; Dandela, R. Recent Advances in Pharmaceutical Cocrystals: From Bench to Market. *Front. Pharmacol.* **2021**, *12*, 780582. https://doi.org/10.3389/fphar.2021.780582.

(42) Https://Www.Crystallizationsystems.Com/News/Navigating-the-Salt-Co-Crystal-Continuum-with-Crystal16/.

(43) Garcia, A.; Meinert, C.; Sugahara, H.; Jones, N.; Hoffmann, S.; Meierhenrich, U. The Astrophysical Formation of Asymmetric Molecules and the Emergence of a Chiral Bias. *Life* **2019**, *9* (1), 29. https://doi.org/10.3390/life9010029.

(44) Aranda-Díaz, A.; Rodrigues, C.; Grote, A.; Sun, J.; Schreck, C.; Hallatschek, O.; Souslov, A.; Möbius, W.; Huang, K. C. Bacterial Filamentation Drives Colony Chirality. *mBio* **2021**, *12* (6), e0154221. https://doi.org/10.1128/mBio.01542-21.

(45) Ben-Jacob, E.; Levine, H. The Artistry of Nature Pattern. *Nature* **2001**, *409*, 985–986. https://doi.org/10.1038/35059178.

(46) Teng, Y.; Gu, C.; Chen, Z.; Jiang, H.; Xiong, Y.; Liu, D.; Xiao, D. Advances and Applications of Chiral Resolution in Pharmaceutical Field. *Chirality* **2022**, *34* (8), 1094–1119. https://doi.org/10.1002/chir.23453.

(47) Sanganyado, E.; Lu, Z.; Fu, Q.; Schlenk, D.; Gan, J. Chiral Pharmaceuticals: A Review on Their Environmental Occurrence and Fate Processes. *Water Res.* **2017**, *124*, 527–542. https://doi.org/10.1016/j.watres.2017.08.003.

(48) Silvestri, I. P.; Colbon, P. J. J. The Growing Importance of Chirality in 3D Chemical Space Exploration and Modern Drug Discovery Approaches for Hit-ID: Topical Innovations. *ACS Med. Chem. Lett.* **2021**, *12* (8), 1220–1229. https://doi.org/10.1021/acsmedchemlett.1c00251.

(49) Putman, J. I.; Armstrong, D. W. Recent Advances in the Field of Chiral Crystallization. *Chirality* **2022**, *34* (10), 1338–1354. https://doi.org/10.1002/chir.23492.

(50) Charpentier, M. D.; Venkatramanan, R.; Rougeot, C.; Leyssens, T.; Johnston, K.; ter Horst, J. H. Multicomponent Chiral Quantification with Ultraviolet Circular Dichroism Spectroscopy: Ternary and Quaternary Phase Diagrams of Levetiracetam. *Mol. Pharmaceutics* **2023**, *20* (1), 616–629. https://doi.org/10.1021/acs.molpharmaceut.2c00825.

(51) Lorenz, H.; Seidel-Morgenstern, A. Processes To Separate Enantiomers. *Angew. Chem. Int. Ed.* **2014**, *53* (5), 1218–1250. https://doi.org/10.1002/anie.201302823.

(52) Ceramella, J.; Iacopetta, D.; Franchini, A.; De Luca, M.; Saturnino, C.; Andreu, I.; Sinicropi, M. S.; Catalano, A. A Look at the Importance of Chirality in Drug Activity: Some Significative Examples. *Appl. Sci.* **2022**, *12* (21), 10909. https://doi.org/10.3390/app122110909.

(53) Maher, T. J.; Johnson, D. A. Review of Chirality and Its Importance in Pharmacology. *Drug Dev. Res.* **1991**, *24* (2), 149–156. https://doi.org/10.1002/ddr.430240202.

(54) Liu, Y.; Wu, Z.; Armstrong, D. W.; Wolosker, H.; Zheng, Y. Detection and Analysis of Chiral Molecules as Disease Biomarkers. *Nat Rev Chem* **2023**, *7* (5), 355–373. https://doi.org/10.1038/s41570-023-00476-z.

(55) Dutta, S.; Gellman, A. J. Enantiomer Surface Chemistry: Conglomerate *versus* Racemate Formation on Surfaces. *Chem. Soc. Rev.* **2017**, *46* (24), 7787–7839. https://doi.org/10.1039/C7CS00555E.

(56) Blackmond, D. G. The Origin of Biological Homochirality. *Cold Spring Harb Perspect Biol* **2019**, *11* (3), a032540. https://doi.org/10.1101/cshperspect.a032540.

(57) Weller, M. G. The Mystery of Homochirality on Earth. *Life* **2024**, *14* (3), 341. https://doi.org/10.3390/life14030341.

(58) Bentley, R. The Nose as a Stereochemist. Enantiomers and Odor. *Chem. Rev.* **2006**, *106* (9), 4099–4112. https://doi.org/10.1021/cr050049t.

(59) H. Brooks, W.; C. Guida, W.; G. Daniel, K. The Significance of Chirality in Drug Design and Development. *CTMC* **2011**, *11* (7), 760–770. https://doi.org/10.2174/156802611795165098.

(60) Rouf, A.; Taneja, S. C. Synthesis of Single-enantiomer Bioactive Molecules: A Brief Overview. *Chirality* **2014**, *26* (2), 63–78. https://doi.org/10.1002/chir.22268.

(61) Sui, J.; Wang, N.; Wang, J.; Huang, X.; Wang, T.; Zhou, L.; Hao, H. Strategies for Chiral Separation: From Racemate to Enantiomer. *Chem. Sci.* **2023**, *14* (43), 11955–12003. https://doi.org/10.1039/D3SC01630G.

(62) Wang, L.; Wang, N.; Sui, J.; Sun, S.; Feng, Z.; Li, G.; Hao, H.; Zhou, L. Case of Chiral Resolution through Converting Two Racemic Compounds into a Conglomerate. *Cryst. Growth Des.* **2023**, *23* (8), 5641–5650. https://doi.org/10.1021/acs.cgd.3c00311.

(63) Pellissier, H. Recent Developments in Dynamic Kinetic Resolution. *Tetrahedron* **2011**, *67* (21), 3769–3802. https://doi.org/10.1016/j.tet.2011.04.001.

(64) Keith, J. M.; Larrow, J. F.; Jacobsen, E. N. Practical Considerations in Kinetic Resolution Reactions. *Adv. Synth. Catal.* **2001**, *343* (1), 5–26. https://doi.org/10.1002/1615-4169(20010129)343:1<5::AID-ADSC5>3.0.CO;2-I.

(65) Imayoshi, A.; Lakshmi, B. V.; Ueda, Y.; Yoshimura, T.; Matayoshi, A.; Furuta, T.; Kawabata, T. Enantioselective Preparation of Mechanically Planar Chiral Rotaxanes by Kinetic Resolution Strategy. *Nat Commun* **2021**, *12* (1), 404. https://doi.org/10.1038/s41467-020-20372-0.

(66) Yi, D.; Bayer, T.; Badenhorst, C. P. S.; Wu, S.; Doerr, M.; Höhne, M.; Bornscheuer, U. T. Recent Trends in Biocatalysis. *Chem. Soc. Rev.* **2021**, *50* (14), 8003–8049. https://doi.org/10.1039/D0CS01575J.

(67) Roddan, R.; Gygli, G.; Sula, A.; Méndez-Sánchez, D.; Pleiss, J.; Ward, R.; Keep, N.; Hailes, H. Acceptance and Kinetic Resolution of α-Methyl-Substituted Aldehydes by Norcoclaurine Synthases. *ACS Catalysis*. 2019.

(68) Kaviani, R.; Jouyban, A.; Shayanfar, A. Chiral Resolution Methods for Racemic Pharmaceuticals Based on Cocrystal Formation. *CrystEngComm* **2023**, *25* (44), 6120–6131. https://doi.org/10.1039/D3CE00853C.

(69) Cavazzini, A.; Pasti, L.; Massi, A.; Marchetti, N.; Dondi, F. Recent Applications in Chiral High Performance Liquid Chromatography: A Review. *Anal. Chim. Acta.* **2011**, *706* (2), 205–222. https://doi.org/10.1016/j.aca.2011.08.038.

(70) Calcaterra, A.; D'Acquarica, I. The Market of Chiral Drugs: Chiral Switches versus de Novo Enantiomerically Pure Compounds. *J. Pharma. Biomed. Anal.* **2018**, *147*, 323–340. https://doi.org/10.1016/j.jpba.2017.07.008.

(71) Tarafder, A.; Miller, L. Chiral Chromatography Method Screening Strategies: Past, Present and Future. *J. Chromatogr., A* **2021**, *1638*, 461878. https://doi.org/10.1016/j.chroma.2021.461878.

(72) Xing, Y.; Li, X.; Guo, X.; Cui, Y. Simultaneous Determination of 18 D-Amino Acids in Rat Plasma by an Ultrahigh-Performance Liquid Chromatography-Tandem Mass Spectrometry Method: Application to Explore the Potential Relationship between Alzheimer's Disease and d-Amino Acid Level Alterations. *Anal Bioanal Chem* **2016**, *408* (1), 141–150. https://doi.org/10.1007/s00216-015-9086-3.

(73) Furusho, A.; Koga, R.; Akita, T.; Mita, M.; Kimura, T.; Hamase, K. Three-Dimensional High-Performance Liquid Chromatographic Determination of Asn, Ser, Ala, and Pro Enantiomers in the Plasma of Patients with Chronic

Kidney Disease. *Anal. Chem.* **2019**, *91* (18), 11569–11575. https://doi.org/10.1021/acs.analchem.9b01615.

(74) Ishii, C.; Hamase, K. Two-Dimensional LC-MS/MS and Three-Dimensional LC Analysis of Chiral Amino Acids and Related Compounds in Real-World Matrices. *J. Pharma. Biomed. Anal.* **2023**, *235*, 115627. https://doi.org/10.1016/j.jpba.2023.115627.

(75) Oyaide, M.; Ishii, C.; Akita, T.; Kimura, T.; Sakai, S.; Mizui, M.; Mita, M.; Ide, T.; Isaka, Y.; Hamase, K. Development of a Three-Dimensional HPLC System for the Determination of Serine, Threonine and Allo-Threonine Enantiomers in the Plasma of Patients with Chronic Kidney Disease. *J. Chromatogr., A* **2024**, *1719*, 464739. https://doi.org/10.1016/j.chroma.2024.464739.

(76) Bosits, M. H.; Bereczki, L.; Bombicz, P.; Szalay, Z.; Pataki, H.; Demeter, Á. Design of Diastereomeric Salt Resolution *via* Multicomponent System Characterization: A Case Study with Hydrate Formation. *CrystEngComm* **2023**, *25* (4), 641–652. https://doi.org/10.1039/D2CE01490D.

(77) Rougeot, C.; Hein, J. E. Application of Continuous Preferential Crystallization to Efficiently Access Enantiopure Chemicals. *Org. Process Res. Dev.* **2015**, *19* (12), 1809–1819. https://doi.org/10.1021/acs.oprd.5b00141.

(78) Vantomme, G.; Crassous, J. Pasteur and Chirality: A Story of How Serendipity Favors the Prepared Minds. *Chirality* **2021**, *33* (10), 597–601. https://doi.org/10.1002/chir.23349.

(79) Ye, X.; Cui, J.; Li, B.; Li, N.; Wang, R.; Yan, Z.; Tan, J.; Zhang, J.; Wan, X. Enantiomer-Selective Magnetization of Conglomerates for Quantitative Chiral Separation. *Nat Commun* **2019**, *10* (1), 1964. https://doi.org/10.1038/s41467-019-09997-y.

(80) Brandel, C.; Amharar, Y.; Rollinger, J. M.; Griesser, U. J.; Cartigny, Y.; Petit, S.; Coquerel, G. Impact of Molecular Flexibility on Double Polymorphism, Solid Solutions and Chiral Discrimination during Crystallization of Diprophylline Enantiomers. *Mol. Pharmaceutics* **2013**, *10* (10), 3850–3861. https://doi.org/10.1021/mp400308u.

(81) Spix, L.; Meekes, H.; Blaauw, R. H.; van Enckevort, W. J. P.; Vlieg, E. Complete Deracemization of Proteinogenic Glutamic Acid Using Viedma Ripening on a Metastable Conglomerate. *Cryst. Growth Des.* **2012**, *12* (11), 5796–5799. https://doi.org/10.1021/cg301343a.

(82) Lorenz, H.; von Langermann, J.; Sadiq, G.; Seaton, C. C.; Davey, R. J.; Seidel-Morgenstern, A. The Phase Behavior and Crystallization of 2-Chloromandelic Acid: The Crystal Structure of the Pure Enantiomer and the Behavior of Its

Metastable Conglomerate. *Cryst. Growth Des.* **2011**, *11* (5), 1549–1556. https://doi.org/10.1021/cg1015077.

(83) Neurohr, C.; Marchivie, M.; Lecomte, S.; Cartigny, Y.; Couvrat, N.; Sanselme, M.; Subra-Paternault, P. Naproxen–Nicotinamide Cocrystals: Racemic and Conglomerate Structures Generated by $CO_2$ Antisolvent Crystallization. *Cryst. Growth Des.* **2015**, *15* (9), 4616–4626. https://doi.org/10.1021/acs.cgd.5b00876.

(84) Li, W. W.; Spix, L.; de Reus, S. C. A.; Meekes, H.; Kramer, H. J. M.; Vlieg, E.; ter Horst, J. H. Deracemization of a Racemic Compound via Its Conglomerate-Forming Salt Using Temperature Cycling. *Cryst. Growth Des.* **2016**, *16* (9), 5563–5570. https://doi.org/10.1021/acs.cgd.6b01034.

(85) Sarmah, K. K.; Rajbongshi, T.; Bhuyan, A.; Thakuria, R. Effect of Solvent Polarity in Mechanochemistry: Preparation of Conglomerate vs. Racemate. *Chem. Commun.* **2019**, *55*, 10900–10903. https://doi.org/10.1039/C9CC05687D.

(86) Gonella, S.; Mahieux, J.; Sanselme, M.; Coquerel, G. Spotting a Conglomerate Is Just Halfway to Achieving a Preparative Resolution by Preferential Crystallization. *Org. Process Res. Dev.* **2012**, *16* (2), 286–293. https://doi.org/10.1021/op200092f.

(87) Harfouche, L. C.; Brandel, C.; Cartigny, Y.; Petit, S.; Coquerel, G. Resolution by Preferential Crystallization of Proxyphylline by Using Its Salicylic Acid Monohydrate Co-Crystal. *Chem Eng & Technol* **2020**, *43* (6), 1093–1098. https://doi.org/10.1002/ceat.202000040.

(88) Buol, X.; Caro Garrido, C.; Robeyns, K.; Tumanov, N.; Collard, L.; Wouters, J.; Leyssens, T. Chiral Resolution of Mandelic Acid through Preferential Cocrystallization with Nefiracetam. *Cryst. Growth Des.* **2020**, *20* (12), 7979–7988. https://doi.org/10.1021/acs.cgd.0c01236.

(89) Zhou, F.; Shemchuk, O.; Charpentier, M. D.; Matheys, C.; Collard, L.; ter Horst, J. H.; Leyssens, T. Simultaneous Chiral Resolution of Two Racemic Compounds by Preferential Cocrystallization**. *Angew. Chem. Int. Ed.* **2021**, *60* (20264 –20268), 20426–20430. https://doi.org/10.1002/ange.202107804.

(90) Rapeenun, P.; Gerard, C. J. J.; Pinètre, C.; Cartigny, Y.; Tinnemans, P.; de Gelder, R.; Flood, A. E.; ter Horst, J. H. Searching for Conglomerate Cocrystals of the Racemic Compound Praziquantel. *Cryst. Growth Des.* **2024**, *24* (1), 480–490. https://doi.org/10.1021/acs.cgd.3c01158.

(91) Lörincz, L.; Zsemberi, M.; Bánsághi, G.; Sohajda, T.; Székely, E. Towards Diastereomeric Pure Salts with Antisolvent Methods. *Chem. Eng. Technol.* **2018**, *41* (7), 1466–1472. https://doi.org/10.1002/ceat.201700429.

(92) Murakami, H. From Racemates to Single Enantiomers – Chiral Synthetic Drugs over the Last 20 Years. In *Novel Optical Resolution Technologies*; Sakai, K., Hirayama, N., Tamura, R., Eds.; Topics in Current Chemistry; Springer Berlin Heidelberg: Berlin, Heidelberg, 2006; Vol. 269, pp 273–299. https://doi.org/10.1007/128_2006_072.

(93) Sánchez-Guadarrama, O.; Mendoza-Navarro, F.; Cedillo-Cruz, A.; Jung-Cook, H.; Arenas-García, J. I.; Delgado-Díaz, A.; Herrera-Ruiz, D.; Morales-Rojas, H.; Höpfl, H. Chiral Resolution of *RS* -Praziquantel via Diastereomeric Co-Crystal Pair Formation with L -Malic Acid. *Cryst. Growth Des.* **2016**, *16* (1), 307–314. https://doi.org/10.1021/acs.cgd.5b01254.

(94) Zhou, F.; Collard, L.; Robeyns, K.; Leyssens, T.; Shemchuk, O. L-Proline, a Resolution Agent Able to Target Both Enantiomers of Mandelic Acid: An Exciting Case of Stoichiometry Controlled Chiral Resolution. *Chem. Commun.* **2022**, *58*, 8560–8563. https://doi.org/10.1039/D2CC02942A.

(95) Springuel, G.; Leyssens, T. Innovative Chiral Resolution Using Enantiospecific Co-Crystallization in Solution. *Cryst. Growth Des.* **2012**, *12* (7), 3374–3378. https://doi.org/10.1021/cg300307z.

(96) Springuel, G.; Collard, L.; Leyssens, T. Ternary and Quaternary Phase Diagrams: Key Tools for Chiral Resolution through Solution Cocrystallization. *CrystEngComm* **2013**, *15* (39), 7951. https://doi.org/10.1039/c3ce41141a.

(97) Zhou, F.; Body, C.; Robeyns, K.; Leyssens, T.; Shemchuk, O. On the Pairwise Cocrystallization of Racemic Compounds. *CrystEngComm* **2023**, *25* (20), 3060–3065. https://doi.org/10.1039/D3CE00226H.

(98) Nulek, T.; Klaysri, R.; Cedeno, R.; Nalaoh, P.; Bureekaew, S.; Promarak, V.; Flood, A. E. Separation of Etiracetam Enantiomers Using Enantiospecific Cocrystallization with 2-Chloromandelic Acid. *ACS Omega* **2022**, *7* (23), 19465–19473. https://doi.org/10.1021/acsomega.2c01165.

(99) Songsermsawad, S.; Nalaoh, P.; Promarak, V.; Flood, A. E. Chiral Resolution of *RS* -Baclofen via a Novel Chiral Cocrystal of *R* -Baclofen and *L* -Mandelic Acid. *Cryst. Growth Des.* **2022**, *22* (4), 2441–2451. https://doi.org/10.1021/acs.cgd.1c01506.

(100) de Meester, J.; Shemchuk, O.; Collard, L.; Wouters, J.; Baillieux, S.; Robeyns, K.; Leyssens, T. Using the Nature of the Achiral Solvent to Orient Chiral Resolution. *CrystEngComm* **2024**. https://doi.org/10.1039/D4CE00124A.

(101) Kawashima, M.; Hirata, R. Epimerization-Crystallization Method in Optical Resolution of 2,2′-Dihydroxy-1,1′-Binaphthyl, and Kinetic Study. *BCSJ* **1993**, *66* (7), 2002–2005. https://doi.org/10.1246/bcsj.66.2002.

(102) Ratajczak-Sitarz, M.; Katrusiak, A.; Gawrońska, K.; Gawroński, J. Racemate Resolution via Diastereomeric Helicates in Hydrogen-Bonded Co-Crystals: The Case of BINOL–Diamine Complexes. *Tetrahedron: Asymmetry* **2007**, *18* (6), 765–773. https://doi.org/10.1016/j.tetasy.2007.03.005.

(103) CrysAlisPro, Version 1.171.37.35; Rigaku Oxford Diffraction.

(104) Sheldrick, G. M. SHELXT – Integrated Space-Group and Crystal-Structure Determination. *Acta Cryst A Found Adv.* **2015**, *71* (1), 3–8. https://doi.org/10.1107/S2053273314026370.

(105) Sheldrick, G. M. Crystal Structure Refinement with *SHELXL*. *Acta Crystallogr C Struct Chem* **2015**, *71* (1), 3–8. https://doi.org/10.1107/S2053229614024218.

(106) Spek, A. L. Structure Validation in Chemical Crystallography. *Acta Crystallogr D Biol Crystallogr* **2009**, *65* (2), 148–155. https://doi.org/10.1107/S090744490804362X.

(107) Macrae, C. F.; Sovago, I.; Cottrell, S. J.; Galek, P. T. A.; McCabe, P.; Pidcock, E.; Platings, M.; Shields, G. P.; Stevens, J. S.; Towler, M.; Wood, P. A. Mercury 4.0: From Visualization to Analysis, Design and Prediction. *J Appl Cryst* **2020**, *53* (1), 226–235. https://doi.org/10.1107/S1600576719014092.

(108) Tayama, E.; Tanaka, H. An Efficient Optical Resolution of Nitrogen-Centered Chiral β-Hydroxy-Tetraalkylammonium Salts via Complexation with (R)-BINOL. *Tetrahedron Lett.* **2007**, *48* (24), 4183–4185. https://doi.org/10.1016/j.tetlet.2007.04.078.

(109) Brunel, J. M. BINOL: A Versatile Chiral Reagent. *Chem. Rev.* **2005**, *105* (3), 857–898. https://doi.org/10.1021/cr040079g.

(110) Chen, Y.; Yekta, S.; Yudin, A. K. Modified BINOL Ligands in Asymmetric Catalysis. *Chem. Rev.* **2003**, *103* (8), 3155–3212. https://doi.org/10.1021/cr020025b.

(111) Love, B. Preparation and Enantiomeric Excess Determination of Optically Active BINOL and BINOL Derivatives. *COS* **2006**, *3* (2), 169–185. https://doi.org/10.2174/157017906776819178.

(112) Ayad, S.; Posey, V.; Das, A.; Montgomery, J. M.; Hanson, K. Enantioenrichment of Racemic BINOL by Way of Excited State Proton Transfer. *Chem. Commun.* **2019**, *55* (9), 1263–1266. https://doi.org/10.1039/C8CC07949H.

(113) Vu, N.; McLeod, G. M.; Hanson, K.; DePrince, A. E. Enhanced Diastereocontrol via Strong Light–Matter Interactions in an Optical Cavity. *J. Phys. Chem. A* **2022**, *126* (49), 9303–9312. https://doi.org/10.1021/acs.jpca.2c07134.

(114) Guillot, M.; de Meester, J.; Huynen, S.; Collard, L.; Robeyns, K.; Riant, O.; Leyssens, T. Cocrystallization-Induced Spontaneous Deracemization: A GeneralThermodynamic Approach to Deracemization. *Angew. Chem. Int. Ed.* **2020**, *132*, 11303–11306. https://doi.org/10.1002/anie.202002464.

(115) Aitipamula, S.; Chow, P. S.; Tan, R. B. H. Polymorphs and Solvates of a Cocrystal Involving an Analgesic Drug, Ethenzamide, and 3,5-Dinitrobenzoic Acid. *Cryst. Growth Des.* **2010**, *10* (5), 2229–2238. https://doi.org/10.1021/cg9015178.

(116) Healy, A. M.; Worku, Z. A.; Kumar, D.; Madi, A. M. Pharmaceutical Solvates, Hydrates and Amorphous Forms: A Special Emphasis on Cocrystals. *Adv. Drug Deliv. Rev.* **2017**, *117*, 25–46. https://doi.org/10.1016/j.addr.2017.03.002.

(117) Yelgaonkar, S. P.; Campillo-Alvarado, G.; MacGillivray, L. R. Phototriggered Guest Release from a Nonporous Organic Crystal: Remarkable Single-Crystal-to-Single-Crystal Transformation of a Binary Cocrystal Solvate to a Ternary Cocrystal. *J. Am. Chem. Soc.* **2020**, *142* (49), 20772–20777. https://doi.org/10.1021/jacs.0c09732.

(118) Sathisaran, I.; Dalvi, S. V. Cocrystallization of an Antiretroviral Drug Nevirapine: An Eutectic, a Cocrystal Solvate, and a Cocrystal Hydrate. *Cryst. Growth Des.* **2021**, *21* (4), 2076–2092. https://doi.org/10.1021/acs.cgd.0c01513.

(119) Shaikh, T. R.; Shelke, N.; Tothadi, S. Multicomponent Solvate Crystals of 3,5-Dinitrobenzoic Acid and Acetamide and CSD Analysis of Solvates. *ACS Omega* **2023**, *8* (27), 24644–24653. https://doi.org/10.1021/acsomega.3c03091.

(120) Kőrösi, M.; Madarász, J.; Sohajda, T.; Székely, E. A Fast, New Method to Enhance the Enantiomeric Purity of Non-Racemic Mixtures: Self-Disproportionation of Enantiomers in the Gas Antisolvent Fractionation of Chlorine-Substituted Mandelic Acid Derivatives. *Tetrahedron: Asymmetry* **2017**, *28* (11), 1568–1572. https://doi.org/10.1016/j.tetasy.2017.09.005.

(121) Kőrösi, M.; Sedon, A.; Komka, K.; Sohajda, T.; Székely, E. Gas Antisolvent Fractionation: A New Method to Obtain Enantiopure Compounds, a Case Study on Mandelic Acid. *Period. Polytech. Chem. Eng.* **2018**, *63* (1), 130–137. https://doi.org/10.3311/PPch.11741.

(122) Knez, Ž.; Markočič, E.; Leitgeb, M.; Primožič, M.; Knez Hrnčič, M.; Škerget, M. Industrial Applications of Supercritical Fluids: A Review. *Energy* **2014**, *77*, 235–243. https://doi.org/10.1016/j.energy.2014.07.044.

(123) Shi, J.; Kang, X.; Mao, L.; Jiang, Y.; Zhao, S.; Liu, Y.; Zhai, B.; Jin, H.; Guo, L. Supercritical CO2-Applied Equipment for Chemical Synthesis and Transformation: Current Status and Perspectives. *Chem. Eng. J.* **2023**, *459*, 141608. https://doi.org/10.1016/j.cej.2023.141608.

(124) Knez, Ž.; Knez Hrnčič, M.; Škerget, M. Particle Formation and Product Formulation Using Supercritical Fluids. *Annu. Rev. Chem. Biomol. Eng.* **2015**, *6* (1), 379–407. https://doi.org/10.1146/annurev-chembioeng-061114-123317.

(125) Leitner, W. Supercritical Carbon Dioxide as a Green Reaction Medium for Catalysis. *Acc. Chem. Res.* **2002**, *35* (9), 746–756. https://doi.org/10.1021/ar010070q.

(126) O'Sullivan, A.; Long, B.; Verma, V.; Ryan, K. M.; Padrela, L. Solid-State and Particle Size Control of Pharmaceutical Cocrystals Using Atomization-Based Techniques. *Int. J. Pharm.* **2022**, *621*, 121798. https://doi.org/10.1016/j.ijpharm.2022.121798.

(127) Ramsey, E.; Sun, Q.; Zhang, Z.; Zhang, C.; Gou, W. Mini-Review: Green Sustainable Processes Using Supercritical Fluid Carbon Dioxide. *J. Environ. Sci.* **2009**, *21* (6), 720–726. https://doi.org/10.1016/S1001-0742(08)62330-X.

(128) Neurohr, C.; Revelli, A.-L.; Billot, P.; Marchivie, M.; Lecomte, S.; Laugier, S.; Massip, S.; Subra-Paternault, P. Naproxen–Nicotinamide Cocrystals Produced by CO2 Antisolvent. *J. Supercrit. Fluids* **2013**, *83*, 78–85. https://doi.org/10.1016/j.supflu.2013.07.008.

(129) Ercicek, F.; Harscoat-Schiavo, C.; Layrisse, P.; Marchivie, M.; Cartigny, Y.; Brandel, C.; Tassaing, T.; Conrad, M.; Marre, S.; Subra-Paternault, P. Naproxen-Bipyridine Cocrystallization Assisted by Pressurized Carbon Dioxide. *J. Supercrit. Fluids* **2023**, *200*, 105976. https://doi.org/10.1016/j.supflu.2023.105976.

(130) Kotbantao, G.; Charoenchaitrakool, M. Processing of Ketoconazole–4-Aminobenzoic Acid Cocrystals Using Dense CO 2 as an Antisolvent. *J. CO2 Utilization* **2017**, *17*, 213–219. https://doi.org/10.1016/j.jcou.2016.12.007.

(131) Ercicek, F.; Marchivie, M.; Nimod, L.; Cercel, H.; Brandel, C.; Ziri, I.; Cartigny, Y.; Monnier, O.; Marre, S.; Denux, D.; Subra-Paternault, P.; Harscoat-Schiavo, C. Unraveling a Unique Metastable Phase of a Proxyphylline Co-Crystal Exclusively Produced by Compressed Carbon Dioxide. *Cryst. Growth Des.*

(132) Varga, D.; Bánsághi, G.; Pérez, J. A. M.; Miskolczi, S.; Hegedűs, L.; Simándi, B.; Székely, E. Chiral Resolution of Racemic Cyclopropanecarboxylic Acids in Supercritical Carbon Dioxide. *Chem Eng & Technol* **2014**, *37* (11), 1885–1890. https://doi.org/10.1002/ceat.201300720.

(133) Bánsághi, G.; Székely, E.; Sevillano, D. M.; Juvancz, Z.; Simándi, B. Diastereomer Salt Formation of Ibuprofen in Supercritical Carbon Dioxide. *J. Supercrit. Fluids* **2012**, *69*, 113–116. https://doi.org/10.1016/j.supflu.2012.05.016.

(134) Lőrincz, L.; Bánsághi, G.; Zsemberi, M.; de Simón Brezmes, S.; Szilágyi, I. M.; Madarász, J.; Sohajda, T.; Székely, E. Diastereomeric Salt Precipitation Based Resolution of Ibuprofen by Gas Antisolvent Method. *J. Supercrit. Fluids* **2016**, *118*, 48–53. https://doi.org/10.1016/j.supflu.2016.07.021.

(135) Zodge, A.; Kőrösi, M.; Madarász, J.; Szilágyi, I. M.; Varga, E.; Székely, E. Gas Antisolvent Fractionation: A New Approach for the Optical Resolution of 4-Chloromandelic Acid. *Period. Polytech. Chem. Eng.* **2019**, *63* (2), 303–311. https://doi.org/10.3311/PPch.12910.

(136) Wang, P.-L.; Wang, H.-B.; Ding, W.-L.; Liu, Z.-Q.; Xing, Z.-T. *N* -(2,6-Dimethylphenyl)-2-(2-Oxo-1-Pyrrolidin-1-Yl)Acetamide. *Acta Crystallogr E Struct Rep Online* **2006**, *62* (9), o3838–o3839. https://doi.org/10.1107/S1600536806031370.

(137) Cameron, T. S.; Duffin, M. DL-Mandelic Acid. *J Mol Biol* **1974**, *3*, 539-541. https://doi.org/10.1016/0022-2836(75)90229-6.

(138) Patil, A. O.; Pennington, W. T.; Paul, I. C.; Curtin, D. Y.; Dykstra, C. E. Reactions of Crystalline (R)-(-)- and (S)-(+)-Mandelic Acid with Amines. Crystal Structure and Dipole Moment of (S)-Mandelic Acid. A Method of Determining Absolute Configuration of Chiral Crystals. *J. Am. Chem. Soc.* **1987**, *109* (5), 1529–1535. https://doi.org/10.1021/ja00239a037.

(139) Harscoat-Schiavo, C.; Neurohr, C.; Lecomte, S.; Marchivie, M.; Subra-Paternault, P. Influence of Isomerism on Recrystallization and Cocrystallization Induced by $CO_2$ as an Antisolvent. *CrystEngComm* **2015**, *17* (29), 5410–5421. https://doi.org/10.1039/C5CE00753D.

(140) Erriguible, A.; Neurohr, C.; Revelli, A.-L.; Laugier, S.; Fevotte, G.; Subra-Paternault, P. Cocrystallization Induced by Compressed CO2 as Antisolvent: Simulation of a Batch Process for the Estimation of Nucleation and Growth Parameters. *J. Supercrit. Fluids* **2015**, *98*, 194–203. https://doi.org/10.1016/j.supflu.2014.12.013.

(141) Kulkarni, S. A.; Kadam, S. S.; Meekes, H.; Stankiewicz, A. I.; ter Horst, J. H. Crystal Nucleation Kinetics from Induction Times and Metastable Zone Widths. *Cryst. Growth Des.* **2013**, *13* (6), 2435–2440. https://doi.org/10.1021/cg400139t.

(142) Spek, A. L. *PLATON* SQUEEZE: A Tool for the Calculation of the Disordered Solvent Contribution to the Calculated Structure Factors. *Acta Crystallogr C Struct Chem* **2015**, *71* (1), 9–18. https://doi.org/10.1107/S2053229614024929.

# Chapter 7. Appendices

# Appendixe A

## Supporting information to Chapter 3

### 1. Interactions with solvents

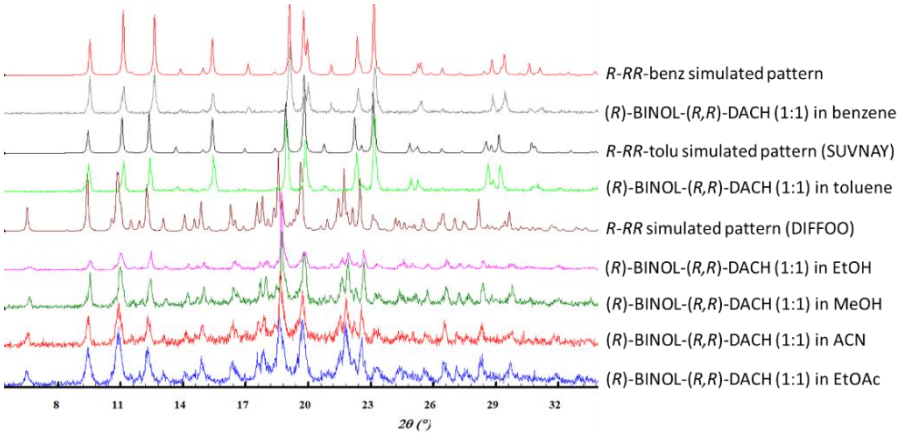


Figure SI-3.1. Comparison of the X-ray diffraction patterns between slurry outcomes of (*R*)-BINOL and (*R*,*R*)-DACH in different solvents.

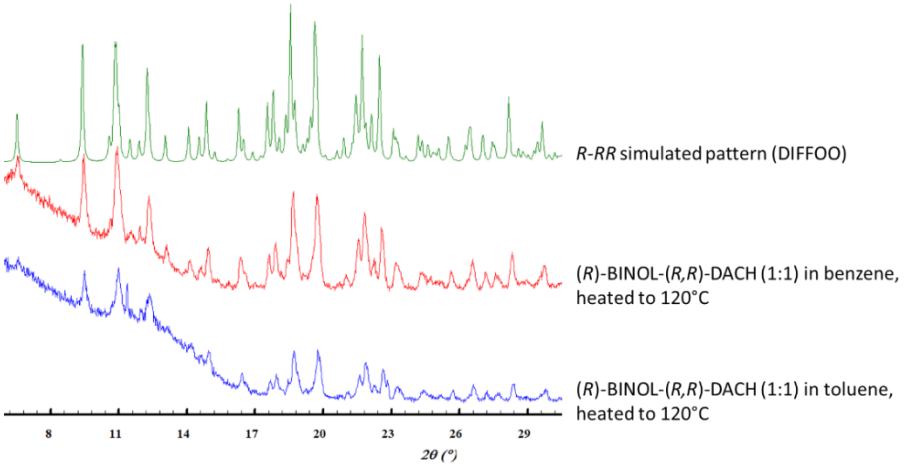


Figure SI-3.2. Comparison of the X-ray diffraction patterns of *R-RR*-tolu and *R-RR*-benz, each heated to 120°C, with the *R-RR* cocrystal.

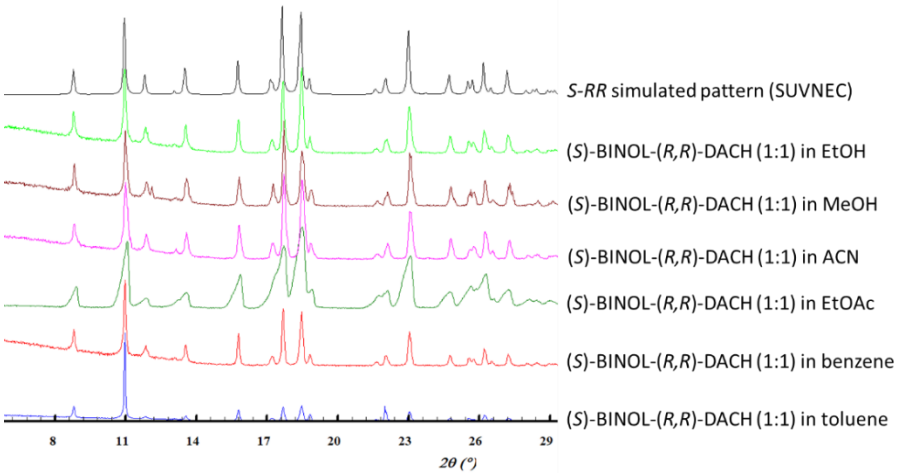


Figure SI-3.3. Comparison of the X-ray diffraction patterns between the slurry outcome of (*S*)-BINOL and (*R*,*R*)-DACH in different solvents.

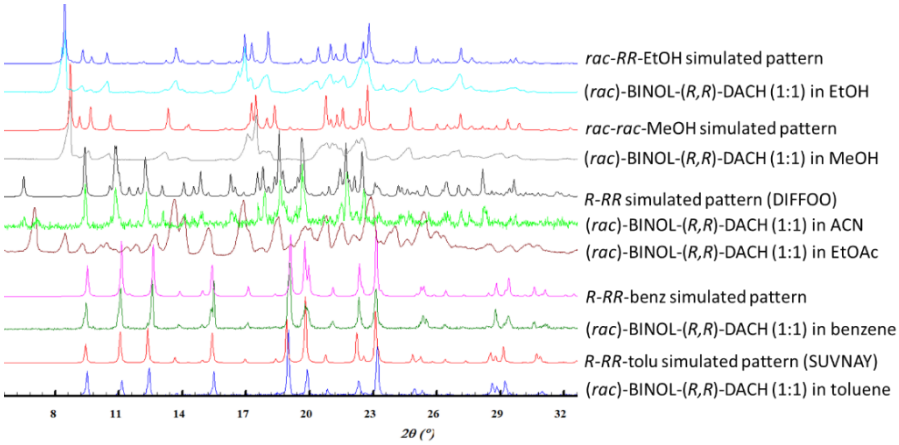


Figure SI-3.4. Comparison of the X-ray diffraction patterns between slurry outcomes of (*rac*)-BINOL and (*R*,*R*)-DACH in different solvents.

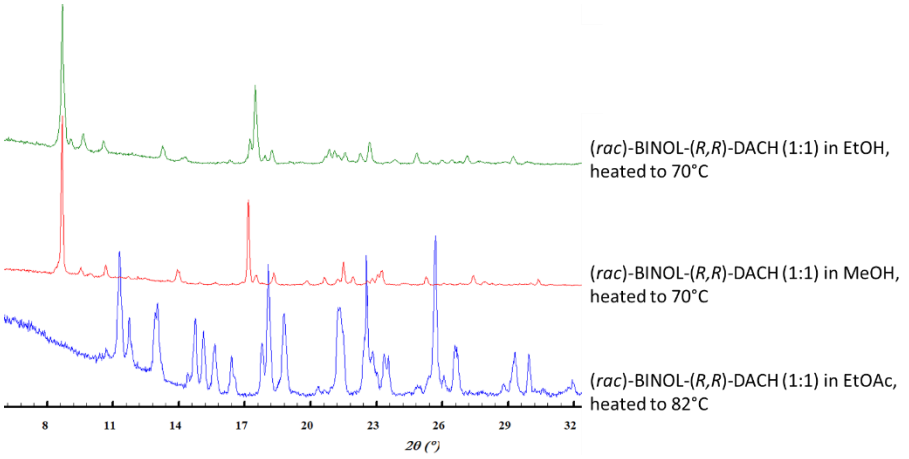


Figure SI-3.5. Comparison of the X-ray diffraction patterns of the powders recovered by slurrying *(rac)*-BINOL and *(R,R)*-DACH in EtOAc, MeOH and EtOH, heated to respectively 82°C, 70°C, and 70°C.

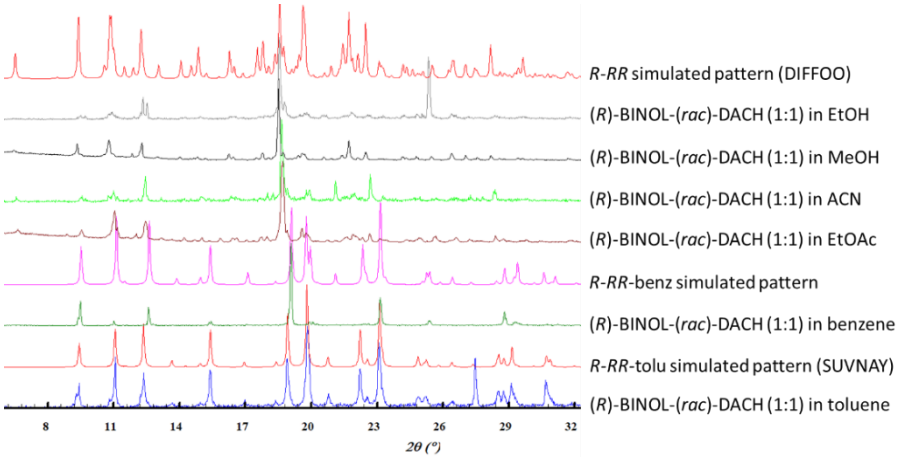


Figure SI-3.6**.** Comparison of the X-ray diffraction patterns between slurry outcomes of (*R*)-BINOL and (*rac*)-DACH in different solvent.

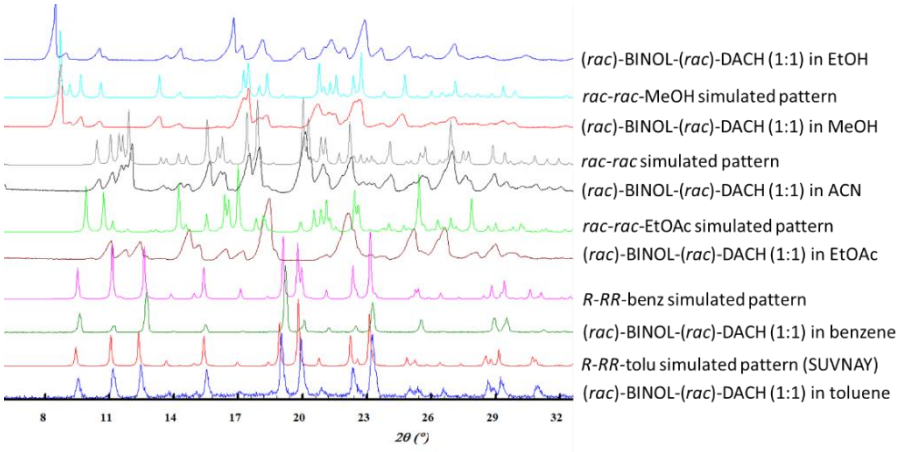


Figure SI-3.7. Comparison of the X-ray diffraction patterns between slurry outcomes of (*rac*)-BINOL and (*rac*)-DACH in different solvents.

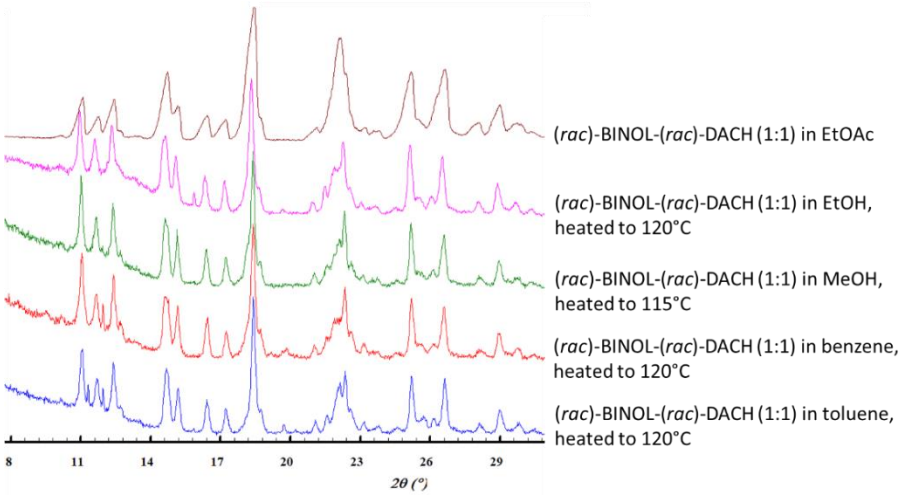


Figure SI-3.8. Comparison of the X-ray diffraction patterns of the powders recovered by slurrying *(rac)*-BINOL and *(rac)*-DACH in toluene, benzene, MeOH and EtOH, heated to respectively 120°C, 120°C, 115°C, and 120°C, with the outcome of the slurry (*rac)*-BINOL and *(rac)*-DACH in EtOAc.

## 2. Structural analysis

Table SI-3.1. Crystallographic data and structure refinement for *R-RR*-benz, 4*rac*-4*RR*-3EtOH-$H_2O$, *rac*-*rac*-EtOAc, *rac*-*rac* and *rac*-*rac*-MeOH phases.

| **Identification code** | **(*R*)-BINOL-(*R,R*)-DACH-benzene *R-RR*-benz** | **4(*rac*)-BINOL-4(*R,R*)-DACH-3EtOH-$H_2O$ *4rac-4RR*-3EtOH-$H_2O$** | **(*rac*)-BINOL-(*rac*)-DACH-EtOAc *rac-rac*-EtOAc** | **(*rac*)-BINOL-(*rac*)-DACH *rac-rac*** | **(*rac*)-BINOL-(*rac*)-DACH-MeOH *rac-rac*-MeOH** |
|---|---|---|---|---|---|
| **Empirical formula** | $C_{32}$ $H_{34}$ $N_2$ $O_2$ | $C_{110}$ $H_{132}$ $N_8$ $O_{12}$ | $C_{28}$ $H_{32}$ $N_2$ $O_3$ | $C_{26}$ $H_{28}$ $N_2$ $O_2$ | $C_{27}$ $H_{32}$ $N_2$ $O_3$ |
| **Formula weight [g/mol ]** | 478.61 | 1758.23 | 444.55 | 400.50 | 432.54 |
| **Temperature [K]** | 297(2) | 297(2) | 297(2) | 297(2) | 297(2) |
| **Wavelength [Å]** | 0.71073 | 0.71073 | 0.71073 | 0.71073 | 0.71073 |
| **Crystal system** | Orthorhombic | Triclinic | Triclinic | Monoclinic | Triclinic |
| **Space group** | $C222_1$ | $P1$ | $P$-1 | $P2_1/c$ | $P$-1 |
| **Unit cell dimensions** | a = 12.3993(15) Å | a = 10.3936(12) Å | a = 8.1693(10) Å | a = 8.1707(5) Å | a = 10.2697(12) Å |
| | b = 14.0194(10) Å | b = 11.2508(9) Å | b = 9.2052(9) Å | b = 29.731(2) Å | b = 11.140(2) Å |
| | c = 15.3719(12) Å | c = 20.951(2) Å | c = 16.684(2) Å | c = 9.0449(6) Å | c = 11.3987(17) Å |
| | α = 90°. | α = 87.176(7)°. | α = 96.026(9)°. | α = 90°. | α = 108.518(16)°. |
| | β= 90°. | β = 89.274(8)°. | β = 95.209(10)°. | β = 101.667(6)°. | β = 101.580(12)°. |
| | γ = 90°. | γ = 76.533(8)°. | γ = 102.224(9)°. | γ = 90°. | γ = 101.228(14)°. |
| **Volume [Å³]** | 2672.1(4) | 2379.6(4) | 1211.1(2) | 2151.8(3) | 1163.6(3) |
| **Z** | 4 | 1 | 2 | 4 | 2 |
| **Density (calculated) [g/cm³]** | 1.190 | 1.227 | 1.219 | 1.236 | 1.235 |
| **Absorption coefficient [mm⁻¹]** | 0.074 | 0.080 | 0.079 | 0.078 | 0.080 |
| **F(000)** | 1024 | 944 | 476 | 856 | 464 |
| **Crystal size [mm³]** | 0.20 x 0.02 x 0.01 | 0.12 x 0.10 x 0.10 | 0.50 x 0.20 x 0.10 | 0.15 x 0.10 x 0.05 | 0.30 x 0.23 x 0.03 |
| **Theta range for data collection** | 3.194 to 23.226°. | 2.561 to 25.252°. | 2.977 to 26.565°. | 2.677 to 25.255°. | 3.251 to 26.299°. |
| **Reflections collected** | 7721 | 41911 | 18971 | 18727 | 16245 |
| **Independent reflections** | 1896 [R(int) = 0.1124] | 17196 [R(int) = 0.0535] | 4925 [R(int) = 0.0258] | 3860 [R(int) = 0.0691] | 4618 [R(int) = 0.0364] |
| **Completeness to theta** | theta = 23.226° 98.4 % | theta = 25.242° 99.8 % | theta = 25.242° 99.4 % | theta = 25.242° 99.4 % | theta = 25.242° 99.3 % |
| **Absorption correction** | Semi-empirical from equivalents | | | | |
| **Max. and min. transmission** | 1.00000 and 0.83528 | 1.00000 and 0.94435 | 1.00000 and 0.94746 | 1.00000 and 0.03073 | 1.00000 and 0.81288 |
| **Refinement method** | Full-matrix least-squares on $F^2$ | | | | |
| **Data / restraints / parameters** | 1896 / 29 / 172 | 17196 / 1172 / 1227 | 4925 / 46 / 343 | 3860 / 0 / 287 | 4618 / 224 / 381 |
| **Goodness-of-fit on F2** | 1.061 | 1.024 | 1.055 | 1.124 | 1.059 |
| **Final R indices [I>2sigma(I)]** | R1 = 0.0612, wR2 = 0.1342 | R1 = 0.0680, wR2 = 0.1648 | R1 = 0.0454, wR2 = 0.1183 | R1 = 0.0831, wR2 = 0.1398 | R1 = 0.0612, wR2 = 0.1531 |
| **R indices (all data)** | R1 = 0.1060, wR2 = 0.1544 | R1 = 0.1197, wR2 = 0.1907 | R1 = 0.0544, wR2 = 0.1239 | R1 = 0.1398, wR2 = 0.1616 | R1 = 0.0793, wR2 = 0.1624 |
| **Absolute structure parameter** | -0.8(10) | 0.2(7) | | | |
| **Extinction coefficient** | n/a | n/a | n/a | n/a | n/a |
| Largest diff. peak and hole **[e.Å⁻³]** | 0.138 and -0.158 | 0.470 and -0.209 | 0.188 and -0.152 | 0.167 and -0.206 | 0.216 and -0.168 |

Table SI-3.2. Hydrogen bonds of the *R-RR* cocrystal (DIFFOO).

| | | | | Interatomic distances (Å) | | | Angle (°) |
|---|---|---|---|---|---|---|---|
| Type | Donor | H… | Acceptor | D-H | H…A | D…A | D-H…A |
| | O1 | --H1 | ..N1 | 0.82 | 1.90 | 2.691(4) | 161 |
| | O2 | -- H8 | .. N2 | 0.82 | 2.09 | 2.796(5) | 144 |
| | N2 | --H27 | ..O1 | 1.04(5) | 2.24(5) | 3.245(5) | 163(4) |
| Intra | N2 | --H27 | ..N1 | 1.04(5) | 2.56(5) | 2.966(6) | 103(3)' |
| | O3 | --H29 | ..N3 | 0.82 | 2.00 | 2.742(4) | 151 |
| | O4 | --H36 | ..N4 | 0.82 | 2.08 | 2.808(4) | 148 |

Table SI-3.3. Hydrogen bonds of the *R-RR*-toluene cocrystal-solvate (SUVNAY).

| | | | | Interatomic distances (Å) | | | Angle (°) |
|---|---|---|---|---|---|---|---|
| Type | Donor | H… | Acceptor | D-H | H…A | D…A | D-H…A |
| | O1 | --H1 | ..N1 | 0.96 | 2.02 | 2.7458(4) | 131 |

Table SI-3.4. CH-π stacking in the *R-RR*-toluene cocrystal-solvate.

| | | Distance (Å) | Angle (°) | Interatomic distances (Å) |
|---|---|---|---|---|
| C-H | Ring | H…Ring | C-H…Ring | C…RingH |
| C7-H7 | Benzene | 2.95 | 175 | 3.9070(6) |
| C7-H7 | Benzene | 2.76 | 155 | 3.6519(6) |

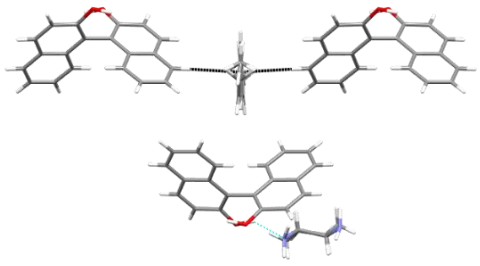

Figure SI-3.9. CH- π interaction of the *R-RR*-tolu cocrystal-solvate, view along *b*-axis.

Table SI-3.5. Hydrogen bonds of the *R*- *RR*-benzene cocrystal-solvate.

| | | | | Interatomic distances (Å) | | | Angle (°) |
|---|---|---|---|---|---|---|---|
| Type | Donor | H… | Acceptor | D-H | H…A | D…A | D-H…A |
| | O1 | --H1 | ..N21 | 0.84(7) | 2.00(8) | 2.768(7) | 151(6) |

Table SI-3.6**.** CH- π stacking in the *R-RR*-benzene cocrystal-solvate, obtained in benzene.

| | | Distance (Å) | Angle (°) | Interatomic distances (Å) |
|---|---|---|---|---|
| C-H | Ring | H…Ring | C-H…Ring | C…RingH |
| C6-H6 | Benzene | 2.88 | 169 | 3.796(8) |
| C6-H6 | Benzene | 2.88 | 169 | 3.796(8) |

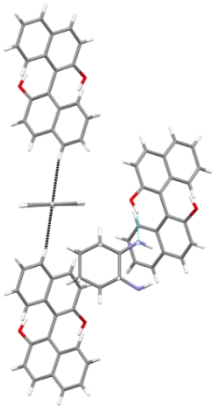

Figure SI-3.10. CH- π interaction of the *R-RR*-benz cocrystal-solvate, view along *a*-axis.

Table SI-3.7**.** Hydrogen bonds of the *S-RR* cocrystal (SUVNEC[102]).

| | | | | Interatomic distances (Å) | | | Angle (°) |
|---|---|---|---|---|---|---|---|
| Type | Donor | H… | Acceptor | D-H | H…A | D…A | D-H…A |
| | O1 | --H1 | ..N1 | 0.96 | 1.85 | 2.737(4) | 153 |
| | O2 | --H2 | ..N2 | 0.96 | 1.88 | 2.813(5) | 164 |

Table SI-3.8. Hydrogen bonds of the 4*rac-4RR*-3EtOH-$H_2O$ cocrystal-salt-solvate, obtained in EtOH.

| | | | | Interatomic distances (Å) | | | Angle (°) |
|---|---|---|---|---|---|---|---|
| Type | Donor | --- H.. | ..Acceptor | D - H | H...A | D...A | D - H...A |
| | N1 | --H1A | ..O62 | 0.89 | 1.90 | 2.792(8) | 178 |
| Intra | N1 | --H1B | ..N8 | 0.89 | 2.37 | 2.787(9) | 109 |
| | N1 | --H1C | ..O161 | 0.89 | 1.85 | 2.735(8) | 176 |
| Intra | N11 | --H11A | ..N18 | 0.89 | 2.34 | 2.798(11) | 112 |
| | N11 | --H11B | ..O71 | 0.89 | 1.98 | 2.862(8) | 173 |
| | N11 | --H11C | ..O171 | 0.89 | 1.90 | 2.759(9) | 160 |
| Intra | N21 | --H21A | ..N28 | 0.89(4) | 2.52(10) | 2.815(13) | 100(7) |
| | N28 | --H28A | ..O152 | 0.89 | 1.90 | 2.785(8) | 172 |
| Intra | N28 | --H28B | ..N21 | 0.89 | 2.37 | 2.815(13) | 111 |
| | N28 | --H28C | ..O181 | 0.89 | 1.92 | 2.807(10) | 172 |
| | N31 | --H31B | ..O101 | 0.89 | 1.93 | 2.816(8) | 170 |
| | N31 | --H31C | ..O191 | 0.89 | 1.85 | 2.719(9) | 164 |
| | N38 | --H38B | ..O131 | 0.89(9) | 2.42(9) | 3.270(14) | 162(6) |
| | O41 | --H41 | ..O71 | 0.82 | 1.83 | 2.620(7) | 161 |
| | O171 | --H71B | ..O62 | 0.91(8) | 1.82(9) | 2.702(8) | 162(7) |
| | O92 | --H92 | ..O62 | 0.82 | 1.87 | 2.613(7) | 150 |
| | O122 | --H122 | ..O152 | 0.82 | 1.85 | 2.628(7) | 157 |
| | O131 | --H131 | ..O101 | 0.82 | 1.87 | 2.612(7) | 150 |
| | O161 | --H161 | ..O71 | 0.82 | 1.78 | 2.601(7) | 174 |
| | O181 | --H181 | ..O101 | 0.82 | 1.91 | 2.680(9) | 157 |
| | O191 | --H183 | ..O152 | 0.82 | 1.85 | 2.636(8) | 160 |

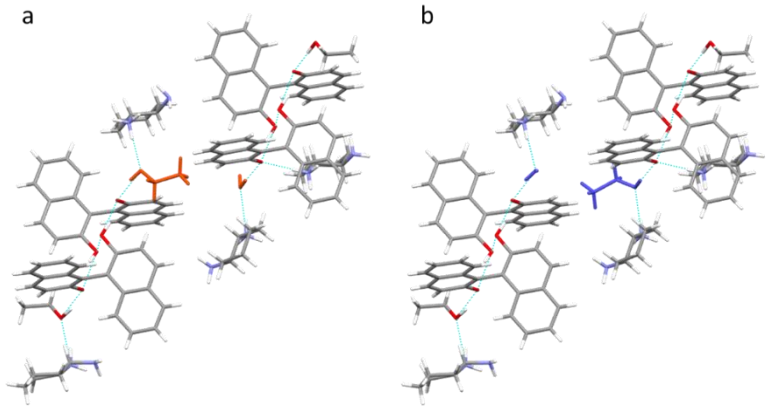


Figure SI-3.11. Asymmetric unit of the 4*rac-4RR*-3EtOH-$H_2O$ phase, view along b-axis. Of the three molecules of EtOH, one is disordered, the molecule of water is also disordered. The disordered molecule of EtOH and the molecule of water can be exchanged, with the major form accounting for 67.8% and the minor form for 32.2%. a) Major form, in orange, b) Minor form, in blue.

Table SI-3.9**.** Hydrogen bonds of the *rac-rac*-MeOH cocrystal-salt-solvate obtained in MeOH.

| | | | | Interatomic distances (Å) | | | Angle (°) |
|---|---|---|---|---|---|---|---|
| Type | Donor | H… | Acceptor | D-H | H…A | D…A | D-H…A |
| | O22 | --H22 | ..O1 | 0.97(3) | 1.68(3) | 2.617(2) | 162(2) |
| Intra | N31 | --H31A | ..N38 | 0.89 | 2.38 | 2.798(15) | 109 |
| | N31 | --H31A | ..N38B | 0.89 | 2.39 | 2.820(19) | 110’ |
| | N31 | --H31B | ..O1 | 0.89 | 1.81 | 2.690(14) | 171 |
| | N31 | --H31C | ..O41 | 0.89 | 2.01 | 2.891(16) | 172 |
| | O41 | --H41 | ..O1 | 0.98(3) | 1.69(3) | 2.656(3) | 173(3) |

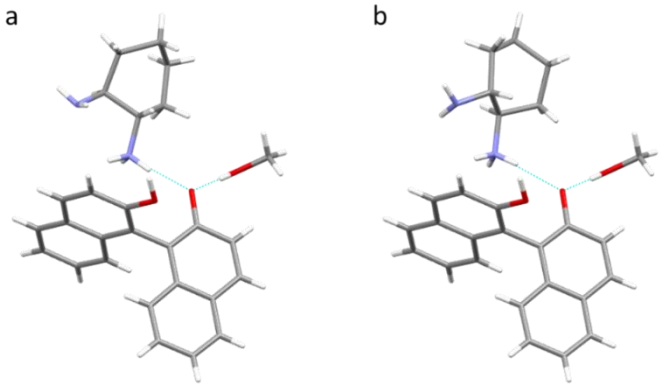


Figure SI-3.12. Asymmetric unit of the *rac-rac*-MeOH phase, view along a-axis. DACH molecule shows S-*R* disorder, as 51%-49%. a) Major form, b) Minor form.

Table SI-3.10**.** Hydrogen bonds of the *rac-rac*-EtOAc cocrystal-solvate, obtained by slow evaporation.

| | | | | Interatomic distances (Å) | | | Angle (°) |
|---|---|---|---|---|---|---|---|
| Type | Donor | H… | Acceptor | D-H | H…A | D…A | D-H…A |
| | O1 | --H1 | ..N31 | 0.91(2) | 1.96(2) | 2.815(2) | 154.8(15) |
| | O22 | --H22 | ..N38 | 0.96(2) | 1.911(17) | 2.763(2) | 146.9(13) |

Table SI-3.11**.** Hydrogen bonds of the *rac-rac* cocrystal obtained in ACN.

| | | | | Interatomic distances (Å) | | | Angle (°) |
|---|---|---|---|---|---|---|---|
| Type | Donor | H… | ..Acceptor | D - H | H...A | D...A | D - H...A |
| | O1 | --H1 | ..N31 | 0.88(3) | 1.98(3) | 2.786(4) | 152(2) |
| | O22 | --H22 | ..N38 | 0.94(3) | 1.98(3) | 2.842(4) | 152(3) |

# 3. **Thermogravimetric analysis**

## 3.1 TGA

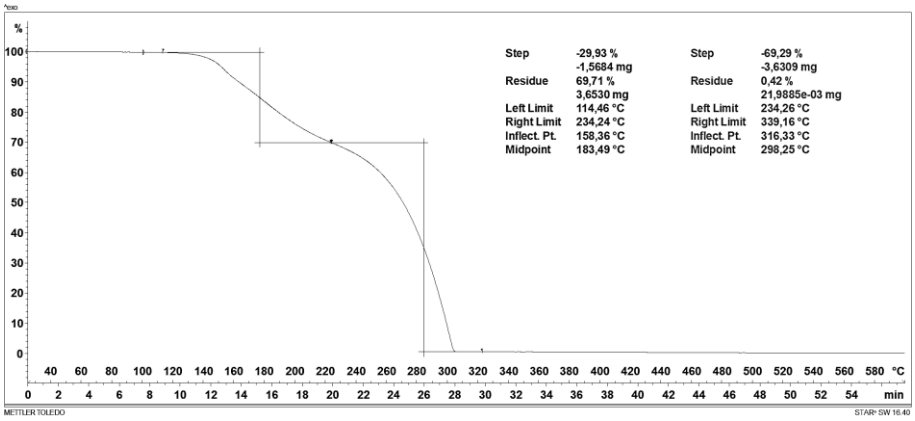


Figure SI-3.13. TGA of the *R-RR* (1:1) cocrystal, obtained by slurrying (*R*)-BINOL and (*R,R*)-DACH in a 1:1 ratio in MeOH. The thermogram is expressed as the weight loss (%) with respect to temperature. It shows two steps mass loss starting at 114°C, consisting in the degradation of the product.

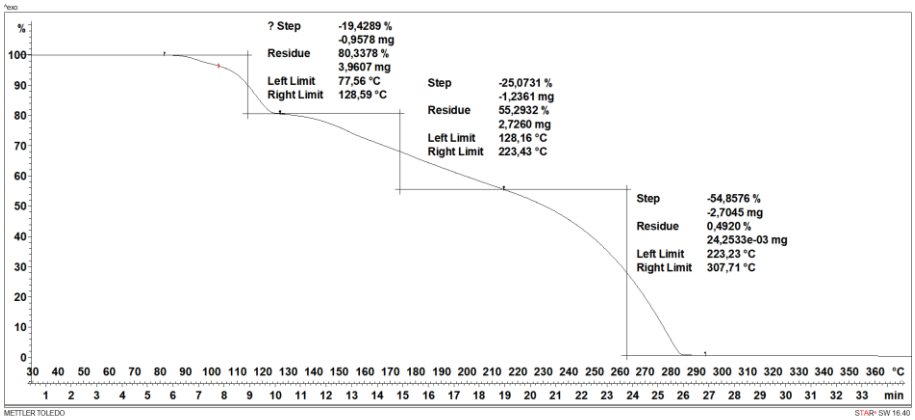


Figure SI-3.14. TGA of the *R-RR*-tolu (1:1:1) cocrystal-solvate, obtained by slurrying (*R*)-BINOL and (*R,R*)-DACH in a 1:1 ratio in toluene. The thermogram is expressed as the weight loss (%) with respect to temperature. It shows three steps in mass loss. The first one (starting at 78°C) consists in the drying of the powder and desolvation of toluene (loss of 1 equivalent of toluene), the second (starting at 128°C) and third (starting at 223°C) consist in the degradation of the *R-RR* compound.

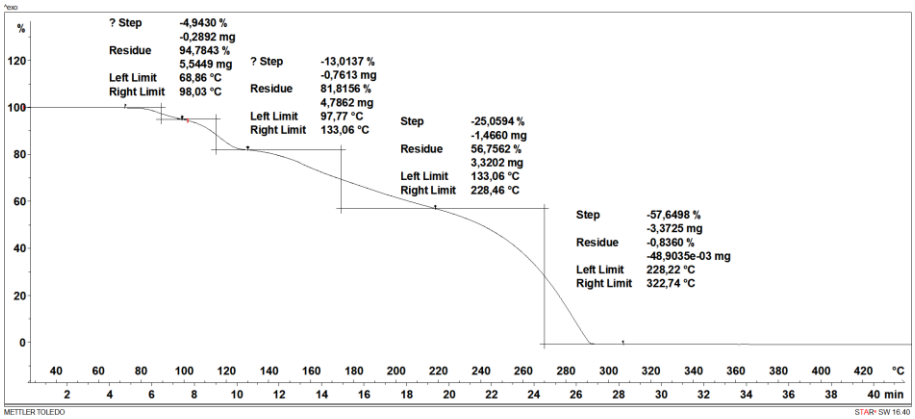


Figure SI-3.15. TGA of the *R-RR*-benz (1:1:1) cocrystal-solvate, obtained by slurrying (*R*)-BINOL and (*R,R*)-DACH in a 1:1 ratio in benzene. The thermogram is expressed as the weight loss (%) with respect to temperature. It shows four steps mass loss. The two first ones (starting at 69°C) consist in the desolvation of benzene (loss of 1.1 equivalent of benzene), the third (starting at 133°C) and fourth (starting at 228°C) consist in the degradation of the *R-RR* compound.

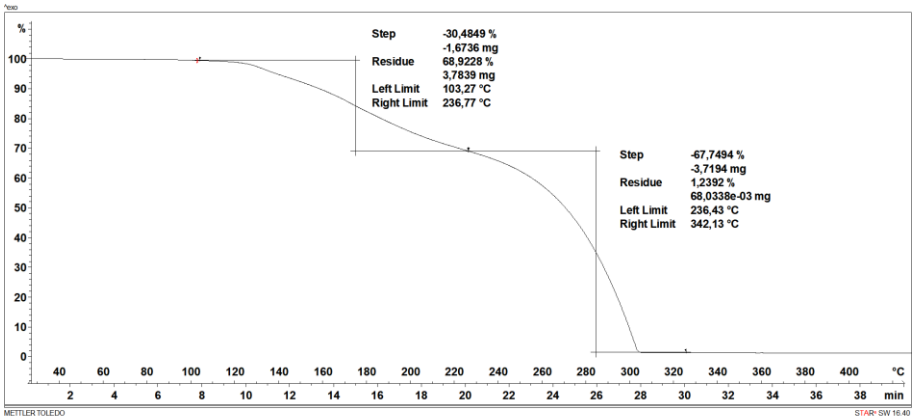


Figure SI-3.16**.** TGA of the *S-RR* (1:1) cocrystal, obtained by slurrying (*S*)-BINOL and (*R,R*)-DACH in a 1:1 ratio in EtOAc. The thermogram is expressed as the weight loss (%) with respect to temperature. It shows two steps mass loss starting at 64°C, consisting in the degradation of the product.

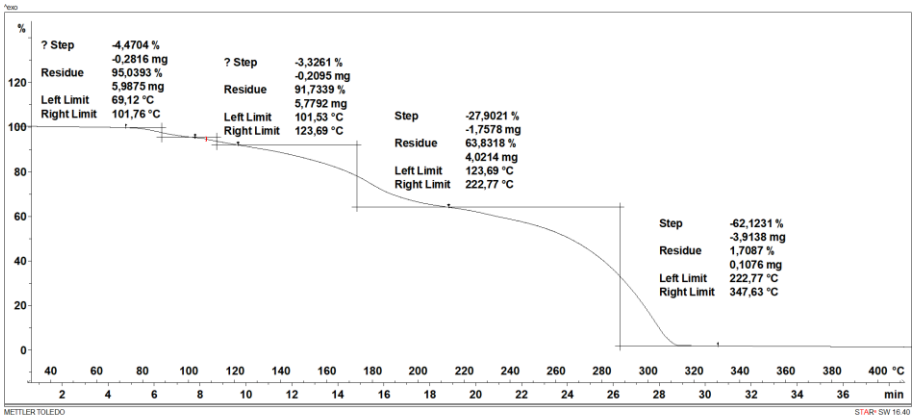


Figure SI-3.17. TGA of the *rac-RR*-MeOH (1:1:1) phase, obtained by slurrying (*rac*)-BINOL and (*R,R*)-DACH in a 1:1 ratio in MeOH. The thermogram is expressed as the weight loss (%) with respect to temperature. It shows four steps in mass loss. The two first ones (starting at 69°C) consist in the desolvation of methanol (loss of 1.1 equivalent of MeOH), the third (starting at 124°C) and fourth (starting at 223°C) consist in the degradation of the *rac-RR* compound.

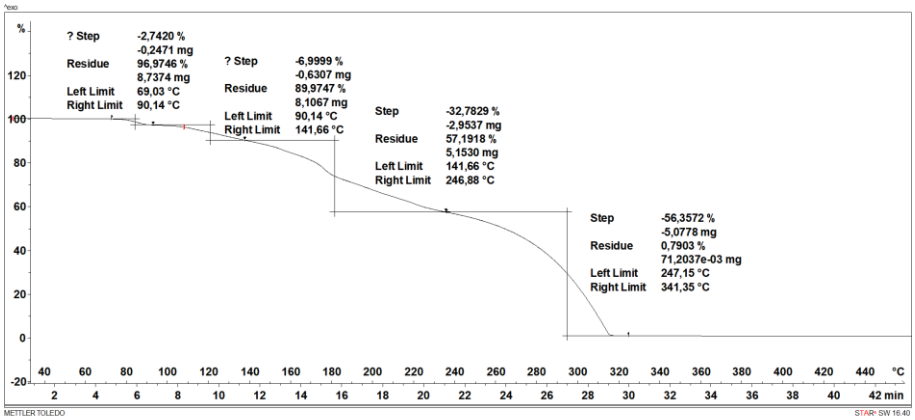


Figure SI-3.18**.** TGA of the 4*rac-4RR*-3EtOH-$H_2O$ (4:4:3:1) phase, obtained by slurrying (*rac*)-BINOL and (*R,R*)-DACH in a 1:1 ratio in EtOH. The thermogram is expressed as the weight loss (%) with respect to temperature. It shows four steps in mass loss. The two first ones (starting at 69°C) consist in the desolvation of ethanol and water, the third (starting at 142°C) and fourth (starting at 247°C) consist in the degradation of the *rac-RR* compound.

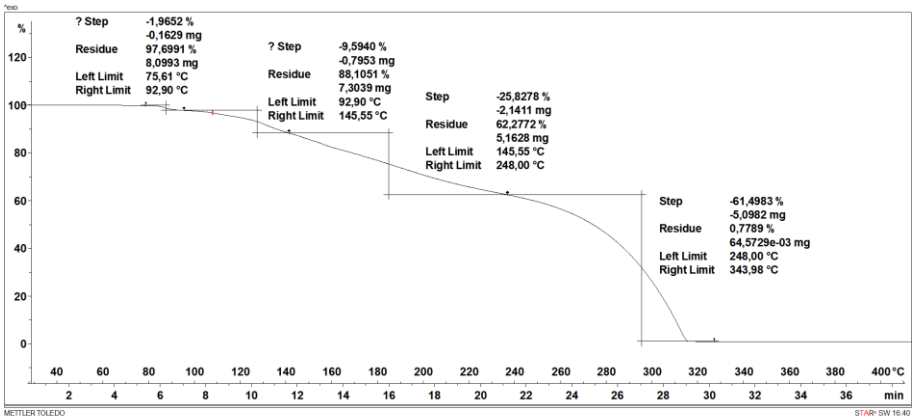


Figure SI-3.19**.** TGA of the new form, obtained by slurrying (*rac*)-BINOL and (*R,R*)-DACH in a 1:1 ratio in EtOAc. The thermogram is expressed as the weight loss (%) with respect to temperature. It shows four steps in mass loss. The two first ones (starting at 77°C) consist in the desolvation of ethyl acetate (loss of 0.6 equivalent of EtOAc), the third (starting at 170°C) and fourth (starting at 250°C) consist in the degradation of the *rac-RR* compound.

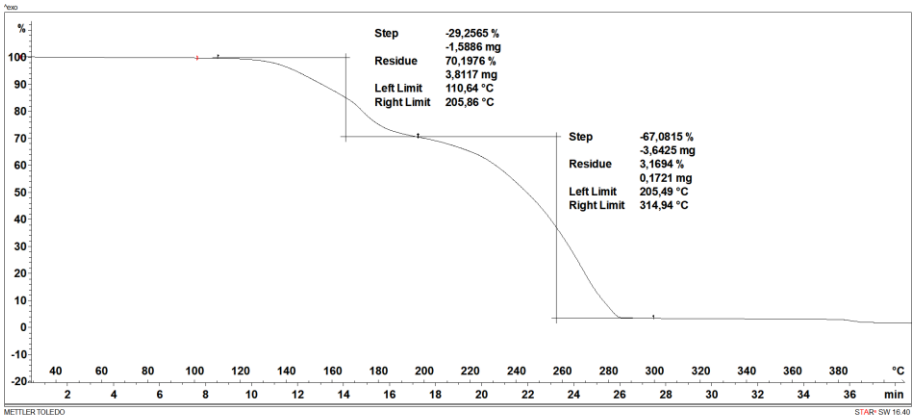


Figure SI-3.20**.** TGA of the newly crystal phase, obtained by slurrying (*rac*)-BINOL and (*rac*)-DACH in a 1:1 ratio in EtOAc. The thermogram is expressed as the weight loss (%) with respect to temperature. It shows two steps mass loss starting at 111°C, consisting in the degradation of the product.

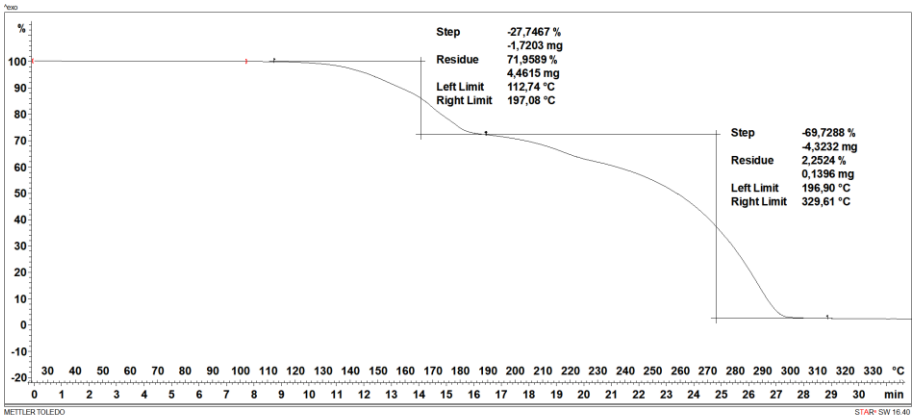


Figure SI-3.21**.** TGA of the *rac*-*rac* (1:1) phase, obtained by slurrying (*rac*)-BINOL and (*rac*)-DACH in a 1:1 ratio in ACN. The thermogram is expressed as the weight loss (%) with respect to temperature. It shows two steps mass loss starting at 113°C, consisting in the degradation of the product.

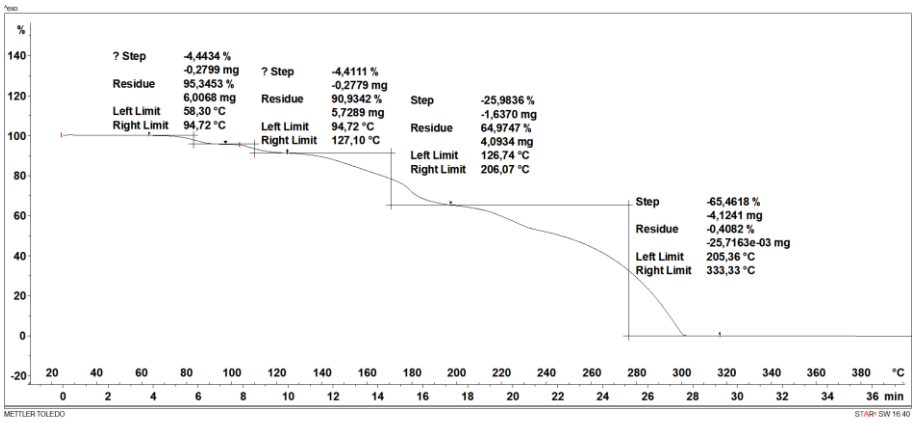


Figure SI-3.22**.** TGA of the *rac*-*rac*-MeOH (1:1:1) phase, obtained by slurrying (*rac*)-BINOL and (*rac*)-DACH in a 1:1 ratio in MeOH. The thermogram is expressed as the weight loss (%) with respect to temperature. It shows a four step mass loss. The two first ones (starting at 58°C) consist in the desolvation of methanol (loss of 1.2 equivalent of MeOH), the third (starting at 127°C) and fourth (starting at 205°C) consist in the degradation of the *rac*-*rac* compound.

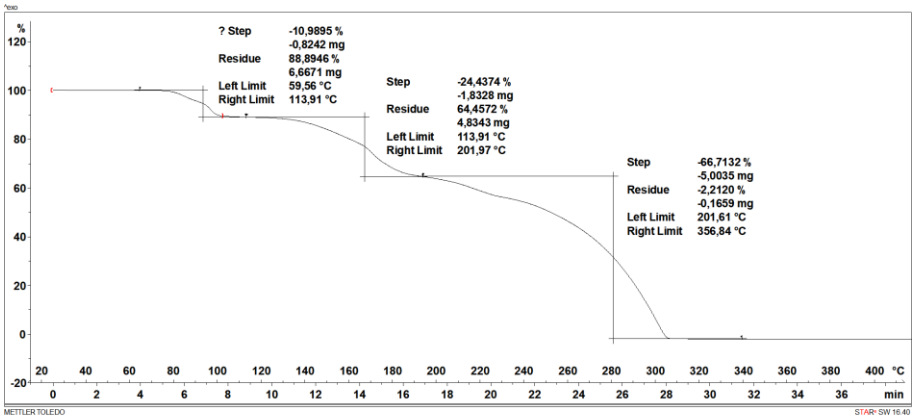


Figure SI-3.23**.** TGA of the newly crystal phase, obtained by slurrying (*rac*)-BINOL and (*rac*)-DACH in a 1:1 ratio in EtOH. The thermogram is expressed as the weight loss (%) with respect to temperature. It shows a three step mass loss. The first one (starting at 60°C) consists in the desolvation of ethanol (loss of 1 equivalent of EtOH), the second (starting at 114°C) and third (starting at 202°C) consist in the degradation of the *rac-rac* compound.

## 3.2 DSC

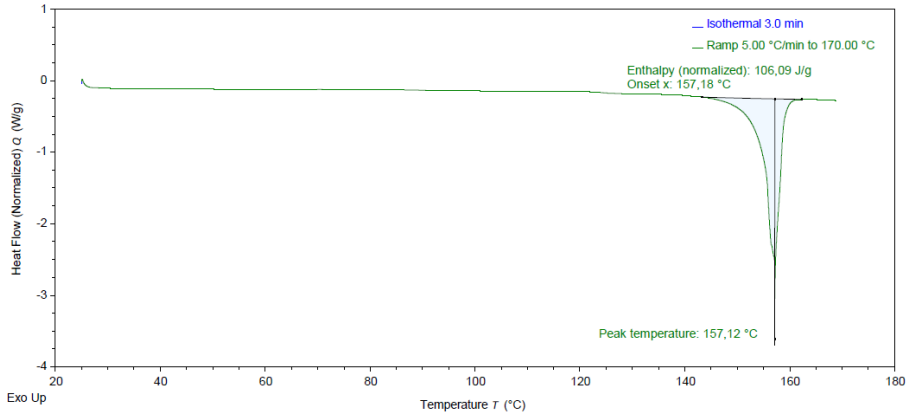


Figure SI-3.24**.** DSC of the *R-RR* (1:1) cocrystal, obtained by slurrying (*R*)BINOL and (*R,R*)-DACH in a 1:1 ratio in EtOH. The thermogram is expressed as the heat flow (Q) with respect to temperature. It shows one peak (157°C) consisting to the melting of the compound.

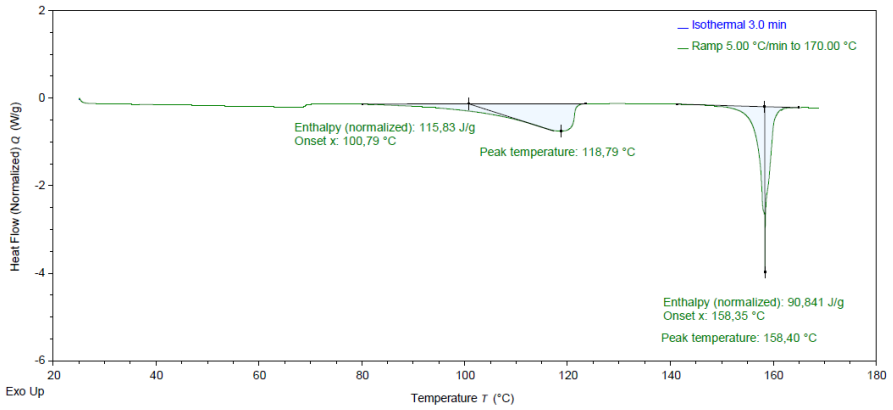


Figure SI-3.25**.** DSC of the *R-RR*-tolu (1:1:1) cocrystal-solvate, obtained by slurrying (*R*)BINOL and (*R,R*)-DACH in a 1:1 ratio in toluene. The thermogram is expressed as the heat flow (Q) with respect to temperature. It shows two peaks. The first one (with an onset of 101°C) corresponds to the desolvation of toluene, the second one (with an onset of 158°C) consists in the melting of the *R-RR* compound.

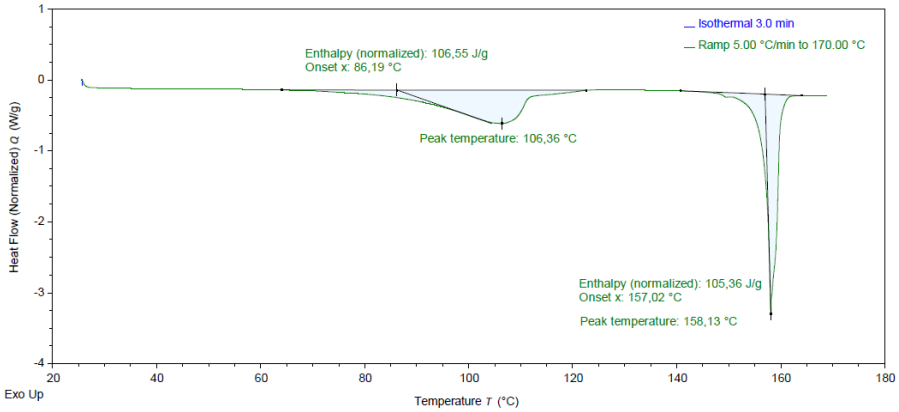


Figure SI-3.26**.** DSC of the *R-RR*-benz (1:1:1) cocrystal-solvate, obtained by slurrying (*R*)BINOL and (*R,R*)-DACH in a 1:1 ratio in benzene. The thermogram is expressed as the heat flow (Q) with respect to temperature. It shows two peaks. The first one (with an onset of 86°C) corresponds to the desolvation of benzene, the second one (with an onset of 158°C) consists in the melting of the *R-RR* compound.

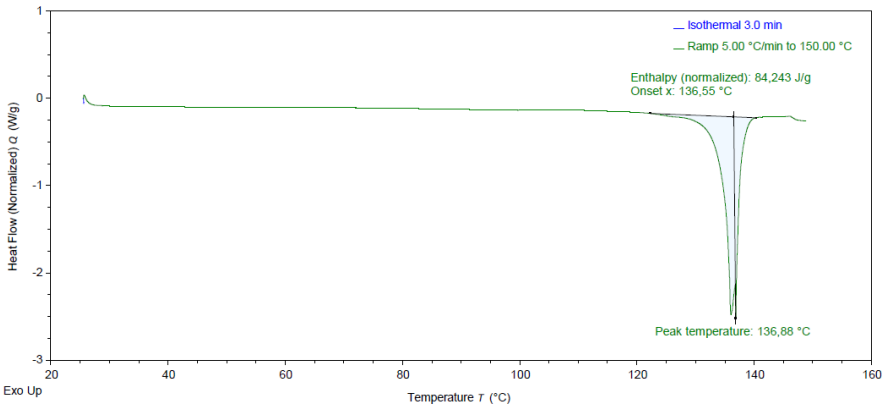


Figure SI-3.27**.** DSC of the *S*-*RR* (1:1) cocrystal, obtained by slurrying (*S*)-BINOL and (*R*,*R*)-DACH in a 1:1 ratio in EtOAc. The thermogram is expressed as the heat flow (Q) with respect to temperature. It shows one peak (with an onset of 137°C) consisting to the melting of the compound.

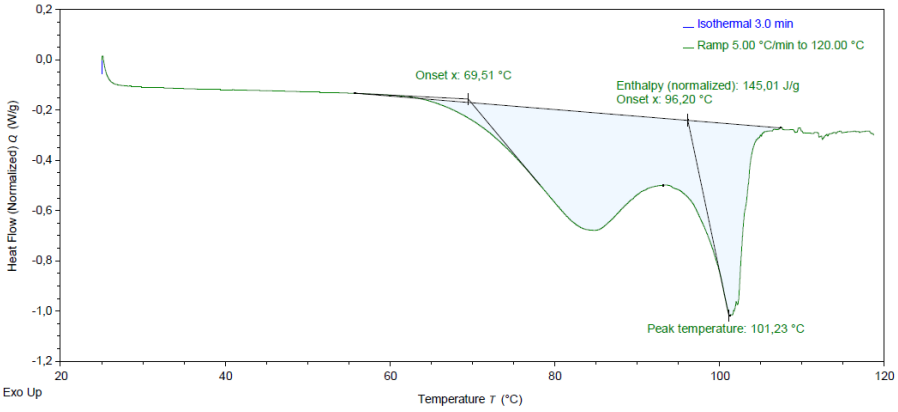


Figure SI-3.28**.** DSC of the *rac*-*RR*-MeOH material, obtained by slurrying (*rac*)-BINOL and (*R*,*R*)-DACH in a 1:1 ratio in MeOH. The thermogram is expressed as the heat flow (Q) with respect to temperature. It shows two peaks (with onsets of respectively 70°C and 96°C), the first one consists of the desolvation of methanol and the second consists of the melting of the *rac*-*RR* compound.

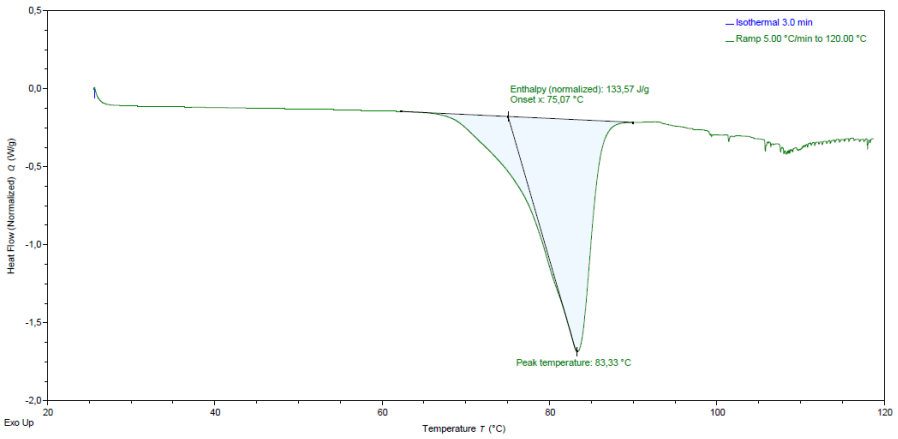


Figure SI-3.29**.** DSC of the 4*rac*-4*RR*-3EtOH-$H_2O$ material, obtained by slurrying (*rac*)-BINOL and (*R*,*R*)-DACH in a 1:1 ratio in EtOH. The thermogram is expressed as the heat flow (Q) with respect to temperature. It shows one shouldered peak (with an onset of 75°C), consisting of the desolvation and melting of the compound, before its degradation.

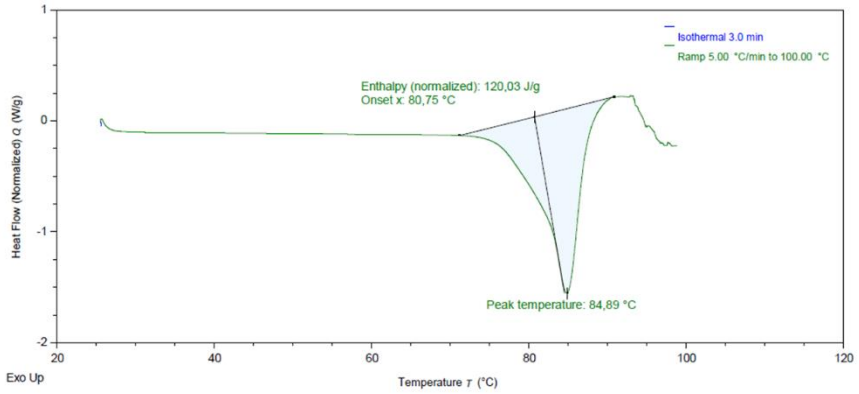


Figure SI-3.30**.** DSC of the material obtained by slurrying (*rac*)-BINOL and (*R*,*R*)-DACH in a 1:1 ratio in EtOAc. The thermogram is expressed as the heat flow (Q) with respect to temperature. It shows one shouldered peak (with an onset of 81°C), consisting of the desolvation and melting of the compound, before its degradation.

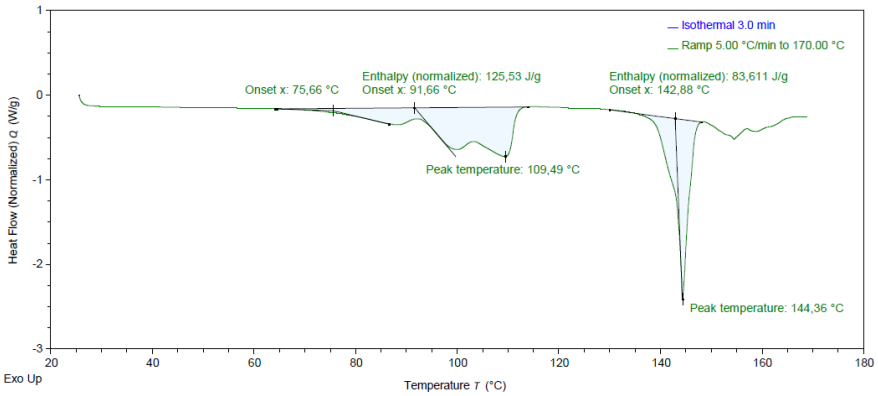


Figure SI-3.31. DSC of the material obtained by slurrying (*rac*)-BINOL and (*rac*)-DACH in a 1:1 ratio in toluene. The thermogram is expressed as the heat flow (Q) with respect to temperature. It shows three shouldered peaks (with an onset of 76°C), consisting of the drying and desolvation of the compound, before its melting (characterized by a peak with an onset of 143°C) and its degradation.

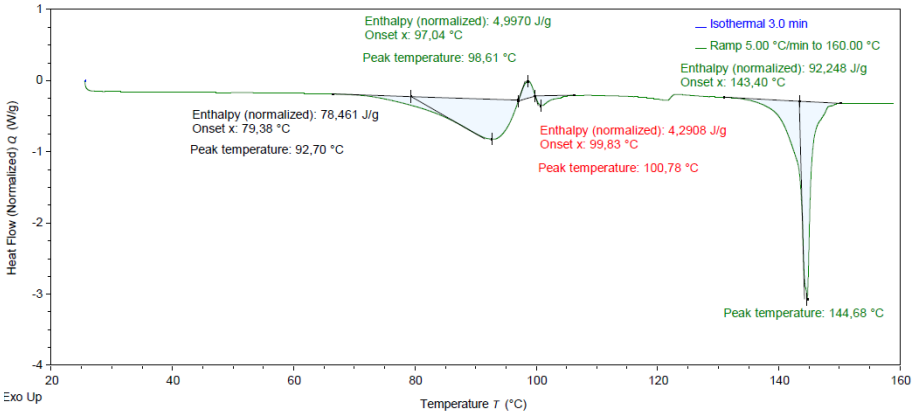


Figure SI-3.32. DSC of the material obtained by slurrying (*rac*)-BINOL and (*rac*)-DACH in a 1:1 ratio in benzene. The thermogram is expressed as the heat flow (Q) with respect to temperature. It shows different events. The first peak (with an onset of 79°C) corresponds to the desolvation of benzene, the second one (exothermic and with an onset of 97°C) consists in the recrystallization of the recovered compound, followed by an endothermic peak (with an onset of 100°C). Finally, the recovered compound melts (characterized by a peak with an onset of 143°C).

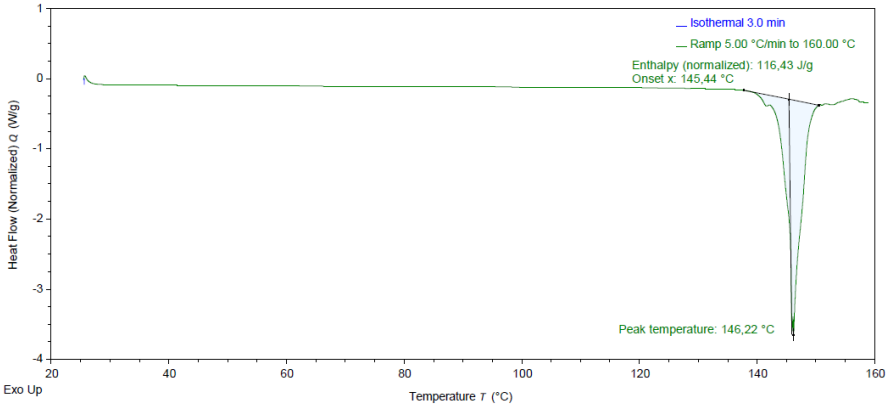


Figure SI-3.33**.** DSC of the material obtained by slurrying (*rac*)-BINOL and (*rac*)-DACH in a 1:1 ratio in EtOAc. The thermogram is expressed as the heat flow (Q) with respect to temperature. It shows one peak (with an onset of 145°C) consisting of the melting of the compound.

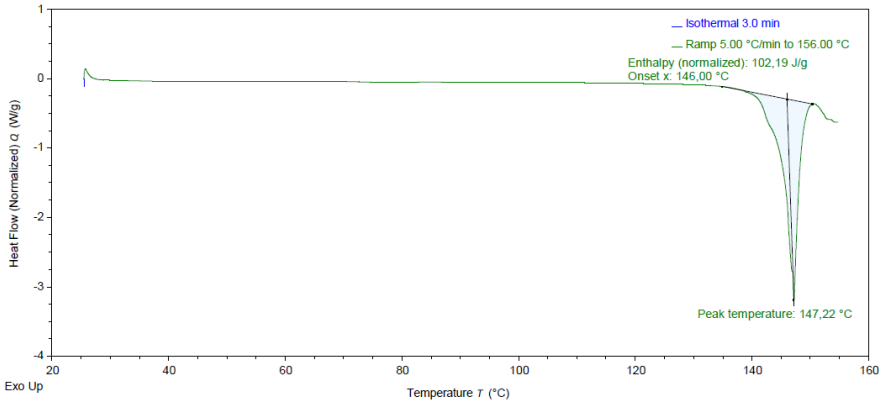


Figure SI-3.34**.** DSC of the *rac*-*rac* cocrystal obtained by slurrying (*rac*)-BINOL and (*rac*)-DACH in a 1:1 ratio in ACN. The thermogram is expressed as the heat flow (Q) with respect to temperature. It shows one peak (with an onset of 146°C) consisting of the melting of the compound.

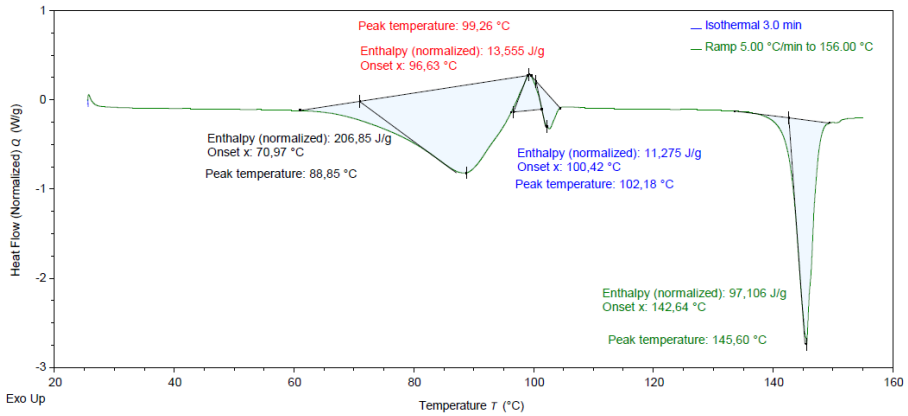


Figure SI-3.35**.** DSC of the *rac*-*rac*-MeOH compound obtained by slurrying (*rac*)-BINOL and (*rac*)-DACH in a 1:1 ratio in MeOH. The thermogram is expressed as the heat flow (Q) with respect to temperature. It shows different events. The first peak (with an onset of 71°C) corresponds to the desolvation of methanol, the second one (exothermic and with an onset of 97°C) consists in the recrystallization of the recovered compound, followed by an endothermic peak (with an onset of 102°C). Finally, the *rac*-*rac* compound melts (characterized by a peak with an onset of 143°C).

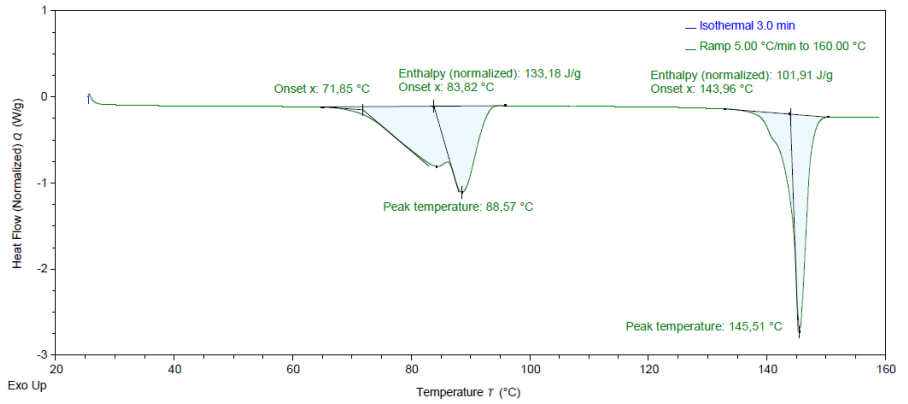


Figure SI-**3.**36**.** DSC of the material obtained by slurrying (*rac*)-BINOL and (*rac*)-DACH in a 1:1 ratio in EtOH. The thermogram is expressed as the heat flow (Q) with respect to temperature. It shows two shouldered peaks (with an onset of 72°C), consisting of the desolvation of ethanol, followed by an endothermic peak (with an onset of 144°C) consisting in the melting of the *rac*-*rac* compound.

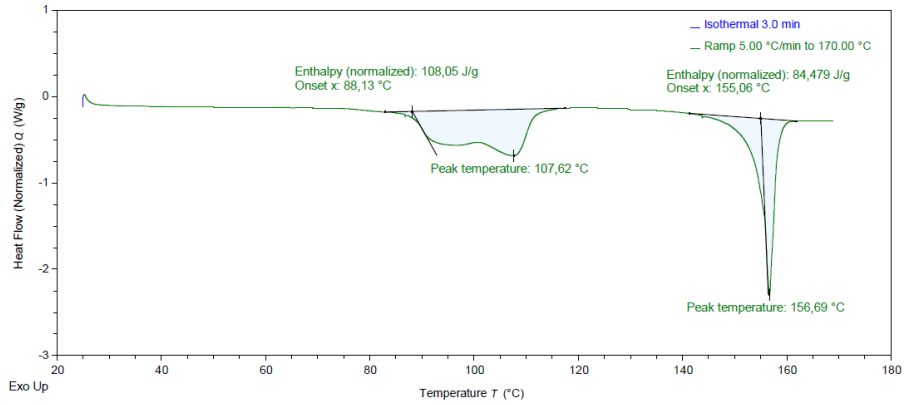


Figure SI-3.37. DSC of the *R-RR*-tolu compound obtained by slurrying (*R*)-BINOL and (*rac*)-DACH in a 1:1 ratio in toluene. The thermogram is expressed as the heat flow (Q) with respect to temperature. It shows two shouldered peaks (with an onset of 88°C), consisting of the desolvation of the toluene, followed by an endothermic peak (with an onset of 155°C) consisting in the melting of the *R-RR* compound.

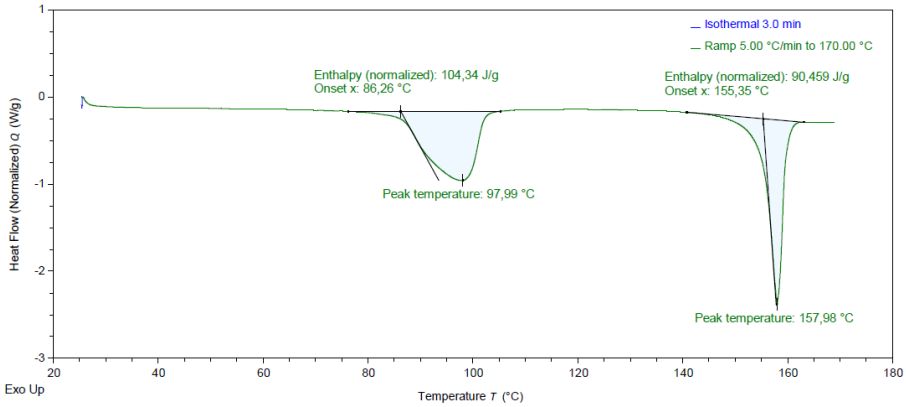


Figure SI-3.38. DSC of the *R-RR*-benz compound obtained by slurrying (*R*)-BINOL and (*rac*)-DACH in a 1:1 ratio in benzene. The thermogram is expressed as the heat flow (Q) with respect to temperature. It shows one broad peak (with an onset of 86°C), consisting of the desolvation of the benzene, followed by an endothermic peak (with an onset of 155°C) consisting in the melting of the *R-RR* compound.

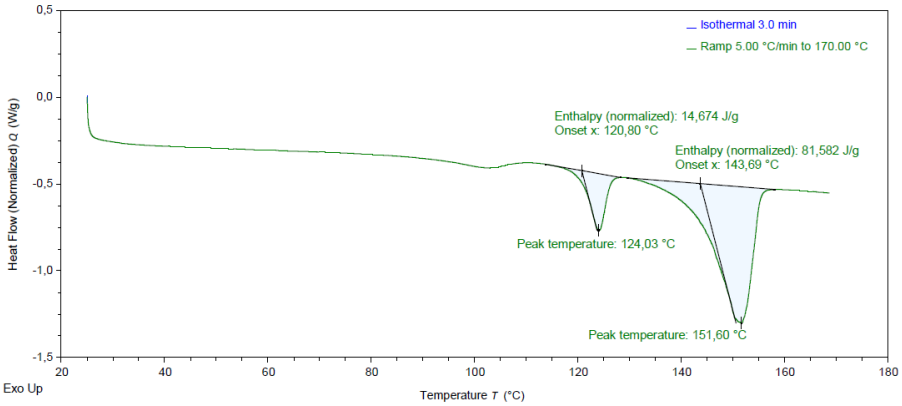


Figure SI-3.39. DSC of the compound obtained by slurrying (*R*)-BINOL and (*rac*)-DACH in a 1:1 ratio in EtOAc. The thermogram is expressed as the heat flow (Q) with respect to temperature. It shows two melting peaks (with onsets of respectively 121°C and 144°C), characteristic of solid solution formation.

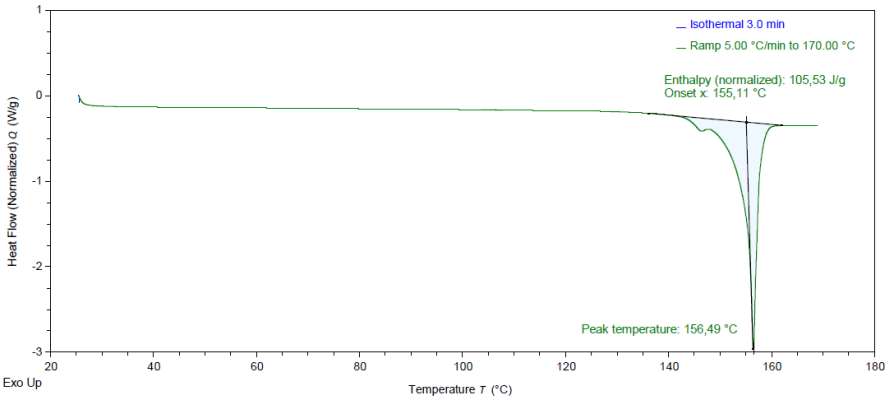


Figure SI-3.40. DSC of the *R-RR* compound obtained by slurrying (*R*)-BINOL and (*rac*)-DACH in a 1:1 ratio in ACN. The thermogram is expressed as the heat flow (Q) with respect to temperature. It shows one peak (with an onset of 155°C), consisting in the melting of the *R-RR* compound.

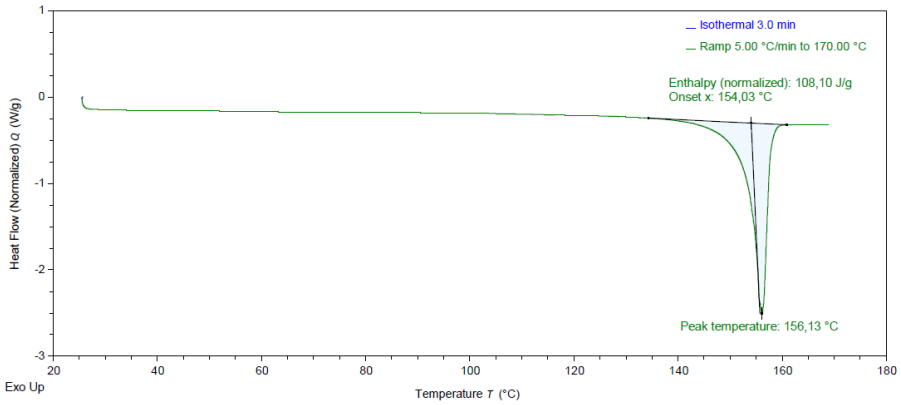


Figure SI-3.41. DSC of the *R-RR* compound obtained by slurrying (*R*)-BINOL and (*rac*)-DACH in a 1:1 ratio in MeOH. The thermogram is expressed as the heat flow (Q) with respect to temperature. It shows one peak (with an onset of 155°C), consisting in the melting of the *R-RR* compound.

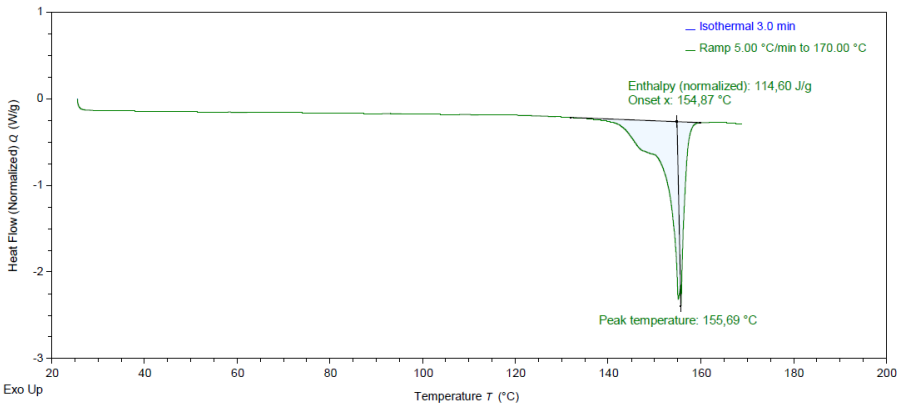


Figure SI-3.42. DSC of the *R-RR* compound obtained by slurrying (*R*)-BINOL and (*rac*)-DACH in a 1:1 ratio in EtOH. The thermogram is expressed as the heat flow (Q) with respect to temperature. It shows one peak (with an onset of 155°C), consisting in the melting of the *R-RR* compound.

## 4. NMR

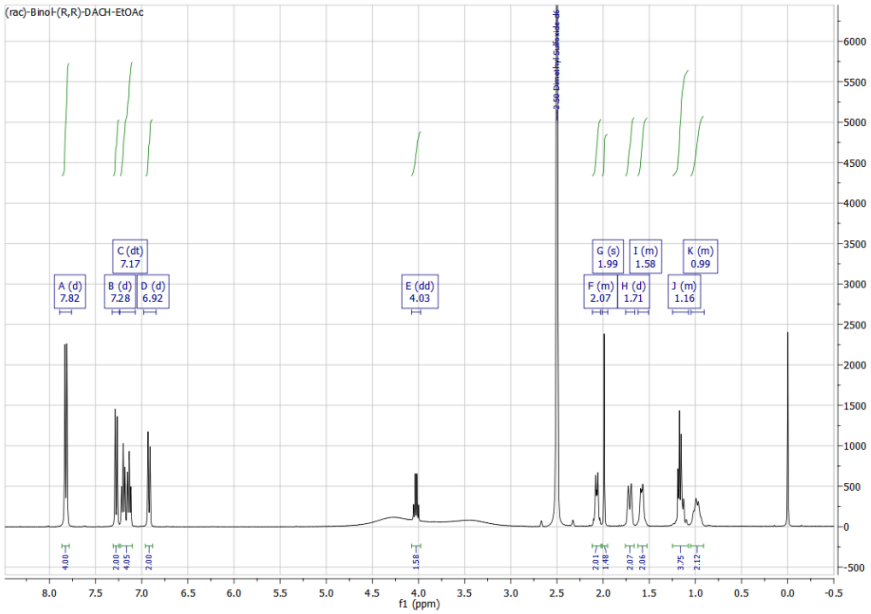


Figure SI-3.43**.** $^{1}$H NRM of the newly crystal phase, obtained by slurrying (*rac*)-BINOL and (*R,R*)-DACH in a 1:1 ratio in EtOAc. The analysis shows a phase composed composed by 1 equivalent of BINOL, 1 equivalent of DACH and 0.5 equivalent of EtOAc.

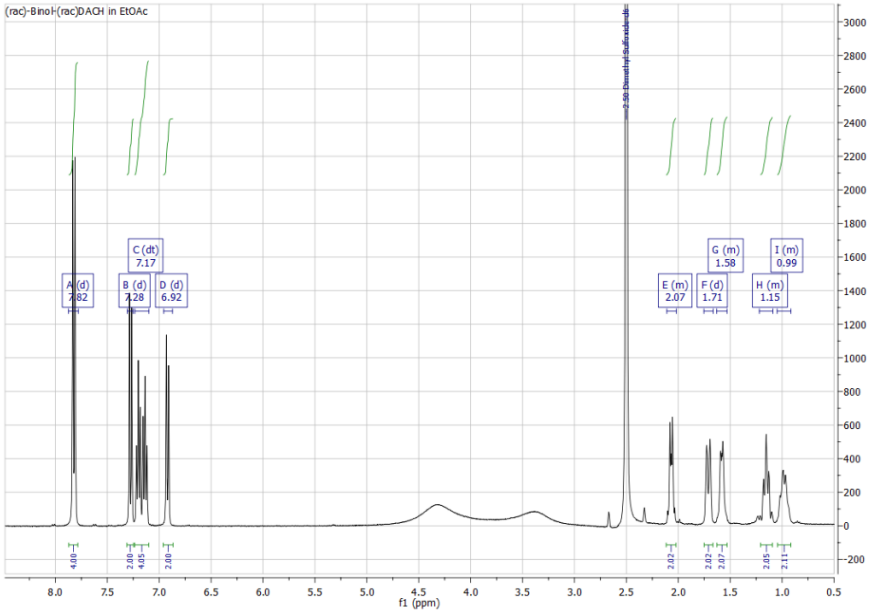


Figure SI-3.44**.** $^{1}$H NRM of the newly crystal phase, obtained by slurrying (*rac*)-BINOL and (*rac*)-DACH in a 1:1 ratio in EtOAc. The analysis shows a phase composed composed by 1 equivalent of BINOL and 1 equivalent of DACH.

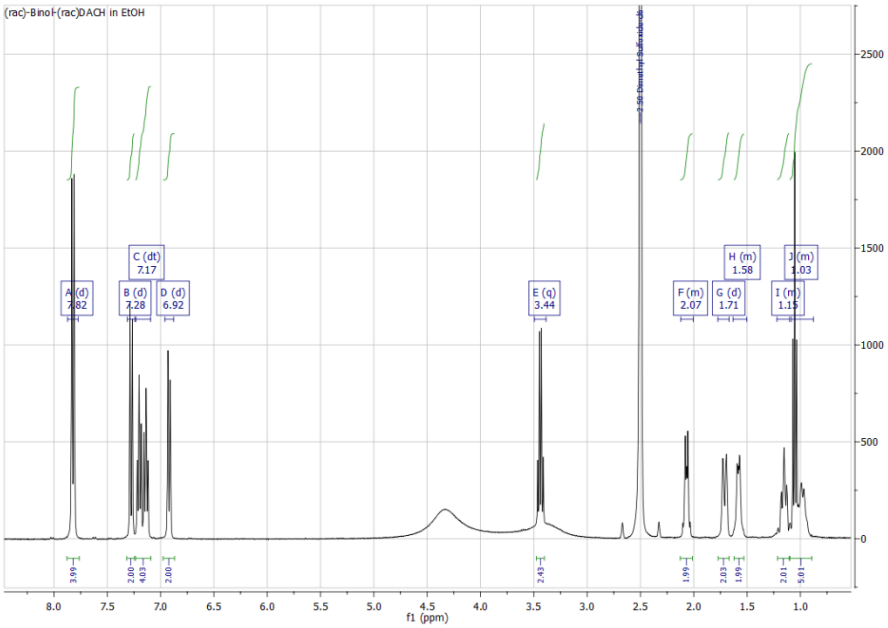


Figure SI-**3**.45**.** $^{1}$H NRM of the newly crystal phase, obtained by slurrying (*rac*)-BINOL and (*rac*)-DACH in a 1:1 ratio in EtOH. The analysis shows a phase composed composed by 1 equivalent of BINOL, 1 equivalent of DACH and 1 equivalent of EtOH.

## 5. cHPLC

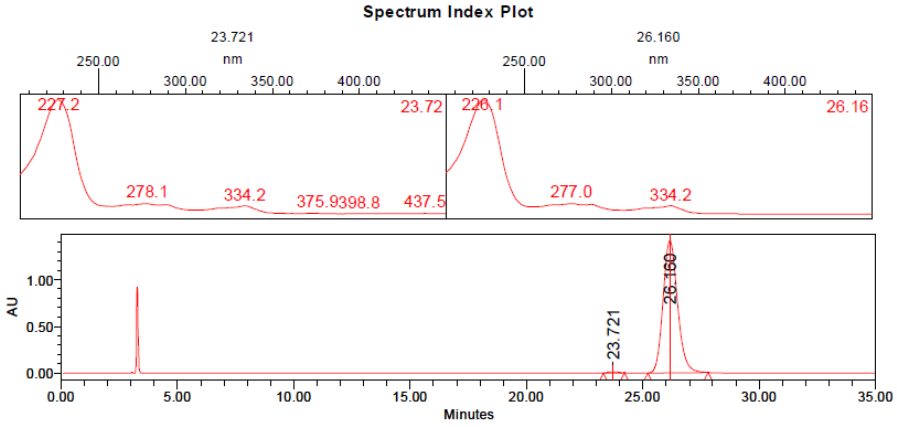


Peak Results

| | Name | RT | Area | % Area |
|---|---|---|---|---|
| 1 | | 23.721 | 357263 | 0.58 |
| 2 | | 26.160 | 61341134 | 99.42 |

Figure SI-3.46. *c*HPLC analysis of the powder recovered from the resolution of (rac)-BINOL by (R,R)-DACH in toluene. The first peak corresponds to (*S*)-Binol and the second to (*R*)-Binol.

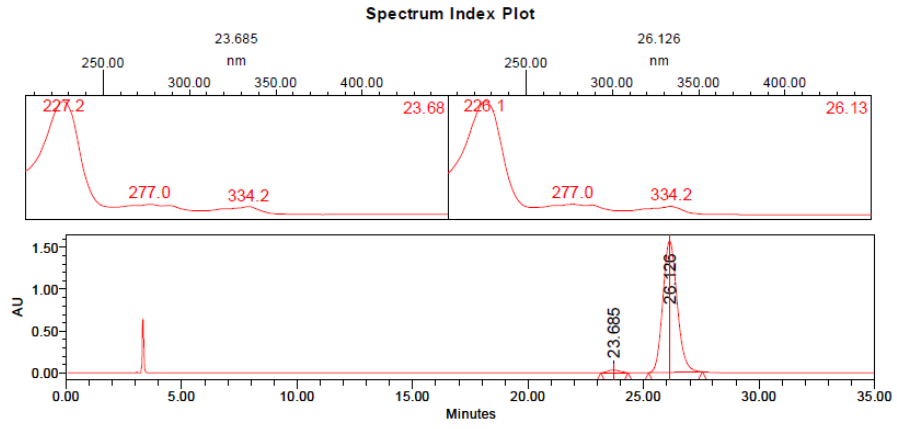


Peak Results

| | Name | RT | Area | % Area |
|---|---|---|---|---|
| 1 | | 23.685 | 1133910 | 1.64 |
| 2 | | 26.126 | 67811586 | 98.36 |

Figure SI-3.47. *c*HPLC analysis of the powder recovered from the resolution of (rac)-BINOL by (R,R)-DACH in benzene. The first peak corresponds to (*S*)-Binol and the second to (*R*)-Binol.

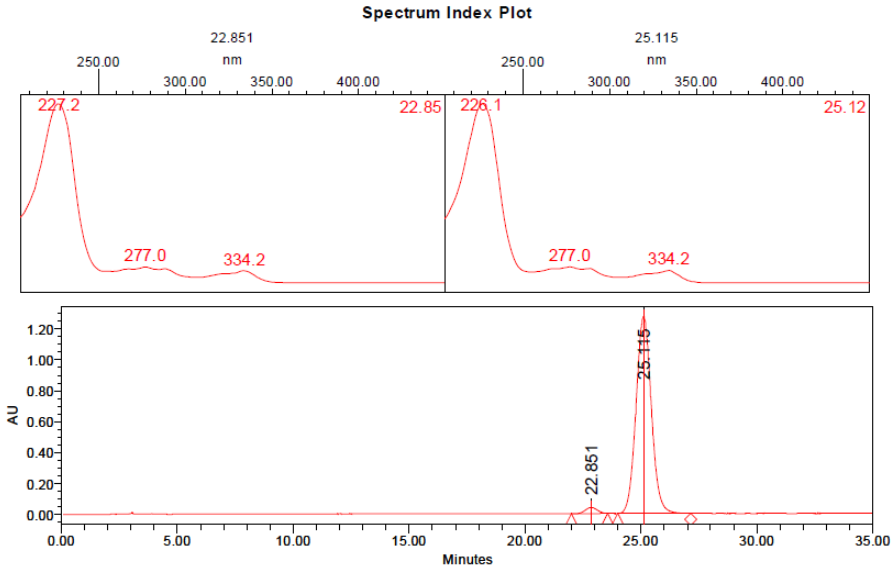


Peak Results

| | Name | RT | Area | % Area |
|---|---|---|---|---|
| 1 | | 22.851 | 1348056 | 2.28 |
| 2 | | 25.115 | 57898025 | 97.72 |

Figure SI-3.48. *c*HPLC analysis of the powder recovered from the resolution of (rac)-BINOL by (R,R)-DACH in ACN. The first peak corresponds to (*S*)-Binol and the second to (*R*)-Binol.

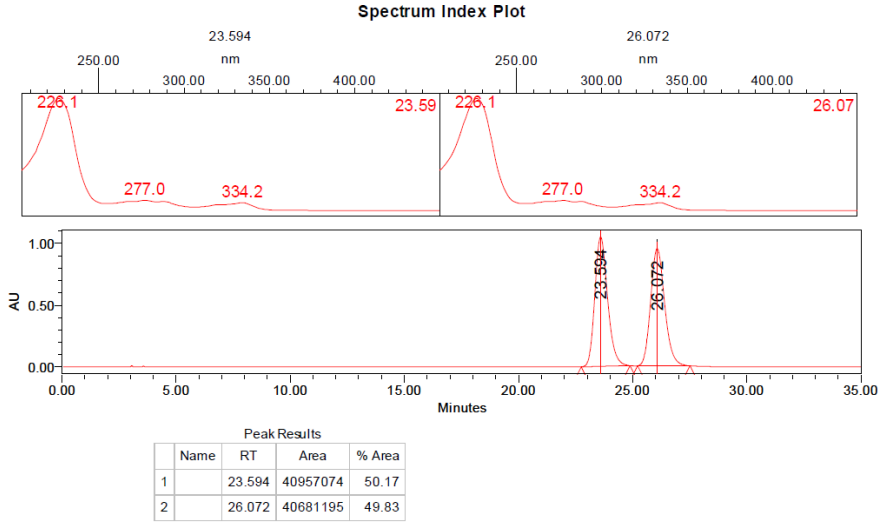


Peak Results

| | Name | RT | Area | % Area |
|---|---|---|---|---|
| 1 | | 23.594 | 40957074 | 50.17 |
| 2 | | 26.072 | 40681195 | 49.83 |

Figure SI-3.49. *c*HPLC analysis of the newly crystal phase, obtained by slurrying (*rac*)-BINOL and (*rac*)-DACH in a 1:1 ratio in EtOAc. The first peak corresponds to (*S*)-Binol and the second to (*R*)-Binol.

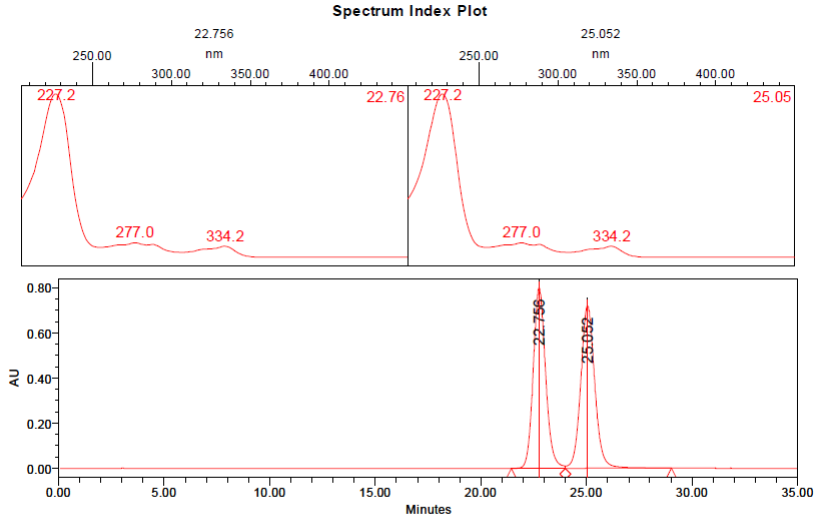


Peak Results

| | Name | RT | Area | % Area |
|---|---|---|---|---|
| 1 | | 22.756 | 32312864 | 49.48 |
| 2 | | 25.052 | 32998280 | 50.52 |

Figure SI-3.50. *c*HPLC analysis of the newly crystal phase, obtained by slurrying (*rac*)-BINOL and (*R*,*R*)-DACH in a 1:1 ratio in EtOAc. The first peak corresponds to (*S*)-Binol and the second to (*R*)-Binol.

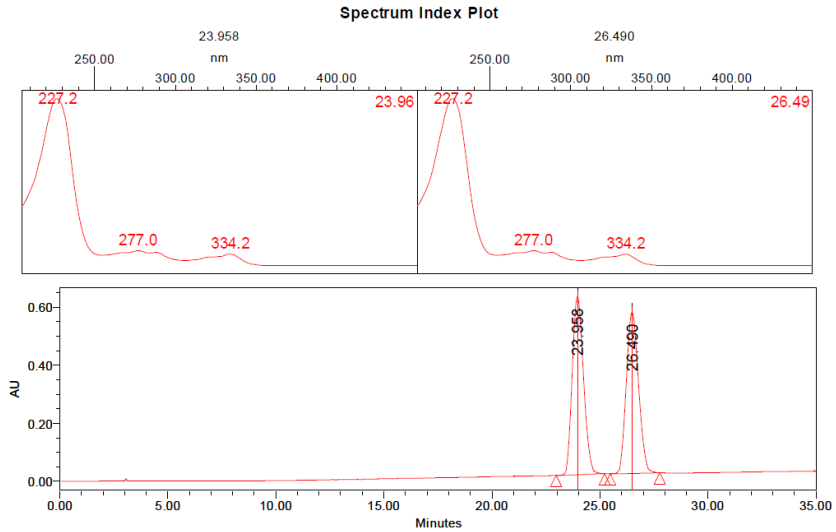


Peak Results

| | Name | RT | Area | % Area |
|---|---|---|---|---|
| 1 | | 23.958 | 22488158 | 50.45 |
| 2 | | 26.490 | 22085534 | 49.55 |

Figure SI-3.51. *c*HPLC analysis of the newly crystal phase, obtained by slurrying (*rac*)-BINOL and (*rac*)-DACH in a 1:1 ratio in EtOH. The first peak corresponds to (*S*)-Binol and the second to (*R*)-Binol.

# Appendixe B

Supporting information to Chapter 4

## 1. Experimental Procedures

### 1.1 Materials

(*S*)-1,1'-bi-2-naphtol (Merck), (*R*)-1,1'-bi-2-naphtol (Fluorochem), (*rac*)-1,1'-bi-2-naphtol (Acros Organics), (*1R, 2R)-N,N′*-Dimethyl-1,2-diphenylethane-1,2-diamine, toluene (VWR chemicals) and benzene (TCI) were purchased from commercial sources and used without further purification.

For convenience, 1,1'-bi-2-naphtol will be abbreviated as BINOL, and N,N′-Dimethyl-1,2-diphenylethane-1,2-diamine as DADPE in the rest of the document.

### 1.2 Slurries

Slurry experiments were performed preparing equimolar suspensions (0.2 mmol) of (*S*)- or (*R*)-BINOL with (*R,R*)-DADPE at 20°C in methanol (MeOH) (0.2 mL), ethanol (EtOH) (1 mL), ethyl acetate (EtOAc) (0.5 mL), dichloromethane (DCM) (0.2 mL), toluene (1 mL), isopropyl alcohol (IPA) (1 mL) and benzene (1 mL). The suspensions were stirred in a Cooling thermomixer HLC at 500 rpm. After 1 day of stirring, the vials were seeded with all possible solid forms, then let to equilibrate for 7 days. The suspensions were then filtered, the powders washed, dried and analyzed using PXRD.

Slurries of (*S*)-BINOL with (*R,R*)-DADPE in the different solvents showed the same diffraction pattern as the reported cocrystal (*S*)-(*R,R*) (CCDC ref code **DICVUH**)[102]. Slurries of (*R*)BINOL with (*R,R*)-DADPE in all solvents except benzene showed the same diffraction pattern as the cocrystal (*R)-(R,R*). Slurry of (*R*)-BINOL with (*R,R*)-DADPE in benzene showed the same diffraction pattern as the cocrystal-solvate (*R*)-(*R,R*)-benzene.

### 1.3 Single crystal formation

#### *1.3.1 (R)-(R,R) cocrystal*

Single crystals of the *(R)-(R,R)* cocrystal were obtained by slow evaporation from toluene, starting from an undersaturated equimolar solution of (*R*)-BINOL and (*R,R*)-DADPE. The solution was left to evaporate slowly at RT. Once crystals formed, a suitable crystal was retrieved and analyzed by SC-XRD

### *1.3.2 (R)-(R,R)-benzene cocrystal solvate*

Single crystals of the *(R)-(R,R)*-benzene cocrystal-solvate were obtained by slow evaporation from benzene, starting from an undersaturated equimolar solution of (*R*)-BINOL and (*R,R*)-DADPE. The solution was left to evaporate slowly at RT. Once crystals formed, a suitable crystal was retrieved and analyzed by SC-XRD.

## 1.4 Solubility determination

The solubility curves were determined using a Crystal16 - Technobis Crystallization System. Different masses of *(S)-(R,R)* or *(R)-(R,R)* were weighed in vials, to which were added a magnetic stirrer and 0.8 mL of solvent. The following temperature profile was then applied:

- From 20°C to 0°C at -0.5°C/min,
- Hold at 0°C for 2 hours,
- Heat to *"desired temperature"* at 0.05°C/min,
- Hold at *"desired temperature"* for 2 hours,
- Cool to 0°C at 0.2°C/min.

For determining the *(R)-(R,R)*-benzene solubility curve, the *(R)-(R,R)* cocrystal was weighed and benzene was added. The mixtures were then let to equilibrate for 48 hours at 20°C under stirring before being placed in the Crystal16.

## 1.5 Ternary phase Diagrams

Slurries of (*rac*)-BINOL with (*R,R*)-DADPE in benzene or toluene were made, seeded after 1 day with all possible solid forms, then stirred for 4 more days at 20°C. After that, the mixtures were filtered and the powders were analyzed by PXRD to determine the solid phase obtained in suspension. When needed, supplementary experiments (NMR and *c*HPLC) were made on the powder to determine the exact nature of the phases.

## 1.6 Upscaled resolutions of BINOL

### *1.6.1 In toluene*

(*rac*)-BINOL (2 g, 6.9852 mmol) and (*R,R*)-DADPE (2.96140 g, 13.9498 mmol) were suspended in toluene (71 mL) in a round bottom flask (100 mL) with a stirring bar. The suspension was seeded with all possible solid forms, then stirred at 20°C at 500rpm for 5 days. The mixture was then filtered and the powder was washed with toluene. The powder (0.60013 g) was analyzed by PXRD and *c*HPLC.

### *1.6.2 In benzene*

(*rac*)-BINOL (2 g, 6.9852 mmol) and (*R,R*)-DADPE (1.93599 g, 9.1195 mmol) were suspended in benzene (46 mL) in a round bottom flask (100 mL) with a stirring bar. The suspension was seeded with all possible solid forms, then stirred at 20°C at 500rpm for 4 days. The mixture was then filtered and the powder was washed with benzene. The powder (0.96503 g) was analyzed by PXRD and *c*HPLC.

## 1.7 Powder X-ray diffraction (PXRD)

PXRD data were collected using a Siemens D5000 diffractometer equipped with a Cu X-ray source operating at 40 kV and 40 mA. A secondary monochromator was used to select the Kα radiation of Cu (λ = 1.5418 Å). A scanning range of 2θ values was applied from 5° to 35°.

## 1.8 Single crystal X-ray diffraction (SC-XRD)

SC-XRD data were collected using a MAR345 image plate detector with Mo Kα radiation (λ = 0.71073 Å), generated by an Incoatec IμS microfocus source. The collected data was integrated and reduced using CrystAlis$^{PRO}$ [103] and the implemented absorption correction was applied. Structure solution was achieved using the dual-space algorithm in SHELXT[104] and the structure was further refined against $F^2$ by SHELXL[105]. All non-hydrogen atoms were refined anisotropically. Symmetry analysis and validation were carried out using PLATON[106]. Figures were generated using the molecular visualization software Mercury 2022.3.0.[107]

*(R)-(R,R)* was measured at room temperature. One phenyl ring was found disordered and refined in two parts to a ratio of 58/42. Similarity restrains are set up between both disordered rings as well as isotropic and rigid bond restraints on the thermal ellipsoids of the disordered parts.

For *(R)-(R,R)*-benzene crystals were transferred to Paratone® N oil to prevent evaporation of benzene. A single crystal was picked up on a nylon loop and quickly flash-frozen in a $N_2$ gas stream at 150 K as tests at room temperature gave only poor diffraction ~2Å. Despite the low-temperature measurement only limited diffraction was observed and ultimately the diffraction limit was set to 1.1 Å during integration, beyond which only poor diffraction was observed.

Both (*R*)-BINOL and (*R,R*)-DADPE are found on a 2-fold crystallographic axis. The benzene molecule that is located inside the pocket surrounded by aromatic rings (Figure 2, in blue) is found close to a 2-fold axis and its occupancy was consequently constraint at 50% (the benzene molecule thus occupies a solvent pocket that is larger than the molecule itself and only loosely interacts with its surroundings). The second benzene molecule that is found in the solvent channel (Figure 4.5, in green) only partially occupies the site and its occupancy was refined to 87%. Possibly the solvent channel contains additional benzene molecules while still in solution (see TGA analysis) but these evaporate the moment the crystal is harvested from the crystallization solution as well as some of the benzene molecules that were located in the solvent channel (Figure 4.5, in green) hence the lower occupancy observed.

The solvent channels with disordered solvent were treated by the SQUEEZE procedure (PLATON[142]) to account for the diffuse electron density (a total of 102 electros were located in the solvent accessible volume of 597 $Å^3$).

Both the (*R*)-BINOL and (*R,R*)-DADPE molecules show disorder. (*R*)-BINOL is completely disordered, for DADPE the phenyl rings are found disordered. Both were refined in 2 parts (72/28) for (R)-BINOL, (63/27) for the phenyl rings of (*R,R*)-DADPE. Both disordered parts were refined to be geometrically similar. For the minor disordered part of the (*R*)-BINOL the thermal ellipsoid were constraint to be identical to the major part. Overall mild isotropic and rigid bond restraints were applied to all carbon atoms and more stringent ones to the disordered

parts of (*R*,*R*)-DADPE. The $NH_2$ group of (*R*,*R*)-DADPE was restraint as an non planar group with geometric restraints on the geometry of the $NH_2$ group and the CNH angle, but no rotational restraints/constraints were set up for this $NH_2$ group.

See point 2 in the Results and Discussion here below for the crystallographic data and refinement details for both reported structures.

## 1.9 Thermal analyses

### *1.9.1 Thermogravimetric analyses (TGA)*

TGA analyses were conducted using a Mettler Toledo TGA/DSC $3^+$ instrument, varying the temperature from 25 to 600°C, with a heating rate of 10°C/min, under nitrogen with a flow rate of 50 mL/min. Solid samples (5-10 mg) were placed in alumina pans.

### *1.9.2 Differential scanning calorimetry analyses (DSC)*

DSC analyses were conducted using a TA Instrument DSC2500. The temperature range employed for (*R*)-(*R*,*R*) and (*S*)-(*R*,*R*) was from 20°C to 170°C, and for *(R)-(R,R)*-benzene from 20°C to 150°C, at a heating rate of 5°C/min under nitrogen with a flow rate of 50 mL/min. Solid samples (5-10 mg) were placed in aluminum pans with perforated lid.

### *1.9.3 Variable temperature Powder X-ray diffraction analysis (VT-PXRD)*

VT-PXRD was conducted using a glass capillary (0.7 mm diameter, Hilgenberg GmbH) filled with *(R)-(R,R)*-benzene. Prior to analysis, the capillary was cut and placed into molten wax on a goniometric head. The analysis was performed using a MAR345 image plate detector using MoKα radiation originating from an Incoatec Source$^{HIGHBRILLIANCE}$ (IμS$^{HIGHBRILLIANCE}$) operating at 50 kV and 1000 μA (parallel beam, ELM47 mirror). X-ray exposures was carried out for 10 min (at 30°C, 60°C, 65°C and 70°C) and 5 min (at 35°C, 40°C, 45°C, 50°C and 55°C), during which the capillary with the sample was rotated by 180°. Diffraction data was integrated using Fit2D software (using data from a 0.1 mm diameter capillary filled with $LaB_6$ as calibrant). Heating the sample-containing capillary was performed with a Leister CH-6060 Sarnen hot air blower (Leister Technologies Benelux B.V.). The air blower was calibrated before the measure by a thermocouple housed in a capillary.

## 1.10 Chiral High-Performance Liquid Chromatography (*c*HPLC)

The separation of (*R*)- and (*S*)-BINOL was performed by Chiral HPLC using a Waters Arc HPLC coupled with a 2998 PDA detector. Both enantiomers of BINOL were separated on a Daicel Chiralpak IA column 250 x 4.6 mm 5 μm with a mix of 90% v/v isohexane, 10% v/v Isopropanol as mobile phase. The separation was performed at 25°C with a flow rate of 1 mL/min.

### 1.11 Nuclear magnetic resonance (NMR)

$^1$H NMR spectra were measured on a 300MHz spectrometer Bruker. Chemical shifts are reported in parts per million (ppm) and were referenced regarding the chemical shift of the peak of the deuterated solvent used ($(CD_3)_2SO$ at 2.50ppm). Spectral multiplicities are described as follows: singlet (s), doublet (d), triplet (t), quartet (q), and multiplet (m).

## 2. Results and Discussion

### 2.1 Nuclear magnetic resonance (NMR)

BINOL = $^1$H NMR (300 MHz, DMSO) δ 9.20 (s, 1H), 7.86 (dd, *J* = 5.2, 3.9 Hz, 2H), 7.31 (d, *J* = 8.9 Hz, 1H), 7.26 – 7.12 (m, 2H), 6.93 (d, *J* = 8.2 Hz, 1H).

DADPE = $^1$H NMR (300 MHz, DMSO) δ 7.23 – 7.02 (m, 1H), 3.81 (s, 1H), 1.94 (s, 1H).

### 2.2 Crystallographic data

#### *2.2.1 Data*

Table SI-4.1. Crystallographic data and structure refinement for (*R*)-(*R,R*) and *(R)-(R,R)*-benzene structures.

| Identification code | (*R*)BINOL-(*R,R*)DADPE<br>***(R)-(R,R)*** | (*R*)BINOL-(*R,R*)DADPE<br>***(R)-(R,R)*-benzene** |
|---|---|---|
| CCDC Number | 2295235 | 2295236 |
| Empirical formula | $C_{20}$ $H_{14}$ $O_2$, $C_{14}$ $H_{16}$ $N_2$ | $C_{20}$ $H_{14}$ $O_2$, $C_{14}$ $H_{16}$ $N_2$, 2.7($C_6$ $H_6$) |
| Formula weight | 498.60 | 710.46 |
| Temperature | 297(2) K | 150(2) K |
| Wavelength | 0.71073 Å | 0.71073 Å |
| Crystal system | Tetragonal | Tetragonal |
| Space group | $P4_12_12$ | $I422$ |
| Unit cell dimensions | a = 13.32025(13) Å | a = 23.5398(17) Å |
| | b = 13.32025(13) Å | b = 23.5398(17) Å |
| | c = 31.8915(6) Å | c = 15.3506(9) Å |
| | α = 90°. | α = 90°. |
| | β = 90°. | β = 90°. |
| | γ = 90°. | γ = 90°. |

| | | |
|---|---|---|
| Volume | 5658.48(15) $Å^3$ | 8506.1(14) $Å^3$ |
| Z | 8 | 8 |
| Density (calculated) | 1.171 $Mg/m^3$ | 1.110 $Mg/m^3$ |
| Absorption coefficient | 0.073 $mm^{-1}$ | 0.067 $mm^{-1}$ |
| F(000) | 2112 | 3023 |
| Crystal size | 0.32 x 0.30 x 0.25 $mm^3$ | 0.50 x 0.04 x 0.04 $mm^3$ |
| Theta range for data collection | 3.125 to 26.616°. | 2.915 to 18.849°. |
| Index ranges | -16<=h<=16, -16<=k<=16, -36<=l<=40 | -21<=h<=21, -21<=k<=21, -13<=l<=13 |
| Reflections collected | 37467 | 11492 |
| Independent reflections | 5837 [R(int) = 0.0584] | 1682 [R(int) = 0.0864] |
| Completeness to theta = 18.849° | 99.2 % | 99.3 % |
| Absorption correction | Semi-empirical from equivalents | Semi-empirical from equivalents |
| Max. and min. transmission | 1.00000 and 0.95306 | 1.00000 and 0.28300 |
| Refinement method | Full-matrix least-squares on $F^2$ | Full-matrix least-squares on $F^2$ |
| Data / restraints / parameters | 5837 / 97 / 382 | 1682 / 408 / 280 |
| Goodness-of-fit on $F^2$ | 1.089 | 1.248 |
| Final R indices [I>2sigma(I)] | R1 = 0.0394, wR2 = 0.1066 | R1 = 0.1165, wR2 = 0.2486 |
| R indices (all data) | R1 = 0.0449, wR2 = 0.1101 | R1 = 0.1477, wR2 = 0.2667 |
| Absolute structure parameter | 0.1(5) | 0.8(10) |
| Extinction coefficient | n/a | n/a |
| Largest diff. peak and hole | 0.121 and -0.116 $e.Å^{-3}$ | 0.237 and -0.226 $e.Å^{-3}$ |

CCDC 2295235 and 2295236 contain the supplementary crystallographic data for this paper. These data can be obtained free of charge from The Cambridge Crystallographic Data Centre via www.ccdc.cam.ac.uk/structures**.**

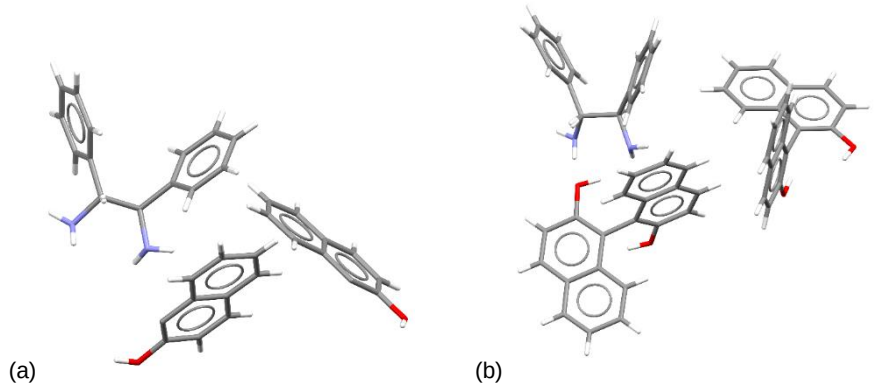

(a) (b)

Figure SI-4.1. (a) Asymmetric unit of the *(R)-(R,R)* cocrystal, (b) expanded asymmetric unit to show full molecules (disorder omitted for clarity).

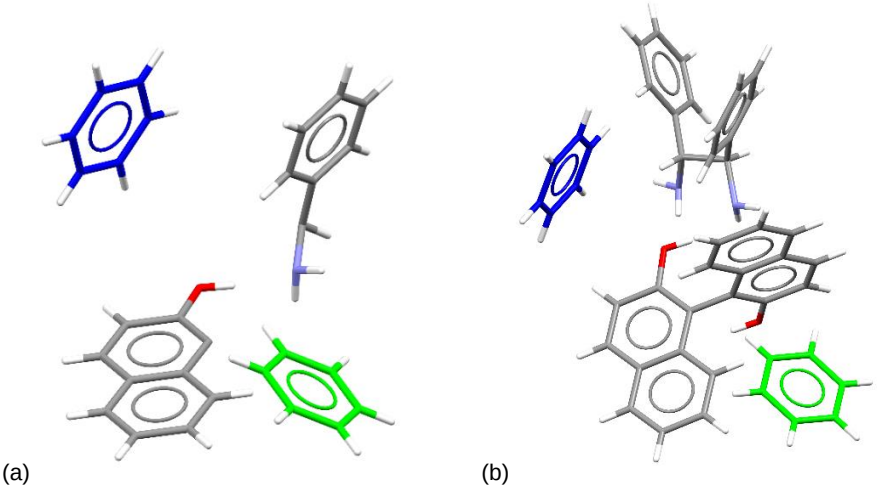

(a) (b)

Figure SI-4.2. (a) Asymmetric unit of the *(R)-(R,R)*-benzene cocrystal-solvate, (b) expanded asymmetric unit to show full molecules (disorder omitted for clarity).

Benzene molecules occupying different sites are represented in blue (surrounded by aromatic rings) and in green (surface of the channel).

### 2.2.2 *Calculation of the void in (R)-(R,R)-benzene cocrystal-solvate structure*

The volume of the voids, where no solvent molecules could be located, were calculated by Platon via Void/SOLV. The total potential solvent area volume = 583.7Å$^3$ (6.7% of the unit cell volume), distributed over two sites surrounding the 4-fold axes (284 Å$^3$, or about 3.33% of the unit cell).

### *2.2.3 Superposition of (R)-(R,R) solvated and non-solvated cocrystal structures.*

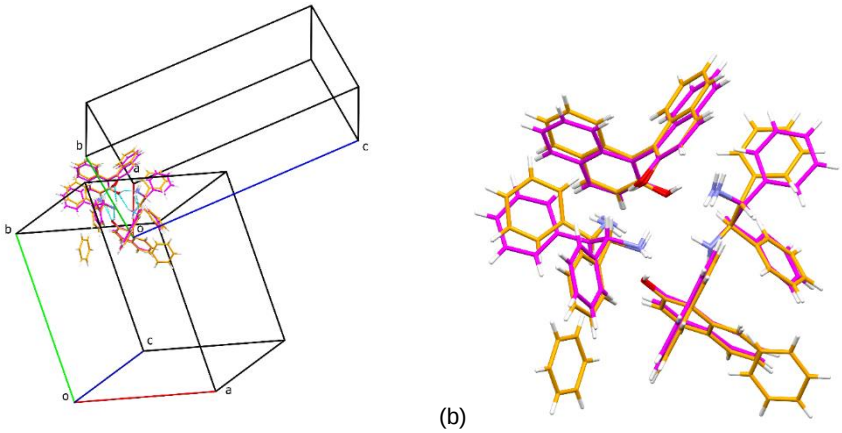


(a) (b)

Figure SI-4.3. (a) Superposition of the crystalline structures *(R)-(R,R)* (pink) and *(R)-(R,R)*-benzene (orange) structural motifs, showing a central common motif (composed of two BINOL and two DADPE molecules). (b) Close-up of the overlaid molecules (disorder omitted for clarity).

# 3. Solvent screening experiment

## 3.1 Experimental data

Table SI-4.2. Experimental data for solvent screening for BINOL:DADPE systems.

| Reagent | | Solvent | BINOL :DADPE (mole ratio) | m (mg) | | V solvent (mL) | P-XRD result |
|---|---|---|---|---|---|---|---|
| | | | | BINOL | DADPE | | |
| (*S*)-BINOL | (*R.R*)-DADPE | MeOH | 1 :1 | 285.89 | 211.42 | 2 | (*S*)-(*R.R*) cocrystal **DICVUH** |
| (*S*)-BINOL | (*R.R*)-DADPE | EtOH | 1 :1 | 186.02 | 211.12 | 2 | (*S*)-(*R.R*) cocrystal **DICVUH** |
| (*S*)-BINOL | (*R.R*)-DADPE | EtOAc | 1:1 | 143.3 | 106.3 | 0.5 | (*S*)-(*R.R*) cocrystal **DICVUH** |
| (*S*)-BINOL | (*R.R*)-DADPE | DCM | 1 :1 | 143.1 | 106.3 | 0.3 | (*S*)-(*R.R*) cocrystal **DICVUH** |
| (*S*)-BINOL | (*R.R*)-DADPE | toluene | 1 :1 | 285.53 | 212.02 | 2 | (*S*)-(*R.R*) cocrystal **DICVUH** |
| (*S*)-BINOL | (*R.R*)-DADPE | IPA | 1 :1 | 143.2 | 106.7 | 0.5 | (*S*)-(*R.R*) cocrystal **DICVUH** |
| (*S*)-BINOL | (*R.R*)-DADPE | benzene | 1 :1 | 143.6 | 106.4 | 2 | (*S*)-(*R.R*) cocrystal **DICVUH** |
| (*R*)-BINOL | (*R.R*)-DADPE | MeOH | 1 :1 | 286.91 | 212.44 | 0.5 | (*R*)-(*R.R*) cocrystal CCDC: **2295235** |
| (*R*)-BINOL | (*R.R*)-DADPE | EtOH | 1 :1 | 286.29 | 211.9 | 2 | (*R*)-(*R.R*) cocrystal CCDC: **2295235** |
| (*R*)-BINOL | (*R.R*)-DADPE | EtOAc | 1 :1 | 143.5 | 105.6 | 0.3 | (*R*)-(*R.R*) cocrystal CCDC: **2295235** |
| (*R*)-BINOL | (*R.R*)-DADPE | DCM | 1 :1 | 143.6 | 106.9 | 0.2 | (*R*)-(*R.R*) cocrystal CCDC: **2295235** |
| (*R*)-BINOL | (*R.R*)-DADPE | toluene | 1 :1 | 186.07 | 211.97 | 2 | (*R*)-(*R.R*) cocrystal CCDC: **2295235** |
| (*R*)-BINOL | (*R.R*)-DADPE | IPA | 1 :1 | 143.2 | 105.1 | 0.5 | (*R*)-(*R.R*) cocrystal CCDC: **2295235** |
| (*R*)-BINOL | (*R.R*)-DADPE | benzene | 1:1 | 143.5 | 105.9 | 2 | (*R*)-(*R.R*)-benzene cocrystal-solvate CCDC: **2295236** |

## 3.2 PXRD patterns

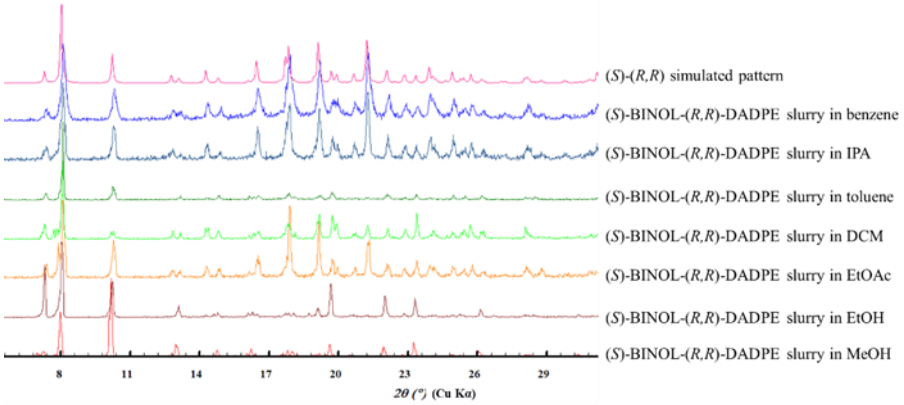


Figure SI-4.4 Comparison of the X-ray diffraction patterns (using Cu Kα) between 1:1 slurry outcomes of (*S*)-Binol and (*R,R*)-DADPE in MeOH (red), EtOH (brown), EtOAc (orange), DCM (light green), toluene (dark green), IPA ( dark blue) and benzene (light blue) and the simulated pattern of the reported *(S)-(R,R)*-cocrystal **DICVUH**[102] (fuchsia).

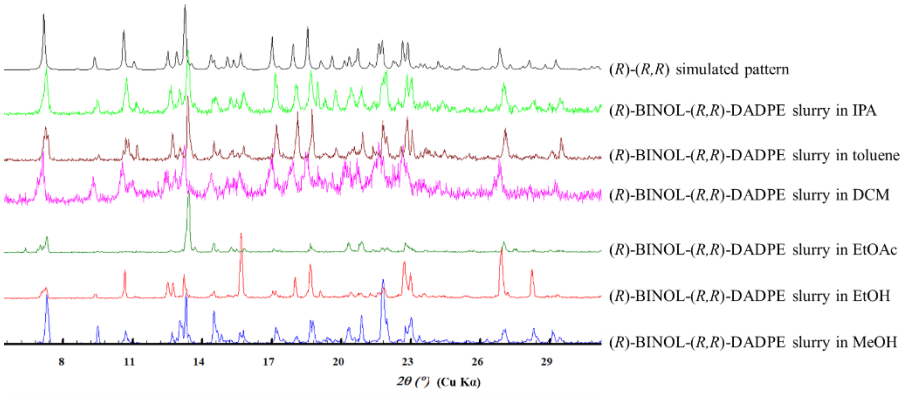


Figure SI-4.5. Comparison of the X-ray diffraction patterns (using Cu Kα) between the 1:1 slurry outcome of (*R*)-Binol and (*R,R*)-DADPE in MeOH ( blue), EtOH (red), EtOAc (dark green), DCM (rose), toluene (brown) and IPA (in light green) and the simulated pattern of the *(R)-(R,R)*-cocrystal (black, current work – CCDC: 2295235).

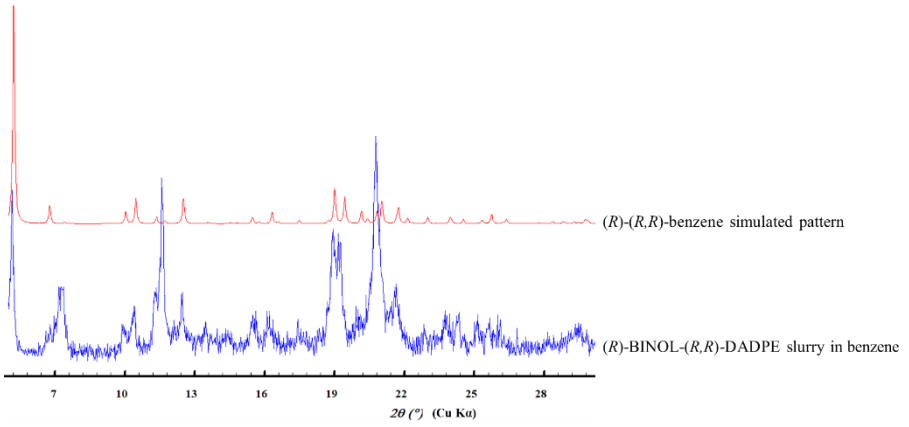


Figure SI-4.6. Comparison of the X-ray diffraction patterns (using Cu Kα) between the 1:1 slurry outcome of (*R*)-Binol and (*R,R*)-DADPE in benzene (blue) and the simulated pattern of the (*R*)-*(R,R*)-benzene cocrystal-solvate (in red, current work – CCDC: 2295236).

There are some intensity differences for low-angle peaks between simulated and experimental patterns. This can be explained by varying degree of pore filling.

# 4. Thermal analyses

## 4.1 Thermogravimetric analyses (TGA)

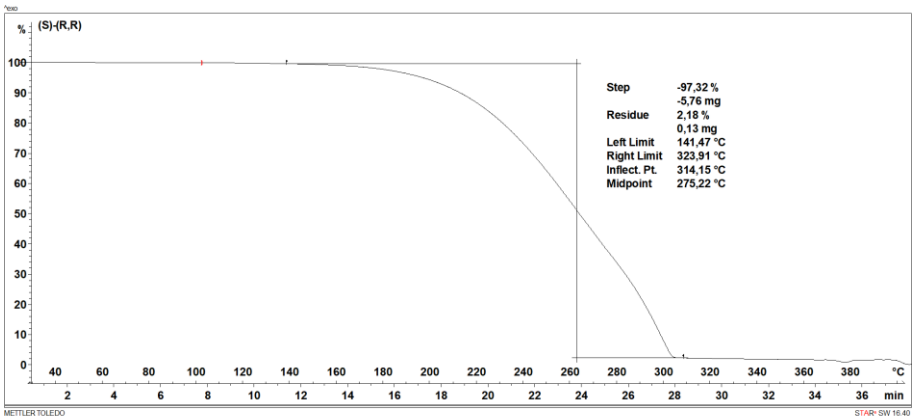


Figure SI-4.7. TGA of the *(S)-(R,R)* cocrystal, obtained slurrying a 1:1 ratio in toluene. The thermogram is expressed as the weight loss (%) with respect to temperature. The thermogram shows a single step mass loss starting at 141°C, consisting in the degradation of the product.

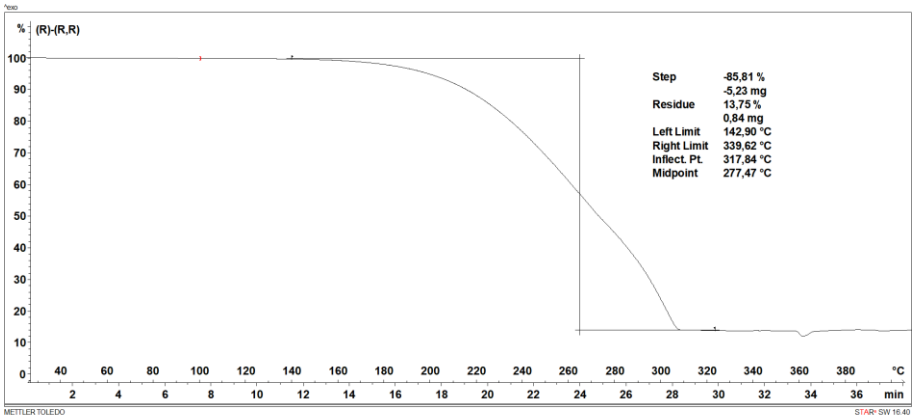


Figure SI-4.8. TGA of the *(R)-(R,R)* cocrystal, obtained slurrying a 1:1 ratio in toluene. The thermogram is expressed as the weight loss (%) with respect to temperature. The thermogram shows a single step mass loss starting at 143°C, consisting in the degradation of the product.

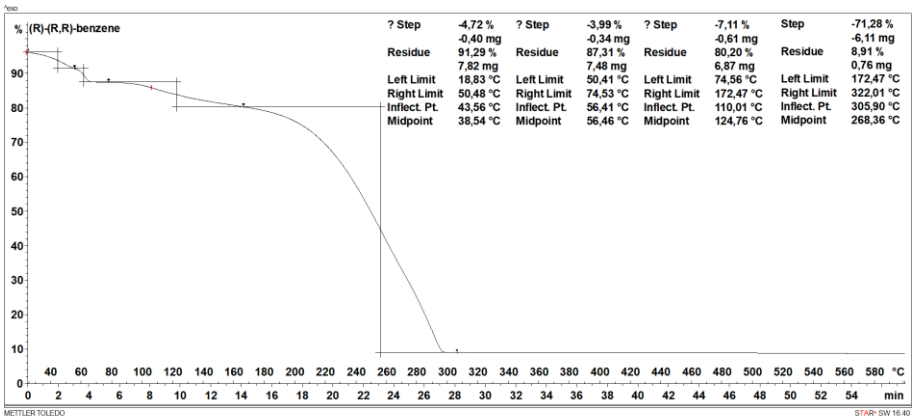


Figure SI-4.9. TGA of the (*R)-(R,R*)-benzene cocrystal-solvate, analyzed directly after filtration and obtained slurrying a 1:1 ratio in benzene. The thermogram is expressed as the weight loss (%) with respect to temperature. The thermogram shows multiple mass changes. The two first ones start at 19°C and consist in desolvation and evaporation of benzene inside the solvent channel (loss of 0.61 equivalent of benzene), the second mass change starts at 75°C and also represents desolvation (loss of 0.49 equivalent of benzene), the third mass change starts at 171°C and consists in the degradation of the compound.

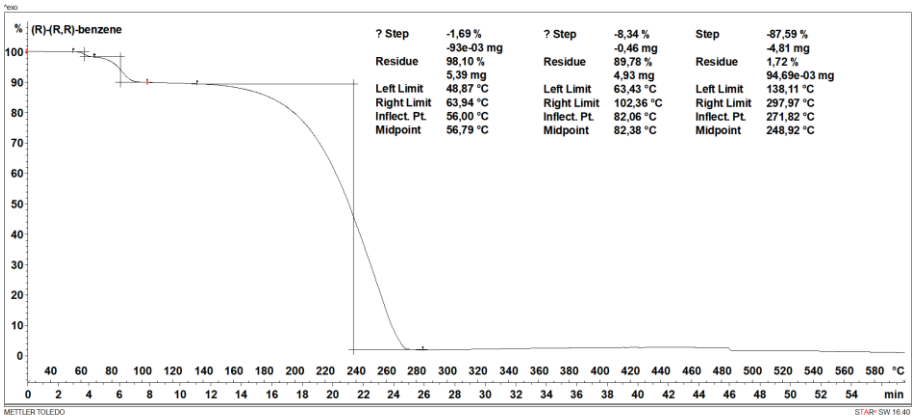


Figure SI-4.10. TGA of the *(R)-(R,R)*-benzene cocrystal-solvate, analyzed one week after filtration and obtained by slurry (1:1) in benzene. The thermogram is expressed as the weight loss (%) with respect to the increase of temperature.

## 4.2 Differential scanning calorimetry analyses (DSC)

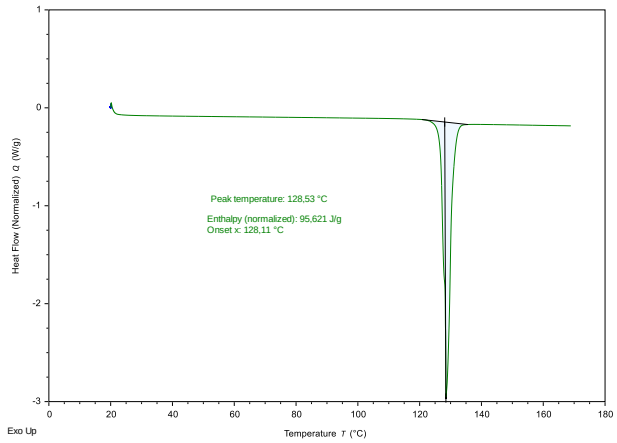


Figure SI-4.11. DSC of the *(S)-(R,R)* cocrystal, obtained slurrying a 1:1 ratio in toluene. The thermogram is expressed in mW with respect to the increase of temperature. The thermogram shows one endothermic peak, with onset at 128°C corresponding to the melt of the *(S)-(R,R)* cocrystal.

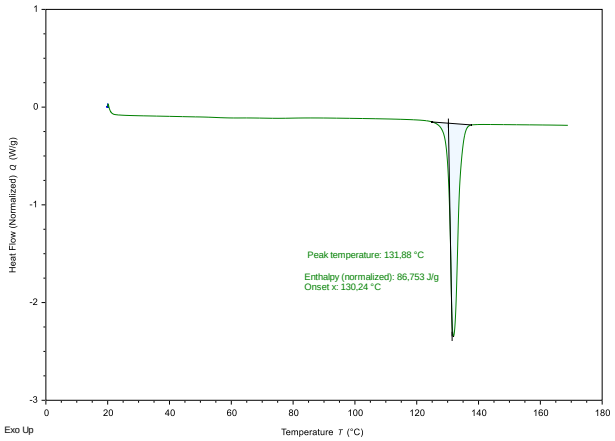


Figure SI-4.12. DSC of the *(R)-(R,R)* cocrystal, obtained slurrying a 1:1 ratio in toluene. The thermogram expressed in mW with respect to the increase of temperature. The thermogram shows one endothermic peak, with onset at 130°C corresponding to the melt of the *(R)-(R,R)* cocrystal.

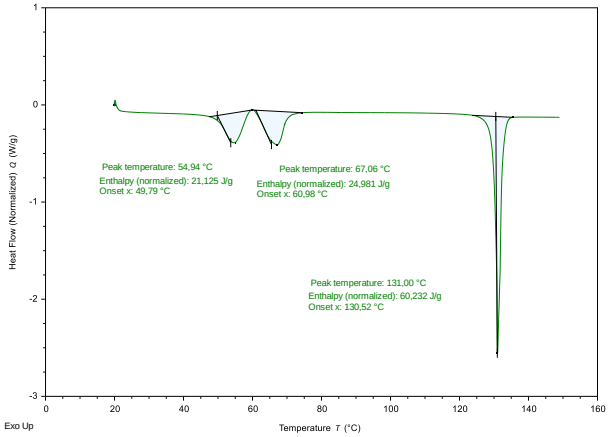


Figure SI-4.13. DSC of the *(R)-(R,R)*-benzene cocrystal-solvate, obtained slurrying a 1:1 mixture in benzene. The thermogram shows three different transitions. The two first endothermic peaks have an onset at respectively 50°C and 61°C, and consist in the desolvation of benzene from the different sites in the crystal and the third endothermic peak, which has an onset at 131°C, consists in the melt of the *(R)-(R,R)* cocrystal.

## 4.3 Variable temperature Powder X-ray diffraction

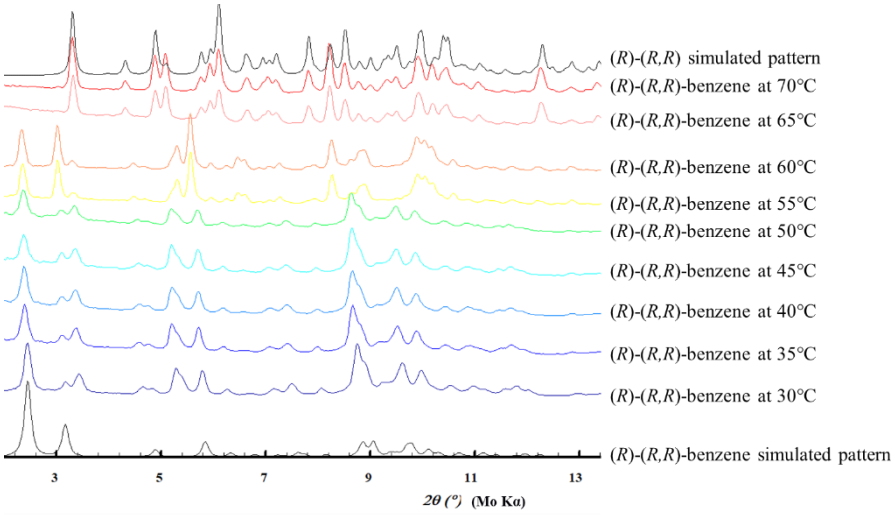


Figure SI-4.14: Variable temperature PXRD patterns (using Mo Kα) for the (*R*)-(*R*,*R*)-benzene cocrystal-solvate, obtained slurrying a 1:1 mixture in benzene and compared to the simulated patterns of the compounds (*R*)-(*R*,*R*)-benzene and *(R)-(R,R)* (black).

In Figures SI-15 to SI-17, Rietveld refinement was done to assign the majority phase for each temperature range. At both 30°C and 60°C, the *(R)-(R,R)*-benzene cocrystal-solvate exists as the dominant phase, at 65°C, the *(R)-(R,R)* cocrystal exists as the dominant phase.

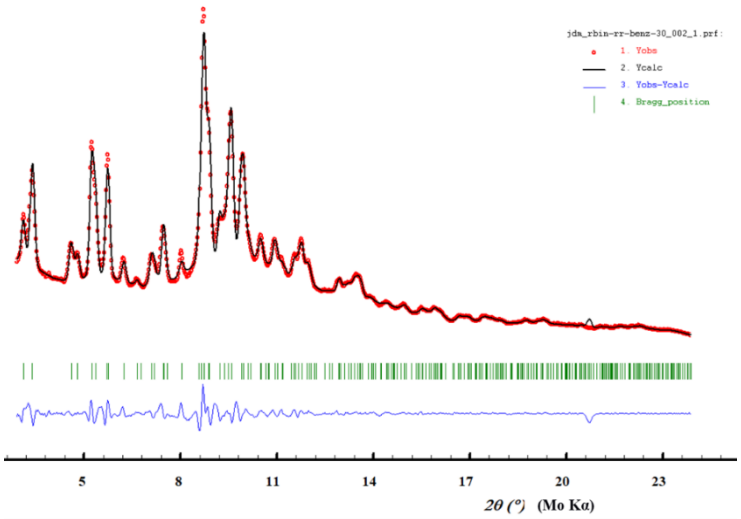


Figure SI-4.15. Profile fitting of Rietveld refinement of the *(R)-(R,R)*-benzene cocrystal-solvate analyzed at 30°C.

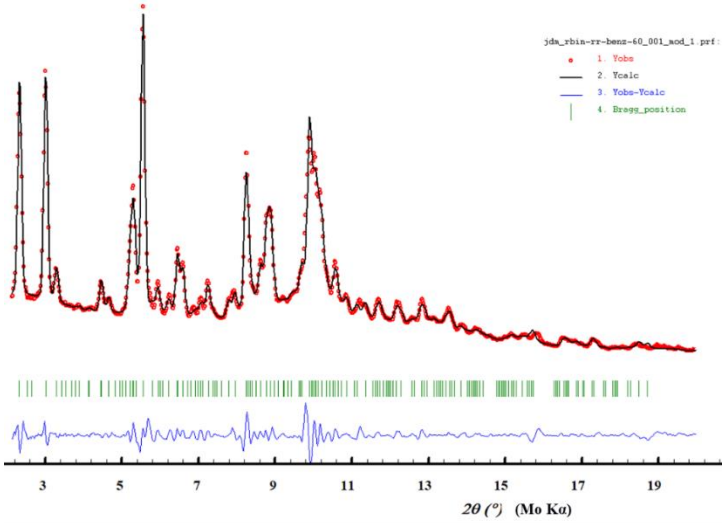


Figure SI-4.16. Profile fitting of Rietveld refinement of the *(R)-(R,R)*-benzene cocrystal-solvate analyzed at 60°C.

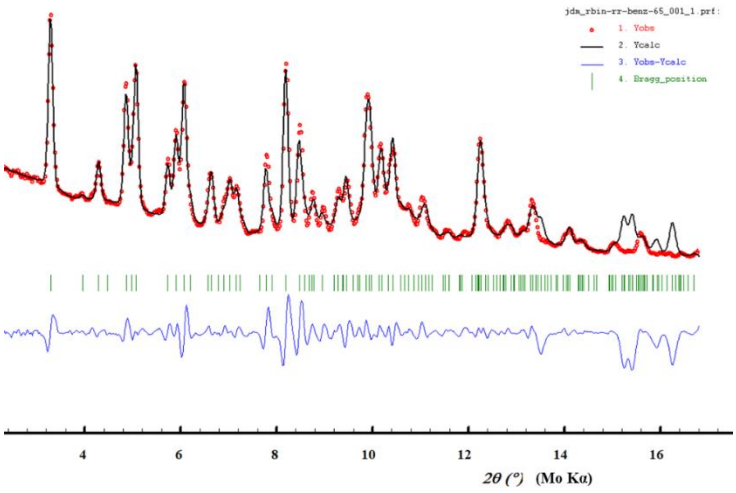


Figure SI-4.17. Profile fitting of Rietveld refinement of the *(R)-(R,R)* cocrystal analyzed at 65°C.

# 5. **Solubility curves**

## 5.1 In methanol (MeOH)

Table SI-4.3. Experimental data for the construction of the solubility curves of *(R)-(R,R)* and (*S)-(R,R*) cocrystals in MeOH.

| m((*S)-(R,R*)) (g) | m(MeOH) (g) | C((*S)-(R,R*)) (g/mL) | T solub (°C) |
|---|---|---|---|
| 0.14998 | 0.64564 | 0.1840 | 16.9 |
| 0.15567 | 0.63865 | 0.1930 | 18.8 |
| 0.14941 | 0.64575 | 0.1832 | 17.5 |
| 0.16501 | 0.63713 | 0.2051 | 21.7 |
| 0.16051 | 0.6515 | 0.1951 | 18.9 |
| 0.16517 | 0.64095 | 0.2041 | 21.1 |
| 0.17373 | 0.64927 | 0.2119 | 21.6 |
| 0.1697 | 0.64066 | 0.2098 | 22 |
| 0.17326 | 0.63935 | 0.2146 | 23.2 |
| 0.18217 | 0.64298 | 0.2244 | 23.8 |
| 0.18254 | 0.64803 | 0.2231 | 23.8 |
| 0.18268 | 0.64564 | 0.2241 | 24.3 |
| 0.19742 | 0.65766 | 0.2377 | 25.8 |
| 0.20031 | 0.64932 | 0.2443 | 26 |
| 0.20422 | 0.60241 | 0.2685 | 28.8 |
| m((*R)-(R,R*)) (g) | m(MeOH) (g) | C((*R)-(R,R*)) (g/mL) | T solub (°C) |
| 0.1496 | 0.64261 | 0.1844 | 18.1 |
| 0.14971 | 0.65269 | 0.1817 | 16.7 |
| 0.15055 | 0.64294 | 0.1855 | 16.8 |
| 0.15978 | 0.63944 | 0.1979 | 19.4 |
| 0.18061 | 0.64131 | 0.2230 | 24 |
| 0.17038 | 0.63975 | 0.2109 | 20 |
| 0.15956 | 0.647 | 0.1953 | 18.5 |
| 0.17066 | 0.63803 | 0.2118 | 20.1 |
| 0.15957 | 0.64004 | 0.1975 | 18.6 |
| 0.18043 | 0.64318 | 0.2222 | 21.9 |
| 0.2003 | 0.63467 | 0.2500 | 26.2 |
| 0.20036 | 0.64365 | 0.2465 | 26.9 |
| 0.20039 | 0.63356 | 0.2505 | 25.7 |
| 0.17029 | 0.64226 | 0.2100 | 21 |
| 0.17985 | 0.63964 | 0.2227 | 22.7 |

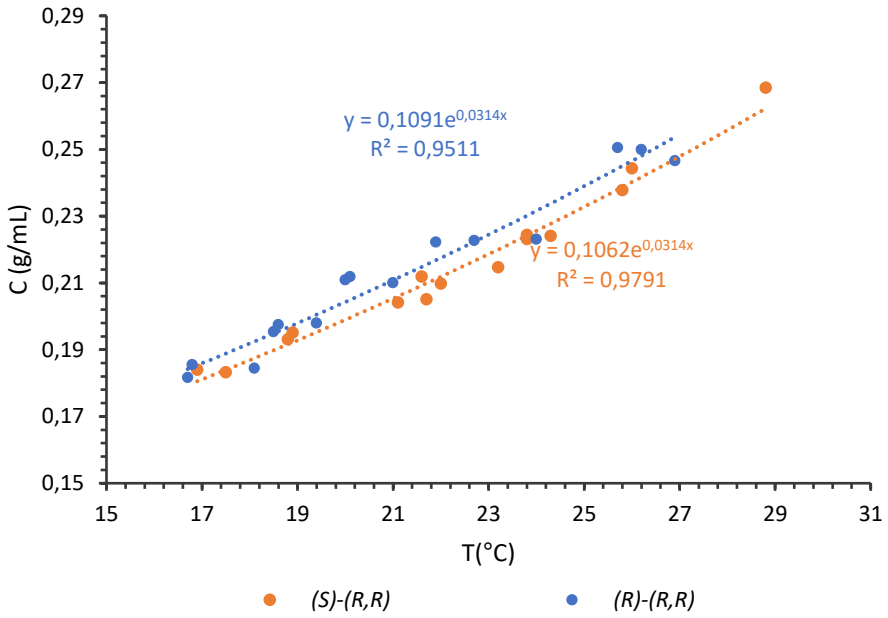


Figure SI-4.18. Solubility curves of (*R*)-(*R*,*R*) and (*S*)-(*R*,*R*) cocrystals in MeOH.

## 5.2 In ethanol (EtOH)

Table SI-4.4. Experimental data for the construction of the solubility curves of *(R)-(R,R)* and (*S*)-(*R*,*R*) cocrystals in EtOH.

| m((*R*)-(*R*,*R*)) (g) | m(EtOH) (g) | C((*R*)-(*R*,*R*)) (g/mL) | T solub (°C) |
|---|---|---|---|
| 0.07064 | 0.6269 | 0.0889 | 23.7 |
| 0.07976 | 0.60643 | 0.1038 | 28.5 |
| 0.0794 | 0.63338 | 0.0989 | 27.1 |
| 0.08088 | 0.63349 | 0.1007 | 28.2 |
| 0.09164 | 0.64836 | 0.1115 | 30.5 |
| 0.0917 | 0.64155 | 0.1128 | 31.1 |
| 0.10029 | 0.63129 | 0.1253 | 33.8 |
| 0.10207 | 0.64542 | 0.1248 | 34.3 |
| 0.11958 | 0.66151 | 0.1426 | 38.4 |
| m((*S*)-(*R*,*R*)) (g) | m(EtOH) (g) | C((*S*)-(*R*,*R*)) (g/mL) | T solub (°C) |
| 0.06991 | 0.64905 | 0.0850 | 26.1 |
| 0.07123 | 0.63756 | 0.0881 | 27.7 |
| 0.06997 | 0.63852 | 0.0865 | 27.2 |
| 0.07933 | 0.64424 | 0.0972 | 29.4 |
| 0.08074 | 0.64962 | 0.0981 | 31.1 |
| 0.08228 | 0.65059 | 0.0998 | 31.5 |

| | | | |
|---|---|---|---|
| 0.08955 | 0.65181 | 0.1084 | 33.3 |
| 0.08972 | 0.64648 | 0.1095 | 34.3 |
| 0.09031 | 0.64127 | 0.1111 | 34.3 |
| 0.10207 | 0.64659 | 0.1246 | 36.4 |
| 0.10014 | 0.65271 | 0.1210 | 36.1 |
| 0.10195 | 0.64847 | 0.1240 | 37.7 |
| 0.12232 | 0.64394 | 0.1499 | 41.4 |
| 0.12225 | 0.64085 | 0.1505 | 41.7 |
| 0.11957 | 0.64137 | 0.1471 | 41.4 |

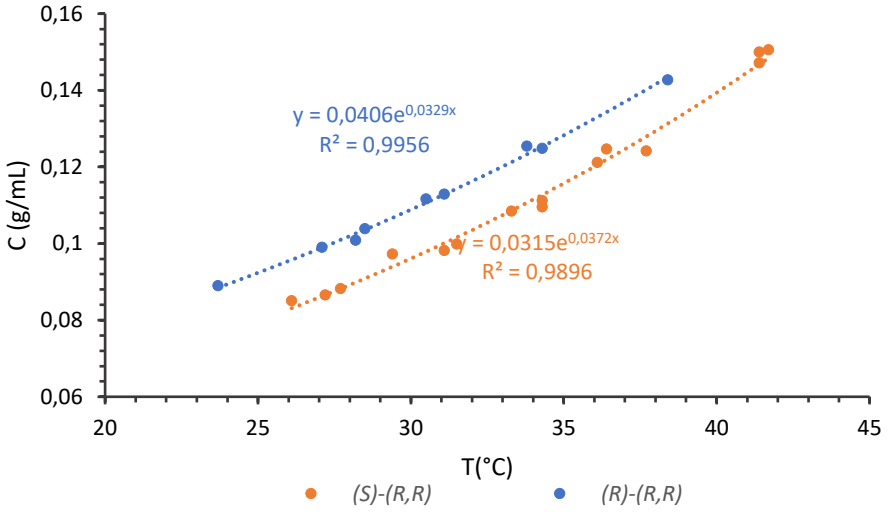


Figure SI-4.19. Solubility curves of *(R)-(R,R)* and *(S)-(R,R)* cocrystals in EtOH.

## 5.3 In isopropyl alcohol (IPA)

Table SI-4.5. Experimental data for the construction of the solubility curves of *(R)-(R,R)* and *(S)-(R,R)* cocrystals in IPA.

| m((*R*)-(*R*,*R*)) (g) | m(EtOH) (g) | C((*R*)-(*R*,*R*)) (g/mL) | T solub (°C) |
|---|---|---|---|
| 0.12917 | 0.61435 | 0.1653 | 54.7 |
| 0.1292 | 0.60698 | 0.1673 | 56.9 |
| 0.12921 | 0.61553 | 0.1650 | 56.6 |
| 0.04914 | 0.61816 | 0.0625 | 32 |
| 0.09832 | 0.6119 | 0.1263 | 47.7 |
| 0.09835 | 0.6159 | 0.1255 | 43.1 |
| 0.06866 | 0.6225 | 0.0867 | 32 |
| 0.06868 | 0.61803 | 0.0873 | 39.4 |
| 0.01826 | 0.62388 | 0.0230 | 16 |
| 0.01833 | 0.62486 | 0.0231 | 11.7 |
| 0.01827 | 0.61564 | 0.0233 | 13.2 |

| m((*S*)-(*R*,*R*)) (g) | m(IPA) (g) | C((*S*)-(*R*,*R*)) (g/mL) | T solub (°C) |
|---|---|---|---|
| 0.13033 | 0.61144 | 0.1675 | 62.6 |
| 0.13024 | 0.60917 | 0.1680 | 62.8 |
| 0.13034 | 0.61842 | 0.1657 | 62.6 |
| 0.09931 | 0.61526 | 0.1269 | 57.8 |
| 0.09925 | 0.62002 | 0.1258 | 59 |
| 0.09923 | 0.61112 | 0.1276 | 59.2 |
| 0.04876 | 0.62099 | 0.0617 | 48.7 |
| 0.0488 | 0.61731 | 0.0621 | 49.4 |
| 0.04882 | 0.60292 | 0.0636 | 50 |
| 0.02074 | 0.6104 | 0.0267 | 31.4 |
| 0.02078 | 0.61673 | 0.0265 | 27.2 |
| 0.02073 | 0.6186 | 0.0263 | 32.1 |

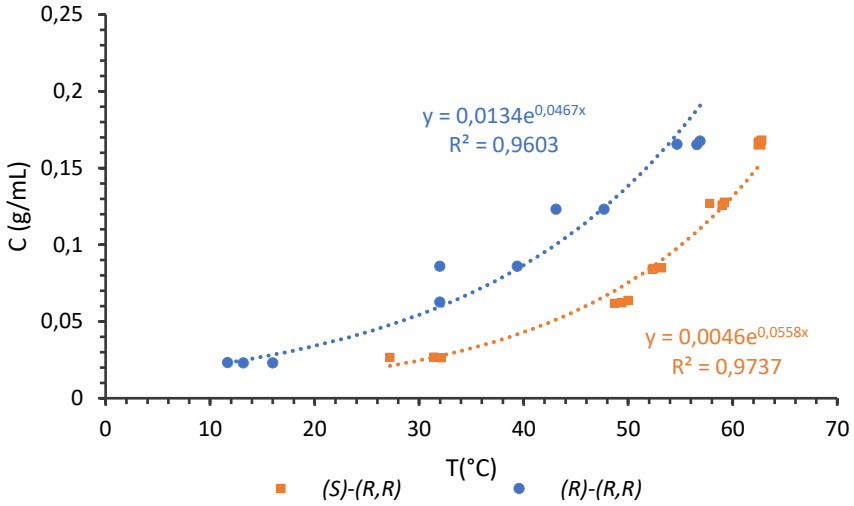


Figure SI-4.20. Solubility curves of (*R*)-(*R*,*R*) and *(S)-(R,R)* cocrystals in IPA.

## 5.4 In toluene

Table SI-4.6. Experimental data for the construction of the solubility curves of *(R)-(R,R)* and *(S)-(R,R)* cocrystals in toluene.

| m((*R*)-(*R*,*R*)) (g) | m(EtOH) (g) | C((*R*)-(*R*,*R*)) (g/mL) | T solub (°C) |
|---|---|---|---|
| 0.05031 | 0.70854 | 0.0616 | 27.5 |
| 0.06944 | 0.70018 | 0.0860 | 31.6 |
| 0.07194 | 0.69934 | 0.0892 | 32.4 |
| 0.06966 | 0.70822 | 0.0853 | 31.8 |
| 0.08147 | 0.70309 | 0.1005 | 35.3 |
| 0.07927 | 0.71615 | 0.0960 | 34.6 |

| | | | |
|---|---|---|---|
| 0.07973 | 0.6961 | 0.0993 | 36.4 |
| 0.09974 | 0.70524 | 0.1226 | 40.8 |
| 0.09955 | 0.69375 | 0.1244 | 41.2 |
| 0.10046 | 0.71079 | 0.1225 | 40.8 |
| m((*S*)-(*R*,*R*)) (g) | m(tolu) (g) | C((*S*)-(*R*,*R*)) (g/mL) | T solub (°C) |
| 0.05072 | 0.70977 | 0.0620 | 43.9 |
| 0.05037 | 0.71068 | 0.0614 | 43.9 |
| 0.05103 | 0.70682 | 0.0626 | 44.8 |
| 0.06035 | 0.71097 | 0.0736 | 46.5 |
| 0.07059 | 0.70935 | 0.0863 | 46.1 |
| 0.08061 | 0.70278 | 0.0994 | 47.3 |
| 0.08255 | 0.69548 | 0.1029 | 48.1 |
| 0.08032 | 0.70418 | 0.0989 | 47.5 |
| 0.09977 | 0.71797 | 0.1205 | 50.5 |
| 0.10116 | 0.70318 | 0.1247 | 51.1 |
| 0.10156 | 0.70455 | 0.1250 | 51.5 |

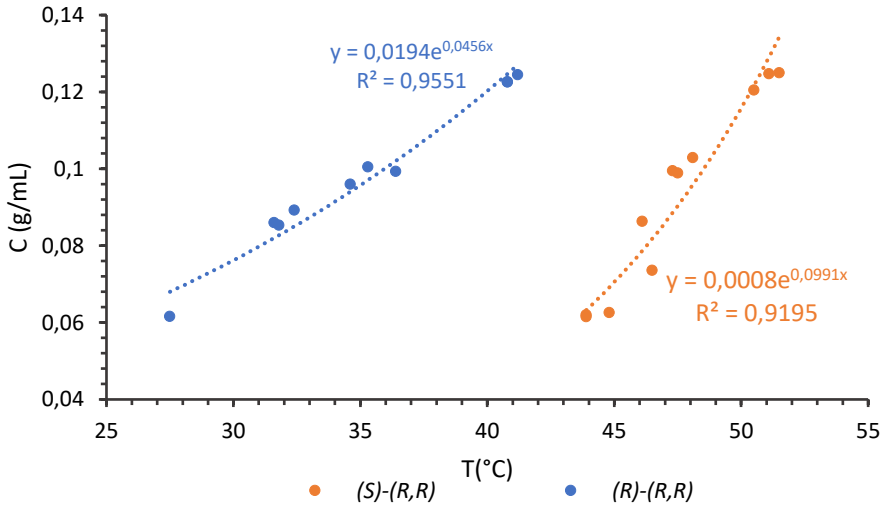


Figure SI-4.21. Solubility curves of *(R)-(R,R)* and *(S)-(R,R)* cocrystals in toluene.

## 5.5 In benzene

Table SI-4.7. Experimental data for the construction of the solubility curves of *(R)-(R,R)*-benzene and *(S)-(R,R)* cocrystals in benzene.

| m((*S*)-(*R*,*R*)) (g) | m(benzene) (g) | C((*S*)-(*R*,*R*)) (g/mL) | T solub (°C) |
|---|---|---|---|
| 0.0442 | 0.9414 | 0.0411 | 20.4 |

| | | | |
|---|---|---|---|
| 0.0507 | 0.8663 | 0.0513 | 23.9 |
| 0.0566 | 0.9257 | 0.0536 | 25.4 |
| 0.0221 | 0.9737 | 0.0199 | 8.1 |
| 0.0273 | 1.0695 | 0.0224 | 8.1 |
| 0.03516 | 0.70284 | 0.0438 | 21.8 |
| 0.03466 | 0.70449 | 0.0431 | 21.6 |
| 0.03554 | 0.70424 | 0.0442 | 22.1 |
| 0.05192 | 0.70538 | 0.0645 | 28.6 |
| 0.04514 | 0.69737 | 0.0567 | 26.6 |
| m((*R*)-(*R*,*R*)) (mg) | m(benzene) (g) | C((*R*)-(*R*,*R*)-benzene) (g/mL) | T solub (°C) |
| 10.13 | 617.5 | 0.0144 | 15.5 |
| 15.13 | 631.01 | 0.0210 | 20.8 |
| 20.31 | 623.98 | 0.0285 | 25.1 |
| 25.22 | 627.73 | 0.0352 | 28.1 |
| 30.21 | 621.04 | 0.0426 | 31.1 |
| 35.26 | 623.03 | 0.0496 | 33.4 |
| 40.08 | 628.36 | 0.0559 | 35.2 |
| 45.06 | 628.83 | 0.0628 | 36.4 |
| 10.13 | 956.6 | 0.0093 | 10.7 |
| 15.13 | 965.44 | 0.0137 | 17.1 |
| 20.31 | 972.53 | 0.0183 | 21 |
| 25.22 | 975.95 | 0.0226 | 24.3 |
| 35.2600 | 971.75 | 0.0318 | 28.7 |
| 40.0800 | 966.35 | 0.0363 | 31.1 |
| 45.0600 | 961.71 | 0.0410 | 32.5 |

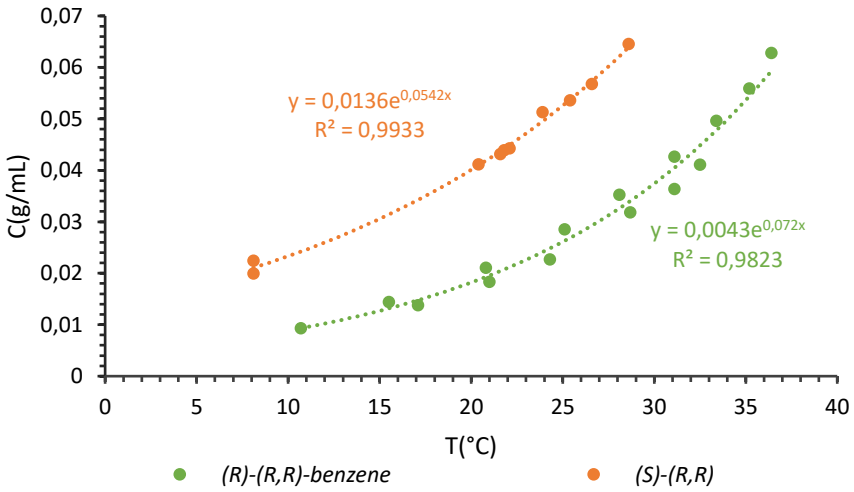


Figure SI-4.22. Solubility curves of *(S)-(R,R)* cocrystal and *(R)-(R,R)*-benzene cocrystal-solvate in benzene.

# 6. Isoplethal ternary diagram experiments and results

## 6.1 In toluene

Table SI-4.8. Experimental data and results for the construction of the isoplethal ternary diagram (*rac*)-BINOL-(*R*,*R*)DADPE-toluene at 20°.

| | | m(tolu) (mg) | m(*rac*)-BINOL) (mg) | m((*R*,*R*)-DADPE) (mg) | %mol(tolu) | %mol((*rac*)-BINOL) | %mol((*R*,*R*)-DADPE) | PXRD results | ratio BINOL:DADPE determined by NMR | ratio (*S*)-/(*R*)-BINOL determined by cHPLC | point |
|---|---|---|---|---|---|---|---|---|---|---|---|
| 98,50% | 1 | 1717,1 | 70,95 | 8,21 | 0,9849 | 0,0131 | 0,0020 | (*rac*)-BINOL | X | x | (*rac*)-BINOL |
| | 2 | 1731,46 | 60,31 | 16,4 | 0,9849 | 0,0110 | 0,0040 | (*rac*)-BINOL | 1 :0 | x | (*rac*)-BINOL |
| | 3 | 1722,97 | 49,3 | 24,14 | 0,9849 | 0,0091 | 0,0060 | (*rac*)-BINOL | 1 :0 | x | (*rac*)-BINOL |
| | 4 | 1716,91 | 38,33 | 32,49 | 0,9848 | 0,0071 | 0,0081 | | | | soluble |
| | 5 | 1715,15 | 27,27 | 40,42 | 0,9849 | 0,0050 | 0,0101 | | | | soluble |
| | 6 | 1711,84 | 16,39 | 48,57 | 0,9848 | 0,0030 | 0,0121 | | | | soluble |
| | 7 | 1723,78 | 5,61 | 56,64 | 0,9849 | 0,0010 | 0,0140 | | | | soluble |
| 97% | 1 | 1724,57 | 144,61 | 16,48 | 0,9698 | 0,0262 | 0,0040 | (*rac*)-BINOL | x | x | (*rac*)-BINOL |
| | 2 | 1713,34 | 127,69 | 28,88 | 0,9697 | 0,0233 | 0,0071 | (*rac*)-BINOL | x | x | (*rac*)-BINOL |
| | 3 | 1716,8 | 111,44 | 41,26 | 0,9696 | 0,0203 | 0,0101 | (*rac*)-BINOL (+ (*S*)-(*R*,*R*)*) | 1 :0,07 | x | (*rac*)-BINOL |
| | 4 | 1736,57 | 88,83 | 57,53 | 0,9701 | 0,0160 | 0,0139 | (*rac*)-BINOL + (*S*)-(R,R) | x | x | (*rac*)-BINOL + (*S*)-(*R*,*R*) |
| | 5 | 1729,85 | 72,22 | 69,91 | 0,9700 | 0,0130 | 0,0170 | (*S*)-(*R*,*R*) | x | 99,88 :0,12 | (*S*)-(*R*,*R*) |
| | 6 | 1723,47 | 55,47 | 82,36 | 0,9698 | 0,0100 | 0,0201 | (*S*)-(*R*,*R*) | x | 100 :0 | (*S*)-(*R*,*R*) |
| | 7 | 1727,03 | 33,41 | 98,65 | 0,9699 | 0,0060 | 0,0240 | | | | soluble |
| | 8 | 1714,13 | 16,71 | 111,23 | 0,9696 | 0,0030 | 0,0273 | | | | soluble |
| | 9 | 1724,54 | 0 | 123,21 | 0,9699 | 0,0000 | 0,0301 | (*R*,*R*)-DADPE | x | x | (*R*,*R*)-DADPE |
| 96% | 1 | 1714,98 | 196,17 | 20,29 | 0,9597 | 0,0353 | 0,0049 | (*rac*)-BINOL | x | x | (*rac*)-BINOL |
| | 2 | 1732,36 | 168,22 | 41,76 | 0,9600 | 0,0300 | 0,0100 | (*rac*)-BINOL | x | x | (*rac*)-BINOL |
| | 3 | 1733,87 | 140,37 | 62,3 | 0,9600 | 0,0250 | 0,0150 | (rac)-BINOL + (*S*)-(*R*,*R*) | x | x | (rac)-BINOL + (*S*)-(*R*,*R*) |
| | 4 | 1727,3 | 112,25 | 83,33 | 0,9598 | 0,0201 | 0,0201 | (rac)-BINOL + (*S*)-(*R*,*R*) | 1 :0,825 | x | (rac)-BINOL + (*S*)-(*R*,*R*) |
| | 5 | 1730,98 | 84,24 | 103,99 | 0,9599 | 0,0150 | 0,0250 | (*S*)-(*R*,*R*) | x | x | (*S*)-(*R*,*R*) |
| | 6 | 1734,49 | 56,14 | 124,98 | 0,9600 | 0,0100 | 0,0300 | (*S*)-(*R*,*R*) | 0,7 :1 | x | (*S*)-(*R*,*R*) + (R,R)-DADPE |
| | 7 | 1723,8 | 28,12 | 145,46 | 0,9598 | 0,0050 | 0,0352 | (*R*,*R*)-DADPE | 0 :1 | x | (*R*,*R*)-DADPE |
| 95% | 1 | 1723,65 | 249,56 | 25,13 | 0,9497 | 0,0443 | 0,0060 | (*rac*)-BINOL | x | x | (*rac*)-BINOL |
| | 2 | 1724,2 | 215,56 | 50,49 | 0,9497 | 0,0382 | 0,0121 | (*rac*)-BINOL + (*S*)-(*R*,*R*) | 1 :0,07 | x | (*rac*)-BINOL |
| | 3 | 1726,41 | 181,59 | 75,46 | 0,9498 | 0,0322 | 0,0180 | (*rac*)-BINOL + (*S*)-(*R*,*R*) | x | x | (*rac*)-BINOL + (*S*)-(*R*,*R*) |
| | 4 | 1718,07 | 147,34 | 100,59 | 0,9497 | 0,0262 | 0,0241 | (*rac*)-BINOL + (S)-(R,R) (+(*R*)-(*R*,*R*)*) | x | x | (*rac*)-BINOL + (*S*)-(*R*,*R*) + (*R*)-(*R*,*R*) |
| | 5 | 1715,05 | 113,5 | 126,16 | 0,9495 | 0,0202 | 0,0303 | (*S*)-(*R*,*R*) | x | 99,45 :0,55 | (*S*)-(*R*,*R*) |
| | 6 | 1733,37 | 79,28 | 151,55 | 0,9500 | 0,0140 | 0,0360 | (*S*)-(*R*,*R*) (+ (*R*,*R*)DADPE*) | 0,89 :1 | x | (*S*)-(*R*,*R*) + (*R*,*R*)-DADPE |
| | 7 | 1722,18 | 45,41 | 176,23 | 0,9498 | 0,0081 | 0,0422 | (*R*,*R*)-DADPE | 0,145 :1 | x | (*S*)-(*R*,*R*) + (*R*,*R*)-DADPE |
| | 8 | 1738,44 | 11,48 | 201,77 | 0,9501 | 0,0020 | 0,0479 | (*R*,*R*)-DADPE | 0 :1 | x | (*R*,*R*)-DADPE |

| | | | | | | | | | | | |
|---|---|---|---|---|---|---|---|---|---|---|---|
| 93% | 1 | 1717,84 | 347,67 | 42,51 | 0,9295 | 0,0605 | 0,0100 | (*rac*)-BINOL | 1 :0 | x | (*rac*)-BINOL |
| | 2 | 1720,35 | 289,79 | 85,37 | 0,9296 | 0,0504 | 0,0200 | (*rac*)-BINOL + (*S*)-(*R,R*) | x | x | (*rac*)-BINOL + (*S*)-(*R,R*) |
| | 3 | 1726,58 | 231,53 | 128,57 | 0,9298 | 0,0401 | 0,0301 | (*rac*)-BINOL + (*S*)-(*R,R*) (+ (*R*)-(*R,R*)*) | x | x | (*rac*)-BINOL + (*S*)-(*R,R*) + (*R*)-(*R,R*) |
| | 4 | 1717,1 | 173,42 | 171,22 | 0,9296 | 0,0302 | 0,0402 | (*rac*)-BINOL + (*S*)-(*R,R*) (+ (R)-(R,R)*) | x | x | (*rac*)-BINOL + (*S*)-(*R,R*) + (*R*)-(*R,R*) |
| | 5 | 1723,23 | 115,64 | 214,74 | 0,9296 | 0,0201 | 0,0503 | (*S*)-(*R,R*) | x | 98,47 :1,53 | (*S*)-(*R,R*) |
| | 6 | 1717,6 | 57,96 | 257,52 | 0,9294 | 0,0101 | 0,0605 | (*R,R*)-DADPE | 0,13 :1 | x | (*S*)-(*R,R*) + (*R,R*)-DADPE |
| 90% | 1 | 1715,58 | 538,8 | 44,29 | 0,8991 | 0,0909 | 0,0101 | (*rac*)-BINOL | 1 :0 | x | (*rac*)-BINOL |
| | 2 | 1719,6 | 478,34 | 88,22 | 0,8995 | 0,0805 | 0,0200 | (*rac*)-BINOL + (*S*)-(*R,R*) | x | x | (*rac*)-BINOL + (*S*)-(*R,R*) |
| | 3 | 1726,56 | 419,01 | 133,33 | 0,8996 | 0,0703 | 0,0302 | (*rac*)-BINOL + (*S*)-(*R,R*) + (*R*)-(*R,R*) | x | x | (*rac*)-BINOL + (*S*)-(*R,R*) + (*R*)-(*R,R*) |
| | 4 | 1728,44 | 359,81 | 177,37 | 0,8997 | 0,0603 | 0,0401 | (*rac*)-BINOL + (*S*)-(*R,R*) + (*R*)-(*R,R*) | x | x | (*rac*)-BINOL + (*S*)-(*R,R*) + (*R*)-(*R,R*) |
| | 5 | 1730,31 | 299,47 | 222,05 | 0,8998 | 0,0501 | 0,0501 | (*S*)-(*R,R*) + (R)-(R,R) (+ (*rac*)-BINOL*) | x | x | (*S*)-(*R,R*) + (R)-(R,R) |
| | 6 | 1725,61 | 239,32 | 266,25 | 0,8996 | 0,0401 | 0,0602 | (*S*)-(*R,R*) + (R)-(R,R) | 0,965 :1 | x | (*S*)-(*R,R*) + (R)-(R,R) |
| | 7 | 1714,44 | 179,88 | 310,86 | 0,8989 | 0,0304 | 0,0707 | (*S*)-(*R,R*) | x | x | (*S*)-(*R,R*) |
| | 8 | 1724,2 | 119,72 | 355,52 | 0,8994 | 0,0201 | 0,0805 | (*S*)-(*R,R*) (+ (*R,R*)-DADPE*) | 0,6 :1 | x | (*S*)-(*R,R*) + (*R,R*)-DADPE |
| | 9 | 1729,85 | 59,61 | 399,53 | 0,8998 | 0,0100 | 0,0902 | (*R,R*)-DADPE | 0,05 :1 | x | (*R,R*)-DADPE |

* only trace amounts are visible

-The three points 95% - 4, 93% - 3 and - 4 (in yellow) were difficult to interpret due to trace amounts. The (*R*)-(*R,R*) cocrystal seemed to present in trace amounts in these samples.

## 6.2 In benzene

Table SI-4.9. Experimental data and results for the construction of the isoplethal ternary diagram (*rac*)-BINOL-(*R,R*)-DADPE-benzene at 20°.

| | | m(benz) (mg) | m((*rac*)-BINOL) (mg) | m((*R*,*R*)-DADPE) (mg) | %mol(benz) | %mol((*rac*)-BINOL) | %mol((*R*,*R*)-DADPE) | PXRD results | ratio BINOL:DADPE determined by NMR | ratio (*S*)-/(*R*)-BINOL determined by cHPLC | point |
|---|---|---|---|---|---|---|---|---|---|---|---|
| 98.50% | 4 | 1736.01 | 58.75 | 28.96 | 0.9849 | 0.0091 | 0.0060 | (*rac*)-BINOL (+ (*R*)-(*R*,*R*)-benzene?) | 1:0.16 | x | (*rac*)-BINOL + (*R*)-(*R*,*R*)-benzene |
| | 5 | 1745.41 | 45.63 | 38.4 | 0.9850 | 0.0070 | 0.0080 | (*R*)-(*R*,*R*)-benzene (+(*rac*)-BINOL*) | 1:0.925 | 4.34:95.66 | (*rac*)-BINOL + (*R*)-(*R*,*R*)-benzene |
| | 6 | 1748.77 | 32.6 | 48.44 | 0.9850 | 0.0050 | 0.0100 | | | | soluble |
| | 7 | 1737.38 | 19.52 | 58.42 | 0.9848 | 0.0030 | 0.0122 | | | | soluble |
| | 8 | 1745.46 | 6.6 | 67.64 | 0.9849 | 0.0010 | 0.0140 | | | | soluble |
| | 9 | 1750 | 0 | 72.5 | 0.9850 | 0.0000 | 0.0150 | (*R*,*R*)-DADPE | X | x | (*R*,*R*)-DADPE |
| 97% | 3 | 1746.43 | 152.26 | 34.2 | 0.9699 | 0.0231 | 0.0070 | (*rac*)-BINOL | 1:0 | x | (*rac*)-BINOL |
| | 4 | 1743.17 | 132.36 | 48.98 | 0.9699 | 0.0201 | 0.0100 | (*rac*)-BINOL (+ (*R*)-(*R*,*R*)-benzene*) | 1:0.245 | x | (*rac*)-BINOL + (*R*)-(*R*,*R*)-benzene |
| | 5 | 1747.61 | 105.86 | 68.79 | 0.9699 | 0.0160 | 0.0140 | (*R*)-(*R*,*R*)-benzene | X | 0.68:99.32 | (*R*)-(*R*,*R*)-benzene |
| | 6 | 1741.96 | 86.06 | 83.31 | 0.9699 | 0.0131 | 0.0171 | (*R*)-(*R*,*R*)-benzene | X | 0.50:99.50 | (*R*)-(*R*,*R*)-benzene |
| | 7 | 1739 | 66.35 | 98.04 | 0.9698 | 0.0101 | 0.0201 | (*R*)-(*R*,*R*)-benzene | X | 0:100 | (*R*)-(*R*,*R*)-benzene |
| | 8 | 1751.62 | 39.72 | 117.72 | 0.9700 | 0.0060 | 0.0240 | (*R*)-(*R*,*R*)-benzene + (*R*,*R*)-DADPE | 0.155:1 | x | (*R*)-(*R*,*R*)-benzene + (*R*,*R*)-DADPE |
| | 9 | 1750.56 | 19.54 | 132.28 | 0.9701 | 0.0030 | 0.0270 | (*R*,*R*)-DADPE | X | x | (*R*,*R*)-DADPE |
| 96% | 2 | 1745.59 | 234.12 | 24.61 | 0.9599 | 0.0351 | 0.0050 | (*rac*)-BINOL | X | x | (*rac*)-BINOL |
| | 3 | 1743.14 | 200.35 | 49.53 | 0.9599 | 0.0301 | 0.0100 | (*rac*)-BINOL | 1:0.1 | x | (*rac*)-BINOL + (*R*)-(*R*,*R*)-benzene |
| | 4 | 1737.81 | 167.25 | 74.37 | 0.9597 | 0.0252 | 0.0151 | (*rac*)-BINOL + (*R*)-(*R*,*R*)-benzene | x | x | (*rac*)-BINOL + (*R*)-(*R*,*R*)-benzene |
| | 5 | 1747.43 | 133.56 | 99.24 | 0.9599 | 0.0200 | 0.0201 | (*R*)-(*R*,*R*)-benzene + (*S*)-(*R*,*R*) | 1:0.965 | x | (*R*)-(*R*,*R*)-benzene + (*S*)-(*R*,*R*) |
| | 6 | 1748.07 | 100.28 | 123.88 | 0.9599 | 0.0150 | 0.0250 | (*R*)-(*R*,*R*)-benzene | x | 1.28:98.72 | (*R*)-(*R*,*R*)-benzene |
| | 7 | 1752.37 | 66.69 | 148.67 | 0.9601 | 0.0100 | 0.0300 | (*R*)-(*R*,*R*)-benzene | 1:0.99 | 0:100 | (*R*)-(*R*,*R*)-benzene |
| | 8 | 1743.7 | 33.54 | 173.01 | 0.9599 | 0.0050 | 0.0350 | (*R*,*R*)-DADPE (+ (*R*)-(*R*,*R*)-benzene*) | (0.087:1) | x | (*R*,*R*)-DADPE |

| | | | | | | | | | | |
|---|---|---|---|---|---|---|---|---|---|---|
| 95% | 2 | 1747,39 | 297,24 | 30,23 | 0,9499 | 0,0441 | 0,0060 | (*rac*)-BINOL | x | (*rac*)-BINOL |
| | 3 | 1748,72 | 256,59 | 60,24 | 0,9499 | 0,0380 | 0,0120 | (*rac*)-BINOL (+ (*R*)-(*R,R*)-benzene*) | 1:0.17 | x | (*rac*)-BINOL + (*R*)-(*R,R*)-benzene |
| | 4 | 1740,16 | 216,37 | 90,24 | 0,9497 | 0,0322 | 0,0181 | (*rac*)-BINOL + (*R*)-(*R,R*)-benzene | x | x | (*rac*)-BINOL + (*R*)-(*R,R*)-benzene |
| | 5 | 1740,08 | 175,55 | 120,2 | 0,9497 | 0,0261 | 0,0241 | (*R*)-(*R,R*)-benzene + (*S*)-(*R,R*) | 1:0.915 | x | (*R*)-(*R,R*)-benzene + (*S*)-(*R,R*) |
| | 6 | 1741,35 | 135,3 | 150,15 | 0,9497 | 0,0201 | 0,0301 | (*R*)-(*R,R*)-benzene + (*S*)-(*R,R*) | x | x | (*R*)-(*R,R*)-benzene + (*S*)-(*R,R*) |
| | 7 | 1746,18 | 94,63 | 180,48 | 0,9498 | 0,0140 | 0,0361 | (*R*)-(*R,R*)-benzene | x | 0,57:99,43 | (*R*)-(*R,R*)-benzene |
| | 8 | 1744,11 | 54,39 | 210,21 | 0,9498 | 0,0081 | 0,0421 | (*R*)-(*R,R*)-DADPE (+(*R*)-(*R,R*)-benzene*) | 0,19:1 | x | (*R*)-(*R,R*)-benzene + (*R,R*)-DADPE |
| | 9 | 1745,38 | 13,25 | 240,42 | 0,9499 | 0,0020 | 0,0481 | (*R,R*)-DADPE | x | x | (*R,R*)-DADPE |
| 93% | 1 | 1752,68 | 414,36 | 51,59 | 0,9300 | 0,0600 | 0,0101 | (*rac*)-BINOL | 1:0.03 | x | (*rac*)-BINOL |
| | 2 | 1733,71 | 345,77 | 102,7 | 0,9292 | 0,0506 | 0,0203 | (*rac*)-BINOL + (*R*)-(*R,R*)-benzene | x | x | (*rac*)-BINOL + (*R*)-(*R,R*)-benzene |
| | 3 | 1742,16 | 276,32 | 153,23 | 0,9297 | 0,0402 | 0,0301 | (*rac*)-BINOL + (*R*)-(*R,R*)-benzene + (*S*)-(*R,R*) | 1:0.675 | x | (*rac*)-BINOL + (*R*)-(*R,R*)-benzene + (*S*)-(*R,R*) |
| | 4 | 1737,74 | 207,1 | 204,28 | 0,9296 | 0,0302 | 0,0402 | (*R*)-(*R,R*)-benzene + (*S*)-(*R,R*) | 1:0.925 | x | (*R*)-(*R,R*)-benzene + (*S*)-(*R,R*) |
| | 5 | 1744,6 | 138,09 | 256,14 | 0,9297 | 0,0201 | 0,0502 | (*R*)-(*R,R*)-benzene | x | 6,31:93,69 | (*R*)-(*R,R*)-benzene + (*S*)-(*R,R*) |
| | 6 | 1752,39 | 69,14 | 307,63 | 0,9299 | 0,0100 | 0,0601 | (*R*)-(*R,R*)-benzene + (*R,R*)-DADPE | 0,158:1 | x | (*R*)-(*R,R*)-benzene + (*R,R*)-DADPE |
| 90% | 1 | 1745,13 | 642,19 | 52,26 | 0,8998 | 0,0903 | 0,0099 | (*rac*)-BINOL | 1:0.025 | | (*rac*)-BINOL |
| | 2 | 1752,06 | 570,29 | 105,86 | 0,9001 | 0,0799 | 0,0200 | (*rac*)-BINOL + (*R*)-(*R,R*)-benzene | 1:0.165 | x | (*rac*)-BINOL + (*R*)-(*R,R*)-benzene |
| | 3 | 1742,57 | 499,48 | 158,75 | 0,8995 | 0,0703 | 0,0302 | (*rac*)-BINOL + (*R*)-(*R,R*)-benzene (+ (*S*)-(*R,R*)*) | 1:0.425 | x | (*rac*)-BINOL + (*R*)-(*R,R*)-benzene + (*S*)-(*R,R*) |
| | 4 | 1750,66 | 428,38 | 211,46 | 0,8999 | 0,0601 | 0,0400 | (*rac*)-BINOL + (*R*)-(*R,R*)-benzene + (*S*)-(*R,R*) | x | x | (*rac*)-BINOL + (*R*)-(*R,R*)-benzene + (*S*)-(*R,R*) |
| | 5 | 1745,47 | 356,92 | 264,55 | 0,8996 | 0,0502 | 0,0502 | (*R*)-(*R,R*)-benzene + (*S*)-(*R,R*) (+(*rac*)-BINOL*) | 1:1.025 | x | (*R*)-(*R,R*)-benzene + (*S*)-(*R,R*) |
| | 6 | 1740,69 | 285,79 | 317,12 | 0,8994 | 0,0403 | 0,0603 | (*R*)-(*R,R*)-benzene + (*S*)-(*R,R*) | x | x | (*R*)-(*R,R*)-benzene + (*S*)-(*R,R*) |
| | 7 | 1751,41 | 214,52 | 370,45 | 0,8999 | 0,0301 | 0,0700 | (*R*)-(*R,R*)-benzene + (*S*)-(*R,R*) | x | x | (*R*)-(*R,R*)-benzene + (*S*)-(*R,R*) |
| | 8 | 1644,68 | 143,03 | 423,16 | 0,8941 | 0,0212 | 0,0846 | (*R*)-(*R,R*)-benzene (+ (*S*)-(*R,R*)*) | x | 3,73:96,27 | (*R*)-(*R,R*)-benzene + (*S*)-(*R,R*) |
| | 9 | 1744,68 | 71,22 | 476,49 | 0,8996 | 0,0100 | 0,0904 | (*R,R*)-DADPE (+ (*R*)-(*R,R*)-benzene*) | 0,12:1 | x | (*R*)-(*R,R*)-benzene + (*R,R*)-DADPE |

* only trace amounts are visible

# 7. Resolution of BINOL with (*S,S*)-DADPE

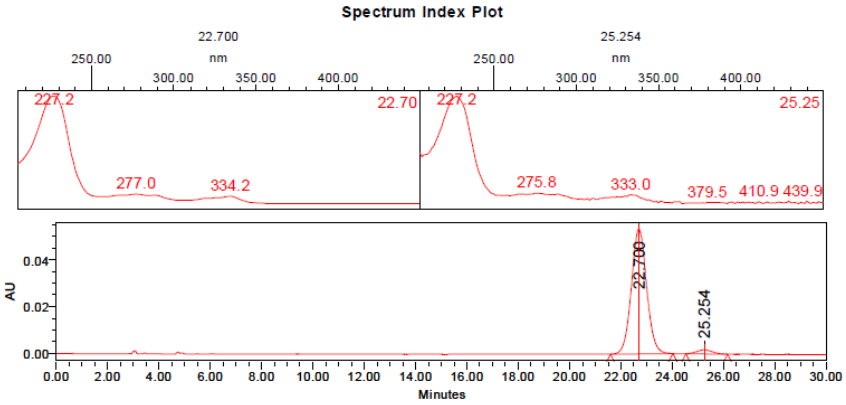


Peak Results

| | Name | RT | Area | % Area |
|---|---|---|---|---|
| 1 | | 22.700 | 2178080 | 96.77 |
| 2 | | 25.254 | 72587 | 3.23 |

Figure SI-4.23. *c*HPLC analysis of the powder recovered from the resolution of (*rac)*-BINOL by (*S,S*)-DADPE in benzene.

# 8. Upscaled resolutions of BINOL

## 8.1 In toluene

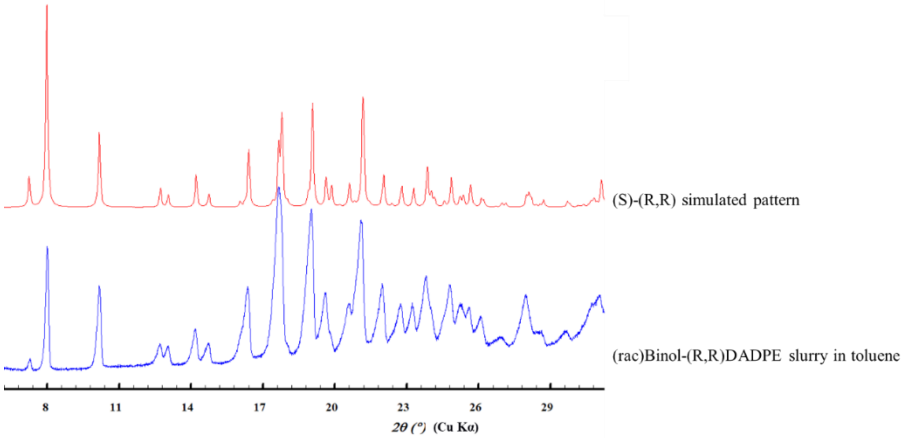


Figure SI-4.24. PXRD (using Cu Kα) of the powder recovered from the resolution of 2 g of (*rac*)-BINOL by (*R,R*)-DADPE in toluene, compared to the simulated pattern of the *(S)-(R,R)* cocrystal (**DICVUH**[102]).

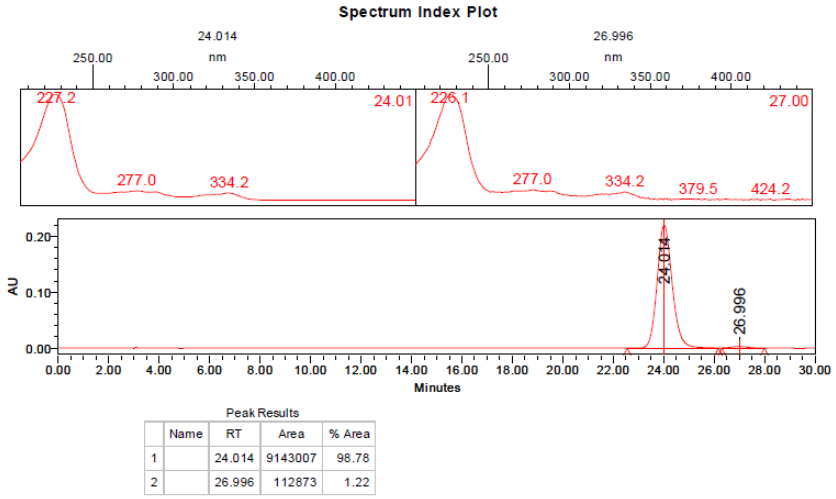


Peak Results

| | Name | RT | Area | % Area |
|---|---|---|---|---|
| 1 | | 24.014 | 9143007 | 98.78 |
| 2 | | 26.996 | 112873 | 1.22 |

Figure SI-4.25. *c*HPLC analysis of the powder recovered from the resolution of 2 g of (*rac*)-BINOL by (*R,R*)-DADPE in toluene.

## 8.2 In benzene

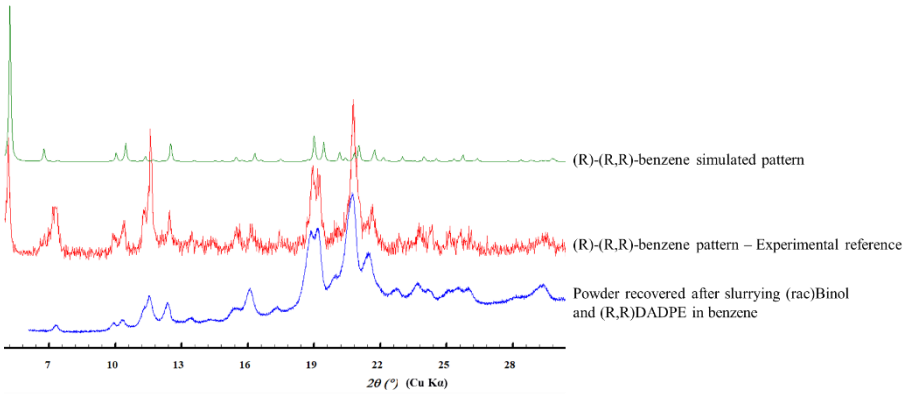


Figure SI-4.26. PXRD (using Cu Kα) of the powder recovered from the resolution of 2 g of (*rac*)-BINOL by (*R,R*)-DADPE in benzene, compared to the measured and the simulated patterns of the *(R)-(R,R)*-benzene cocrystal-solvate.

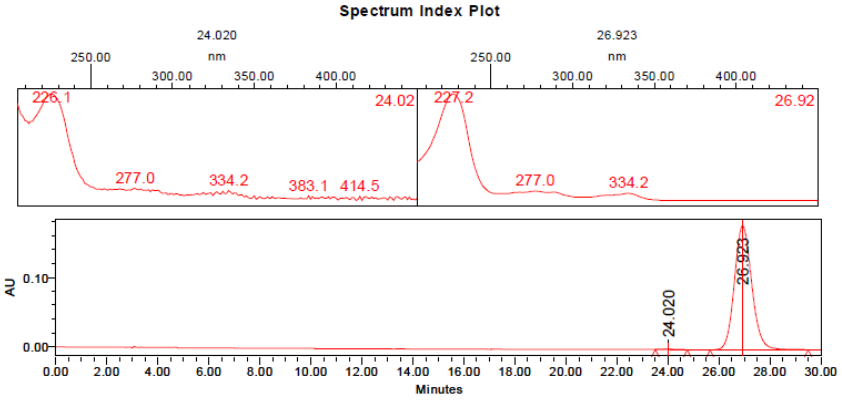


Peak Results

| | Name | RT | Area | % Area |
|---|---|---|---|---|
| 1 | | 24.020 | 29781 | 0.35 |
| 2 | | 26.923 | 8392381 | 99.65 |

Figure SI-4.27. *c*HPLC analysis of the powder recovered from the resolution of 2 g of (*rac*)-BINOL by (*R*,*R*)-DADPE in benzene.

# Appendixe C

Supporting information to Chapter 5

## 1. *r*HPLC

### 1.1 Calibration lines for the nefi and MA dosage

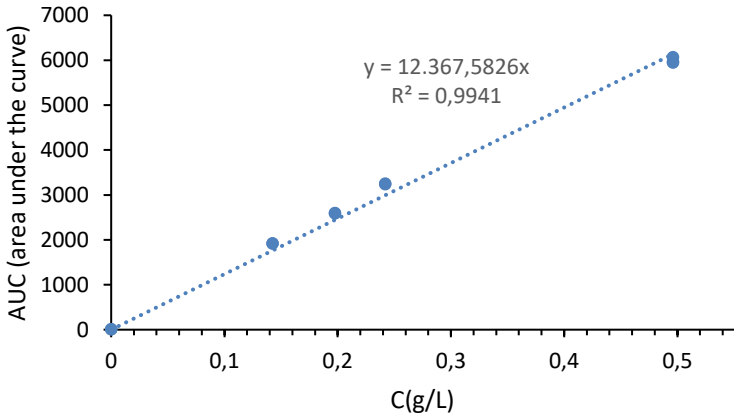


Figure SI-5.1. Calibration line for nefiracetam dosage in *r*HPLC (λ = 210nm). The compounds were dissolved in a solution composed by 50 vol.% acetonitrile, 50 vol.% Milli-Q water.

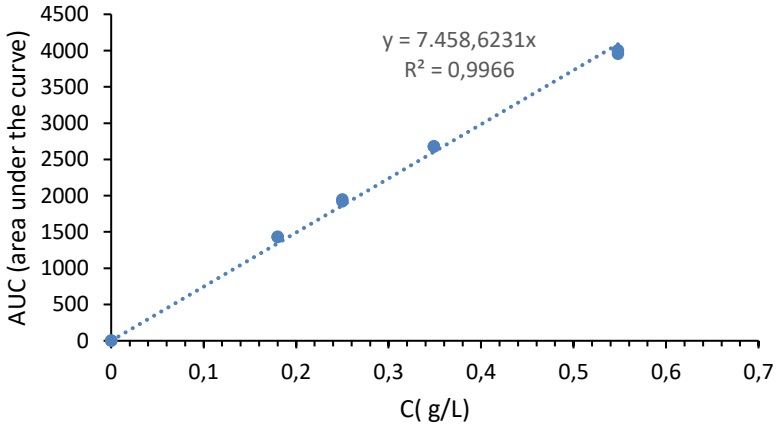


Figure SI-5.2. Calibration line for mandelic acid dosage in *r*HPLC (λ = 210nm). The compounds were dissolved in a solution composed by 50 vol.% acetonitrile, 50 vol.% Milli-Q water.

## 1.2 Dosage

Table SI-5.1. Powder compositions based upon *r*HPLC calibration (λ = 210nm). The samples were dissolved in a solution composed by 50 vol.% acetonitrile, 50 vol.% Milli-Q water.

| Sample | AUC(MA) | AUC(nefi) | C(MA) (g/L) | C(nefi (g/L) | C(MA) (mmol/L) | C(nefi (mmol/L) | eq(MA) | eq(nefi) |
|---|---|---|---|---|---|---|---|---|
| 1-reacA | 1925.9 | 5019.8 | 0.2582 | 0.4059 | 1.6971 | 1.6479 | 1 | 0.97 |
| 1-reacB | 1729.5 | 4556.7 | 0.2319 | 0.3684 | 1.5240 | 1.4959 | 1 | 0.98 |
| 2-reacA | 1603.1 | 4263.2 | 0.2149 | 0.3447 | 1.4126 | 1.3995 | 1 | 0.99 |
| 2-reacB | 1508.2 | 4044.7 | 0.2022 | 0.3270 | 1.3290 | 1.3278 | 1 | 1.00 |
| 3-reacA | 1731.2 | 4547.1 | 0.2321 | 0.3677 | 1.5255 | 1.4927 | 1 | 0.98 |
| 3-reacB | 1673.1 | 4484.4 | 0.2243 | 0.3626 | 1.4743 | 1.4722 | 1 | 1.00 |
| 4-reacA | 1461.7 | 4237.2 | 0.1960 | 0.3426 | 1.2880 | 1.3910 | 1 | 1.08 |
| 4-reacB | 1424.7 | 4007.7 | 0.1910 | 0.3240 | 1.2554 | 1.3157 | 1 | 1.05 |
| 5-reacA | 1491.9 | 4514.1 | 0.2000 | 0.3650 | 1.3146 | 1.4819 | 1 | 1.13 |
| 5-reacB | 1539.2 | 4660.4 | 0.2064 | 0.3768 | 1.3563 | 1.5299 | 1 | 1.13 |
| 6-reacA | 1437.3 | 3783.2 | 0.1927 | 0.3059 | 1.2665 | 1.2420 | 1 | 0.98 |
| 6-reacB | 1098.9 | 2962.7 | 0.1473 | 0.2396 | 0.9683 | 0.9726 | 1 | 1.00 |
| 7-CylA | 1369.8 | 3979.9 | 0.1837 | 0.3218 | 1.2071 | 1.3065 | 1 | 1.08 |
| 7-CylB | 1566.2 | 4559.6 | 0.2100 | 0.3687 | 1.3801 | 1.4968 | 1 | 1.08 |

| | | | | | | | | |
|---|---|---|---|---|---|---|---|---|
| 8-CylA | 1440 | 4037.5 | 0.1931 | 0.3265 | 1.2689 | 1.3254 | 1 | 1.04 |
| 8-CylB | 1560.8 | 4332.2 | 0.2093 | 0.3503 | 1.3754 | 1.4222 | 1 | 1.03 |
| 9-CylA | 1595.3 | 4401.7 | 0.2139 | 0.3559 | 1.4058 | 1.4450 | 1 | 1.03 |
| 9-CylB | 1373.4 | 3950.1 | 0.1841 | 0.3194 | 1.2102 | 1.2968 | 1 | 1.07 |
| 10-CylA | 1553.8 | 4258.6 | 0.2083 | 0.3443 | 1.3692 | 1.3980 | 1 | 1.02 |
| 10-CylB | 1526.9 | 4155.3 | 0.2047 | 0.3360 | 1.3455 | 1.3641 | 1 | 1.01 |
| 11-CylA | 1499.9 | 4076.7 | 0.2011 | 0.3296 | 1.3217 | 1.3383 | 1 | 1.01 |
| 11-CylB | 1589.9 | 4300.6 | 0.2132 | 0.3477 | 1.4010 | 1.4118 | 1 | 1.01 |
| 17-cylA | 1703.4 | 4550.1 | 0.2284 | 0.3679 | 1.5010 | 1.4937 | 1 | 1.00 |
| 17-cylB | 1383.4 | 3702.7 | 0.1855 | 0.2994 | 1.2190 | 1.2155 | 1 | 1.00 |
| 21-cyl1A | 1517.3 | 4204.8 | 0.2034 | 0.3400 | 1.3370 | 1.3804 | 1 | 1.03 |
| 21-cyl1B | 1405.9 | 3911.9 | 0.1885 | 0.3163 | 1.2389 | 1.2842 | 1 | 1.04 |
| 21-cyl2A | 1593.6 | 4332.5 | 0.2137 | 0.3503 | 1.4043 | 1.4223 | 1 | 1.01 |
| 21-cyl2B | 1844 | 5024.1 | 0.2472 | 0.4062 | 1.6249 | 1.6493 | 1 | 1.02 |
| 16-cylA | 1533.6 | 4120.2 | 0.2056 | 0.3331 | 1.3514 | 1.3526 | 1 | 1.00 |
| 16-cylB | 1942 | 5003.2 | 0.2604 | 0.4045 | 1.7113 | 1.6425 | 1 | 0.96 |

## 2. XRPD

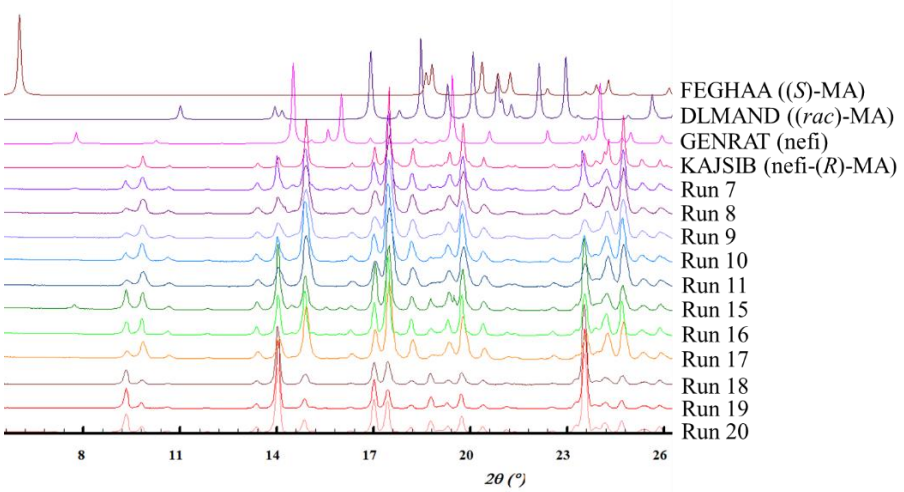


Figure SI-5.3. Comparison of the XRPD patterns (using Cu Kα) of the powder recovered on the seeded cylinder of Runs 7, 8, 9, 10, 11, 15, 16, 17, 18, 19, and 20 and the simulated patterns of the reported nefi-(*R*)-MA-cocrystal (CCDC refcode KAJSIB)[88] and parent compounds nefi (CCDC refcode GENRAT)[136], (*rac*)-MA (CCDC refcode DLMAND)[137], and (*S*)-MA (CCDC refcode FEGHAA)[138].

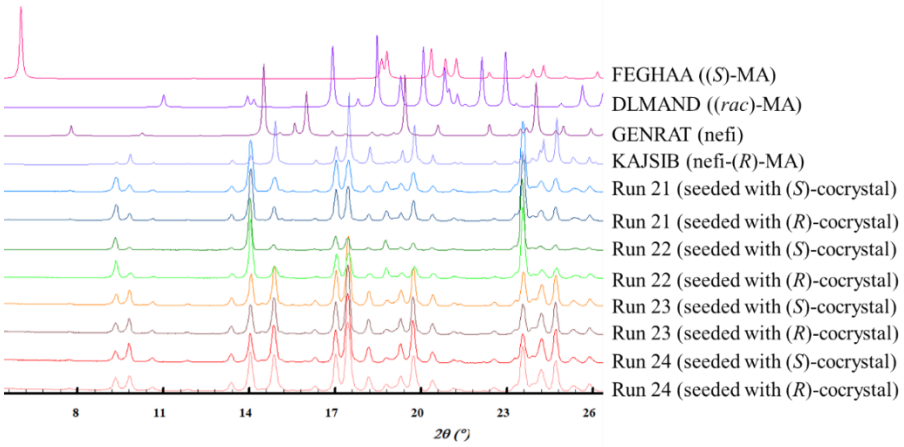


Figure SI-5.4. Comparison of the XRPD patterns (using Cu Kα) of the powder recovered on both halves of the seeded cylinder of Runs 21, 22, 23, and 24 and the simulated patterns of the reported nefi-(*R*)-MA-cocrystal (CCDC refcode KAJSIB)[88] and parent compounds nefi (CCDC refcode GENRAT)[136], (*rac*)-MA (CCDC refcode DLMAND)[137], and (*S*)-MA (CCDC refcode FEGHAA)[138].

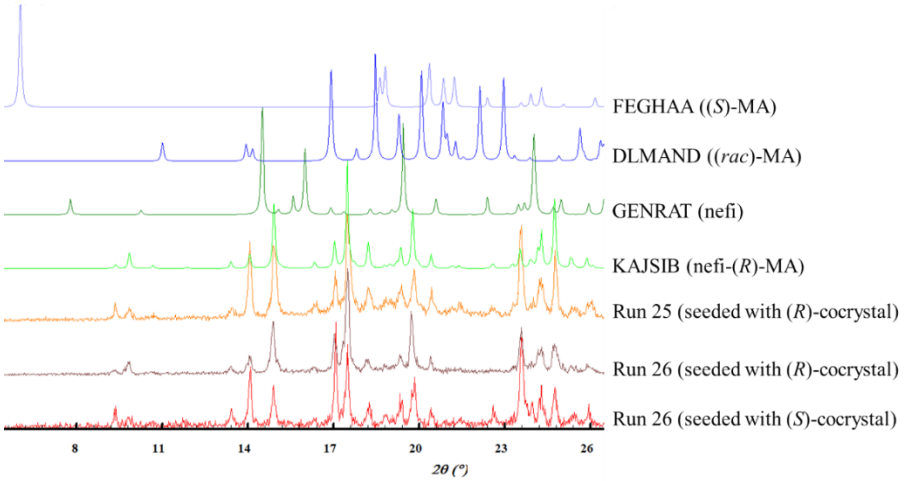


Figure SI-5.5. Comparison of the XRPD patterns (using Cu Kα) of the powder recovered on the lower seeded cylinder of Run 25 (not enough powder was recovered on its upper seeded cylinder for the XRPD analysis), on both pieces of the seeded cylinder of Run 26, and the simulated patterns of the reported nefi-(*R*)-MA-cocrystal (CCDC refcode KAJSIB)[88] and parent compounds nefi (CCDC refcode GENRAT)[136], (*rac*)-MA (CCDC refcode DLMAND)[137], and (*S*)-MA (CCDC refcode FEGHAA)[138].

# Appendixe D

## Characteristics of the solvents used

Table SI-6.1. Properties of the solvents used in this work.

| | **Toluene** | **Benzene** | **EtOAc** | **ACN** | **DCM** | **Acetone** | **MeOH** | **EtOH** | **IPA** | **Isobutanol** |
|---|---|---|---|---|---|---|---|---|---|---|
| Chemical formula | $C_6H_5CH_3$ | $C_6H_6$ | $C_4H_8O_2$ | $C_2H_3N$ | $CH_2Cl_2$ | $C_3H_6O$ | $CH_3OH$ | $C_2H_6O$ | $C_3H_8O$ | $C_4H_{10}O$ |
| Dipole moment (D) | 0.31 | 0 | 1.88 | 3.93 | 1.14 | 2.69 | 2.87 | 1.66 | 1.69 | 1.79 |
| MW ($g.mol^{-1}$) | 92.14 | 78.11 | 88.11 | 41.05 | 84.93 | 58.08 | 32.04 | 46.07 | 60.10 | 74.12 |
| Density | 0.867 | 0.876 | 0.902 | 0.786 | 1.33 | 0.784 | 0.792 | 0.789 | 0.786 | 0.802 |
| Melting point (°C) | -95 | 5.5 | -83.6 | -45 | -96.7 | -95 | -97.6 | -114.1 | -89 | -108 |
| Boiling point (°C) | 110.6 | 80.1 | 77.1 | 82 | 39.6 | 56 | 64.7 | 78.37 | 82.3 | 108 |
| Danger | Flammable<br>Irritant<br>Cause drowsiness<br>Cause genetic defects | Flammable<br>Irritant<br>Carcinogenic<br>Cause genetic defects<br>Harmful to aquatic life | Flammable<br>Irritant | Flammable<br>Irritant<br>Toxic | Irritant<br>Cause drowsiness<br>Toxic<br>Suspected carcinogenic | Flammable<br>Irritant<br>Cause drowsiness | Flammable<br>Toxic | Flammable<br>Eye irritant | Flammable<br>Eye irritant<br>Cause drowsiness | Flammable<br>Irritant<br>Cause drowsiness |

| | | | | | | | | | | |
|---|---|---|---|---|---|---|---|---|---|---|
| | Suspected teratogenic<br><br>Harmful to aquatic life | | | | | | | | | |